Politecnico di Milano
Dipartimento di Matematica

Ph.D. programme in
Mathematical Models and Methods in Engineering

Mathematical modelling of soft and active matter

Candidate:
Davide Riccobelli

Advisor:
Prof. Pasquale Ciarletta

Chair of The Doctoral Program:
Prof. Irene Sabadini

XXXI cycle

CONTENTS

ABSTRACT v
ACKNOWLEDGEMENTS vii
1 INTRODUCTION 1
  1.1 Basic notions of non-linear elasticity 1
    1.1.1 Kinematics and balance equations 1
    1.1.2 Constitutive laws in hyperelasticity 3
    1.1.3 Well posedness of the non-linear elastic problem 5
  1.2 Active materials 8
    1.2.1 Growth and remodelling 9
    1.2.2 Active strain *versus* active stress 9
  1.3 Morpho–elasticity 10
  1.4 Outline of the thesis 12
2 ON THE EXISTENCE OF ELASTIC MINIMIZERS FOR INITIALLY STRESSED MATERIALS 13
  2.1 Background and notation 15
  2.2 Mathematical frameworks for initially stressed materials 17
    2.2.1 The theory of elastic distortions 17
    2.2.2 The theory of initially stressed bodies 19
  2.3 Existence of a relaxed state 22
  2.4 Existence of elastic minimizers for initially stressed bodies 24
  2.5 An illustrating example: the relaxed state of a soft disc with anisotropic initial stress 28
  2.6 Discussion and concluding remarks 30
3 MODELLING OF ACTIVE PHENOMENA IN BIOLOGICAL TISSUES 33
  3.1 Activation of a muscle as a mapping of stress-strain curves 33
    3.1.1 The active strain approach 34
    3.1.2 Activation as a linear mapping 35
    3.1.3 An alternative approach: the mixture active strain approach 37
    3.1.4 Discussion and concluding remarks 43
  3.2 Solid tumours are poroelastic solids with a chemo–mechanical feedback on growth 44
    3.2.1 Background: elementary rheology and growth theory 45
    3.2.2 Are solid tumours fluids? 46
    3.2.3 Growth and stress 48
    3.2.4 Mechanobiological feedback and equilibrium 51
    3.2.5 Dynamics of the nutrient and inhomogeneity of growth 53
    3.2.6 Numerical simulations 54
    3.2.7 Discussion and concluding remarks 60
    3.2.8 Appendix – Stability of the homogeneous solution 62

4 PATTERN FORMATION IN SOFT MATTER 65
4.1 Morpho–elastic model of the tortuous tumour vessels 66
4.1.1 The elastic model 67
4.1.2 Linear stability analysis 70
4.1.3 Post-buckling behaviour 77
4.1.4 Discussion and concluding remarks 80
4.1.5 Appendix – Expressions of the components of the Stroh matrix 81
4.2 Shape transitions in a soft sphere with residual stresses 83
4.2.1 The elastic model 83
4.2.2 Incremental problem and linear stability analysis 87
4.2.3 Finite element implementation and post-buckling analysis 95
4.2.4 Discussion and concluding remarks 100
4.3 Rayleigh–Taylor instability in soft elastic layers 102
4.3.1 The non-linear elastic problem and its basic solution . . . 103
4.3.2 Linear stability analysis of the basic solution 105
4.3.3 Post-buckling analysis 110
4.3.4 Discussion and concluding remarks 115
4.3.5 Appendix – Structure of the matrix M 117
4.3.6 Appendix – Expressions of the coefficients c_j 117
5 CONCLUSIONS AND PERSPECTIVES 119
BIBLIOGRAPHY 125

ABSTRACT

This thesis focuses on the mathematical modelling of soft and active solid matter using continuum mechanics. An elastic body is said to be soft if it can undergo large deformations; it is said to posses an active behaviour when it can rearrange its micro-structure in presence of external stimuli, not necessarily of mechanical nature. Examples of active processes are biological growth or the contraction of dielectric elastomers provoked by an electromagnetic field.

The research activities undertaken concerned both analytical and numerical tasks to solve some physical problems in this field. In particular, we focused on:

- the constitutive theory of soft materials with initial stresses,
- the mathematical modelling of active phenomena in biological matter,
- the formation of patterns in soft solids due to a mechanical instability.

The thesis is organized as follows. In Chapter 1, we briefly expose some basic notions of non-linear elasticity. We review the fundamental literature on the mathematical modelling of biological growth and muscle contraction, and on an emerging field in mechanics, called morpho–elasticity.

In Chapter 2, we investigate the mathematical description of elastic bodies possessing a non-vanishing distribution of initial stress, i.e. the Cauchy stress in the undeformed reference configuration. We provide new mathematical and physical interpretations of the required constitutive restrictions, proving the existence of energy minimizers in the framework of the theory of initially stressed materials.

In Chapter 3, we propose new mathematical models of active processes in soft biological matter, particularly focusing on tumour growth and muscular contraction. We show that it is not possible to recover the experimental stress-stretch curve corresponding to a uniaxial deformation of a skeletal muscle using the active strain method, based on a multiplicative decomposition of the deformation gradient. Instead, we propose an alternative model based on a mixture approach, called *mixture active strain*. Moreover, we show that solid tumours behave as growing poroelastic materials, where the growth is modulated by a chemo–mechanical feedback. The results of our model are in very good agreement with both *in-vitro* and *ex-vivo* experimental data.

In Chapter 4, we model morpho–elastic phenomena in both living and inert soft matter. First, we investigate the mechanics of tumour capillaries, showing that the incompatible axial growth of the straight vessel can trigger an elastic instability, generating a tortuous shape. Second, we study how residual stresses can induce mechanical instabilities in soft spheres, e.g. in growing tumour masses. Considering several spatial distributions of the residual stress field, we prove that different topological transitions occur in the sphere where the hoop residual stress reaches its maximum compressive value. Third, we show that gravity bulk force can cause an elastic instability in soft elastic bilayers. We show that the non-linear elastic effects saturate the dynamic instability of the bifurcated solutions that characterize fluid-like matter, displaying a rich morphological diagram where both digitations and stable wrinkling can emerge.

Finally, the results of this thesis prove how the combination of nonlinearities and nonconvexity in elastic mixed boundary value problems may emerge as complex physical phenomena, whose understanding requires the development of novel mathematical tools (Chapter 5).

ACKNOWLEDGEMENTS

This thesis is the joint result of three years of work and of the guidance of many people who have supported me during this journey.

First, this thesis would not ever be finished without the help and the endless patience of Pasquale Ciarletta, who has been a valuable scientific reference, an helpful and supportive advisor, aiding me to overcome the difficulties encountered during these years. I wish to thank Davide Ambrosi, for his continuous support and patience, it has been a wonderful experience to learn from him and to work together.

I would also like to thank Prof. Lev Truskinovsky and Prof. Corrado Maurini for warmly welcoming me in Paris and for the help they gave me during the six months I have spent at the ESPCI and at the Université Pierre et Marie Curie. I am thankful with Prof. Dominic Vella for having been so kind and helpful during my visiting period in Oxford.

I also wish to thank all the people that shared this trip with me. I am especially grateful to Abramo Agosti, Giulia Bevilacqua, Simone Pezzuto and Matteo Taffetani for their valuable suggestions and support.

I thank Giulia Giantesio, Luca Lussardi, Alfredo Marzocchi and Alessandro Musesti for suggesting me to continue my studies and for having instilled in me the passion for mathematics and continuum mechanics.

Finally, I would not have achieved this result without the love and help of my parents and Cecilia, thank you for always supporting me.

1 INTRODUCTION

This thesis deals with the mathematical modelling of soft and active solid bodies using continuum mechanics. An elastic material is said to be soft if it can undergo very large deformations. Furthermore, a material is said to possess an active behaviour if it can rearrange its micro-structure in response to non-mechanical stimuli.

The mathematical modelling of soft and active materials poses several open challenges. First, soft solids may be subjected to large deformations, thus the constitutive laws should take into account both physical and geometrical non-linearities. Moreover, active materials are open thermo-dynamical systems that generally operate in out-of-equilibrium conditions, driven by the micro-scale flux of multiphysics energies, e.g. of chemical or electrical origin, that are transformed into mechanical energy.

This work is motivated by the increasing interest in developing accurate models of soft and active materials for engineering applications, such as the design of new metamaterials using additive manufacturing. It also responds to a basic science interest for providing a mathematical understanding of some processes in developmental biology, such as the emergence of shape and the generation of active stresses in living matter.

In the following, we summarize the basic mathematical notions characterizing the theoretical background of this thesis.

1.1 BASIC NOTIONS OF NON-LINEAR ELASTICITY

In this Section, we collect some basic notions of non-linear elasticity. After introducing the kinematic description of the main balance laws, we focus on the mathematical well-posedness of constitutive models in hyperelasticity.

1.1.1 Kinematics and balance equations

We denote by $\mathcal{L}(\mathbb{R}^n)$ the set of all the automorphisms of $\mathbb{R}^n$, and by $\mathcal{L}^+(\mathbb{R}^n)$ the group (with respect to the operation of function composition) of all the linear applications belonging to $\mathcal{L}(\mathbb{R}^n)$ with positive determinant.

Let $\mathcal{O}(\mathbb{R}^n)$ be the group such that

$$\mathsf{Q}^T\mathsf{Q} = \mathsf{I} \qquad \forall \mathsf{Q} \in \mathcal{L}(\mathbb{R}^n)$$

where I is the identity.

We indicate with $\mathcal{O}^+(\mathbb{R}^n) \subset \mathcal{O}(\mathbb{R}^n)$ the group of all the elements of $\mathcal{O}(\mathbb{R}^n)$ with positive determinant; if $n = 3$, this group coincides with the set of the rigid rotations. We also introduce the set $\mathcal{S}(\mathbb{R}^n)$ of all the symmetric linear applications belonging to $\mathcal{L}(\mathbb{R}^n)$.

Denoting by $\mathbb{E}^3$ the three-dimensional Euclidean space, we call *reference configuration* of the body a regular subset Ω_0 of $\mathbb{E}^3$.

Let $\boldsymbol{X} \in \Omega_0$ be the *Lagrangian* or *Material coordinate* of a point. The motion is described by the vector field $\boldsymbol{\varphi}$, called *deformation*:

$$\boldsymbol{\varphi} : \Omega_0 \to \mathbb{R}^3.$$

We indicate with $\Omega := \boldsymbol{\varphi}(\Omega_0)$ the deformed configuration of the body. Let $\boldsymbol{x}(t) = \boldsymbol{\varphi}(\boldsymbol{X}, t)$ be the *Eulerian* or *spatial coordinate* of the point $\boldsymbol{X}$. We indicate with $\mathsf{F} = \operatorname{Grad} \boldsymbol{\varphi}$ the *deformation gradient*. We assume that $J = \det \mathsf{F} > 0$, so that $\mathsf{F}(\boldsymbol{X}) \in \mathcal{L}^+(\mathbb{R}^3)$.

The vector

$$\boldsymbol{u}(\boldsymbol{X}) = \boldsymbol{\varphi}(\boldsymbol{X}) - \boldsymbol{X}$$

is the *displacement* of a point $\boldsymbol{X} \in \Omega_0$, so that $\mathsf{F} = \mathsf{I} + \operatorname{Grad} \boldsymbol{u}$, where I is the identity matrix. We consider bodies with a continuous distribution of mass. Let ρ be the density field, imposing the conservation of mass for each subset of Ω, we obtain

$$\rho J = \rho_0$$

where ρ_0 is the mass density in the reference configuration.

The following Cauchy postulate allows to model the internal forces exchanged within the body *Cauchy postulate*:

Axiom 1.1.1. *If $S \subset \Omega$ is a surface with normal $\boldsymbol{n}$, there exists a vector field*

$$\boldsymbol{t}(\boldsymbol{x}, S)$$

representing the density of force per unit area exerted through S by a material from one side of S to the other.

This assumption states that the internal forces act like a flux through S. We can now state the conservation of linear momentum in Eulerian form. Its expression in the quasi static case reads

$$\int_P \rho \boldsymbol{b}\, dx + \int_{\partial P} \boldsymbol{t}\, ds = \boldsymbol{0}, \tag{1.1}$$

where $\boldsymbol{b}$ is the density of external force per unit mass and P is a regular subset of Ω. We now illustrate the Cauchy theorem, a milestone of continuum mechanics [102].

Theorem 1.1.1 (Cauchy stress theorem). *For each $\boldsymbol{x} \in \Omega$ the vector field $\boldsymbol{t}(\boldsymbol{x}, \boldsymbol{n})$ is linear in $\boldsymbol{n}$; in other words, there is a tensor field T, called* Cauchy stress tensor, *such that*

$$\mathsf{T}\boldsymbol{n} = \boldsymbol{t}.$$

Moreover T *is symmetric if and only if the conservation of angular moment holds, i.e.:*

$$\int_P \rho \boldsymbol{x} \times \boldsymbol{b}\, d\boldsymbol{x} + \int_{\partial P} \boldsymbol{x} \times \boldsymbol{t}\, ds = \mathbf{0}. \tag{1.2}$$

Applying the Cauchy stress theorem and the divergence theorem, it follows that

$$\rho \boldsymbol{b} + \operatorname{div} \mathsf{T} = \mathbf{0}, \tag{1.3}$$

which gives the balance of linear momentum.

For an elastic body, it is assumed that the Cauchy stress tensor depends on the deformation gradient, i.e.

$$\mathsf{T} = \mathsf{T}(\boldsymbol{X}, \mathsf{F}(\boldsymbol{X})).$$

The Cauchy stress tensor describes the contact force per unit area in the deformed configuration. Its counterpart in the reference configuration is the *first Piola-Kirchhoff stress tensor* P, defined as the Piola transformation of T, i.e.

$$\mathsf{P} = J\mathsf{F}^{-1}\mathsf{T}. \tag{1.4}$$

Setting now $\boldsymbol{B} = J\boldsymbol{b}$, we can state the Lagrangian form of the equation of equilibrium:

$$\operatorname{Div} \mathsf{P} + \rho_0 \boldsymbol{B} = \mathbf{0}.$$

Finally, we impose Dirichlet boundary conditions on a part of the boundary, enforcing the displacement on a subset Γ_0, and Neumann boundary conditions on the remaining part, describing the force applied on a subset Γ_1, leading to the following mixed boundary value problem

$$\begin{cases} \operatorname{Div} \mathsf{P} + \rho_0 \boldsymbol{B} = \mathbf{0}, & \text{in } \Omega_0 \\ \boldsymbol{u} = \boldsymbol{u}_0, & \text{on } \Gamma_0 \\ \mathsf{P}^T \boldsymbol{N} = \boldsymbol{s}_0, & \text{on } \Gamma_1 \\ \Gamma_0 \cap \Gamma_1 = \emptyset,\ \Gamma_0 \cup \Gamma_1 = \partial\Omega_0. \end{cases}$$

which represents a general form of a boundary value problem in nonlinear elasticity.

1.1.2 Constitutive laws in hyperelasticity

A material is said to be *perfectly elastic* if it does not produce entropy when deformed [209, 113]. Thus the internal dissipation is zero during any admissible motion and the second law of thermodynamics degenerates into an equality. Such a material is said to be *hyperelastic* if there exists a free energy density ψ, also known as *strain energy density*, depending only on the deformation gradient.

Exploiting the Clausius-Duhem form of the second law of thermodynamics, it is possible to prove that the constitutive equation for a hyperelastic material reads:

$$\mathsf{P} = \frac{\partial \psi}{\partial \mathsf{F}} \qquad P_{ij} = \frac{\partial \psi}{\partial F_{ji}},$$

where ψ may depend on the material position $\boldsymbol{X}$ if the body is inhomogeneous.

One of the first soft material that has been extensively studied is rubber. Indeed, from the pioneering work of Treloar [208] it was clear that the theory of linear elasticity is not appropriate to model rubbery materials, in particular in the regime of large deformations (see Fig. 1.1). Rubber can indeed maintain an elastic behaviour even when subjected to extension of over 400% with respect to the initial length.

To reproduce experimental results of the finite deformation of soft tissues it is necessary to exploit nonlinear constitutive relations [209]. The dependence of ψ on F can be restricted making use of the constitutive restrictions of continuum mechanics. Indeed, the energy must be independent of the position of the reference frame, leading to the *frame indifference axiom*, stating that

$$\psi(\mathsf{F}) = \psi(\mathsf{QF}) \qquad \forall \mathsf{F} \in \mathcal{L}^+(\mathbb{R}^3) \text{ and } \forall \mathsf{Q} \in \mathcal{O}^+(\mathbb{R}^3).$$

A direct consequence of this assumption, together with the polar decomposition theorem, is that a strain energy function is frame indifferent if and only if

$$\psi(\mathsf{F}) = \hat{\psi}(\mathsf{C}),$$

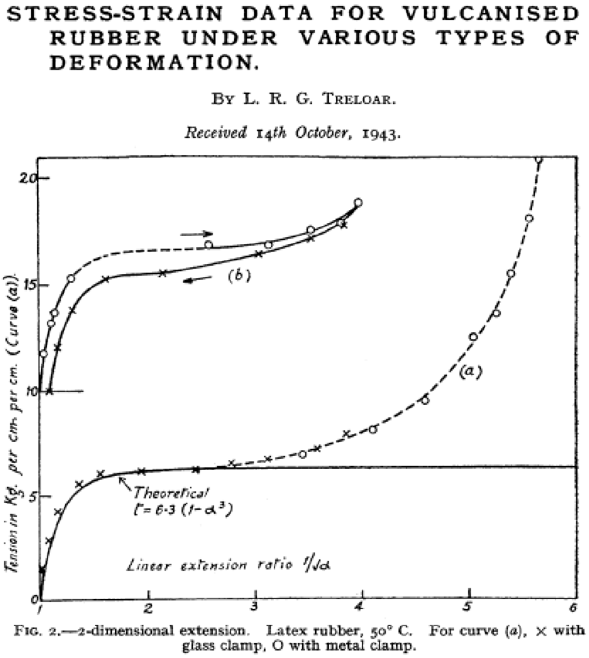

STRESS-STRAIN DATA FOR VULCANISED RUBBER UNDER VARIOUS TYPES OF DEFORMATION.

By L. R. G. Treloar.

Received 14th October, 1943.

Fig. 2.—2-dimensional extension. Latex rubber, 50° C. For curve (a), × with glass clamp, O with metal clamp.

Figure 1.1: Stress–strain curve of 2 dimensional extension of rubber, from [208]

where $\mathsf{C} = \mathsf{F}^T\mathsf{F}$ is the right Cauchy-Green tensor.

Moreover, ψ should also satisfy the so called *non-degeneracy axiom* in order to avoid the possibility to infinitely deform the material with a finite amount of energy:

$$\begin{cases} \psi(\mathsf{F}) \to +\infty & \text{when } \det \mathsf{F} \to 0^+ \\ \psi(\mathsf{F}) \to +\infty & \text{when } |\mathsf{F}| + \left|\mathsf{F}^{-1}\right| \to +\infty \end{cases}$$

where $|\mathsf{F}| = \sqrt{\mathrm{tr}(\mathsf{F}^T\mathsf{F})}$. It is possible to prove that, if a material response is isotropic (i.e. $\psi(\mathsf{F}) = \psi(\mathsf{FQ})$ for all $\mathsf{Q} \in \mathcal{O}^+(\mathbb{R}^3)$), then the strain energy density can be expressed as a function of the principal invariants of the right Cauchy-Green tensor C [180], namely

$$\psi = \psi(I_1, I_2, I_3),$$

where

$$I_1 = \mathrm{tr}\,\mathsf{C}, \quad I_2 = \frac{(\mathrm{tr}\,\mathsf{C})^2 - \mathrm{tr}\,\mathsf{C}^2}{2}, \quad I_3 = \det \mathsf{C}.$$

If the material is incompressible, i.e. $\det \mathsf{F} = 1$, a simple non-linear elastic model is given by

$$\psi(\mathsf{F}) = C_{10}(I_1 - 3) + C_{01}(I_2 - 3),$$

which is the so called Mooney–Rivlin [144, 180] strain energy, where C_{10} and C_{01} are two material parameters, so that

$$\frac{C_{10} + C_{01}}{2}$$

is the shear modulus. With the assumption $C_{01} = 0$, we obtain the neo–Hookean model [144, 206, 207].

1.1.3 Well posedness of the non-linear elastic problem

The mathematical well-posedness of the nonlinear elastic problem has been extensively studied since the second half of the past century. While the existence [85, 114] and the uniqueness [123] of the solution of the mixed boundary value problem of linear elastostatics can be proved exploiting the convexity of the strain energy, the non-linear problem is much more complicated.

Let us introduce the strain energy functional, defined as

$$\mathcal{E}[\boldsymbol{\varphi}] = \int_{\Omega_0} \psi(\mathrm{Grad}\,\boldsymbol{\varphi})\, d\boldsymbol{X},$$

let $\mathcal{W}[\boldsymbol{\varphi}]$ be the total work of the external forces, defined as

$$\mathcal{W}[\boldsymbol{\varphi}] = \int_{\Omega_0} \rho_0 \boldsymbol{B} \cdot \boldsymbol{\varphi}\, d\boldsymbol{X} + \int_{\Gamma_1} \boldsymbol{s}_0 \cdot \boldsymbol{\varphi}\, dS$$

so, the total mechanical energy of the body is given by the functional

$$\mathcal{F}[\boldsymbol{\varphi}] = \mathcal{E}[\boldsymbol{\varphi}] - \mathcal{W}[\boldsymbol{\varphi}].$$

The convexity of the strain energy density would imply the existence of elastic minimizers due to the weak lower semicontinuity (WLSC) of the energy functional $\mathcal{F}$ with respect to the weak convergence in $W^{1,p}(\Omega_0, \mathbb{R}^3)$ [81] with $1 < p < \infty$, where $W^{1,p}(U, V)$ denotes the Sobolev space of all the functions

$$f : U \to V \qquad U \subset \mathbb{R}^n,\, V \subset \mathbb{R}^k$$

such that there exists the first weak derivative and both the function and the first weak derivative belong to the Lesbegue space $L^p(U, V)$.

If a functional is WLSC, we can apply the direct method of calculus of variations, ensuring the existence of a minimizer of the functional [81]. Indeed, all the critical points of a functional must satisfy the Euler-Lagrange equation which, in the case of the energy functional $\mathcal{F}$, coincides with the equation of motion.

However, the main issue is the lack of convexity of the strain energy $\mathcal{E}$. Indeed, convexity is incompatible with the constitutive assumption of continuum mechanics, such as frame-indifference and non-degeneracy of the strain energy [61, 54]. Thus, different conditions, weaker than convexity, should be considered to exploit the direct method of calculus of variations for proving the existence of energy minimizers.

A physically motivated requirement is the so called Legendre-Hadamard condition, or strong ellipticity, stating that

$$\frac{\partial^2 \psi(\mathsf{F})}{\partial \mathsf{F} \partial \mathsf{F}} (\boldsymbol{a} \otimes \boldsymbol{b}) \cdot \boldsymbol{a} \otimes \boldsymbol{b} \geq 0, \qquad \forall \boldsymbol{a}, \boldsymbol{b} \in \mathbb{R}^3,\, |\boldsymbol{a}| = |\boldsymbol{b}| = 1.$$

The Legendre-Hadamard condition with a strict inequality implies that body waves can propagate in an elastic medium with a real velocity. An equivalent property is the so called rank-1 convexity, stating that the function f

$$f(t) = \psi(\mathsf{F} + t\boldsymbol{a} \otimes \boldsymbol{b})$$

is convex for all $\boldsymbol{a}, \boldsymbol{b} \in \mathbb{R}^3$ with $|\boldsymbol{a}| = |\boldsymbol{b}| = 1$. However, even if it is a physically motivated requirement, strong ellipticity does not ensure the WLSC of $\mathcal{E}$.

In 1952, Morrey [147] introduced the more restrictive conditions of quasi-convexity, strictly linked to the WLSC of the energy functional.

Definition 1.1.1. *Let $\psi : \mathcal{L}^+(\mathbb{R}^3) \to \mathbb{R}$ be a continuous function. The strain energy density ψ is* quasi-convex *if, for all $\mathsf{F} \in \mathcal{L}^+(\mathbb{R}^3)$ and for all the functions $\boldsymbol{\zeta} \in C_0^1(\Omega_0, \mathbb{R}^3)$ the following inequality holds:*

$$\int_{\Omega_0} \psi(\mathsf{F} + \operatorname{Grad} \boldsymbol{\zeta}(\boldsymbol{X}))\, d\boldsymbol{X} \geq |\Omega_0| \psi(\mathsf{F}),$$

where $C_0^1(U, V)$ indicates the set of all functions $f : U \to V$ with compact support and that are differentiable with a continuous first derivative and $|\Omega_0|$ denotes the Lebesgue measure of Ω_0.

Quasi-convexity is a non-local condition that rarely provides an operative rule for constitutive modelling.

It is possible to prove that all convex function ψ are also quasi-convex. Most importantly, if an energy functional is weakly lower semicontinuous, then the strain energy density is quasi-convex. The converse of the previous theorem is also true: Acerbi and Fusco proved that if the strain energy density is quasi-convex and satisfies some growth condition, $\mathcal{E}[\boldsymbol{\varphi}]$ is WLSC with respect to the weak convergence in $W^{1,p}(\Omega_0, \mathbb{R}^3)$ [1]. Moreover, quasi-convexity implies the Legendre-Hadamard condition, so that quasi-convexity is a stricter condition than rank-1 convexity. However, even if the quasi-convexity is a very important property, it is very hard to prove that a function possesses this feature.

A more restrictive property (but easier to prove) is polyconvexity:

Definition 1.1.2. *A strain energy density* $\psi(\mathsf{F})$ *is said* polyconvex *if there exists a convex function* $h : \mathbb{R}^{19} \to \mathbb{R}$ *such that*

$$\psi(\mathsf{F}) = h(\mathsf{F}, \operatorname{Cof}\mathsf{F}, \det\mathsf{F}),$$

for all $\mathsf{F} \in \mathcal{L}^+(\mathbb{R}^3)$.

Polyconvexity is a more restrictive condition than quasi-convexity. Indeed, if ψ is a finite polyconvex function, then it is also quasi-convex.

The existence of solutions of the non-linear elastic problem for polyconvex strain energy functional has been proven by Ball [23] under some regularity assumptions on the strain energy and on the reference domain. It is reported here in the following Theorem.

Theorem 1.1.2. *Let* $\Omega_0 \subset \mathbb{R}^3$ *be a connected, bounded and open subset with a regular boundary and let* $\psi : \Omega_0 \times \mathcal{L}^+(\mathbb{R}^3) \to \mathbb{R}$ *be a strain energy density such that:*

(i) (polyconvexity) There exists a Carathéodory function $g : \Omega_0 \times \mathbb{R}^{19}$ *such that* $g(\boldsymbol{X}, \cdot)$ *is convex and such that*

$$\psi(\boldsymbol{X}, \mathsf{F}) = g(\boldsymbol{X}, \mathsf{F}, \operatorname{Cof}\mathsf{F}, \det\mathsf{F}), \qquad \forall \mathsf{F} \in \mathcal{L}^+(\mathbb{R}^3).$$

(ii) (continuity at the infinity) if $\mathsf{F}_h \to \mathsf{F}$, $\mathsf{C}_h \to \mathsf{C}$ *and* $\delta_h \to 0^+$, *then*

$$\lim_{h\to\infty} g(\boldsymbol{X}, \mathsf{F}_h, \mathsf{C}_h, \delta_h) = +\infty$$

(iii) (coercivity) there exist $\alpha > 0$, $\beta \in \mathbb{R}$, $p \geq 2$, $q \geq p/(p-1)$, $r > 1$ *such that:*

$$g(\boldsymbol{X}, \mathsf{F}, \mathsf{C}, \delta) \geq \alpha(|\mathsf{F}|^p + |\mathsf{C}|^q + \delta^r) + \beta \qquad \forall \mathsf{F}, \mathsf{C} \in \mathcal{L}(\mathbb{R}^3), \delta > 0.$$

We assume that there exist two disjointed subsets Γ_0, Γ_1 *such that* $\partial\Omega_0 = \Gamma_0 \cup \Gamma_1$ *and such that* $|\Gamma_0| > 0$. *Let* $\boldsymbol{f} : \Omega_0 \to \mathbb{R}^3$ *and* $\boldsymbol{s}_0 : \Gamma_1 \to \mathbb{R}^3$ *measurable such that the application*

$$\mathcal{W}[\boldsymbol{\varphi}] = \int_{\Omega_0} \boldsymbol{f} \cdot \boldsymbol{\varphi}\, d\boldsymbol{X} + \int_{\Gamma_1} \boldsymbol{s}_0 \cdot \boldsymbol{\varphi}\, dS$$

is continuous on $W^{1,p}(\Omega_0, \mathbb{R}^3)$*. Finally let* $\boldsymbol{\varphi}_0 : \Gamma_0 \to \mathbb{R}^3$ *be a measurable function and such that the set*

$$U = \Big\{ \boldsymbol{\varphi} \in W^{1,p}(\Omega_0, \mathbb{R}^3) \mid \operatorname{Cof} \operatorname{Grad} \boldsymbol{\varphi} \in L^q, \det \operatorname{Grad} \boldsymbol{\varphi} \in L^r, \\ \det \operatorname{Grad} \boldsymbol{\varphi} > 0 \text{ a.e. in } \Omega_0, \boldsymbol{\varphi} = \boldsymbol{\varphi}_0 \text{ on } \Gamma_0 \Big\}. \quad (1.5)$$

is non-empty.

Then, defining the functional $\mathcal{F} : U \to \mathbb{R} \cup \{+\infty\}$ *as*

$$\mathcal{F}[\boldsymbol{\varphi}] = \mathcal{E}[\boldsymbol{\varphi}] - \mathcal{W}[\boldsymbol{\varphi}]$$

and assuming that $\inf \mathcal{F}[\boldsymbol{\varphi}] < +\infty$*, there exists*

$$\min_{\boldsymbol{\varphi} \in U} \mathcal{F}[\boldsymbol{\varphi}].$$

In summary, the existence of a solution for a non-linear elastic problems can be proved by introducing a different condition than the convexity of its strain energy. The uniqueness of the solution for a non-linear elastic problem will depend on the combination of both geometrical and constitutive non-linearities. The conditions related to the lack of local uniqueness in non-linear elasticity lead to identify the onset of material and structural instability, which are related to a different topology at the admissible variation [99].

1.2 ACTIVE MATERIALS

Active media are open thermodynamical systems working in out of equilibrium conditions and subjected to multiphysical energy flux. For examples, in sarcomeres, the functional units of muscles, the presence of both a chemical potential due to Calcium ions and electrical stimuli, induces an active contraction in muscles, converting chemical and electrical potential energies into mechanical stress and heat.

The mathematical modelling of the active kinematics of these materials is a rapidly developing research field that poses several challenges, since active phenomena have a complex, multi-physical and non-linear nature. Active materials are found in both biological media, such as the muscle tissue [125] or solid tumors [7], and inert matter, such as dielectric elastomers [163, 63] or hydrogels[135, 27]. In all these cases, there is a dissipative consumption of the non-mechanical energy involved in the process. Thus, contrarily to the theory of hyperelasticity, an inequality should be considered in the second law of thermodynamics. Many attempts have been performed to extend the classical theory of non-linear elasticity in order to capture the active behaviour of active materials.

In this thesis we focus on the mathematical modelling of two categories of active processes in living matter: growth, and the active generation of stress.

1.2.1 Growth and remodelling

One of the possible outcomes of an active process is change of the macroscopic shape thanks to the microscopic rearrangement of matter [5]. Such a reorganization of matter is called *remodelling* in absence of mass generation, it is named *growth* otherwise [78, 95]. The local distortion of the material caused by growth or remodelling may however lead to a geometrically incompatible configuration with a non-Eucliedan metric. The restoration of compatibility is possible through an elastic distortion of the local unstressed configuration. This elastic process generates residual stress inside the body [109], defined as the stress field present in a body in absence of external forces.

The response of residually stressed materials has been modelled exploiting two main approaches. The first one is based on a multiplicative decomposition of the deformation gradient into two contributions

$$\mathsf{F} = \mathsf{F}_e \mathsf{G} \tag{1.6}$$

where G is the tensor field describing the inelastic change of shape induced by the microstructural rearrangement of the matter while F_e accounts for the elastic deformation of the body [126, 128, 181]. The time evolution of the tensor G should be in agreement with the second law of thermodynamics; an example is provided by the following growth law [6]:

$$\dot{\mathsf{G}} = -\mathsf{K}(\mathsf{E} - \mathsf{E}_0)$$

where K is a symmetric positive definite matrix, E_0 is the target, or homeostatic, stress, while E is the Eshelby stress tensor, defined as

$$\mathsf{E} = \psi(\mathsf{F})\mathsf{I} - \mathsf{F}^T \mathsf{P}^T.$$

Such a constitutive law is supported also by experimental evidence; in fact, many growth processes are modulated by the stress of the medium. For example Helmlinger et al. [106] studied the influence of stress exerted on a multicellular tumour spheroid while Yamamoto et al. [216] investigated the effect of mechanical stress on the growth of cultured collagen fascicles.

A different approach to model residual stresses is the so-called theory of initially stressed materials, in which the strain energy density is assumed to depend on both the deformation gradient and on the residual stress field Σ, namely

$$\psi = \psi(\mathsf{F}; \Sigma).$$

Both approaches are reviewed in Chapter 2 where we investigate the influence of the constitutive assumptions on the existence of elastic minimizers.

1.2.2 Active strain *versus* active stress

Another interesting process is the active generation of mechanical stress, where chemical or electrical energy is converted into mechanical stress as a result of a dissipative process. In this respect, important examples are muscle tissue and dielectric elastomers.

The *active strain* approach[125] uses the multiplicative decomposition (1.6), where G accounts for the local distortion caused by the active stress. Such an approach is reviewed in Chapter 3.

A different approach considers an additive split for the active stress[9], so that:

$$\mathsf{P} = \frac{\partial \psi}{\partial \mathsf{F}} + \mathsf{P}_{\text{act}},$$

and the Piola stress is given by the sum of an elastic and an active contribution. The tensor P_{act} should be constitutively provided by the means of an evolution law which is usually a function of the deformation gradient and of the physical quantities underlying the active generation of stress (e.g. electrical field, concentration of chemical reagents).

In Chapter 3 we study both active processes. First, we model the active growth of a multicellular tumour spheroid, exploiting a chemo-mechanical feedback law, we then critically review the active strain approach for the modelling of muscle tissue, taking into account *in vivo* experimental results.

1.3 MORPHO—ELASTICITY

As previously discussed, the convexity of the strain energy is mathematically incompatible with the constitutive assumptions of non-linear elasticity. As a result, the non-uniqueness of the solution of a non-linear elastic problem can give rise to several morphological transitions that are governed by geometrical and constitutive non-linearities.

Geometric non-linearities can trigger the loss of uniqueness also in linear elastic problems, such as the buckling of a column subjected to an external load (see Fig. 1.2). This problem was studied first by L. Euler. He proved that, if the column is subjected to a load higher than τ_{cr}, defined as

$$\tau_{\text{cr}} = \frac{\pi^2 EI}{L^2},$$

it will deviate from its straight configuration (here E is the Young modulus, I is the inertia moment with respect to the axis of the column and L is the length of the column).

In the theory of non-linear elasticity, geometrical and physical non-linearities (i.e. non-linearities included in the constitutive stress-strain relations) are coupled. The first one leads to the so-called structural instability, such as buckling, the second one is related to material instability such as creasing, namely the formation of sharp furrows at the free surface of a compressed elastic slab.

Methods of perturbation theory can be applied to study the stability of solutions in finite elasticity. The basic approach to study structural instabilities in non-linear elastic media is based on the *theory of incremental deformations superposed on a finite strain* [29, 31, 124, 156]. Analogously to the method of linearisation used to study the stability of a solution of a non-linear differential equation, let $\boldsymbol{u}_0$ be a displacement field solution of the elastic problem. We indicate with Ω the actual configuration corresponding to the displacement field $\boldsymbol{u}_0$. A small displacement $\delta\boldsymbol{u}$, called incremental displacement field, is added to $\boldsymbol{u}_0$, so that

$$\boldsymbol{u} = \boldsymbol{u}_0 + \delta\boldsymbol{u}.$$

If we assume that $\delta\boldsymbol{u}$ is small with respect to the $W^{1,\infty}(\Omega, \mathbb{R}^3)$ norm, we can linearise the non-linear elastic problem about the configuration Ω, considering $\delta\boldsymbol{u}$ as the unknown of the incremental equations. A bifurcation occurs if the linearised incremental problem admits a non null solution. Similar perturbation techniques have been devolped also for viscoelastic solids by Dixit et al. [71].

One of the most classical examples is provided by the compression of a half-space composed of a neo–Hookean material, first studied by M. Biot [30]. When the body is compressed in a direction parallel to the free surface beyond a critical value, the homogeneous solution becomes unstable. Even if this is one of the first and apparently one of the most simple example of instability in a non-linear elastic body, its behavior is still not completely understood and it is still an open problem [112, 44, 56].

Elastic instabilities may be triggered not only by an applied stretch but also by active phenomena. In fact, whenever such underlying transformations introduce a geometrical incompatibility in the micro–structure, a state of internal

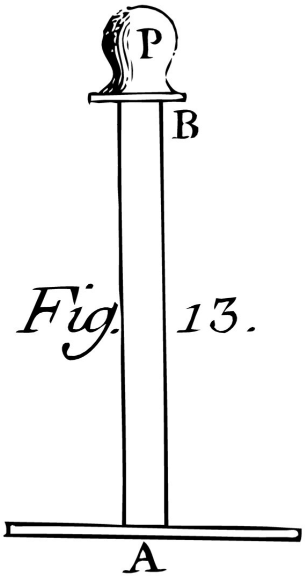

Figure 1.2: Illustration of the Euler problem, taken from the original article of L. Euler [80]

stress arises in the material in order to accommodate these misfits. The accumulation of such internal stresses beyond a critical threshold may drive the onset of an elastic bifurcation.

Several models have successfully described many morphological transitions in living and inert matter [26, 96, 62, 67]. The theoretical study of these models have led to the development of a new field, called *morpho-elasticity*. Its aim is to describe how different shapes and patterns emerge as a result of active processes and elastic instabilities in soft matter. This vibrant research field has rapidly developed in the last decade, pushed by the technological availability of experimental devices controlling the extreme deformations of soft incompressible materials, such as hydrogels [202, 66, 122] and elastomers [218, 121].

1.4 OUTLINE OF THE THESIS

The thesis is divided into five chapters. In Chapter 2 we address the issue of the existence of elastic minimizers in the framework of the theory of initially stressed materials. In fact, in the modelling of soft and active solids, we usually exploit a reference configuration that does not coincide with the relaxed one. We study the influence that the constitutive assumptions has on the well posedness of the non-linear elastic problem and we investigate the mechanical interpretation of these constitutive restrictions. We also analyse the influence that some of these assumptions, such as the so called initial stress reference independence, have on the mechanical properties of the materials.

In Chapter 3, we address the issue of modelling growth and active generation of stress in living matter. First, we mathematically describe the growth of a solid tumours introducing a new growth law based on a chemo-mechanical feedback. Our model is then compared with in vitro and ex vivo experimental results. Second, we study the process of activation in muscles. The *active strain* approach is reviewed, comparing the outcomes of this method with experimental results on the uniaxial traction of a skeletal muscle.

In Chapter 4, we study morpho–elastic processes and pattern formation in soft matter. Indeed, topological transitions can appear as result of the accumulation of mechanical stress due to the application of large strains or the activation of the material. First, we propose a new model of the morphogenetic mechanisms underlying the tortuosity of tumour capillaries. Second, we study the stability of an initially stressed sphere. Finally, we investigate the elastic equivalent of the Rayleigh-Taylor instability in fluids.

Finally, in Chapter 5, we summarize the main results of the thesis, together with some concluding remarks.

2 ON THE EXISTENCE OF ELASTIC MINIMIZERS FOR INITIALLY STRESSED MATERIALS

In many cases, it is convenient to model active elastic bodies exploiting a reference configuration which does not coincide with the relaxed one. More in general, we call these media initially stressed bodies.

The stress field in the reference configuration Σ is called initial stress and must satisfy the equilibrium equations. Initial stresses are commonly observed in soft materials. The presence of external stimuli in active matter, e.g. an electric field in dielectric elastomers, generate a distortion of the microstructure of the material that is made physically compatible by the emergence of an internal state of stress. In living matter, initial stresses are also known as residual stresses [109, 118, 119, 120], and they result from incompatible growth processes both in healthy and pathological conditions [198, 59]. Such residual stresses not only may enhance the functionality and the efficiency of biological structures, e.g. in arteries [53], but they may also be used to trigger a programmed shape transition through a mechanical instability, forming complex patterns such as the intestinal villi [57] or the brain sulci [24].

From a constitutive viewpoint, a well established approach to account for initial stresses is based on the multiplicative decomposition of the deformation gradient into an elastic deformation tensor and an incompatible tensor [28, 126, 128]. In Chapter 2, we review this approach reffering to it as the *theory of elastic distortions*. This method was initially applied to provide a kinematic description of crystal plasticity [174], and later adapted to describe active phenomena, such as the muscle contraction [125, 200] and the volumetric growth [181].

The main assumption behind this theory is that the properties of the material does not change during the material activation, only the spatial distribution of matter is affected [78]. Indeed, the theory of elastic distortions is well suited to model the remodelling and the volumetric growth of a body.

Assuming a material isomorphism for the strain energy function, the initial stress is constitutively related to the elastic deformation tensor from the virtual incompatible state. Since the tensor describing the inelastic distortion is not necessarily the gradient of a deformation, it maps the unloaded configuration into a virtual state that may not possess a Euclidean metric [120]. Accordingly, the main drawback of this approach is that such a virtual state may not be achieved in physical practice, not even by cutting procedures, and the tensor describing the inelastic distortion must be assumed a priori in order to generate a self-equilibrated state of initial stresses.

A less restrictive mathematical framework accounts for initial stresses by formulating implicit constitutive equations linking the Helmoltz free energy, the initial stress and the kinematic quantities possibly mapping the evolving natural states of the materials [167]. For soft solids, this constitutive approach has shown that there exists a far richer class of non-dissipative materials than the class of bodies that is usually understood as being elastic [168].

As first discussed in [189], objectivity is enforced for an initially stressed material made by an isotropic material by considering a dependence on the ten invariants of the deformation gradient and the initial stress tensor. Under the incompressibility constraint, it has been shown that only eight invariants are independent [191]. This method has been widely used to model initially stressed materials; applications of this theory include of wave propagation in soft media [190, 157], the modeling residual stress in living tissues [212] and the stability of residually stressed materials [60, 182, 179].

The main advantage of this approach is that the initial stress tensor Σ belongs to the set of the divergence-free symmetric tensor fields satisfying the boundary condition in the given reference configuration, whilst it is still unclear which physical restrictions must be imposed for the well-posedness of the elastic problem. A basic constitutive restriction known as the initial stress compatibility condition (ISCC) imposes that the Cauchy stress reduces to the initial stress when the deformation tensor is equal to the matrix identity [189, 97]. By imposing ISCC and the polyconvexity of the resulting strain energy function in the absence of initial stresses, few constitutive relations have been proposed. A simple functional expression has been proposed in [139], containing material parameters that also depend on the particular choice of the reference configuration, as generally prescribed by [209]. A more restrictive constitutive class has been proposed in [97], assuming that the material parameters do not change under a change of reference configuration. This assumption has lead to define a new condition. i.e. the initial stress reference independence (ISRI) [98], that is inspired by the multiplicative decomposition approach.

These two methods are frequently used in the modelling of active soft matter. However, the link between the existence of elastic minimizers and the constitutive assumptions for initially stressed materials subjected to finite deformations is still not fully investigated. As a common background for the topics of the next Chapters, in Chapter 2, we review both the methods and we aim at clarifying some constitutive aspects of the mathematical theory of initially stressed materials, unravelling the main implications of imposing the ISRI condition on the existence of elastic minimizers.

The Chapter is organized as follows. In Section 2.1, we provide some basic kinematic and constitutive notions for nonlinear elastic materials. In Section 2.2, we introduce the main differences of the proposed mathematical framework for initially stressed materials with respect to the theory of elastic distortions, discussing the mechanical signification of the ISCC and the ISRI conditions. In Section 2.3, we prove the local existence of a relaxed state for each material

point. In Section 2.4, we prove that the residual stresses provoke an elastic distortion on the transformation of the symmetry group. We also give en existence theorem for the elastic minimizers for the proposed constitutive choice of the initially stressed material. In Section 2.5, we use the proposed framework to solve the physical problem of an elastic disc subjected to an anisotropic initial stress. Finally, the results are summarized and critically discussed in the last section.
The results of this chapter lead to the following publication:

D. Riccobelli, A. Agosti, and P. Ciarletta. On the existence of elastic minimizers for initially stressed materials. *Philosophical Transactions of the Royal Society A: Mathematical, Physical and Engineering Sciences*, in press

2.1 BACKGROUND AND NOTATION

We denote by $\mathcal{L}(\mathbb{R}^n)$ the set of all the automorphisms of $\mathbb{R}^n$, and with $\mathcal{L}^+(\mathbb{R}^n)$ the group (with respect to the operation of function composition) of all the linear applications belonging to $\mathcal{L}(\mathbb{R}^n)$ with positive determinant.

Let $\mathcal{O}(\mathbb{R}^n)$ be the group such that

$$\mathsf{Q}^T\mathsf{Q} = \mathsf{I}$$

where $\mathsf{Q} \in \mathcal{L}(\mathbb{R}^n)$ and I is the identity.

We indicate with $\mathcal{O}^+(\mathbb{R}^n) \subset \mathcal{O}(\mathbb{R}^n)$ the group of all the elements of $\mathcal{O}(\mathbb{R}^n)$ with positive determinant; if $n = 3$, this group coincides with the set of the rigid rotations. We also introduce the set $\mathcal{S}(\mathbb{R}^n)$ of all the symmetric linear applications that belong to $\mathcal{L}(\mathbb{R}^n)$.

Let the open set $\Omega_0 \subset \mathbb{R}^3$ be the reference configuration of a body and $\boldsymbol{X} \in \Omega_0$ the material point. We denote the deformation field by $\boldsymbol{\varphi} \in C^2(\Omega_0, \mathbb{R}^3)$that maps the reference domain Ω_0 to the actual configuration Ω.

Accordingly, the deformation gradient reads $\mathsf{F} = \operatorname{Grad}\boldsymbol{\varphi}$. If the body is made of a homogeneous elastic material, we assume a purely elastic constitutive behavior such that the Cauchy stress tensor T_0 depends on the deformation gradient F.

We say that the body has a relaxed reference configuration if

$$\mathsf{T}_0(\mathsf{I}) = 0, \tag{2.1}$$

where T_0 is the Cauchy stress and I is the identity tensor.

If the body is composed of a hyperelastic material, we denote its strain energy density in a point $\boldsymbol{X}$ with $\psi_0(\mathsf{F}(\boldsymbol{X})) : \mathcal{L}^+(\mathbb{R}^3) \to \mathbb{R}$. Whenever appropriate, we omit the explicit dependence of the physical quantities on the material position $\boldsymbol{X}$. The first Piola–Kirchhoff and the Cauchy stress tensor are given by

$$\mathsf{P}_0(\mathsf{F}) = \frac{\partial \psi_0}{\partial \mathsf{F}} \qquad \mathsf{T}_0(\mathsf{F}) = \frac{1}{\det \mathsf{F}}\mathsf{F}\mathsf{P}_0(\mathsf{F}),$$

Table 2.1: List of functional spaces

Symbol	Definition
$\mathcal{L}(\mathbb{R}^n)$	Set of all the linear applications from $\mathbb{R}^n$ to $\mathbb{R}^n$.
$\mathcal{L}^+(\mathbb{R}^n)$	Set of all the $\mathsf{L} \in \mathcal{L}(\mathbb{R}^n)$ such that $\det \mathsf{L} > 0$.
$\mathcal{O}(\mathbb{R}^n)$	Set of all the orthogonal tensors $\mathsf{Q} \in \mathcal{L}(\mathbb{R}^n)$, namely all the Q such that $\mathsf{Q}^T\mathsf{Q} = \mathsf{I}$.
$\mathcal{O}^+(\mathbb{R}^n)$	Set of all $\mathsf{Q} \in \mathcal{O}(\mathbb{R}^n)$ such that $\det \mathsf{Q} > 0$.
$\mathcal{S}(\mathbb{R}^n)$	Set of all the symmetric linear applications from $\mathbb{R}^n$ to $\mathbb{R}^n$, namely all the $\mathsf{L} \in \mathcal{L}(\mathbb{R}^n)$ such that $\mathsf{L}^T = \mathsf{L}$
$\mathcal{L}_1^+(\mathbb{R}^n)$	Special unitary group, namely the subset of $\mathcal{L}^+(\mathbb{R}^n)$ with determinant 1.
$\mathcal{D}$	Denotes $\mathcal{L}^+(\mathbb{R}^n)$ for a compressible material, or $\mathcal{L}_1^+(\mathbb{R}^n)$ for an incompressible material.
$C^0(U, V)$	Set of all the continuous function from the set $U \subseteq \mathbb{R}^n$ to the set $V \subseteq \mathbb{R}^N$.
$C^k(U, V)$	Set of all the function from the set $U \subseteq \mathbb{R}^n$ to the set $V \subseteq \mathbb{R}^N$ admitting continuous derivatives of order k.
$L^p(U, V)$	Set of all the function from the set $U \subseteq \mathbb{R}^n$ to the set $V \subseteq \mathbb{R}^N$ with finite L^p norm.
$W^{1,p}(U, V)$	Sobolev space of all the functions from the set $U \subseteq \mathbb{R}^n$ to the set $V \subseteq \mathbb{R}^N$, where both the functions and their weak partial derivatives belong to $L^p(U, V)$.

respectively.

In order to account for an incompressibility constraint, we introduce the following group:

$$\mathcal{L}_\delta^+(\mathbb{R}^3) = \left\{\mathsf{F} \in \mathcal{L}^+(\mathbb{R}^n) \mid \det \mathsf{F} = \delta\right\}.$$

Accordingly, the domain of the strain energy density ψ_0 is given by $\mathcal{L}_1^+(\mathbb{R}^3)$, where the argument is the special unitary group. However, it is convenient to introduce an extension of ψ_0 to all $\mathcal{L}^+(\mathbb{R}^3)$ and then to use the method of Lagrangian multiplier to enforce the incompressibility constraint. Let $\tilde{\psi}_0 : \mathcal{L}^+(\mathbb{R}^3) \to \mathbb{R}$ such that

$$\tilde{\psi}_0(\mathsf{F}) = \psi_0(\mathsf{F}) \qquad \forall \mathsf{F} \in \mathcal{L}_1^+(\mathbb{R}^3), \tag{2.2}$$

a possible extension is given by

$$\tilde{\psi}_0(\mathsf{F}) = \psi_0((\det \mathsf{F})^{-1/3}\mathsf{F}).$$

So, the first Piola–Kirchhoff and the Cauchy stress tensors are given by

$$\mathsf{P}_0(\mathsf{F}, p) = \frac{\partial \tilde{\psi}_0}{\partial \mathsf{F}} - p\mathsf{F}^{-1} \qquad \mathsf{T}_0(\mathsf{F}, p) = \mathsf{F}\mathsf{P}_0(\mathsf{F}, p),$$

where p is the Lagrangian multiplier. For the sake of simplicity, in the following we will omit the distinction between $\tilde{\psi}_0$ and ψ_0 wherever appropriate and we denote by $\mathcal{D}$ either the group $\mathcal{L}^+(\mathbb{R}^3)$, if the material is unconstrained, or the group $\mathcal{L}_1^+(\mathbb{R}^3)$, if the material is incompressible.

We denote by

$$I_1(\mathsf{C}) = \mathrm{tr}(\mathsf{C}), \qquad I_2(\mathsf{C}) = \frac{(\mathrm{tr}\,\mathsf{C})^2 - \mathrm{tr}(\mathsf{C}^2)}{2}, \qquad I_3(\mathsf{C}) = \det(\mathsf{C}), \tag{2.3}$$

the principal invariants of C, where $\mathsf{C} = \mathsf{F}^T\mathsf{F}$ is the right Cauchy–Green strain tensor.

We finally introduce a fundamental notion for the existence of minimizers in nonlinear elastic materials, known as the non-degeneracy axiom [23]:

Axiom 2.1.1 (Non-degeneracy for a hyperelastic body)**.** *Let ψ_0 be a strain energy density, we say that ψ_0 is non-degenerate if*

$$\begin{cases} \psi_0(\mathsf{F}) \to +\infty & \textit{when } \det \mathsf{F} \to 0^+ \\ \psi_0(\mathsf{F}) \to +\infty & \textit{when } |\mathsf{F}| + \left|\mathsf{F}^{-1}\right| \to +\infty \end{cases} \tag{2.4}$$

where $|\mathsf{F}| = \sqrt{\mathrm{tr}(\mathsf{F}^T\mathsf{F})}$.

The last condition of (2.4) indeed ensures that the hyperelastic energy goes to infinity as soon as one of the principal invariants (2.3) goes to $+\infty$. If the material is incompressible, only the second equation of (2.4) applies. For the ease of the readers, we collect all the symbols used to denote the functional spaces in Table 2.1.

2.2 MATHEMATICAL FRAMEWORKS FOR INITIALLY STRESSED MATERIALS

In this section, we summarize the basic features of two mathematical frameworks used to model nonlinear elastic materials whose unloaded reference configuration is not stress-free, namely the theory of elastic distortions and the theory of initially stressed bodies.

2.2.1 The theory of elastic distortions

If the relation (2.1) does not hold, the material is subjected to a state of stress in the reference configuration. A classical constitutive approach consists in assuming a multiplicative decomposition of the deformation gradient [181], such that:

$$\mathsf{F} = \mathsf{F}_e\mathsf{G}. \tag{2.5}$$

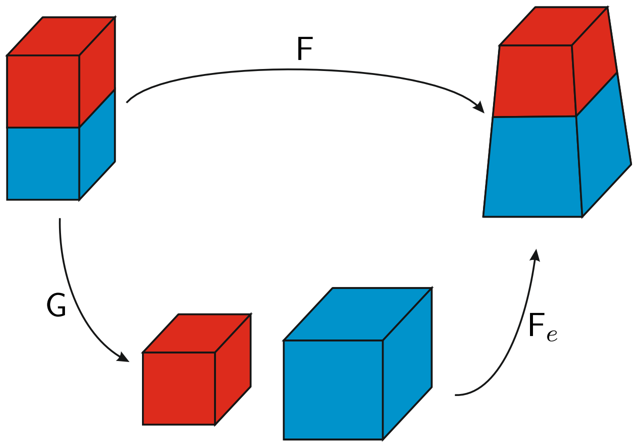

Figure 2.1: Clockwise representation of the reference, the actual and the relaxed configuration described by the multiplicative decomposition of the deformation gradient given by (2.5).

where G is the tensor field that describes the elastic distortion from the reference configuration to the relaxed one, whilst F_e represents the elastic distortion that restores the geometrical compatibility under the action of external tractions (as depicted in Fig. 2.1). Since the underlying metric is not Euclidean whence G is not a gradient of a deformation field, it may be impossible to attain a stress-free configuration in the physical world. In the last decades, the distortion tensor G has been advocated to model different biological processes, such as volumetric growth [70], remodelling [79] and active strains [125, 200].

In physical practice, it is assumed the initial stress in the body is generated by a distortion of the reference configuration. Consequently, the strain energy function depends on the distorted metric, given by FG^{-1}.

If the material is incompressible, this constraint is imposed on the elastic tensor, whilst the distortion tensor also describes the local change of volume, such that:

$$\det F_e = 1 \quad \Rightarrow \quad \det F = \det G = \delta.$$

Accordingly, the strain energy density of the material is given by :

$$\psi_G(F) = (\det G)\psi_0(FG^{-1}). \tag{2.6}$$

From standard application of the second law of the thermodynamics in the Clausius-Duhem form, the first Piola–Kirchhoff and Cauchy stress read

$$P_G(F) = (\det G)\frac{\partial \psi_0(FG^{-1})}{\partial F}, \qquad T_G(F) = \frac{1}{\det F} F P_0(\boldsymbol{X}, F). \tag{2.7}$$

The theory of distortions provides a transparent explanation for the transformation law of the material properties. Let $\mathcal{G}$ be the material symmetry group of a hyperelastic material, it is defined as the set of all the tensors $\mathsf{Q} \in \mathcal{L}_1^+(\mathbb{R}^3)$ such that

$$\mathsf{T}(\mathsf{F}) = \mathsf{T}(\mathsf{FQ}), \qquad \forall \mathsf{F} \in \mathcal{D}; \tag{2.8}$$

where the response function T may eventually depend on the local distortion G.

An equivalent definition for a hyperelastic material can be given as the set of all $\mathsf{Q} \in \mathcal{L}_1^+(\mathbb{R}^3)$ such that

$$\psi(\mathsf{F}) = \psi(\mathsf{FQ}), \qquad \forall \mathsf{F} \in \mathcal{D}.$$

If we exploit the theory of elastic distortions, let $\mathcal{G}$ be the material symmetry group of the corresponding strain energy density ψ_0. It has been shown that [78]:

$$\begin{aligned}\psi_{\mathsf{G}}(\mathsf{F}) &= (\det \mathsf{G})\psi_0(\mathsf{F}\mathsf{G}^{-1}) = \\ &= (\det \mathsf{G})\psi_0(\mathsf{F}\mathsf{G}^{-1}\mathsf{Q}) = \\ &= (\det \mathsf{G})\psi_0(\mathsf{F}\mathsf{G}^{-1}\mathsf{Q}\mathsf{G}\mathsf{G}^{-1}) = \\ &= \psi_{\mathsf{G}}(\mathsf{F}\mathsf{G}^{-1}\mathsf{Q}\mathsf{G})\end{aligned} \qquad \forall \mathsf{Q} \in \mathcal{G}_0 \tag{2.9}$$

Thus, the material symmetry group of the initially stressed material is given by

$$\mathcal{G}_{\mathsf{G}} = \mathsf{G}^{-1}\mathcal{G}_0\mathsf{G}.$$

Notably, $\mathcal{G}_{\mathsf{G}}$ is the conjugate group of $\mathcal{G}_0$ through G.

The main drawback of the theory of elastic distortions is that G has to be provided by means of a constitutive assumption. Nonetheless, since the underlying metric may not be Euclidean, the values of its components cannot be directly inferred in many physical problems. An experimental attempt to search for a stress–free configuration consists in performing several (ideally infinite) cuts in the body to release the local stresses stored inside the material [9, 198, 59, 53, 10]. Although successful in simple system models [25, 148, 57], this approach is unsuitable when interested in investigating the effect of a generic state of initial stress on the material response. In the following, we describe how this difficulty can be circumvented by building a constitutive theory that explicitly depends on the underlying spatial distribution of internal stresses.

2.2.2 The theory of initially stressed bodies

Alternatively, it can be assumed that the material response depends on both the deformation applied on the body and on the initial stress, intended as the existing stress field Σ in the undeformed reference configuration, i.e. the Cauchy stress when the body is undeformed. This assumption has been discussed in [118, 119, 120], such that the material response in a point $\boldsymbol{X}$ of the body reads

$$\mathsf{T} = \mathsf{T}(\mathsf{F}; \Sigma(\boldsymbol{X})), \tag{2.10}$$

where T is the Cauchy stress. We remark that the initial stress tensor field

$$\Sigma : \Omega_0 \to \mathcal{S}(\mathbb{R}^3)$$

generally depends on the material position vector $\boldsymbol{X}$; we omit such an explicit notation in the following for the sake of brevity wherever appropriate. We denote by $\mathsf{S} \in \mathcal{S}(\mathbb{R}^3)$ the specific expression of the initial stress in a point $\boldsymbol{X}$, namely $\mathsf{S} = \Sigma(\boldsymbol{X})$ for a given $\boldsymbol{X} \in \Omega_0$.

The function $\mathsf{T} : \mathcal{D} \times \mathcal{S}(\mathbb{R}^3) \to \mathcal{S}(\mathbb{R}^3)$ must satisfy certain restrictions. First, in the absence of initial stresses, the strain energy function must obey the standard requirements ensuring the existence of elastic minimizers in nonlinear elasticity. Second, the constitutive response should be such that the Cauchy stress is equal to the initial stress in the absence of any elastic deformations. This is referred to as ISCC, i.e. *initial stress compatibility condition*, [189] and reads:

$$\mathsf{T}(\mathsf{I}; \mathsf{S}) = \mathsf{S} \qquad \forall \mathsf{S} \in \mathcal{S}(\mathbb{R}^3). \tag{2.11}$$

A subclass of material responses in which the strain energy function depends only on the elastic deformation and the initial stress, but not explicitly on the choice of the reference configuration, has been proposed in [97, 98]. Under this constitutive assumption, it is possible to introduce another restriction called Initial Stress Reference Independence (ISRI), stating that

$$\mathsf{T}(\mathsf{F}_2\mathsf{F}_1; \mathsf{S}) = \mathsf{T}\left(\mathsf{F}_2; \mathsf{T}(\mathsf{F}_1; \mathsf{S})\right), \quad \forall \mathsf{S} \in \mathcal{S}(\mathbb{R}^3). \tag{2.12}$$

In this work we give a new mechanical interpretation of such a restrictive condition and we discuss its mathematical implications for the existence of elastic minimizers. The condition (2.12) imposes that there is no energy dissipation resulting from the elastic deformation and represents a frame invariance requirement: the deformation field solution of the elastic problem must not depend on the choice of the reference configuration [97, 98].

If the material is hyperelastic, we can assume that the strain energy function reads [189]:

$$\psi : \mathcal{L}^+(\mathbb{R}^3) \times \mathcal{S}(\mathbb{R}^3) \to \mathbb{R}. \tag{2.13}$$

Recalling the values of the material parameters are assumed to be independent on the choice of the initially stressed configuration, the first Piola–Kirchhoff tensor P and the Cauchy stress tensor T read:

$$\begin{cases} \mathsf{P}(\mathsf{F}; \mathsf{S}) = \dfrac{\partial \psi}{\partial \mathsf{F}}(\mathsf{F}; \mathsf{S}), \\ \mathsf{T}(\mathsf{F}; \mathsf{S}) = \dfrac{1}{\det \mathsf{F}} \mathsf{F}\mathsf{P}(\mathsf{F}; \mathsf{S}), \end{cases} \qquad \mathsf{F} \in \mathcal{L}^+(\mathbb{R}^3), \quad \mathsf{S} \in \mathcal{S}(\mathbb{R}^3). \tag{2.14}$$

Under the incompressibility constraint, the strain energy density is a function such that

$$\psi : \mathcal{L}_1^+(\mathbb{R}^3) \times \mathcal{S}(\mathbb{R}^3) \to \mathbb{R},$$

as done in (2.2), we introduce an extension $\tilde{\psi}$ of ψ to all $\mathcal{L}^+(\mathbb{R}^3)$ to define the stress tensors, namely

$$\tilde{\psi}(\mathsf{F};\mathsf{S}) = \psi(\mathsf{F};\mathsf{S}) \qquad \forall \mathsf{F} \in \mathcal{L}_1^+(\mathbb{R}^3), \quad \forall \mathsf{S} \in \mathcal{S}(\mathbb{R}^3); \tag{2.15}$$

a possible extension is given by:

$$\tilde{\psi}(\mathsf{F};\mathsf{S}) = \psi((\det \mathsf{F})^{-1/3}\mathsf{F};\mathsf{S}).$$

The Piola–Kirchhoff and the Cauchy stress tensors are given by

$$\begin{cases} \mathsf{P}(\mathsf{F},p;\mathsf{S}) = \dfrac{\partial\tilde{\psi}}{\partial \mathsf{F}}(\mathsf{F};\mathsf{S}) - p\mathsf{F}^{-1}, \\ \mathsf{T}(\mathsf{F},p;\mathsf{S}) = \mathsf{F}\mathsf{P}(\mathsf{F},p;\mathsf{S}), \end{cases} \quad \mathsf{F} \in \mathcal{L}_1^+(\mathbb{R}^3), \quad \mathsf{S} \in \mathcal{S}(\mathbb{R}^3).$$

For the sake of simplicity, we omit the difference between $\tilde{\psi}$ and ψ wherever appropriate. For hyperelastic materials, we remind that (2.12) can be reformulated as an equivalent condition to be imposed on the functional dependence of the strain energy function [98]. We give further mathematical details of this important result in the following, proving that the restriction imposed on the strain energy density is a consequence of (2.12).

Proposition 2.2.1. *Let $\psi : \mathcal{D} \times \mathcal{S}(\mathbb{R}^3) \to \mathbb{R}$ be a strain energy density, and assume that the ISCC (2.11) and the ISRI conditions (2.12) hold. Then, for all $\mathsf{F}_1, \mathsf{F}_2 \in \mathcal{D}$ and for all $\mathsf{S} \in \mathcal{S}(\mathbb{R}^3)$, the following relation must hold:*

$$\psi(\mathsf{F}_2\mathsf{F}_1;\mathsf{S}) = (\det \mathsf{F}_1)\psi(\mathsf{F}_2;\mathsf{T}(\mathsf{F}_1;\mathsf{S})). \tag{2.16}$$

Proof. For the sake of brevity, let ψ be the strain energy of a compressible material (the incompressible case is analogous). The ISRI condition (2.12) reads

$$\frac{1}{\det \mathsf{F}_1 \det \mathsf{F}_2}\mathsf{F}_2\mathsf{F}_1\frac{\partial\psi}{\partial \mathsf{F}}(\mathsf{F}_2\mathsf{F}_1;\mathsf{S}) = \frac{1}{\det \mathsf{F}_2}\mathsf{F}_2\frac{\partial\psi}{\partial \mathsf{F}_2}(\mathsf{F}_2;\mathsf{T}(\mathsf{F}_1;\mathsf{S})). \tag{2.17}$$

Since $\mathsf{F} = \mathsf{F}_2\mathsf{F}_1$, then, by using the chain rule, we obtain

$$\frac{\partial\psi}{\partial \mathsf{F}_2} = \mathsf{F}_1\frac{\partial\psi}{\partial \mathsf{F}}$$

and the equation (2.17) becomes

$$\frac{\partial\psi}{\partial \mathsf{F}}(\mathsf{F}_2\mathsf{F}_1;\mathsf{S}) = \det \mathsf{F}_1\frac{\partial\psi(\mathsf{F}\mathsf{F}_1^{-1},\mathsf{T}(\mathsf{F}_1;\mathsf{S}))}{\partial \mathsf{F}}.$$

We find that $\psi(\mathsf{F}_2\mathsf{F}_1;\mathsf{S}) = (\det \mathsf{F}_1)\psi(\mathsf{F}_2;\mathsf{T}(\mathsf{F}_1;\mathsf{S})) + C$. Setting $\mathsf{F}_1 = \mathsf{I}$ and making use of (2.11) we find that $C = 0$ and we get the claim. ☐

In the next sections, we prove the local existence of a relaxed state around each material point and a theorem on the existence of elastic minimizers for a strain energy of the form given by (2.13).

2.3 EXISTENCE OF A RELAXED STATE

In the theory of elastic distortions, we must provide a constitutive form for the tensor field that we should apply locally to each point in the reference configuration to obtain the (virtual) relaxed one [181]. This theoretical framework has strong mathematical properties. Indeed, if ψ_0 is polyconvex, then also ψ_{G} (defined in (2.6)) inherits such a property [150]. As discussed earlier, this approach is straightforward but only suitable in simple system models, since it requires the a priori knowledge of the virtual relaxed state.

In this section we prove a theorem on the existence of relaxed configuration using the constitutive framework of initially stressed bodies. Moreover, we prove that, if a strain energy satisfy the ISRI (2.16) and $\psi(\cdot, 0)$ is polyconvex, then $\psi(\cdot, \mathsf{S})$ is polyconvex for all $\mathsf{S} \in \mathcal{S}(\mathbb{R}^3)$.

First, we give the following statement of the non-degeneracy axiom for this class of materials.

Axiom 2.3.1 (Non-degeneracy for an initially stressed body)**.** *Let* $\psi : \mathcal{L}^+(\mathbb{R}^3) \times \mathcal{S}(\mathbb{R}^3) \to \mathbb{R}$ *be the strain energy density of an initially stressed body. We say that* ψ *is non-degenerate if*

$$\begin{cases} \psi(\mathsf{F};\mathsf{S}) \to +\infty & \textit{when } \det \mathsf{F} \to 0^+, \\ \psi(\mathsf{F};\mathsf{S}) \to +\infty & \textit{when } |\mathsf{F}| + \left|\mathsf{F}^{-1}\right| \to +\infty. \end{cases} \qquad \forall \mathsf{S} \in \mathcal{S}(\mathbb{R}^3). \tag{2.18}$$

We now derive the existence of a point-like relaxed state associated to each point of the initially stressed configuration. In [119], a stress-free virtual state is defined for each material point in the initially stressed configuration by considering the limiting behavior as the radius of the spherical neighborhood tends to zero. Its existence required the following hypotheses: $\Sigma \in C^1(\Omega_0, \mathcal{S}(\mathbb{R}^3))$, $\psi = \psi(\mathsf{F}; \Sigma(\boldsymbol{X}))$ being twice differentiable with respect to both arguments, and the distortion from the neighborhood of each point to the free state to be once differentiable in space. Here we are going to obtain a proof of existence of a virtual state using weaker hypotheses.

Theorem 2.3.1 (Existence of a relaxed state)**.** *Let* ψ *be a non-degenerate strain energy density in the sense of* (2.18)*. We also assume that* $\psi(\cdot, \mathsf{S})$ *is at least* C^1 *and proper, i.e. it is not identically equal to* $+\infty$*, for all* $\mathsf{S} \in \mathcal{S}(\mathbb{R}^3)$*.*

Then, for each $\boldsymbol{X} \in \Omega_0$*, given* $\Sigma(\boldsymbol{X}) \in \mathcal{S}(\mathbb{R}^3)$*, there exists a local distortion* $\mathsf{G}_{\Sigma(\boldsymbol{X})}$ *such that*

$$\mathsf{T}(\mathsf{G}_{\Sigma(\boldsymbol{X})}; \Sigma(\boldsymbol{X})) = 0.$$

Proof. Let ψ be the strain energy of a compressible material.

We denote by $f_{\Sigma(\boldsymbol{X})} = \psi(\cdot; \Sigma(\boldsymbol{X}))$. The domain of the function $f_{\Sigma(\boldsymbol{X})}$ is given by $\mathcal{D} = \mathcal{L}^+(\mathbb{R}^3)$. Thus, from the non-degenericity axiom (2.3.1), we get

$$f_{\Sigma(\boldsymbol{X})}(\mathsf{F}) \to +\infty \qquad \text{when } \det \mathsf{F} \to 0^+ \text{ or } |\mathsf{F}| \to +\infty. \tag{2.19}$$

Since the function $f_{\Sigma(X)}$ is continuous and proper, it must be bounded from below, hence there exists a value $m \in \mathbb{R}$ such that $f_{\Sigma(X)}(\mathsf{F}) > m$ for all F. Moreover, there exists a value $M > m$ such that

$$f^{-1}_{\Sigma(X)}\left([m, M] \cap \mathrm{Im}(f_{\Sigma(X)})\right) = U \neq \emptyset, \qquad U \subset \mathcal{L}^+(\mathbb{R}^3). \tag{2.20}$$

where with $f^{-1}_{\Sigma(X)}(A)$ we denote the pre–image of the subset $A \subseteq \mathrm{Im}(f_{\Sigma(X)})$ through the function $f_{\Sigma(X)}$.

The non-empty set U is bounded as a direct consequence of the coercivity property expressed in (2.18). Thus, there exists a minimum of $f_{\Sigma(X)}$ in $\bar{U}$, where $\bar{U}$ is the closure of U.

The tensor that realizes such a minimum may be not unique as exposed in the following Remark 2.3.1. Let us denote with $\mathsf{G}_{\Sigma(X)}$ one of them. Since (2.19) holds, the tensors $\mathsf{G}_{\Sigma(X)}$ cannot belong to the boundary of the set $\mathcal{L}^+(\mathbb{R}^3)$ and it is a critical point for $\psi(\cdot; \Sigma(X))$.

From (2.14), we get

$$\mathsf{T}(\mathsf{G}_{\Sigma(X)}; \Sigma(X)) = 0. \tag{2.21}$$

If the material is incompressible, following the same argument, there exists a tensor $\mathsf{G}_{\Sigma(X)}$ such that

$$\mathsf{G}_{\Sigma(X)} \in \operatorname*{arg\,min}_{\mathsf{F}\in\mathcal{D}} f_{\Sigma(X)}(\mathsf{F})$$

where in this case $\mathcal{D} = \mathcal{L}^+_1(\mathbb{R}^3)$. We define a new function $\hat{\psi}$ such that

$$\begin{cases} \hat{\psi} : \mathcal{L}^+(\mathbb{R}^3) \times \mathbb{R} \times \mathcal{S}(\mathbb{R}^3) \to \mathbb{R} \\ \hat{\psi}(\mathsf{F}, p; \mathsf{S}) = \tilde{\psi}(\mathsf{F}; \mathsf{S}) - p(\det \mathsf{F} - 1) \end{cases}$$

where $\tilde{\psi}$ is an extension of ψ as defined in (2.15).

Since $\mathsf{G}_{\Sigma(X)}$ is a minimum for ψ in $\mathcal{L}^+_1(\mathbb{R}^3)$, there exists a $p_{\Sigma(X)} \in \mathbb{R}$ such that $(\mathsf{G}_{\Sigma(X)}, p_{\Sigma(X)})$ is a critical point for $\hat{\psi}$ [76], so that

$$\frac{\partial \hat{\psi}}{\partial \mathsf{F}}(\mathsf{G}_{\Sigma(X)}, p_{\Sigma(X)}; \Sigma(X)) = \frac{\partial \tilde{\psi}}{\partial \mathsf{F}}(\mathsf{G}_{\Sigma(X)}; \Sigma(X)) - p_{\Sigma(X)}\mathsf{G}^{-T}_{\Sigma(X)} = 0,$$

and thus $\mathsf{T}(\mathsf{G}_{\Sigma(X)}, p_{\Sigma(X)}; \Sigma(X)) = 0$. This concludes the proof. ☐

Remark 2.3.1. *Given an initial stress tensor, this Theorem implies that there exists a tensor $\mathsf{G}_{\Sigma(X)}$ that locally maps the body to an unstressed state. Such a distortion is not unique in general: if Q belongs to the material symmetry group of ψ, then also $\mathsf{T}(\mathsf{G}_{\Sigma(X)}\mathsf{Q}; \Sigma(X)) = 0$.*

Remark 2.3.2. *The collection of local maps*

$$\widehat{\mathsf{G}}[\Sigma](X) := \mathsf{G}_{\Sigma(X)},$$

which transform each point of the reference configuration into a point in the local unstressed virtual state, satisfies $\widehat{\mathsf{G}}[\Sigma] \in \mathcal{B}(\Omega_0, \mathcal{D})$, where $\mathcal{B}(\Omega_0, \mathcal{D})$ denotes the set of *all the bounded function $f : \Omega_0 \to \mathcal{D}$. Moreover, the tensor map $\widehat{\mathsf{G}}[\Sigma]$ may not be geometrically compatible, i.e. there could not exist any differentiable vector field $\boldsymbol{\varphi}_{\widehat{\mathsf{G}}}$ such that $\operatorname{Grad}\boldsymbol{\varphi}_{\widehat{\mathsf{G}}} = \widehat{\mathsf{G}}[\Sigma]$. In this case, there does not exist a deformation that maps the reference configuration of the residually stressed material into a relaxed one. In fact, assuming that the reference configuration is simply connected, such a deformation exists if and only if*

$$\operatorname{rot}\widehat{\mathsf{G}}[\Sigma] = \mathbf{0}.$$

In the following, we call $\widehat{\mathsf{G}}[\Sigma]$ the relaxing map.

Remark 2.3.3. *By simple application of the mean stress theorem [101], in the absence of surface tractions and body forces we obtain*

$$\frac{1}{|\Omega_0|}\int_{\Omega_0} \Sigma\, d\boldsymbol{X} = \frac{1}{|\Omega_0|}\left(\int_{\partial\Omega_0} \boldsymbol{X} \otimes (\Sigma \boldsymbol{N})\, dS - \int_{\Omega_0} \boldsymbol{X} \otimes \operatorname{Div}\Sigma\, d\boldsymbol{X}\right) = 0$$

so that the mean value of the initial stress tensor is zero. Thus, the Cartesian components of the residual stress tensor are necessarily spatially inhomogeneous whenever $\Sigma \neq 0$ [110]. Accordingly, the functional form of the map $\widehat{\mathsf{G}}[\Sigma]$ is also inhomogeneous. A homogeneous initial stress Σ can only exist if surface tractions or body forces are applied.

Remark 2.3.4. *Note that in the case in which Σ has singular values over a set $S_\infty \subset \Omega_0$ we are requiring the hypothesis that $\psi(\cdot;\Sigma(\boldsymbol{X}))$ remains a proper function, i.e. it is not identically equal to $+\infty$, when $\boldsymbol{X} \in S_\infty$. Due to the continuity of $\psi(\cdot,\mathsf{S})$, this ensures that $\widehat{\mathsf{G}}[\Sigma](\boldsymbol{X})$ is bounded when $\boldsymbol{X} \in S_\infty$, as it will be shown in Section 2.5.*

2.4 EXISTENCE OF ELASTIC MINIMIZERS FOR INITIALLY STRESSED BODIES

In this section, we prove that if the strain energy density ψ satisfies the assumption of Theorem 2.3.1, then ψ satisfies the ISRI (2.16) if and only if it is expressible using the theory of elastic distortion (2.6).

Theorem 2.4.1. *Let ψ satisfy the hypotheses of Theorem 2.3.1 and the ISCC condition. We denote by ψ_0 the strain energy of the material in the absence of initial stresses, being*

$$\psi_0(\mathsf{F}) = \psi(\mathsf{F}; 0).$$

Then, the function ψ satisfy the ISRI (2.16) *if and only if we can express it as*

$$\psi(\mathsf{F};\Sigma(\boldsymbol{X})) = (\det\widehat{\mathsf{G}}[\Sigma](\boldsymbol{X}))\psi_0(\mathsf{F}\widehat{\mathsf{G}}[\Sigma](\boldsymbol{X})^{-1}) = \psi_{\widehat{\mathsf{G}}[\Sigma](\boldsymbol{X})}(\mathsf{F})$$

where $\widehat{\mathsf{G}}[\Sigma](\boldsymbol{X})$ is a function such that

$$\mathsf{T}(\widehat{\mathsf{G}}[\Sigma](\boldsymbol{X});\Sigma(\boldsymbol{X})) = 0.$$

Proof. It is proved in [98] that the strain energy $\psi_{\widehat{\mathsf{G}}[\Sigma](\boldsymbol{X})}$ satisfies the ISRI.

Let ψ be a strain energy which satisfies the ISRI and such that $\psi(\mathsf{F};0) = \psi_0(\mathsf{F})$. The existence of the function $\widehat{\mathsf{G}}[\Sigma](\boldsymbol{X})$ is guaranteed by the Theorem 2.3.1.

Omitting the explicit dependence on $\boldsymbol{X}$ for the sake of compactness, we obtain:

$$\begin{aligned}\psi(\mathsf{F};\Sigma) &= \psi(\mathsf{F}\widehat{\mathsf{G}}[\Sigma]^{-1}\widehat{\mathsf{G}}[\Sigma];\Sigma) = \\ &= (\det\widehat{\mathsf{G}}[\Sigma])\psi(\mathsf{F}\widehat{\mathsf{G}}[\Sigma]^{-1},\mathsf{T}(\widehat{\mathsf{G}}[\Sigma];\Sigma)) = \\ &= (\det\widehat{\mathsf{G}}[\Sigma])\psi(\mathsf{F}\widehat{\mathsf{G}}[\Sigma]^{-1},0) = \\ &= (\det\widehat{\mathsf{G}}[\Sigma])\psi_0(\mathsf{F}\widehat{\mathsf{G}}[\Sigma]^{-1}) = \psi_{\widehat{\mathsf{G}}[\Sigma]}(\mathsf{F})\end{aligned}$$

that concludes the proof. □

We also introduce the following useful Lemma:

Lemma 2.4.1. *Let $\psi(\mathsf{F};\Sigma(\boldsymbol{X}))$ be a strain energy density satisfying the hypotheses of Theorem 2.3.1, the ISRI and such that $\psi(\mathsf{F};0)$ is polyconvex. Then $\psi(\mathsf{F};\Sigma(\boldsymbol{X}))$ is polyconvex for all $\boldsymbol{X}\in\Omega_0$.*

Proof. From the Theorem 2.4.1, we get

$$\psi(\mathsf{F};\Sigma(\boldsymbol{X})) = (\det\widehat{\mathsf{G}}[\Sigma](\boldsymbol{X}))\psi(\mathsf{F}\widehat{\mathsf{G}}[\Sigma](\boldsymbol{X})^{-1};0).$$

Following the Remark 2.3.2, we have that $\widehat{\mathsf{G}}[\Sigma] \in \mathcal{B}(\Omega_0,\mathcal{L}^+(\mathbb{R}^3))$ and the Lemma is a direct consequence of the Lemma 6.5 in [150]. □

Indeed, under some regularity assumptions, if the strain energy density ψ is polyconvex in the relaxed case, then it is polyconvex for all $\Sigma:\Omega_0\to\mathcal{S}(\mathbb{R}^3)$. It is now possible to prove a theorem of existence of elastic minimizers for initially stressed bodies.

Theorem 2.4.2 (Existence of elastic minimizers)**.** *Let $\Omega_0\subset\mathbb{R}^3$ be a connected, bounded and open subset with a regular boundary and let $\psi(\mathsf{F};\Sigma(\boldsymbol{X}))$ be a strain energy density for an initially stressed material, with $\psi(\cdot;\Sigma(\boldsymbol{X}))\in C^1(\mathcal{L}^+(\mathbb{R}^3))$ and $\psi(\mathsf{F};\cdot)\in C^0(\mathcal{S}(\mathbb{R}^3))$. Let $\Sigma:\Omega_0\to\mathcal{S}(\mathbb{R}^3)$ be a measurable function.*

We assume that:

(i) (initial stress independence and non–degeneracy) ψ fulfills the hypotheses of Theorem 2.3.1 and the ISRI condition (2.16)*;*

(ii) (polyconvexity of the relaxed energy) in the absence of initial stresses, the strain energy density $\psi(\mathsf{F};0)$ is polyconvex with respect to F, namely there exists a convex function $h:\mathcal{L}(\mathbb{R}^3)\times\mathcal{L}(\mathbb{R}^3)\times(0,+\infty)\to\mathbb{R}$ such that

$$\psi(\mathsf{F};0) = h(\mathsf{F},\operatorname{Cof}\mathsf{F},\det\mathsf{F})$$

(iii) (coercivity of the relaxed energy) there exist $\alpha>0$, $\beta\in\mathbb{R}$, $p\geq 2$, $q\geq p/(p-1)$, $r>1$ such that:

$$h(\mathsf{F},\mathsf{C},\delta)\geq\alpha(|\mathsf{F}|^p+|\mathsf{C}|^q+\delta^r)+\beta,\qquad\forall\mathsf{F},\mathsf{C}\in\mathcal{L}(\mathbb{R}^3),\ \delta>0.$$

We assume that there exist two disjointed subset Γ_0, Γ_1 *such that* $\partial\Omega_0 = \Gamma_0 \cup \Gamma_1$ *and such that* $|\Gamma_0| > 0$. *Let* $\boldsymbol{f} : \Omega_0 \to \mathbb{R}^3$ *and* $\boldsymbol{t} : \Gamma_1 \to \mathbb{R}^3$ *measurable such that the application*

$$L[\boldsymbol{\varphi}] = \int_{\Omega_0} \boldsymbol{f} \cdot \boldsymbol{\varphi}\, d\boldsymbol{X} + \int_{\Gamma_1} \boldsymbol{t} \cdot \boldsymbol{\varphi}\, dS$$

is continuous on $W^{1,p}(\Omega_0, \mathbb{R}^3)$. *Finally let* $\boldsymbol{\varphi}_0 : \Gamma_0 \to \mathbb{R}^3$ *be a measurable function and such that the set*

$$U = \Big\{ \boldsymbol{\varphi} \in W^{1,p}(\Omega_0, \mathbb{R}^3) \mid \operatorname{Cof} \operatorname{Grad} \boldsymbol{\varphi} \in L^q,\ \det \operatorname{Grad} \boldsymbol{\varphi} \in L^r, \\ \det \operatorname{Grad} \boldsymbol{\varphi} > 0 \textit{ a.e. in } \Omega_0,\ \boldsymbol{\varphi} = \boldsymbol{\varphi}_0 \textit{ on } \Gamma_0 \Big\}. \quad (2.22)$$

is non-empty.

Then, defining the functional $\mathcal{F} : U \to \mathbb{R} \cup \{+\infty\}$ *as*

$$\mathcal{F}[\boldsymbol{\varphi}] = \int_{\Omega_0} \psi(\operatorname{Grad} \boldsymbol{\varphi}; \Sigma(\boldsymbol{X}))d\boldsymbol{X} - L[\boldsymbol{\varphi}]$$

and assuming that $\inf \mathcal{F}[\boldsymbol{\varphi}] < +\infty$, *there exists an elastic minimizer*

$$\min_{\boldsymbol{\varphi} \in U} \mathcal{F}[\boldsymbol{\varphi}].$$

Proof. Using the Theorem 2.4.1, from (i) we have that

$$\psi(\mathsf{F}; \Sigma(\boldsymbol{X})) = (\det \widehat{\mathsf{G}}[\Sigma](\boldsymbol{X}))\psi_0(\mathsf{F}\widehat{\mathsf{G}}[\Sigma](\boldsymbol{X})^{-1}) =: \Psi(\boldsymbol{X}, \mathsf{F}). \quad (2.23)$$

We prove the claim as a direct application of the Theorem 7.3 in [23]. Here we only sketch the proof, pointing to [23] for the details.

Since Σ is measurable and $\psi(\mathsf{F}, \cdot)$ is continuous for all F, then $\Psi(\boldsymbol{X}, \mathsf{F})$ is a Carathéodory function, i.e. it is continuous with respect to F a.e. in Ω_0 and measurable in Ω_0 for all $\mathsf{F} \in \mathcal{L}^+(\mathbb{R}^3)$. Hence, the functional $\mathcal{F}$ is well defined.

By simple application of Lemma 2.4.1 and (ii), $\Psi(\boldsymbol{X}, \mathsf{F})$ is polyconvex a.e. in Ω_0. The coercivity of $\mathcal{F}$ is enforced a.e. in Ω_0 by the hypothesis (iii), the boundedness of $\widehat{\mathsf{G}}[\Sigma]$ in Remark 2.3.2 and the continuity of L in $W^{1,p}(\Omega_0, \mathbb{R}^3)$. The non-degeneracy of $\Psi(\boldsymbol{X}, \mathsf{F})$ for $\det \mathsf{F} \to 0^+$ is given by (i). Hence, by applying the standard methods of the calculus of variations, we can show the existence of infimizing sequences $\boldsymbol{\varphi}_k \in U$ which admit weakly converging subsequences to a limit point $\boldsymbol{\varphi} \in U$. Since the functional $\mathcal{F}$ is lower semicontinuous as a consequence of its policonvexity, the weak limit $\boldsymbol{\varphi} \in U$ minimizes $\mathcal{F}$.

□

Such a Theorem is a standard application of Ball's theorem on the existence of solutions in nonlinear elasticity [23]. The main result obtained in this section is that *the ISRI automatically guarantees that the polyconvexity is preserved for all the initial stress fields if it holds for* $\Sigma = 0$. Conversely, if we do not assume the ISRI, the polyconvexity of the strain energy density should be imposed by a suitable constitutive restriction on the dependence with respect to the initial stress field.

According to the Theorem 2.4.1, imposing the ISRI condition is equivalent to require that the initial stress tensor Σ is generated by an elastic distortion given by $\widehat{\mathsf{G}}[\Sigma]$.

Conversely, if the ISRI does not hold, the dependence of the stored elastic energy on the choice of the reference configuration is not solely related to the the corresponding variation of the initial stress. Thus, the material properties may depend on the specific initial stress field.

For the sake of clarity, let us investigate how the material symmetry group depends on the presence of an initial stress within the body. We denote by $\mathcal{G}_0$ the material symmetry group of the relaxed state around a material point $\boldsymbol{X}$. In view of Theorem 2.4.1 and following the same computation of (2.9), if the strain energy fulfills the ISRI condition for a generic initial stress field S and for all $\mathsf{Q} \in \mathcal{G}_0$, we get that the material symmetry group $\mathcal{G}_\mathsf{S}$ of the initially stressed body is given by

$$\mathcal{G}_\mathsf{S} = \mathsf{G}_\mathsf{S}^{-1} \mathcal{G}_0 \mathsf{G}_\mathsf{S},$$

where the tensor G_S is defined in Theorem 2.3.1. Hence, the group $\mathcal{G}_\mathsf{S}$ is conjugated to the group $\mathcal{G}_0$ through the tensor G_S, exactly as in the theory of elastic distortions (2.9).

Conversely, we now consider a strain energy of the form

$$\psi(\mathsf{F}; \mathsf{S}) = f(I_1(\mathsf{C}) - 3) + g(J_1 - \operatorname{tr} \mathsf{S}) \tag{2.24}$$

where $J_1 = \operatorname{tr}(\mathsf{SC})$, and the function f and g must be such that the energy density (2.24) satisfies the ISCC (2.11) and g is non-constant. If the material is initially unstressed (i.e. $\mathsf{S} = 0$), the strain energy density (2.24) defines a general isotropic nonlinear elastic response and the material symmetry group is given by

$$\mathcal{G}_0 = \mathcal{O}^+(\mathbb{R}^3).$$

However, if we consider an initial stress $\mathsf{S} = \alpha \boldsymbol{M} \otimes \boldsymbol{M}$, where $\boldsymbol{M}$ is a unit vector, we observe a change in the nature of the material symmetry group. In fact, considering that

$$\operatorname{tr}(\mathsf{S}\mathsf{Q}^T\mathsf{C}\mathsf{Q}) = \operatorname{tr}(\mathsf{SC}) \quad \forall \mathsf{F} \in \mathcal{D} \qquad \Longleftrightarrow \qquad \mathsf{Q}\boldsymbol{M} = \boldsymbol{M}.$$

The material symmetry group $\mathcal{G}_\mathsf{S}$ is given by

$$\mathcal{G}_\mathsf{S} = \left\{ \mathsf{Q} \in \mathcal{O}^+(\mathbb{R}^3) \mid \mathsf{Q}\boldsymbol{M} = \boldsymbol{M} \right\},$$

so that the material is not anymore isotropic but transversely isotropic.

Thus, if the material does not satisfy the ISRI, the material symmetry group $\mathcal{G}_\mathsf{S}$ is not conjugated with $\mathcal{G}_0$ and it is not possible to obtain the material symmetry group $\mathcal{G}_0$ by an elastic distortion of the material. In other words, if the ISRI condition is not fulfilled, the body may change its material symmetry group depending on the imposed initial stress field, leading to a modification of the material response.

2.5 AN ILLUSTRATING EXAMPLE: THE RELAXED STATE OF A SOFT DISC WITH ANISOTROPIC INITIAL STRESS

As an example, we consider a disc of radius R_0 composed of an incompressible nonlinear elastic material subjected to planar strains and initial stresses. Let $(\boldsymbol{E}_R, \boldsymbol{E}_\Theta)$ and $(\boldsymbol{e}_r, \boldsymbol{e}_\theta)$ be the cylindrical vector basis in Lagrangian and Eulerian coordinates respectively. We assume that the initial stress is axis-symmetric, having the following general form

$$\Sigma = \left(\alpha + \beta \log\left(\frac{R}{R_0}\right)\right) \boldsymbol{E}_R \otimes \boldsymbol{E}_R + \left(\gamma + \beta \log\left(\frac{R}{R_0}\right)\right) \boldsymbol{E}_\Theta \otimes \boldsymbol{E}_\Theta. \tag{2.25}$$

The body in the reference configuration must obey the linear momentum balance, that in the absence of bulk forces reads

$$\operatorname{Div} \Sigma = \mathbf{0}. \tag{2.26}$$

Since the residual stress tensor Σ depends only on the radial coordinate R, (2.26) reduces to the following scalar equation

$$\frac{d\Sigma_{RR}}{dR} + \frac{\Sigma_{RR} - \Sigma_{\Theta\Theta}}{R} = 0;$$

that is fulfilled if and only if

$$\beta = \gamma - \alpha.$$

If the disc is not subjected to any external traction, then $\Sigma_{RR}(R_0) = 0$, so that $\alpha = 0$. We now aim at calculating the elastic minimizer corresponding to this particular choice of the initial stresses. Let $\psi(\mathsf{F}; \Sigma)$ be the strain energy density of the initially stressed disc. We assume that in the absence of residual stresses, the material behaves as a general isotropic material, such that

$$\psi(\mathsf{F}; 0) = f(I_1(\mathsf{C}) - 2)$$

where $f : [0, +\infty[\to \mathbb{R}$ is a convex function of its scalar argument. In view of Theorem 2.4.1, $\psi(\mathsf{F}; \Sigma) = \psi(\mathsf{F}\widehat{\mathsf{G}}^{-1}[\Sigma]; 0)$. Using the polar decomposition $\widehat{\mathsf{G}}[\Sigma] = \mathsf{R}\mathsf{U}_{\widehat{\mathsf{G}}}$ where the tensor R is a proper orthogonal tensor and $\mathsf{U}_{\widehat{\mathsf{G}}}$ is the corresponding right stretch tensor, we denote the metric tensor of the initial elastic distortion by

$$\tilde{\mathsf{B}} = \widehat{\mathsf{G}}[\Sigma]^{-1}\widehat{\mathsf{G}}[\Sigma]^{-T} = \mathsf{U}_{\widehat{\mathsf{G}}}^{-2}, \tag{2.27}$$

where $\lambda_{\widehat{\mathsf{G}}}$ is the principal eigenvalue of $\mathsf{U}_{\widehat{\mathsf{G}}}$. Accordingly, the ISCC condition (2.11) imposes:

$$\Sigma = 2f'(I_1(\tilde{\mathsf{B}}) - 2)\tilde{\mathsf{B}} - p_\Sigma \mathsf{I} \tag{2.28}$$

where p_Σ acts as the Lagrange multiplier enforcing the incompressibility of the metric tensor. From the expression of the initial stress (2.25) and the equations

(2.27)-(2.28), we get that $\mathsf{U}_{\widehat{\mathsf{G}}}$ is diagonal with respect to the cylindrical vector basis, thus

$$\mathsf{U}_{\widehat{\mathsf{G}}} = \mathrm{diag}(\lambda_{\widehat{\mathsf{G}}}, \lambda_{\widehat{\mathsf{G}}}^{-1}).$$

Considering that

$$\mathrm{tr}(\widehat{\mathsf{G}}[\Sigma]^{-T}\mathsf{F}^T\mathsf{F}\widehat{\mathsf{G}}[\Sigma]^{-1}) = \mathrm{tr}(\tilde{\mathsf{B}}\mathsf{C})$$

by enforcing the ISRI condition we can write the strain energy density as

$$\psi(\mathsf{F};\,\Sigma) = f(\mathrm{tr}(\tilde{\mathsf{B}}\mathsf{C}) - 2).$$

By applying the trace and the determinant operator on both sides of (2.28), we obtain respectively

$$\begin{cases} p_\Sigma = f'(I_1(\tilde{\mathsf{B}}) - 2)I_1(\tilde{\mathsf{B}}) - \dfrac{I_1(\Sigma)}{2} \\ I_3(\Sigma) + I_1(\Sigma)p_\Sigma + p_\Sigma^2 = 4(f'(I_1(\tilde{\mathsf{B}}) - 2))^2 \end{cases} \tag{2.29}$$

where $I_1(\Sigma) = \mathrm{tr}\,\Sigma$ and $I_3(\Sigma) = \det\Sigma$. After substituting in (2.29) the first equation into the second one, we get

$$\frac{I_1(\Sigma)^2}{4} - I_3(\Sigma) = (f'(I_1(\tilde{\mathsf{B}}) - 2))^2(I_1(\tilde{\mathsf{B}})^2 - 4) \tag{2.30}$$

The term $\frac{I_1(\Sigma)^2}{4} - I_3(\Sigma) = \frac{(\Sigma_{RR}-\Sigma_{\Theta\Theta})^2}{4}$ is always positive. Since $f(x)$ is strictly convex with a minimum in $x = 0$, the rhs of (2.30) is a positive–definite, strictly monotone function of $I_1(\tilde{\mathsf{B}})$ Thus, (2.30) is invertible and the principal eigenvalue $\lambda_{\widehat{\mathsf{G}}} = \lambda_{\widehat{\mathsf{G}}}(\Sigma_{RR}, \Sigma_{\Theta\Theta})$ is given by:

$$\left(\left(\lambda_{\widehat{\mathsf{G}}}^2 + \lambda_{\widehat{\mathsf{G}}}^{-2}\right)^2 - 4\right)(f'(\lambda_{\widehat{\mathsf{G}}}^2 + \lambda_{\widehat{\mathsf{G}}}^{-2} - 2))^2 = \frac{(\Sigma_{RR} - \Sigma_{\Theta\Theta})^2}{4}. \tag{2.31}$$

We multiply each side of (2.28) by C on the right, by applying the trace operator we get

$$\mathrm{tr}(\tilde{\mathsf{B}}\mathsf{C}) = \frac{J_1 + p_\Sigma I_1}{2f'(\lambda_{\widehat{\mathsf{G}}}^2 + \lambda_{\widehat{\mathsf{G}}}^{-2} - 2)}.$$

Accordingly, the strain energy function $\psi(\mathsf{F};\,\Sigma)$ for an initially stressed isotropic material reads

$$\psi(\mathsf{F};\,\Sigma) = f\left(\frac{J_1 + p_\Sigma I_1}{2f'(\lambda_{\widehat{\mathsf{G}}}^2 + \lambda_{\widehat{\mathsf{G}}}^{-2} - 2)} - 2\right). \tag{2.32}$$

Note that the relaxing map corresponding to (2.32) is the map $\widehat{\mathsf{G}}[\Sigma]$ as defined by (2.27) and (2.28), since we have written $\psi(\mathsf{F};\,\Sigma)$ as $\psi(\mathsf{F}\widehat{\mathsf{G}}^{-1}[\Sigma];\,0)$.

A mapping whose deformation gradient corresponds to $\mathsf{U}_{\widehat{\mathsf{G}}}$ is given by

$$r = \lambda_{\widehat{\mathsf{G}}}R, \quad \theta = \frac{\Theta}{\lambda_{\widehat{\mathsf{G}}}^2}, \quad z = Z \tag{2.33}$$

This relaxing map corresponds to a controllable deformation for isotropic materials, meaning that it can be supported by surface tractions alone at equilibrium. It describes the opening of the initial disc into a circular sector, corresponding to non-homogeneous displacements and homogeneous strains [193, 192]. In fact, we remark that (2.33) does not globally map a physically compatible configuration even if the Riemann curvature of the underlying metric tensor is zero. This can be easily checked since the curl operator of the deformation tensor corresponding to (2.33) is not zero if $\lambda_{\widehat{\mathsf{G}}} \neq 1$. From (2.31), this condition implies $\Sigma_{RR} \neq \Sigma_{\Theta\Theta}$, or equivalently $\gamma \neq 0$. Therefore, the relaxing map given by (2.33) is a non-uniform controllable stress state with uniform deviatoric invariants. The latter is the necessary condition for stress controllability given in [45].

2.6 DISCUSSION AND CONCLUDING REMARKS

This work proved novel insights on the link between the existence of elastic minimizers and the constitutive assumptions for initially stressed materials subjected to finite deformations.

Assuming a strain energy density in the form $\psi(\mathsf{F}; \Sigma)$ and a non-degeneracy axiom, we clarified the mathematical implications of assuming the ISRI condition as a constitutive restriction. Theorem 2.3.1 proves the existence of a relaxed state given by the tensor function $\widehat{\mathsf{G}}[\Sigma]$ as an implicit function of the initial stress distribution. The tensor $\widehat{\mathsf{G}}[\Sigma]$ is generally not unique, and can be transformed accordingly to the symmetry group of ψ. Moreover, Theorem 2.4.1 proves that each strain energy density function $\psi(\mathsf{F}; \Sigma)$ that satisfies the ISRI condition can be written as $\psi(\mathsf{F}; \Sigma) = (\det \widehat{\mathsf{G}}[\Sigma])\, \psi(\mathsf{F}\widehat{\mathsf{G}}[\Sigma]^{-1}; 0)$. Thus, we prove that the material symmetry group of the initially stressed material satisfying the ISRI condition locally changes as we vary Σ according to the theory of elastic distortions.

Furthermore, we have used the previous results of Ball to prove the existence Theorem 2.4.2 of the elastic minimizers for a strain energy density in the form $\psi(\mathsf{F}; \Sigma)$, that satisfies the ISRI condition under suitable constitutive restrictions. Such a result is based on the proof that the polyconvexity of the strain energy density of an initially stressed material is automatically inherited for all Σ if it holds in the case $\Sigma = 0$, given some necessary conditions on the non-degeneracy and the regularity of $\psi(\cdot, \Sigma)$.

Whilst the theory of elastic distortion requires an a priori choice of the virtual incompatible state, the constitutive restrictions on $\psi(\mathsf{F}; \Sigma)$ ensure the existence of the elastic minimizers corresponding to the physically observable distribution of the initial stresses. In an illustrative example, we have shown how to calculate the relaxed state of an incompressible isotropic disc as a function of the axis-symmetric distribution of initial stresses.

We finally remark that the ISRI condition should be assumed for the materials that do not undergo a change in the underlying material structure, so that the initial stresses arise only in response to an elastic distortion. This happens, for example, for the residual stresses generated by a differential growth. By using the classification proposed by Epstein [78], the ISRI condition is indeed well suited for modeling the growth or the remodelling of a soft material, namely a change of shape that does not affect the material properties and the microstructure of the material. On the contrary, when there is a modification of the microstructure that involves a change in the material properties, the ISRI condition would be physically flawed and other constitutive choices should be done.

Our results prove useful guidelines for the constitutive restrictions on the strain energy densities of initially stresses materials, having important applications for the study of the morphological stability and wave propagation analysis in soft tissues [59], and the non-destructive evaluation of residual stresses generated by a differential growth in biological materials [132, 75].

3 MODELLING OF ACTIVE PHENOMENA IN BIOLOGICAL TISSUES

In this Chapter, we aim at modelling active phenomena in living matter, focusing the attention on two important processes: the active contraction of muscle tissue and the growth of biological materials.

The work is organized as follows: in Section 3.1 we compare the experimental results on the uniaxial traction of a skeletal muscle with the theoretical prediction of the active strain model, more into detail in Section 3.1.1 we review the active strain approach and its mathematical properties, in Section 3.1.2 we compare the experimental data of Hawkins and Bey [104] with the predicted stress-stretch curves predicted by the active strain approach. In Section 3.1.3 we propose an alternative model based on the mixture active strain method.

In Section 3.2, we mathematically describe solid tumour growth exploiting a non-linear poroelastic model: in Section 3.2.1 we review the model of tumour growth, discussing the differences between fluid-like models and solid-like models. In Section 3.2.2 we discuss the limitations of the fluid models of tumours. In Section 3.2.3, we introduce the poroelastic model and in Section 3.2.4the growth law which includes a mechanical feedback. In Section 3.2.5 we enrich the mechanical model describing the dynamics of the nutrient of the cells. Finally, in Section 3.2.6 we present the results of the numerical simulations of the chemo–mechanical model, comparing them with *in vitro* and *ex vivo* experiments.
The results of this chapter lead to the following publications:

D. Riccobelli and D. Ambrosi. Activation of a muscle as a mapping of stress strain curves. *Submitted*
D. Ambrosi, S. Pezzuto, D. Riccobelli, T. Stylianopoulos, and P. Ciarletta. Solid tumors are poroelastic solids with a chemo-mechanical feedback on growth. *Journal of Elasticity*, 129(1-2):107–124, 2017

3.1 ACTIVATION OF A MUSCLE AS A MAPPING OF STRESS–STRAIN CURVES

An important example of active material is provided by the muscle tissue, which can contract in presence of an electrical stimulus. A correct constitutive modeling of both the active and passive behavior is crucial for several biomechanical systems, such as the modelization of the heart and of the skeletal muscles.

A mathematical description of the muscle tissue poses several challenges. First, nonlinear constitutive laws are required since a muscle can undergo large deformations. Moreover, a muscle, seen as a material, is strongly anisotropic due to the presence of muscle fibers; in particular it can be suitably represented as transversely isotropic (as in the case of the skeletal muscle) or orthotropic material (as happens in the myocardium, due to the different orientation of the fibers). Furthermore, the process of activation of a muscle is very complex and involves several mechanisms at the microstructural level [46, 173].

A robust constitutive model accounting for the ability of a muscle to contract is far from being established. During the last few decades, several methods have been developed to model the active behavior of muscles in the framework of continuum mechanics [149, 9]. The most popular one is the so called active stress [9]. Such an approach involves an additive split of the total stress into a passive and an active component [194, 160, 152]. Another approach is the *active strain*, a technique based on the theory of elastic distortions. In a biomechanical context, such an approach was first introduced by Kondaurov and Nikitin, and further developed by Taber and Perucchio [125, 200, 149]. The active strain has been employed in several models (e.g. [52, 184, 153, 165]) due to its robust mathematical properties and the clear physical interpretation: the muscle contraction corresponds to a geometrical remodelling of the body [78, 175].

While the active strain approach guarantees some suitable mathematical properties, the flexibility of the active stress in general allows a better accordance with the experimental results [9, 184, 105, 93]. Nevertheless, the preservation of the well posedness of the mathematical problem is not always guaranteed by the latter approach [162, 9] and could manifest itself in unexpected numerical issues. The active stress formulation is so general that includes the active strain as a particular case [93].

The aim of this Section is to compare experimental data on the uniaxial isometric activation of a skeletal muscle [215, 104] with a stress field predicted by the active strain theory. We show that a plain active strain approach is intrinsically unable to reproduce experimental data, but suitable modifications can be effective in this respect.

3.1.1 The active strain approach

We denote by $\mathcal{L}^+(\mathbb{R}^3)$ the set of all the linear maps $\mathsf{L} : \mathbb{R}^3 \to \mathbb{R}^3$ with positive determinant. Moreover, we indicate with $\mathcal{U}^+(\mathbb{R}^3)$ the subset of $\mathcal{L}^+(\mathbb{R}^3)$ composed of all the linear applications L such that $\det \mathsf{L} = 1$

Let Ω_0 and Ω_e be the reference and the actual configuration of an elastic body respectively. We denote with $\boldsymbol{X} \in \Omega_0$ the material position vector and with $\boldsymbol{\varphi} : \Omega_0 \to \Omega_e$ the motion function. We denote by $\mathsf{F} = \operatorname{Grad} \boldsymbol{\varphi}$ the deformation gradient tensor.

We assume that the material is incompressible and hyperelastic and we denote by ψ_0 the strain energy density of the passive material. Thus, the first Piola–Kirchhoff stress of the passive material is given by

$$\mathsf{P}_0 = \frac{\partial \psi_0}{\partial \mathsf{F}} - p\mathsf{F}^{-1}, \qquad (P_0)_{ij} = \frac{\partial \psi_0}{\partial F_{ji}} - pF_{ij}^{-1}; \tag{3.1}$$

where p is the Lagrangian multiplier that enforces the incompressibility constraint $\det \mathsf{F} = 1$.

When the body is activated, we assume that the deformation gradient admits a multiplicative decomposition of the form

$$\mathsf{F} = \mathsf{F}_\mathrm{e}\mathsf{F}_\mathrm{a}, \tag{3.2}$$

where F_a accounts for the local distortion of the material due to the activation.

Such an approach is inspired by the theory of elastoplasticity, the decomposition (3.2) is usually referred as *Kröner-Lee* decomposition; to the best of our knowledge, its first application in the field of biomechanics is due to Taber and Perucchio [200].

The distortion field $\mathsf{F}_\mathrm{a} : \Omega_0 \to \mathcal{U}^+(\mathbb{R}^3)$ is to be constitutively prescribed. As far as it concerns the activation of a muscle, we assume that F_a determines no variation in the local volume, hence $\det \mathsf{F}_\mathrm{a} = 1$.

The activation-induced distortion of the body can lead to a geometrically incompatible configuration, namely there may not exist a vector map such that F_a is its gradient: F_a is not integrable. The integrability of F is restored by another component F_e that accounts for the elastic distortion of the body [181].

The tensor field F_e describes the elastic "deformation" due to the presence of external and internal forces and to the restoration of the geometrical compatibility. Hence, the strain energy of the activated material $\psi : \Omega_0 \to \Omega_\mathrm{e}$ is given by

$$\psi(\mathsf{F}) = \psi_0(\mathsf{F}_\mathrm{e}) = \psi_0(\mathsf{F}\mathsf{F}_\mathrm{a}^{-1}), \tag{3.3}$$

and the first Piola–Kirchhoff stress tensor reads

$$\mathsf{P} = \frac{\partial \psi}{\partial \mathsf{F}} - p\mathsf{F}^{-1} = \mathsf{F}_\mathrm{a}^{-1}\frac{\partial \psi}{\partial \mathsf{F}_\mathrm{e}} - p\mathsf{F}^{-1}.$$

The active strain approach possesses nice mathematical properties. In fact, if the strain energy density ψ_0 is rank-one convex or polyconvex, then ψ preserves such properties [150, 9].

3.1.2 Activation as a linear mapping

The aim of this section is to compare the experimental results on the isometric uniaxial activation of a skeletal muscle with the stress fields predicted by the active strain approach. We will focus on the work of Hawkins and Bey

[104] who performed traction experiments on a rat tibialis anterior muscle in isometric conditions.

We denote the local direction of the fibers by the vector field $\boldsymbol{M}$ with $|\boldsymbol{M}| = 1$. A common choice for F_a inspired by the microstructural architecture, is given by

$$\mathsf{F}_a = (1-\gamma)\mathsf{M} + \frac{1}{\sqrt{1-\gamma}}(\mathsf{I} - \mathsf{M}), \tag{3.4}$$

where $0 \leq \gamma < 1$ is a parameter that describes the microstructural degree of contraction of the muscle (0 corresponds to the relaxed muscle), $\mathsf{M} = \boldsymbol{M} \otimes \boldsymbol{M}$ and $\otimes$ denotes the diadic product. By performing such a choice for the active strain F_a we assume that the contraction of the sarcomere preserves the cylindrical symmetry along the axis identified by the direction $\boldsymbol{M}$.

Let us denote with F_λ the deformation gradient that corresponds to the uniaxial deformation along the anisotropic direction $\boldsymbol{M}$, i.e.

$$\mathsf{F}_\lambda = \lambda\mathsf{M} + \frac{1}{\sqrt{\lambda}}(\mathsf{I} - \mathsf{M}). \tag{3.5}$$

Making use of (3.1), we can define the function ϕ as

$$\phi\,(\lambda) := \psi_0(\mathsf{F}_\lambda),$$

in the passive case. Because of the specific form of the active deformation (3.4), in a uniaxial deformation (3.5) the strain energy density takes the specific form

$$\psi(\mathsf{F}_\lambda) = \phi\left(\frac{\lambda}{1-\gamma}\right). \tag{3.6}$$

Differentiating $\psi(\mathsf{F}_\lambda)$ with respect to λ, we obtain the principal stress in the direction $\boldsymbol{M}$:

$$P_{\boldsymbol{M}}(\lambda, \gamma) = \frac{d\psi(\mathsf{F}_\lambda)}{d\lambda}, \tag{3.7}$$

so that, exploiting the relation (3.6) and applying the chain rule, we get

$$P_{\boldsymbol{M}}(\lambda, \gamma) = \frac{1}{1-\gamma}\phi'\left(\frac{\lambda}{1-\gamma}\right).$$

Out of a rescaling of the strain and stress, the stress-stretch relation $P(\lambda, \gamma)$ is therefore completely characterized by its passive behaviour. In fact, if we know the passive response

$$P_{\boldsymbol{M}}(\lambda, 0) = \frac{d\psi_0(\mathsf{F}_\lambda)}{d\lambda} = \phi'(\lambda),$$

then if the muscle is activated we can obtain $P_{\boldsymbol{M}}(\lambda, \gamma)$ by rescaling the variable of the function $\phi(\lambda)$.

Indeed, from (3.7) we can observe that

$$P_{\boldsymbol{M}}(\lambda, \gamma) = \frac{1}{1-\gamma}\phi'\left(\frac{\lambda}{1-\gamma}\right) = \frac{1}{1-\gamma}P_{\boldsymbol{M}}\left(\frac{\lambda}{1-\gamma}, 0\right). \tag{3.8}$$

Thus, the stress-stretch curve of the activated muscle can be straightforwardly obtained by rescaling the stress and the strain variables by the same factor $(1-\gamma)^{-1}$.

Unfortunately, such a representation of the activation process is too restrictive to reproduce the experimental results obtained from measuring P_M in a tetanized muscle [215, 104]. Hawkins and Bey measured the stress-strain relation of the passive muscle and of the tetanized muscle in isometric conditions (Fig. 3.1). In fact, from the experimental plot in Fig. 3.1 (top) we observe that the passive material exhibits a strain hardening effect when $\lambda \geq 1.3$. When the muscle is activated, the curve stress vs strain has a completely different slope: there is a change of concavity and a strain hardening for $\lambda \geq 1.3$ and no self-similar transformation reproduces it.

A qualitative attempt to fit of the physiological plot using the active strain approach is obtained by mapping the experimental curve of the passive muscle in Fig. 3.1 (top) into the activated one by the rescaling defined by the equation (3.8) according to the following procedure. Every point of the stress-stretch plane (λ_0, P_0) that belongs to the stress-stretch curve of the passive material can be mapped on the activated curve making use of (3.8). Indeed, we get that the rescaling

$$(\lambda, P) = \left(\lambda_0(1-\gamma), \frac{P_0}{1-\gamma}\right), \tag{3.9}$$

provides the stress-stretch curve of the activated material.

Such a rescaling is applied to the passive curve for several γ and the results are shown in Fig. 3.1 (bottom). It is apparent that in this way it is not possible to obtain a stress-stretch curve that fits the experimental data for the contracted muscle. In fact, the strain hardening is anticipated as we increase γ and the curve obtained interpolating the experimental data is not convex for $0.7 < \lambda < 1.2$. Thus, the active strain approach cannot reproduce the uniaxial deformation of a contracted skeletal muscle.

We remark that the result of this section do not assume any specific strain energy function to model the passive behavior of the muscle; it is just a rescaling of an experimental curve. Our unique assumption is that the activation of the muscle reads as a contraction along the direction of the fibers that preserves volumes, as in equation (3.4).

3.1.3 An alternative approach: the mixture active strain approach

A possible alternative method is to model the muscle as a material composed of two solid phases, only one of them actively contributing to the muscle contraction.

Let us consider a strain energy density such that

$$\psi = \psi_{\text{iso}} + \psi_{\text{ani}}$$

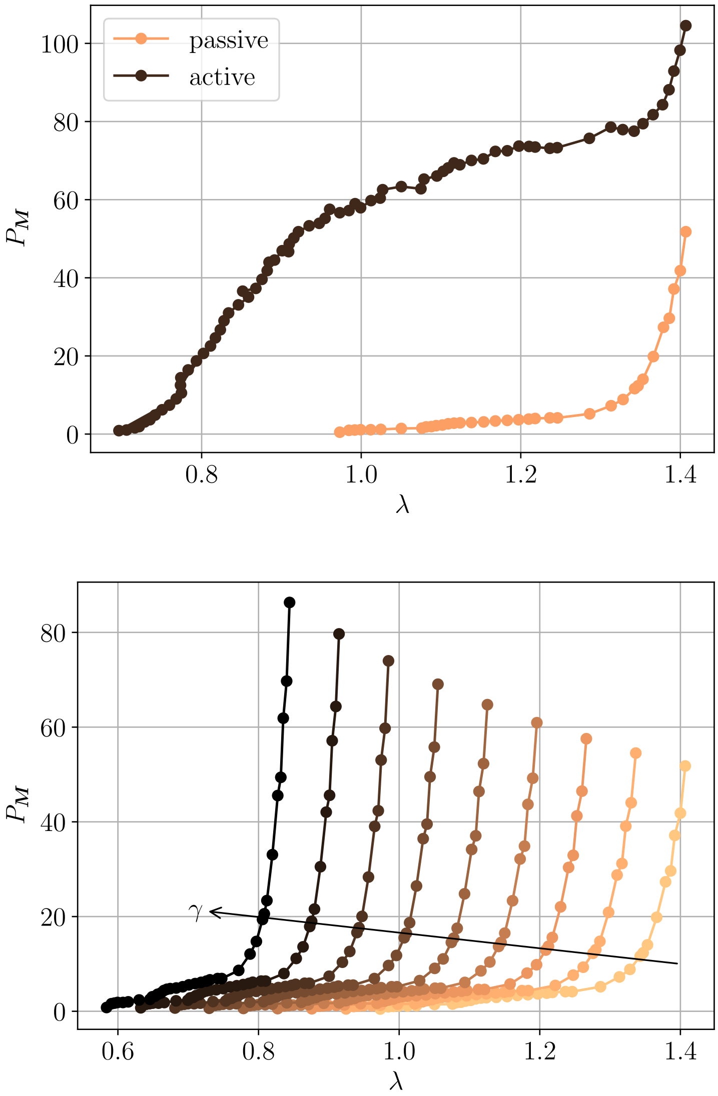

Figure 3.1: (top) Stress-stretch data obtained from the uniaxial traction experiments of Hawkins and Bey [104]. (bottom) Stress-stretch curves of the uniaxial traction obtained from the passive data by assuming the active strain approach and using (3.9), here γ varies from 0 up to 0.4 by steps of 0.05. The arrow denotes the direction along which γ grows.

where ψ_{iso} is the isotropic part of the strain energy whilst ψ_{ani} describes the contribution provided by the fibers. We assume that ψ_{iso} is only passive and does not give any contribution to the active behavior of the muscle.

The only part of the energy that can provide an active contribution is the function ψ_{ani}. Thus, we describe the muscle as a mixture of passive (like elastin, randomly distributed collagen) and active materials (like the sarcomeres). We call this approach *mixture active strain* [107, 94, 159, 93].

The first Piola–Kirchhoff stress now reads

$$\mathsf{P} = \frac{\partial \psi_{\text{iso}}}{\partial \mathsf{F}} + \frac{\partial \psi_{\text{ani}}}{\partial \mathsf{F}} - p\mathsf{F}^{-1}$$

while the principal stress in the direction $\boldsymbol{M}$, denoted by $P_{\boldsymbol{M}}$, produced by the deformation F_λ is

$$P_{\boldsymbol{M}}(\lambda, \gamma) = P_{\boldsymbol{M}}^{\text{iso}}(\lambda) + P_{\boldsymbol{M}}^{\text{ani}}(\lambda, \gamma)$$

where

$$P_{\boldsymbol{M}}^{\text{iso}}(\lambda) = \frac{d\psi_{\text{iso}}(\mathsf{F}_\lambda)}{d\lambda} \qquad P_{\boldsymbol{M}}^{\text{ani}}(\lambda, \gamma) = \frac{d\psi_{\text{ani}}(\mathsf{F}_\lambda \mathsf{F}_{\text{a}}^{-1})}{d\lambda}.$$

In analogy with (3.8) we can introduce the following representation

$$P_{\boldsymbol{M}}^{\text{ani}}(\lambda, \gamma) = \frac{1}{1-\gamma} P_{\boldsymbol{M}}^{\text{ani}}\left(\frac{\lambda}{1-\gamma}, 0\right).$$

Hence, the purely active contribution arising from the contraction of the muscle is due to the anisotropic contribution and it is given by

$$P_{\boldsymbol{M}}^{\text{act}}(\lambda, \gamma) = P_{\boldsymbol{M}}(\lambda, \gamma) - P_{\boldsymbol{M}}(\lambda, 0) = \frac{1}{1-\gamma} P_{\boldsymbol{M}}^{\text{ani}}\left(\frac{\lambda}{1-\gamma}, 0\right) - P_{\boldsymbol{M}}^{\text{ani}}(\lambda, 0).$$

Such a function is expected to fit the experimental data of Hawkins and Bey [104] relative to the active contribution to the stress $P_{\boldsymbol{M}}$ (see Fig. 3.1). Indeed, setting $\gamma = \gamma_{\text{max}}$ corresponding to the maximal contraction of the sarcomere, we get that $P_{\boldsymbol{M}}^{\text{act}}(\lambda, \gamma_{\text{max}})$ should reproduce the difference between the stress generated by the tetanized muscle and the stress generated by the passive body: to perform this comparison, we have to chose a specific strain energy density.

Let us introduce the following invariants

$$I_1 = \operatorname{tr}\mathsf{C}, \qquad J = \det \mathsf{F}, \qquad I_4 = \operatorname{tr}(\mathsf{CM}),$$

where $\mathsf{C} = \mathsf{F}^T\mathsf{F}$ is the right Cauchy-Green tensor.

We choose to model the isotropic part of the muscle as a Gent material [90], so that the strain energy density is given by

$$\psi_{\text{iso}}(\mathsf{F}) = -\frac{\mu I_{\text{max}}}{2} \log\left(1 - \frac{I_1 - 3}{I_{\text{max}}}\right) \tag{3.10}$$

where μ is the shear modulus and I_{max} is a parameter that sets the maximum value reachable by I_1.

The anisotropic part of the strain energy is instead given by

$$\psi_{\text{ani}}(\mathsf{F}) = \alpha\left(\sqrt[4]{I_4} - 1\right)^2. \tag{3.11}$$

Thus the fibres contribute to the strain energy only if there is a deformation in the direction $\boldsymbol{M}$. We remark that the constitutive choice (3.10), while specific, is very popular in the mechanics of soft tissues [90, 115, 116, 169, 170]. The anisotropic component of the strain energy (3.11) usually in literature involves the square root I_4 [48]. In this work we adopt a power law with a smaller exponent (fourth order root) to account for the reported change in convexity of P_M versus λ (see Fig. 3.1 top).

The total strain energy of the activated material is hence given by

$$\psi(\mathsf{F}) = \psi_{\text{iso}}(\mathsf{F}) + (\det \mathsf{F}_{\text{a}})\psi_{\text{ani}}(\mathsf{F}\mathsf{F}_{\text{a}}^{-1}) \tag{3.12}$$

where F_{a} is given by (3.4).

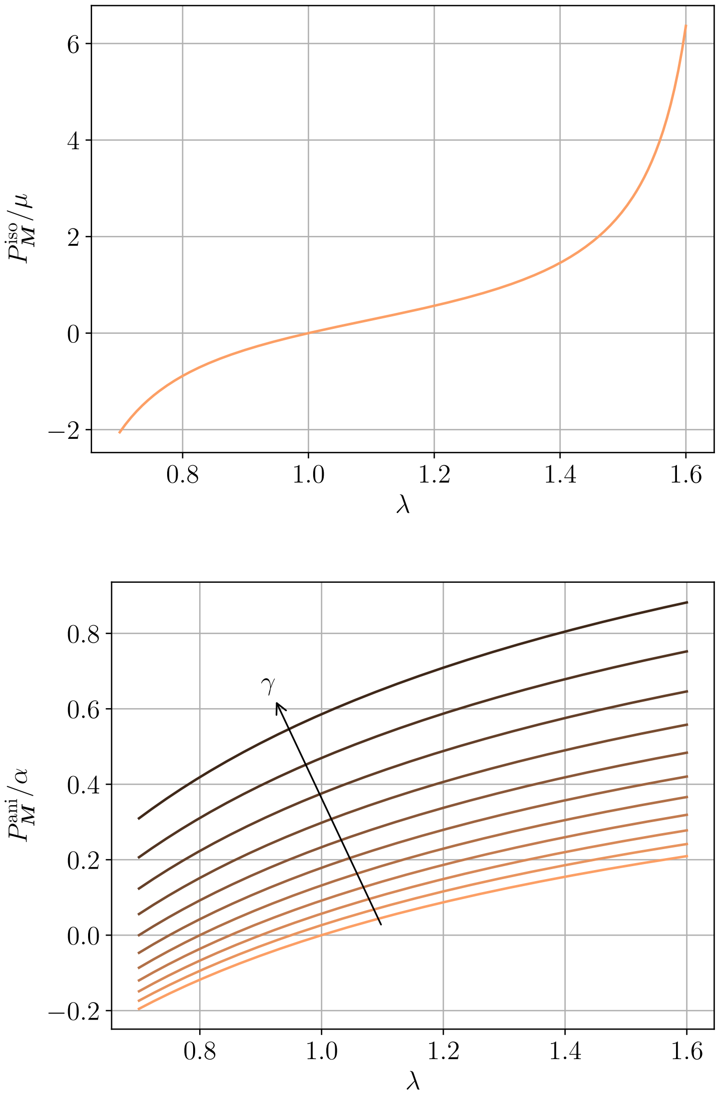

Figure 3.2: Plot of the normalized principal stresses P_M^{iso}/μ (top) and P_M^{ani}/α (bottom). The parameter I_{max} has been set equal to 1 and γ varies between 0 and 0.5 by steps of 0.05.

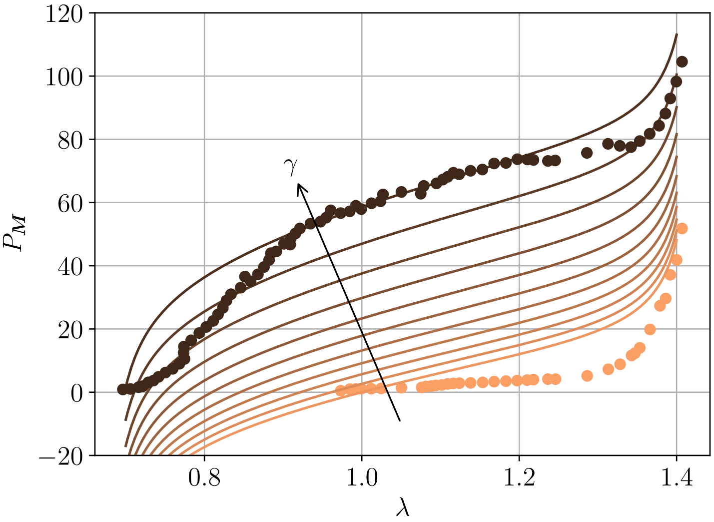

Figure 3.3: Plot of P_M when $\mu = 5$ kPa, $I_{\max} = 0.45$, $\alpha = 100$ kPa and γ varies from 0 to 0.5 with steps of 0.05.

Thus, for $\det \mathsf{F}_\mathrm{a} = 1$ the Piola–Kirchhoff stress tensor reads

$$\mathsf{P}(\mathsf{F}) = \mathsf{P}_{\mathrm{iso}}(\mathsf{F}) + \mathsf{F}_\mathrm{a}^{-1}\mathsf{P}_{\mathrm{ani}}(\mathsf{F}\mathsf{F}_\mathrm{a}^{-1}) - p\mathsf{F}^{-1},$$

where

$$\mathsf{P}_{\mathrm{iso}}(\mathsf{F}) = \frac{\partial \psi_{\mathrm{iso}}}{\partial \mathsf{F}} = \mu \left(1 - \frac{I_1 - 3}{I_{\max}}\right)^{-1} \mathsf{F}^T,$$
$$\mathsf{P}_{\mathrm{ani}}(\mathsf{F}) = \frac{\partial \psi_{\mathrm{ani}}}{\partial \mathsf{F}} = \alpha \frac{\sqrt[4]{I_4} - 1}{\sqrt[4]{I_4^3}} \mathsf{M}\mathsf{F}^T.$$

In particular, in the case of a uniaxial deformation in the direction $\boldsymbol{M}$, we can compute the principal stresses $P_{\boldsymbol{M}}$ and $P_{\boldsymbol{M}}^{\mathrm{ani}}$ in the direction $\boldsymbol{M}$, namely

$$P_{\boldsymbol{M}}^{\mathrm{iso}}(\lambda) = \frac{d\psi_{\mathrm{iso}}(\mathsf{F}_\lambda)}{d\lambda} = \mu \left(1 - \frac{\lambda^2 + 2\lambda^{-1} - 3}{I_{\max}}\right)^{-1} \left(\lambda - \lambda^{-1}\right)$$
$$P_{\boldsymbol{M}}^{\mathrm{ani}}(\lambda, \gamma) = \frac{d\psi_{\mathrm{ani}}(\mathsf{F}_\lambda \mathsf{F}_\mathrm{a}^{-1})}{d\lambda} = \frac{\alpha}{1-\gamma} \frac{\sqrt{\frac{\lambda}{1-\gamma}} - 1}{\sqrt{\frac{\lambda}{1-\gamma}}}.$$

Thus, the total principal stress

$$P_{\boldsymbol{M}}(\lambda, \gamma) = P_{\boldsymbol{M}}^{\mathrm{iso}}(\lambda) + P_{\boldsymbol{M}}^{\mathrm{ani}}(\lambda, \gamma)$$

is given by

$$P_{\boldsymbol{M}}(\lambda, \gamma) = \mu \left(1 - \frac{\lambda^2 + 2\lambda^{-1} - 3}{I_{\max}}\right)^{-1} \left(\lambda - \lambda^{-1}\right) + \frac{\alpha}{1-\gamma} \frac{\sqrt{\frac{\lambda}{1-\gamma}} - 1}{\sqrt{\frac{\lambda}{1-\gamma}}}.$$

In Fig. 3.2 we plot the principal stresses $P_M^{\text{iso}}(\lambda)$ and $P_M^{\text{ani}}(\lambda, \gamma)$ normalized with respect to μ and α, respectively. In Fig. 3.3 we plot the total principal stress $P_M(\lambda, \gamma)$ where we set $\mu = 5$ kPa, $I_{\max} = 0.45$, $\alpha = 100$ kPa. Increasing the activation parameter γ, the stress-stretch relationship is in good agreement with the experimental data of Fig. 3.1 for $\gamma \sim 0.5$.

The model however has some limitations: the passive curve overestimate the stress for $\lambda \simeq 1.2$. Moreover, the compressive branch of the passive curve can not be compared with measures. In the experimental literature, some works report that the passive stress generated performing a uniaxial compression along the direction of the fibers is lower than the one occurring in extension [210]. However, other works report a behaviour in compression with the stress of the same order of magnitude of the stress obtained in extension, in one case even higher [217, 36, 35] (see [210] for a comparison between the data). Our model predicts a behaviour which is similar to the second case. In order to obtain a softer behaviour in compression, it would be necessary to exploit a more involved expression of the strain energy densities ψ_{iso} and ψ_{ani} (e.g. considering an anisotropic energy also for the passive constituent of the muscle).

Summarizing, we have shown that by using an active strain approach on the anisotropic part of the strain energy density only, one can quantitatively reproduce the behaviour of the skeletal muscle in extension. The mixed active strain approach allows to overcome two limitations of the "pure" active strain. First, increasing the activation parameter, the strain stiffening appears always at $\lambda = 1.3$. Second, we observe a change of concavity in the stress-strain curve in the tetanized case ($\gamma = 0.5$) at $\lambda \simeq 1.1$ (Fig. 3.3). Mathematical issues raised by the mixture active strain are the subject of the next Section.

3.1.3.1 *Material symmetry group and muscle activation*

Even if the mixture active strain approach better fits the experimental data with respect to the active strain, it remains an open question whether such approach preserves or not some mathematical properties. For the "global" active strain approach (3.3), rank-one convexity is preserved [9]; in the mixture approach, if the strain energy functional is rank-one convex globally in the passive case, we cannot state rank-one convexity without further assumptions on ψ_{iso} and ψ_{ani}. If both ψ_{iso} and ψ_{ani} are rank-one convex, then

$$\delta\mathsf{F} : \frac{\partial^2\psi(\mathsf{F})}{\partial\mathsf{F}\partial\mathsf{F}} : \delta\mathsf{F} = \delta\mathsf{F} : \frac{\partial^2\psi_{\text{iso}}(\mathsf{F})}{\partial\mathsf{F}\partial\mathsf{F}} : \delta\mathsf{F} + \delta\mathsf{F}\mathsf{F}_a^{-1} : \frac{\partial^2\psi_{\text{ani}}(\mathsf{F})}{\partial\mathsf{F}\partial\mathsf{F}} : \delta\mathsf{F}\mathsf{F}_a^{-1} > 0$$

for all $\delta\mathsf{F}$ which are rank-one since also $\delta\mathsf{F}\mathsf{F}_a^{-1}$ is a rank-one tensor [9]. If the material is incompressible, $\delta\mathsf{F}$ must also belong to the tangent space to the manifold $\det\mathsf{F} = 1$, namely $\mathsf{F}^{-T} : \delta\mathsf{F} = 0$.

The same happens for polyconvexity: if both the ψ_{iso} and ψ_{ani} are polyconvex in the passive case, then the polyconvexity is preserved in the active case. This is a direct consequence of Lemma 6.5 in [150].

The active strain preserves the material properties during muscle contraction. Indeed, the multiplicative decomposition of the deformation gradient is equivalent to a remodelling, leading to a change of the relaxed state of the body [77, 78]. Other methods, such as the active stress or the mixture active strain, do not correspond to a remodelling and a modification the material properties, such as the shear modulus or the material symmetries, can take place as a consequence of material activation. If we use the language introduced by Epstein [78], there is change of the *archetype* of the body.

It is expected that the symmetry group of the material is preserved, during muscle activation, since the contraction of sarcomeres does not generate any new structural anisotropy. Let

$$\begin{aligned}\mathcal{G}_{\text{iso}} &= \left\{\mathsf{Q} \in \mathcal{U}^{+}(\mathbb{R}^3) \mid \psi_{\text{iso}}(\mathsf{FQ}) = \psi_{\text{iso}}(\mathsf{F})\, \forall \mathsf{F} \in \mathcal{U}^{+}(\mathbb{R}^3)\right\},\\ \mathcal{G}_{\text{ani}} &= \left\{\mathsf{Q} \in \mathcal{U}^{+}(\mathbb{R}^3) \mid \psi_{\text{ani}}(\mathsf{FQ}) = \psi_{\text{ani}}(\mathsf{F})\, \forall \mathsf{F} \in \mathcal{U}^{+}(\mathbb{R}^3)\right\}.\end{aligned}$$

The material symmetry group of the passive muscle is given by $\mathcal{G} = \mathcal{G}_{\text{iso}} \cap \mathcal{G}_{\text{ani}}$. If the muscle is activated, the material symmetry group of the anisotropic part of the energy becomes [78]

$$\widehat{\mathcal{G}}_{\text{ani}} = \mathsf{F}_{\text{a}}^{-1}\mathcal{G}\mathsf{F}_{\text{a}},$$

and so the material symmetry group of the whole energy reads $\widehat{\mathcal{G}} = \mathcal{G}_{\text{iso}} \cap \widehat{\mathcal{G}}_{\text{ani}}$.

It is easy to verify that if ψ_{iso} is isotropic and ψ_{ani} is transversely isotropic with direction of symmetry $\boldsymbol{M}$, if we apply an activation of the form (3.4), then the symmetry group of the material is not modified by the mixture active strain, i.e. $\mathcal{G} = \widehat{\mathcal{G}}$.

Summarizing, the active strain approach corresponds to a remodelling [78, 175]: there is only a morphological change in the relaxed configuration and the properties of the material are conserved. In the previous sections, we have proved that the active strain cannot fit the experimental data of the uniaxial extension of a skeletal muscle. During muscle contraction, the mutual positions of the actin and myosin filaments change, leading to a modification of the microstructure: the increased number of cross bridges should result into a different stiffness of the tissue. The active strain approach allows to describe the modification of shape induced by muscle contraction but it does not take into account the evolution of the material properties induced by the formation of cross bridges (i.e. the shear modulus of the material does not change).

Conversely, the mixture active strain approach correctly reproduces the experimental data for the uniaxial traction of the muscle, without changing the symmetry group of the material.

3.1.4 Discussion and concluding remarks

We have analyzed some aspects related to the modelization of muscle activation. First, in Section 3.1.1 we have provided a review of the active strain approach for modeling the activation of an elastic medium. In Section 3.1.2

we have compared theoretical predictions vs. experimental data provided by Hawkins and Bey [104]. We have showed that, independently from the chosen passive model, the active strain approach cannot reproduce the stress-stretch curve of the tetanized tibialis anterior muscle.

According to the classification made by Epstein [78], the active strain approach corresponds to a remodelling of a material, namely a change of shape that does not affect the material properties and the microstructure. The inadequacy discussed above shows that the contraction of the muscle is not a simple remodelling and the microstructure of the tissue and the material properties change.

Since it is not possible to model the skeletal muscle contraction as a pure remodelling, in Section 3.1.3 we have proposed a model of the muscle alternative to the active strain obtained by a mixture approach, applying the Kröner–Lee decomposition of the deformation gradient only on one component (the anisotropic part) of the strain energy density. To make quantitative comparisons, we have used a Gent strain energy density for the isotropic part and the strain energy (3.11) for the anisotropic one. Such a simple approach, called mixture active strain, provides results which are in good agreement with the experimental ones.

Convexity properties are preserved if both the isotropic and the anisotropic part of the strain energy are polyconvex or rank-one convex. Also the material symmetry group is preserved if ψ_{ani} is transversely isotropic along the direction $\boldsymbol{M}$ and F_{a} has the form (3.4).

It is to be remarked that while a correct representation of the stretch-stress curve for uniaxial homogeneous deformation is a mandatory requirement, it is not sufficient to obtain a reliable model for a generic deformation, in particular in shear [93]; a deeper understanding of the possible change in the microstructure and in the material properties due to the process of muscle activation is required.

The results of this work may support the development of models of the muscle tissue activity: a reliable mathematical description of the skeletal muscles or of the whole heart are active and open research topics in biomechanics and in the field of biomedical engineering.

3.2 SOLID TUMOURS ARE POROELASTIC SOLIDS WITH A CHEMO–MECHANICAL FEEDBACK ON GROWTH

Solid tumours can be regarded as active materials, since malignant cells duplicate in presence of nutrient. After Folkman & Hochberg [86], the *multicellar spheroid* is a standard *i*n vitro system used to evaluate the uncontrolled duplication rate of a tumour cell aggregate. A tumour spheroid is a cluster of cells floating in a culture medium, it is an ensemble of cells freely proliferating in an environment with large availability of nutrient. The malignant cells have lost the ability to self–regulate their own number through a normal apoptosis mechanism, regulated by the homeostasis with the environment; they duplicate in an uncontrolled manner, isotropically, producing a nearly spherical shape. In the standard free–growth case, a plot of the diameter of the tumour vs. time typically exhibits an early stage of exponential growth, followed by a linear one. The transition from one regime to the other is mainly regulated by the availability of nutrient, that is driven by diffusion through the intercellular space. In fact, when the size of the tumour $R_o(t)$ is smaller than the typical diffusion length, the nutrient is everywhere available in the spheroid and the growth is volumetric [8]:

$$\frac{dR_o^3}{dt} \simeq {R_o}^3,$$

so that $R_o \simeq e^t$. Conversely, when the diameter of the spheroid is much larger than the penetration length of the nutrient, one obtains surface growth, that is

$$\frac{dR_o^3}{dt} \simeq {R_o}^2,$$

and $R_o \simeq t$. In a realistic intermediate regime, the concentration of nutrients decays exponentially with the radius [100], favouring the external proliferation vs the internal one. The mechanism underlying cell duplication and, in particular, the influence of the mechanical stress on growth is still not completely understood.

The work of Chapter 3.2 is motivated by a number of recent experiments that demonstrate the dependence of the growth rate of a tumour spheroid on the mechanical load at the boundary. Some papers report a reduced apoptosis, with no significant changes in proliferation [106]. According to others, the cell division, rather than the cell death rate, is affected by stress [143]. To disentangle the puzzle of the biological feedback of stress on growth, in Chapter 3.2 we discuss the rheology of the cellular aggregate as a living material, to point out its constitutive properties. We illustrate a number of arguments that support the hypothesis that a solid tumour is a poroelastic material, where the cells and the extra-cellular matrix represent the solid elastic component. A mathematical model based on such an assumption is able to predict inhomogeneities that can not be justified by fluid-like assumptions.

3.2.1 Background: elementary rheology and growth theory

The simplest distinction among fluid and solid materials can be based on an elementary ideal experiment: under a pure shear load fluids flow, while solids do not, at the time scale of interest. This draconian categorization encompasses also viscoelastic materials, as they typically exhibit fluid-like or solid-like properties depending on the relaxation time scales. As an example, a "Maxwell fluid" behaves as a solid if observed at a time scale much smaller than its relaxation time. Analogously, a "Kelvin solid" flows like a fluid when observed on short enough time scales. Things become a little bit more complex when flow is prompted only above a yield stress, but the distinction persists when loads are neatly below or beyond the threshold.

Many biological materials are composed by a mixture of several components: interstitial fluid, different species of cells, collagen fibres, and so on. For these microscopically heterogeneous materials the overall mechanical behavior is represented, at the macroscale, by the superposition of single phase contributions, proportionally to the volume fraction occupied by each component. The archetypical example of a mixture is a porous elastic material permeated by a fluid: the stress in a poroelastic medium is the sum of the interstitial pressure of the fluid plus the solid stress, which is proportional to the solid volume fraction.

Fluids and solids behave in a very different manner when internal stresses arise not because of external loads, but as due to the inner material reorganization (growth and remodelling). The simplest example are thermal stresses in inhomogeneously heated materials with temperature-dependent density: residual stresses relax in fluids, not in solids. The persistence of residual stress is therefore the signature of solid-like behavior which has to be properly addressed in a modelling framework. In case of small strains, linearized elasticity applies and stress (and strains) can be superimposed. In case of large strains, as it is often the case with soft matter, a multiplicative decomposition of the tensor gradient of deformation has to be introduced.

For our purposes, we represent the motion of every material point of a continuous body as a smooth invertible map $\boldsymbol{\varphi}(\mathbf{X})$ with Jacobian $\mathsf{F} = \frac{\partial \varphi}{\partial \mathbf{X}}$. For a nonlinear elastic material the strain energy is $\psi(\mathsf{F})$; when the body grows and residual stress is present, the strain energy rewrites

$$\psi(\mathsf{F}\mathsf{G}^{-1}) \tag{3.13}$$

where G is usually called “growth tensor”.

3.2.2 Are solid tumours fluids?

While the availability of nutrients is the major factor affecting tumour growth, other external agents can play a role. The mechanical influence of external loading on tumour growth has been first demonstrated by Helmlinger *e*t al. [106]. They designed an experimental setup in order to control the load applied at the boundary of tumour cell spheroids *i*n vitro in agarose gels, and checked the influence of such a stressed state on the growth rate of the multicell spheroid. They compared the free growth of a floating multicell spheroid with the size of cell aggregates placed into the agarose gel. The gel is produced at a given (known) stiffness by suitably tuning the concentration of the solid phase. As the spheroid grows, it displaces the surrounding gel, which then exerts a compressive force at the surface of the tumour spheroid. An *a priori* mechanical characterization of the gel allows to calculate the pressure exerted by the gel on the spheroid, depending on its radius.

The main result of the experiments carried out by the group of Rakesh Jain [106] is that the stress field reduces the final size of the spheroids, with a decreased apoptosis and non significant changes in proliferation. It is therefore clear that a precise determination of the constitutive laws that characterize the mechanical behavior of a tumour spheroid is a pre-requisite in order to assess a reliable stress–growth relationship.

Early attempts in this respect assumed that a cell conglomerate behaves like a viscoelastic fluid, able to bear a static load because of its surface tension [87]. At equilibrium, measurements of the curvature radius of a loaded sample provide the surface tension of the “fluid".

According to the Laplace formula, the pressure jump across a curved interface between two fluids is inversely proportional to the radius of the curvature. If the spheroid is loaded with the force F acting on a contact surface A, by continuity of the stress, the inner pressure is F/A and therefore

$$\frac{F}{A} = \sigma \left(\frac{1}{R_1} + \frac{1}{R_2} \right) \tag{3.14}$$

where σ is the surface tension and R_1, R_2 are the curvature radii of the free surface. According to the experiments, the surface tension of a cell aggregate ranges in $1 - 22 \cdot 10^{-3}$ Newton/meter (as a reference value, the surface tension of the water is about $72 \cdot 10^{-3}$ Newton/meter). Relaxation times range between 1 and 50 seconds [87].

The opposite approach is to describe a solid tumour as a viscoelastic solid. In this case, at equilibrium the external load should be balanced by the stress in the body, depending on the strain of its material points. Assuming an homogeneous deformation and using the same data provided by the experiments above, one can estimate the Young modulus E according to the following rule:

$$\frac{F}{A} = E \frac{h - h_0}{h_0} \tag{3.15}$$

where h, h_0 are the height of the loaded and unloaded sample, respectively. In this case one finds $E \simeq 4$ kPa, a typical soft–range value for living cells [127].

A second argument supporting the assumption of solid–like constitutive equations is based on the spatial correlation between stress and apoptosis–mitosis in loaded ellipsoidal spheroids [51]. The non–homogeneous proliferation pattern can be produced only by a solid-like material: a hydrostatic generates a pressure independent on the position in any symmetric geometry, while in a solid material, high stress concentrates around the tips.

Furthermore, the work by Netti et al. [151] support the view that tumours behave as solid-like materials. In their study, stress-relaxation experiments of various tumour types in confined compression were performed and at the end of the experiment all tumours equilibrated in a constant, non-zero stress, typical of viscoelastic solids.

Finally, evidence of residual stress in murine and human tumours is reported by Stylianopoulos et al [198]. They cut the tumour azimuthally and observed an opening angle, which is the signature of a solid like behavior. Residual stress is likely produced by an inhomogeneous duplication rate of the cells as well as by mechanical interactions between the cells and extracellular matrix components, particularly collagen and hyaluronic acid, that strain the tumour microenvironment. Only solids can contain residual stress, due to the evolution of their relaxed configuration produced by incompatible growth [7]: energy can be elastically stored in the unloaded body only if it is a solid. In particular, Stylianopoulos et al. observed a compressive residual stress (i.e. negative opening angle) in the kernel and a tensile residual stress (positive opening angle) in the outer shell of the tumour. This behaviour is paradoxical in terms of availability of nutrients: their concentration is larger near the boundary, thus favoring proliferation and eventually producing compressive stress. In a solid tumour *in vivo*, this intuitive explanation does not work and we address such a puzzle in the next sections.

3.2.3 Growth and stress

An evocative definition of a tumour is "a living system that has lost its self–regulating ability towards homeostasis". In other words, tumour cells do not correctly detect or elaborate the external signals that should regulate its proliferation and apoptosis, and duplicate without control. When the stress state of the system is not in homeostatic mechanical equilibrium, it remodels (growing or resorbing matter) until the target tensional state is recovered. In this respect, all the genetic information that detail the shape and function of organs are encoded in the target stress. A suggestive mechanical interpretation of a tumour therefore naturally arises: a tumour is an open system (in terms of mass and energy) with a damaged inner mechano-biological control inducing a disregulation of tensional homeostatis, i.e. the feedback that normally self–regulates growth in terms of stress–modulated control does not properly work. In other words, tumour cells regulate production and consumption not according to a benefit of the whole organism but only in view of maximum invasion of malignant cells: the control on growth does indeed exist, also as a function of available nutrients, but the corresponding duplication/apoptosis strategy has a different aim.

The experiments illustrated in the section above do not only demonstrate the existence of residual stress in tumours, but they also show that the inhomogeneous proliferation and apoptosis, triggered by the differential availability of nutrients, is enhanced in a mechanically loaded spheroid. Their main result is that mechanical stress affects proliferation and apoptosis inside the spheroid in a non–homogeneous way, a correlation existing between strong apoptosis and high stress.

In another series of experiments, the compression of the spheroid is controlled by the concentration of a large molecule (Dextran) soluted in the bath [142, 143]. As Dextran molecules cannot enter neither the cell membrane nor the interstitial (intracellular) space, an imbalance of osmotic pressure at the boundary loads the cellular aggregate. It is reported that for larger concentrations of Dextran the diameter of the spheroid grows slower and reaches a plateau at smaller radius, in agreement with the results of Helmlinger et al [106]. While a single cell is almost incompressible with respect to the pressure due to the concentration of Dextran, the volume of the cell aggregate strongly depends on the osmotic pressure [141]. The reduction in volume in the cellular aggregate therefore mainly occurs because of reduction of the intercellular space, in the inner region of the spheroid.

The large number of available data suggests that a cell aggregate behaves as a poroelastic material. The mathematical modelling of solid tumours as porous deformable media has been addressed in a number of papers [43, 11, 183]; it a suitable mechanical framework to account for the coupled dynamics of cells and extracellular matrix (the solid matrix) and interstitial fluid. The interstitial flow is typically represented by a Darcy-type equation, while the mass exchange among phases which allows a prediction of the growth of the mass.

In the experimental setup by Montel et al. [142, 143] the porous media theory offers a transparent explanation for interplay between the pressure of the fluid, the chemical potential of the Dextran and the stress in the solid matrix. The external load at the boundary is the sum of two terms: the pressure of the fluid plus the chemical potential of the Dextran. Observing that the diameter of the macromolecules is typically larger than the size of the intracellular pores, we split the fluid load into two contributions: one that balances the interstitial pressure, the other one loading the solid (cellular) component. Formally, we assume that the global balance at the boundary

$$(-p - p_D)_{\text{out}}\, \boldsymbol{n} = (\mathsf{T} - p\mathsf{I})_{\text{in}}\, \boldsymbol{n}, \tag{3.16}$$

splits into

$$-p_{\text{out}} = -p_{\text{in}}, \tag{3.17}$$

$$-p_D \boldsymbol{n} = \mathsf{T}\boldsymbol{n}, \tag{3.18}$$

where p is the pressure of the interstitial fluid, p_D is the osmotic pressure contribution due to the concentration of Dextran, T is the Cauchy stress tensor in the cellular aggregate, I is the identity tensor and $\boldsymbol{n}$ is the outgoing normal (radially directed) vector. This assumption is in agreement with the observation that the solid stress is not affected by the interstitial fluid pressure [198].

On the basis of this hypothesis, the stress state in the loaded spheroid can be determined solving the force balance equations for the solid component only. Assuming spherical symmetry, the tensor gradient of deformation and the growth tensor read

$$\mathsf{F} = \operatorname{diag}\left(r', \frac{r}{R}, \frac{r}{R}\right), \qquad \mathsf{G} = g(r)\,\mathsf{I}, \tag{3.19}$$

where $r(R,t)$ is the radial coordinate of the material point that was in R at time $t = 0$, I is the identity tensor and the prime $'$ denotes derivation in R. The solid component of the poroelastic spheroid must satisfy the force balance equation

$$\frac{d}{dr}T_{rr} + \frac{2}{r}\left(T_{rr} - T_{\theta\theta}\right) = 0, \tag{3.20}$$

with boundary conditions

$$r(0,t) = 0, \qquad T_{rr}(r_o) = -p_D. \tag{3.21}$$

where $r_o = r(R_o, t)$. A simple representation of an hyperelastic compressible material is provided by the strain energy

$$\hat{\psi}(\mathsf{F}) = \frac{\mu}{2}\left(\mathsf{F}\cdot\mathsf{F} - 2\log(\det\mathsf{F}) - 3\right). \tag{3.22}$$

If the material grows, the strain energy depends on the growth tensor too, through a classical multiplicative decomposition

$$\psi(\mathsf{F}\mathsf{G}^{-1}) = \frac{\mu}{2}\left(\mathsf{F}\mathsf{G}^{-1}\cdot\mathsf{F}\mathsf{G}^{-1} - 2\log(\det(\mathsf{F}\mathsf{G}^{-1})) - 3\right). \tag{3.23}$$

where μ is the shear elastic modulus. First variation and pull back to the reference configuration yields the first Piola-Kirchhoff stress

$$\mathsf{P} = \mu\det(\mathsf{G})\left(\mathsf{G}^{-1}\mathsf{G}^{-T}\mathsf{F}^{T} - \mathsf{F}^{-1}\right). \tag{3.24}$$

where, explicitly,

$$P_{RR} = \mu g^3\left(\frac{r'}{g^2} - \frac{1}{r'}\right), \qquad P_{\Theta\Theta} = \mu g^3\left(\frac{r}{Rg^2} - \frac{R}{r}\right). \tag{3.25}$$

The force balance equation (3.20) in material coordinates reads

$$\frac{d}{dR}P_{RR} + \frac{2}{R}\left(P_{RR} - P_{\Theta\Theta}\right) = 0, \tag{3.26}$$

or, explicitly,

$$\frac{d}{dR}\left(r'g - \frac{g^3}{r'}\right) = 2\left(g\frac{r}{R^2} - \frac{g^3}{r} - g\frac{r'}{R} + \frac{g^3}{r'R}\right) \tag{3.27}$$

to be supplemented by boundary conditions (3.21) rewritten in material coordinates

$$P_{RR}(R_o) = (\det\mathsf{F})\,T_{rr}\,F_{rr}^{-1}|_{R_0} = -(\det\mathsf{F})\,p_D\,F_{rr}^{-1}|_{R_0} \tag{3.28}$$

or, explicitly

$$\mu g^3 \left(\frac{r'}{g^2} - \frac{1}{r'} \right) |_{R_0} = -p_D \frac{r^2}{R^2} |_{R_0}. \tag{3.29}$$

For constant g the force balance equation (3.27) with boundary conditions (3.29) has solution

$$r(R; g) = \gamma g R \tag{3.30}$$

where γ is the positive root of the third order polynomial

$$f(\gamma) = p_D \gamma^3 + \mu \gamma^2 - \mu = 0. \tag{3.31}$$

One may notice that $f(0) = -\mu < 0$ while f' is always positive, therefore the root is unique. Moreover $f(1) = p_D > 0$, so that it must be $0 < \gamma < 1$.

Remark 3.2.1. *One could observe that poroelasticity has been advocated for the model above, but its use is apparently very limited: there is no interstitial fluid flow, and the porosity, the volume fraction of solid vs. liquid component, is not even mentioned. There is a rationale behind such a minimal choice. Fluid flow is so slow that it carries no contribution in the stress balance equation; of course, mass exchange among species is the true physical mechanism for the growth of the tumour mass, however here it is directly incorporated in the growth tensor* G*. Secondly, the porosity of the matrix should contribute to the stress tensor* T *with a multiplicative factor depending on the determinant of the gradient of deformation; as a matter of fact, we incorporate such a contribution in the compressibility of the strain energy function* (3.22)*. The numerical results to be illustrated in the next sections will confirm that good predictions can be obtained even with such a simple constitutive law, thus confirming that the theory weakly depends on the specific constitutive equation for the strain energy density of the solid matrix. The crucial ingredient of the model is the multiphase split of the load at the boundary into a fluid and a solid component* (3.19)*.*

3.2.4 Mechanobiological feedback and equilibrium

In the general case, a growth law for G is to be supplemented to close the differential equation (3.27-3.29). We consider first the case of growth controlled by a mechanical feedback only. If nutrients are largely available everywhere, the growth in time is expected to depend on the stress only. In finite elasticity, the growth must depend on an invariant measure of the stress. A thermodynamically consistent choice is to adopt the dependence on the Eshelby stress [6]. To minimize the calculations, while preserving the essential biophysical features, we chose here to measure the stress in terms of the second Piola-Kirchhoff tensor S, which reads

$$\mathsf{S} = \mathsf{P}\mathsf{F}^{-T}. \tag{3.32}$$

The mitotic rate of single tumour cells is known to be inhibited by compression [106], and promoted by tension [50], and a very simple growth law that can account for such a behavior is

$$\dot{g} = \frac{g}{\tau}\left(1 + \frac{\operatorname{tr} \mathsf{S}}{3\kappa\mu} - \frac{g}{\alpha}\right) \tag{3.33}$$

where $1/\tau$ is the mitotic rate in absence of external stimuli, $\kappa\mu$ is a threshold stress and the last term in brackets accounts for apoptosis, the natural cellular death rate. We highlight that the assumption of an isotropic growth tensor allows to set a functional dependence on the trace of S. For a general anisotropic growth a more complex dependence on the principal stresses would be needed, guided by thermo-mechanical requirements.
Consider the unloaded case first: $-p_D = 0$ and at time $t = 0$ the solid component has $g = 1$. As $\mathsf{S} = 0$, the evolution in time of G is autonomous and independent of the radial position, so that $g(t)$ is constant in space and its evolution in time initially follows the well known exponential growth in size of the cell aggregate up to a saturation dictated by the value of α. The solid component of the poroelastic spheroid is therefore relaxed, exactly as a sponge in the deep ocean, where the interstitial pressure balances the head of the water.
If Dextran is present, the extra pressure compresses the cellular phase and triggers the mechanobiological feedback via equations (3.33). The growth $g(t)$ is given by the solution of the first order ordinary differential equation

$$\dot{g} = \frac{g}{\tau}\left(1 - g\left(\frac{\gamma p_D}{\kappa\mu} + \frac{1}{\alpha}\right)\right). \tag{3.34}$$

Equation (3.34) has two equilibrium points: $g = 0$, always unstable, and

$$g_e = \frac{\alpha\kappa\mu}{\alpha\gamma p_D + \kappa\mu} \tag{3.35}$$

which is always stable (for the fixed $r(R;t)$ of (3.30)). The mathematical model therefore predicts the following scenario, corresponding to the observed dynamics. For null osmotic pressure, the system grows exponentially, then it tends to saturation. For sufficiently large osmotic pressure the stable equilibrium depends on the applied pressure p_D. After derivation of equations (3.31) and (3.35) we get

$$\frac{dg_e}{dp_D} = -\frac{\alpha^2\kappa\mu}{(\alpha\gamma p_D + \kappa\mu)^2}\frac{\gamma\,(2\gamma p_D + 2\mu)}{3\gamma p_D + 2\mu} < 0. \tag{3.36}$$

The solution of equation (3.34) explains the plateau in growth vs time reported for loaded spheroids at different Dextran concentrations, but it does not account for the radial density inhomogeneities observed in excised aggregates. Remaining in a purely mechanical setting, an explanation for such a discrepancy between theory and experiments could be provided by the possible onset of an instability for the equilibrium solution (3.34) of the coupled problem. This question is addressed in the appendix, where we study the stability of the solution of the nonlinear system (3.27) and (3.33) with boundary conditions (3.29) in order to explain the emergence of inhomogeneity. The result of the analysis is that the small perturbations are always damped in time, so that a purely mechanical framework cannot account for the observed dependency of growth on the radial coordinate. The biophysics of the system needs therefore to be enriched: in the next section we show that the kinetics of nutrients can trigger dependence of the asymptotic state on the radial coordinate.

3.2.5 Dynamics of the nutrient and inhomogeneity of growth

In an avascular tumour, nutrients are provided to malignant cells by diffusion through the boundary of the spheroid. The balance between diffusion and uptake is fast with respect to the growth times (one hour vs. days) and obeys a linear reaction–diffusion equation:

$$-\frac{1}{r^2}\frac{d}{dr}\left(r^2\frac{dc}{dr}\right) = -\frac{c}{\lambda^2}. \tag{3.37}$$

with boundary conditions

$$\frac{dc}{dr}|_{r=0} = 0, \qquad c(r_0) = c_0, \tag{3.38}$$

where the decay length λ is on the order of 100-200 micrometers and c_0 is the external (constant) concentration. We remind that the boundary value problems refers to the avascular phase of tumour growth. At later stages, neovascularization can be triggered after the diffusion-limited radius is reached. In such a case, a distributed nutrient supply from the tumour vascular network should also be taken into consideration.

During the avascular growth phase, the concentration profile can be calculated by direct integration of the equation in spatial coordinates [100], yielding an exponential decay of the concentration of nutrient going from the boundary to the center of the spheroid:

$$c(r) = c_0 \frac{r_0}{\sinh(r_0/\lambda)} \frac{\sinh(r/\lambda)}{r}. \tag{3.39}$$

To account for the combined action of stress and nutrient pattern, we propose to rephrase equation (3.34) to the following growth law

$$\dot{g} = \frac{g}{\tau}c\left(1 + c\left(\frac{\operatorname{tr} S}{3\kappa\mu} - \frac{g}{\alpha}\right)\right). \tag{3.40}$$

According to equation (3.40), the proliferation of the malignant cells is enhanced by the availability of nutrient, as it is usually assumed in mathematical models that do not specifically account for mechanics. In the same way as in equation (3.33), it is expected that the system reaches an equilibrium when the term in brackets vanishes: a plateau in size is observed for large enough times. The novelty of this growth law is that the equilibrium does not correspond to an homogeneous growth tensor $g\mathsf{I}$, but it depends on the radial position through the concentration of nutrient, thus originating an inhomogeneous residual stress. Using numerical simulations, in the next sections we are able to show that the predicted residual stress is in agreement with the reported opening angles from cutting experiments.

3.2.6 Numerical simulations

Numerical integration of equations (3.27) and (3.40) with boundary conditions (3.29) and initial conditions

$$r(R,t=0) = R, \qquad g(R,t=0) = 1 \tag{3.41}$$

is performed using a finite difference scheme with centered discretization in space and a fourth order Runge-Kutta scheme in time. The parameters used in the numerical simulations are $\tau = 2.5$ days, $\kappa = 2.9$ kPa, $\alpha = 3.7$, $\lambda = 250\,\mu$m and $\mu = 10$ kPa. The initial radius is $100\,\mu$m, the final simulation time is $t_f = 25$ days and the boundary condition of (3.37) is $c_0 = 1$.
The volume of the spheroid initially grows very rapidly for all values of p_D. At large times, for null or small values of osmotic pressure the slope of the curve becomes very small, and it becomes horizontal for large p_D (Figure 3.4).

As expected, the non-uniform pattern of nutrients triggers a weak inhomogeneity in growth. While the predicted growth pattern cannot be directly compared with data, it is indirectly supported by the residual stress that it produces by the relation (3.13). The radial and hoop component of the residual stress are plotted in Figures 3.5 and 3.6 versus the radial coordinate at equilibrium.

As expected, the radial stress vanishes on the boundary of the spheroid, while it is internally compressive. Conversely, the hoop stress changes sign, being compressive in the core and tensional in the outer layer. Such a residual stress distribution is stable against both circumferential and azimuthal perturbations of the tumour boundary, as investigated in [55].

Data on residual stress of *in vitro* tumour spheroids are not available, probably because they are too soft and do not reach a size such that a mechanical manipulation and a precise cut can be operated. However the pattern reported in Figure 3.5 and Figure 3.6 is in qualitative agreement with experiments on (much bigger) human tumours implanted in mice [198]. Stylianopoulos et al. observe that cells at the periphery of the spheroid are restricted by the surrounding tissue and thus, during radial tumour growth they develop tensile circumferential forces. Surrounding tissues in vivo would then produce on the tumour a compressive hydrostatic pressure increasing with the tumour growth. Furthermore, Figures 3 and 4 depict that the magnitude of stress - either compressive

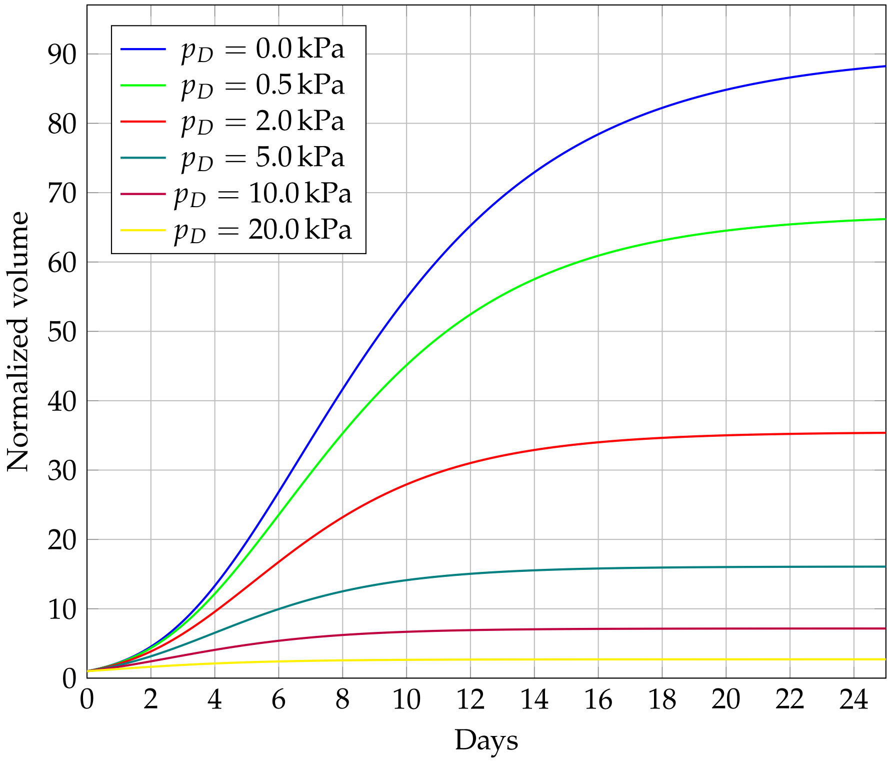

Figure 3.4: Volume of a spheroid vs. time for different values of the osmotic pressure.

or tensile - increases as the osmotic pressure exerted on the cells, p_D, decreases. This is explained by the fact that for low osmotic pressures the tumour becomes larger in size and the stresses increase.

If the external pressure is removed, the radius quickly grows and reaches the same value of the free-growth case (Figure 3.7), in agreement with the experimental results [142].

3.2.6.1 *Stress release in a cut spheroid*

A quantitative comparison among observed and predicted residual stress can be obtained on the basis of the opening angle of cut specimens. To this aim, tumour spheroids have been grown in mice and then they have been cut along their azimuthal plane for about 80% of their diameter. The spheroids then partially relax their residual stress: the cut surface opens up at the periphery while the inner region swells (see figure 3.8). Figure 3.9 depicts the cutting experiments for breast and pancreatic tumours implanted in nude mice, also reporting the tumour opening length and the maximum residual stresses within the tumour specimens.

The observed behavior, which is in qualitative agreement with our predictions in the stress pattern in small, *in vitro*, spheroids, can be quantitatively compared with opening angles data on the basis of a three dimensional numer-

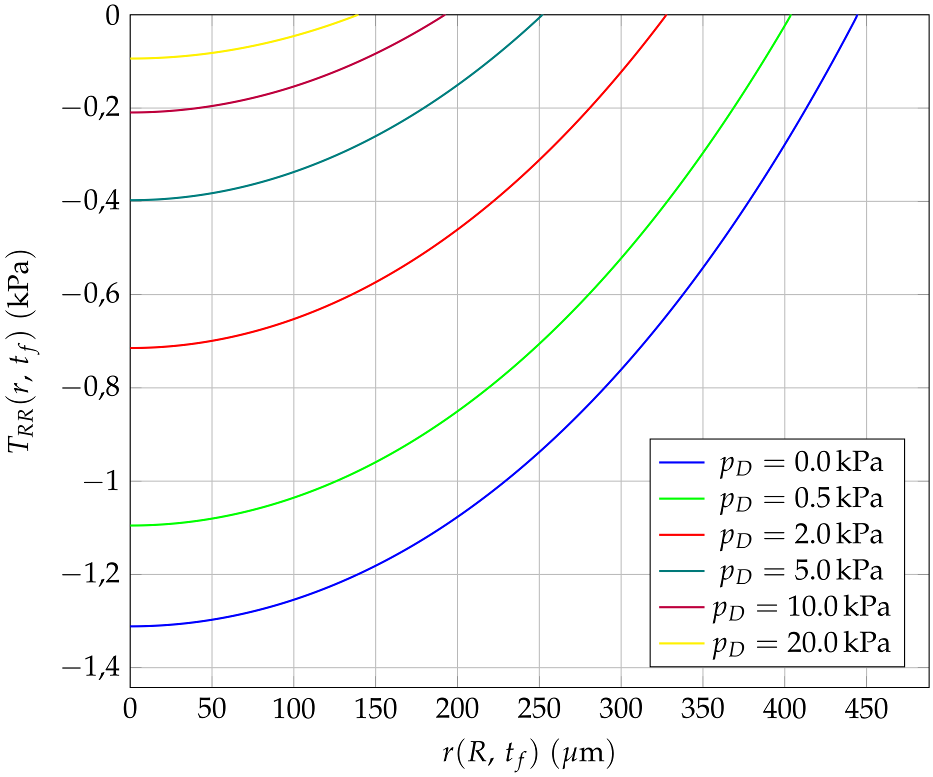

Figure 3.5: Radial residual stress versus the radial position at final time for different values of the osmotic pressure.

ical simulation only. As a matter of fact, an axial cut of a ring preserves the cylindrical symmetry of the problem [68], while an azimuthal cut of a sphere breaks it.

Numerical simulations are obtained using a finite element code that solves the equation of finite elasticity on a spherical wedge. The computation reproduces the physical observations: the spheroid grows under spherical symmetry which is eventually broken by the cut. We therefore use the growth tensor computed under radial symmetry assumption and we evaluate the opening angle that it produces.

The 3D numerical problem is based on FEniCS [4]. The computational domain is discretized with quadratic tetrahedral elements, with an average diameter of 10 μm. Since we expect near to singular stresses around the edge of the cut, the mesh is gradually refined nearby this edge to one twentieth of the original size. The mesh contains roughly 28 143 elements and it has been produced by Gmsh [91]. The non-linear variational problem is discretized with quadratic isoparametric finite elements, and the final problem has 137 949 degrees of freedom. The solver for non-linear problem is based on a modified Newton's method specifically designed for variational inequalities, and implemented in the PETSc framework [21]. The solver can deal with inequality con-

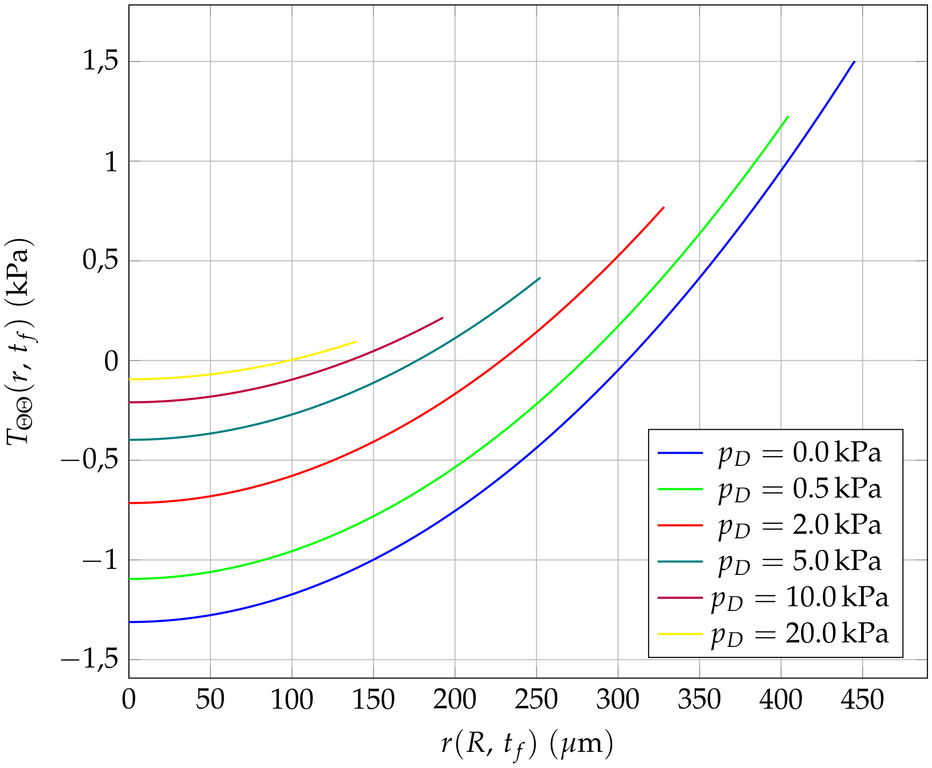

Figure 3.6: Hoop residual stress versus the radial coordinate at final time for different values of the osmotic pressure.

straints, as we have on the cut boundary surface to avoid self-contact during the swelling. The solver for the linear system is MUMPS [14].

The simulation is performed in two steps: first, we apply a homogeneous growth tensor obtained by averaging the target one, while keeping the cut sealed; then, we release the cut and we enforce the final growth tensor. This strategy facilitates the convergence of the non-linear solver, which performs 40 iterations at most. A relative error below 1% on the opening angle is observed when the mesh is uniformly refined, certificating the numerical convergence.

Boundary conditions, reported in Figure 3.10, apply as follows: the outer boundary is stress-free, the cut surface is enforced to have non-negative displacement in the normal direction to avoid self-contact, and on the internal, intact, portion of the boundary symmetry arguments yield null normal displacement and while the other components of the displacement must have null derivative with respect to the normal direction. In Figure 3.11 the deformed configuration obtained after a vertical cut of 80% of the diameter is shown.

The parameters used in the numerical simulations are $\tau = 2.5$ days, $\kappa = 33.35$, $\alpha = 37$, $\lambda = 2.5$ mm, $\mu = 27.0$ kPa and $p_D = 5.0$ kPa. The initial radius is 100 μm, the simulation ends at $t = 50$ days and the boundary condition of (3.37) is $c_0 = 1$. In the numerical experiment the tumour opens with an angle of 11.70°, corresponding to 1.41 mm of opening length. The final volume is 169.84 mm^3.

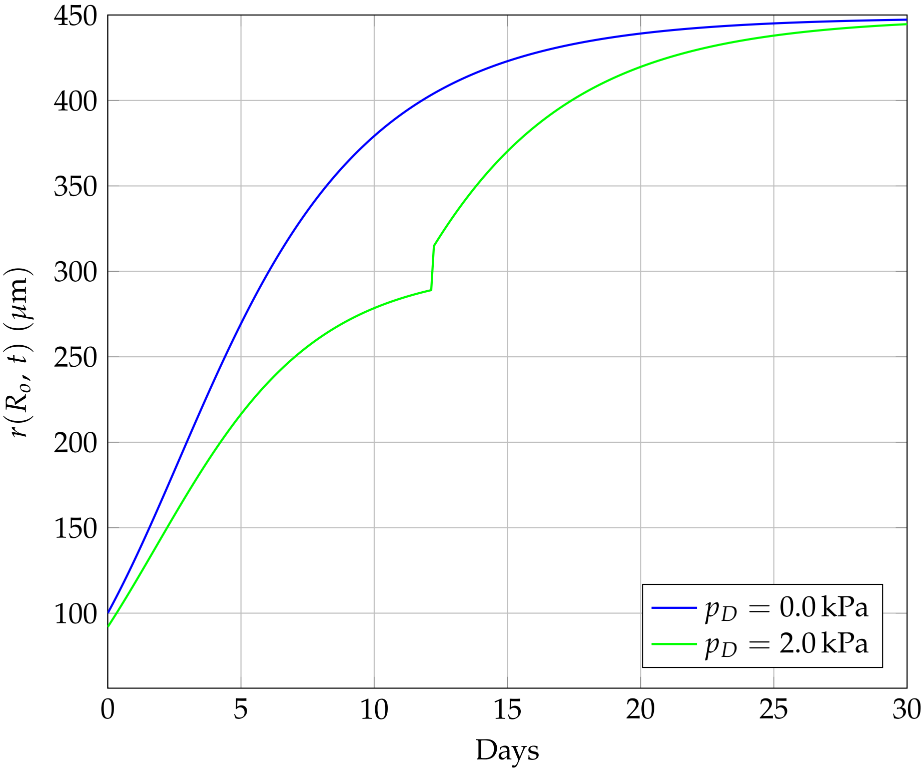

Figure 3.7: Radius of the spheroid vs. time for $p_D = 0$ (blue line) and $p_D = 2000$ Pa (green line). After 12 days the external pressure is removed and the system returns the curve corresponding to the unloaded state.

The inner-most part of the cut, for about 20% of the diameter, is in self-contact, certificating that this portion of the tumour tends to swell outward after the cut. It is to be remarked that the diffusion length assumed here is larger than the one used for small in vitro spheroids.

These results are in agreement with the *ex-vivo* experiments: the opening length, the final volume and the hoop stress are very close to the reported ones for the MiaPaCa2 tumour number 4 (see Figure 3.9) [198].

In order to investigate the relationship between the heterogeneity in the growth tensor and the opening angle, we have performed a numerical experiment where the difference between the growth at the center and the boundary of the tumour is stepwise increased from zero to a value of 20. Table 3.1 summarizes the result of the simulation. As expected from the theory, a uniform growth yields no residual stress and the tumour does not open after the cut (first column of the table). On the other hand, the greater the difference in growth between the center and the boundary, the larger the opening length and consequently the opening angle (from the second column of the table). The volume is mostly affected by the average value of the growth over the entire domain, and not by the heterogeneity. The numerical experiment also shows that

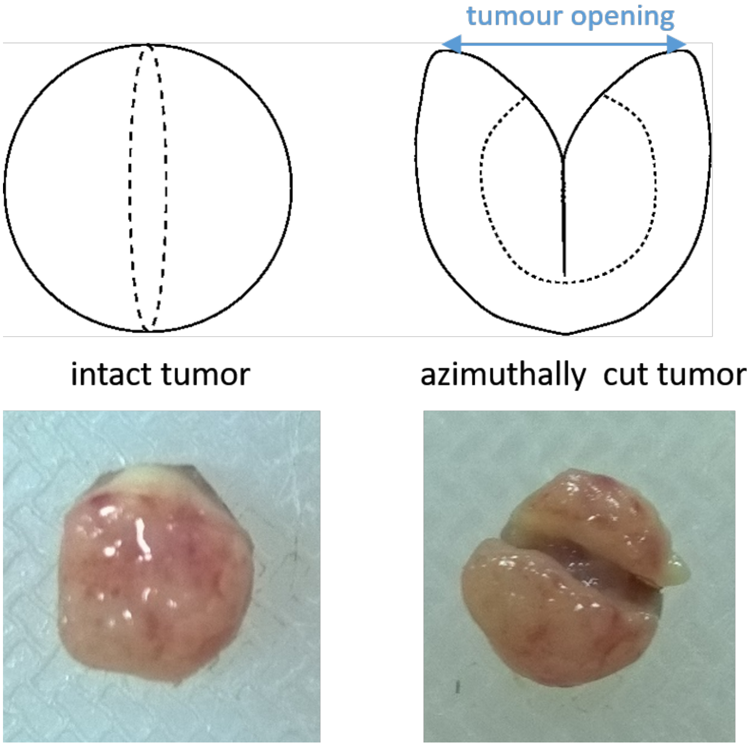

Figure 3.8: An intact, residually stressed spheroid (left) is cut along an azimuthal plane for 80 % of its diameter. The outer region opens up while the inner one swells(right), thus distribution of residual stress that goes from compressive to tensile along the radial coordinate.

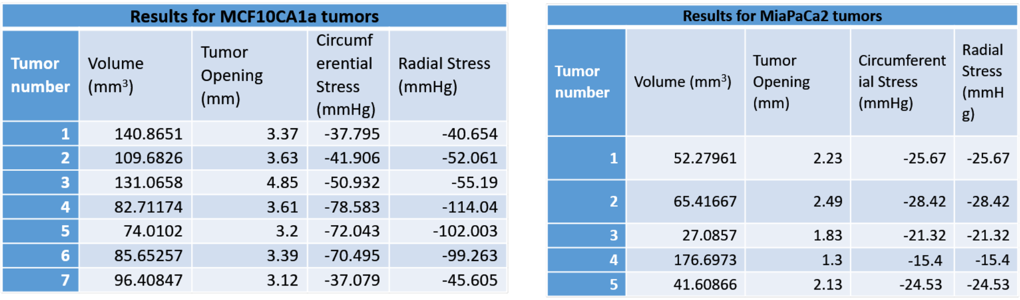

Results for MCF10CA1a tumors

Tumor number	Volume (mm^3)	Tumor Opening (mm)	Circumferential Stress (mmHg)	Radial Stress (mmHg)
1	140.8651	3.37	-37.795	-40.654
2	109.6826	3.63	-41.906	-52.061
3	131.0658	4.85	-50.932	-55.19
4	82.71174	3.61	-78.583	-114.04
5	74.0102	3.2	-72.043	-102.003
6	85.65257	3.39	-70.495	-99.263
7	96.40847	3.12	-37.079	-45.605

Results for MiaPaCa2 tumors

Tumor number	Volume (mm^3)	Tumor Opening (mm)	Circumferential Stress (mmHg)	Radial Stress (mmHg)
1	52.27961	2.23	-25.67	-25.67
2	65.41667	2.49	-28.42	-28.42
3	27.0857	1.83	-21.32	-21.32
4	176.6973	1.3	-15.4	-15.4
5	41.60866	2.13	-24.53	-24.53

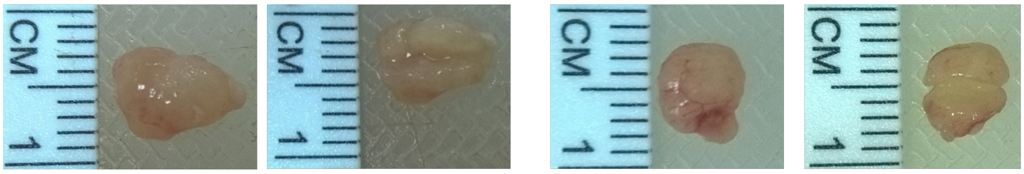

Figure 3.9: Tables with experimental measures (top) of cutting experiments (bottom) for MCF10CA1a breast tumour cells (left) and for MiaPaCa2 pancreatic tumour cells (right) implanted orthotopically in the mammary fat pad of nude mice.

the angle linearly increases with the difference in growth of about 8° every 10 units per mm of growth.

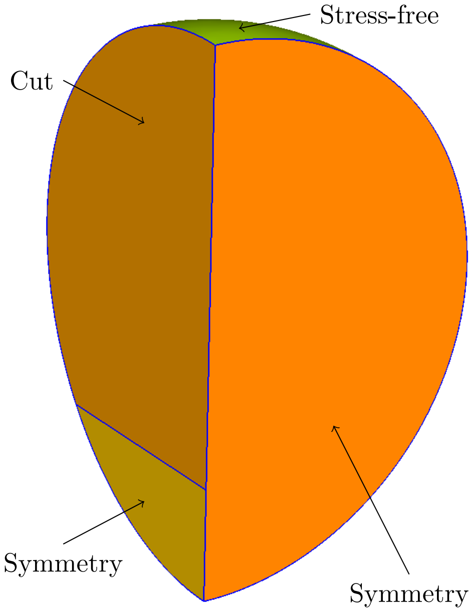

Figure 3.10: Computational domain and boundary conditions for the 3d numerical experiment of the opening angle. The "symmetry" label indicates that the surface is fixed in the normal direction. The vertical cut is 80% of the diameter deep.

$g(R=0)$	45.0	44.0	43.0	42.0	41.0	40.0
$g(R=R0)$	45.0	48.0	51.0	54.0	57.0	60.0
opening length [mm]	0.0	0.540	1.12	1.70	2.30	2.92
opening angle [deg]	0.0	3.43	6.94	10.5	14.2	18.0
volume [mm^3]	94.7	94.8	95.0	95.4	95.9	96.6

Table 3.1: Numerical result of a stepwise increase of the difference in growth between the center and the boundary of the tumour. The growth function $g(R)$ is linear in the radial component.

3.2.7 Discussion and concluding remarks

The growth of a tumour spheroid can be controlled using mechanical stress: when an osmotic pressure is applied at the boundary, the radius of the aggregate grows in time until it reaches an equilibrium volume which inversely depends on the load. The size control is fully reversible: when traction is released, the cellular matrix relaxes and returns the original growth curve. The observation that the intercellular space forms a pore-like structure, that macro-

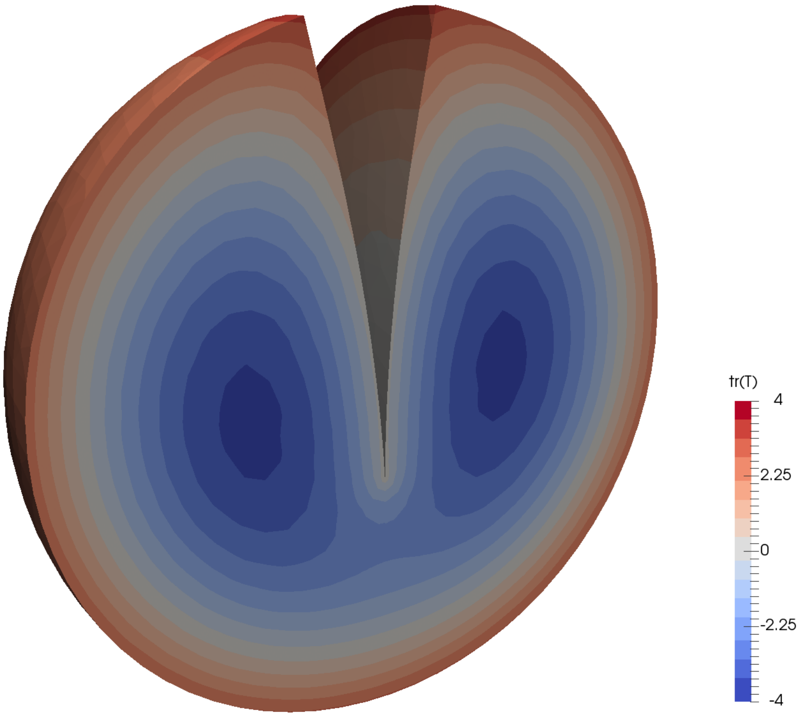

Figure 3.11: Current configuration of an unloaded grown sphere with initial radius of 100 μm. The sphere is azimuthally cut at the final time. The parameters in the simulation are: $\tau = 2.5$ days, $\kappa = 33.35$, $\alpha = 37$, $\lambda = 2.5$ mm, $\mu = 27.0$ kPa and $p_D = 5.0$ kPa. The domain of the numerical simulation is a quarter of a sphere. For the sake of graphical clarity of the opening angle, the spherical wedge is combined with its symmetric counterpart. The body is unloaded but not stress free: the color map represents the trace of the Cauchy stress tensor. The lowest part of the cut is partially resew by the swelling.

molecules cannot enter, suggests to represent mechanically the cellular aggregate as a poroelastic material [138]. The evidence of a residual stress leads to the assumption that the solid phase is hyperelastic: the large compliance of the cell aggregate is due to the squeezing of the intracellular fluid and the corresponding reduction of the intracellular space, while the single cells are much stiffer [141]. Boundary conditions are split accordingly: the osmotic pressure generated by the Dextran solution of the surrounding fluid loads the solid phase only.

The exponential decay in the pattern of nutrients makes the proliferation process of a sufficiently large loaded spheroid inhomogeneous and the generated residual stress depends on the radial position: it is compressive near the center and tensional at the periphery [198]. This feature is paradoxical when compared with the usual scenario: large availability of nutrients at the periphery of the spheroid is expected to favour the proliferation and, therefore, emergence of compressive residual stress. The dynamics of tumour growth is apparently different: tumour cells duplicate (or control their apoptosis) on the basis of the available nutrients, but their *target stress* modulates so as to produce compression in regions with small concentration of nutrients. In other words, the reported radial distribution of residual stress can be explained only admitting that in the inner regions, where the concentration of nutrients is very small, malignant cells slow down their apoptotic rate, in agreement with the observations of Helmlinger et al [106].

After a standard multiplicative decomposition of the tensor gradient of deformation to account for growth, we introduce a simple law of biomechanical feedback, and we are eventually able to explain the observed dynamics. On the basis of such a conjecture, we were able to reproduce growth profiles of tumour spheroids for different values of the applied load and the open angles of mice bearing breast tumours. Particularly for the second result, the solid phase of mice bearing tumours apart from cells consists also of the extra-cellular matrix, which can contribute to the development of residual stress. Here the mechanical contribution of all components of the tumour are resumed in the solid phase, and the growth tensor G accounts also for the possible tensional contribution due to the elongation of the collagen fibres.

Our mechanobiological model explains the observed smaller asymptotic volume as a function of increasing osmotic load on the basis of a stress-growth coupling. At later stages, not covered by the present model, when the radial inhomogeneity is fully developed, the solid (cellular) component of the spheroid undergoes a stress per volume fraction larger than a threshold that takes it into the plastic regime [12]; then cells start flowing centripetally, producing an internalization of the cells from the periphery to the center of the tumour [73, 65].

3.2.8 Appendix – Stability of the homogeneous solution

The integration of the "stress-modulated growth" illustrated in the previous section predicts a spatially homogeneous solution, parametrically depending on the time-dependent growth rate. The growth $g(R;t)$ is independent of the radial position because the stress is the same everywhere. In such a purely mechanical setting we now study the stability of the homogeneous solution (3.30) and (3.35). In other words, the question is whether the spatial inhomogeneity observed in grown spheroids could be produced by the mechanobiological feedback, thus amplifying the spatial perturbations of the stress to yield inhomogeneous growth.

To investigate this hypothesis we consider the following perturbation of the homogeneous solution:

$$r(R,t) = \gamma g_0(t)R + \rho(R,t), \qquad \gamma g_0(t)R \gg \rho(R,t) \tag{3.42}$$

$$g(R,t) = g_0(t) + \delta(R,t), \qquad g_0(t) \gg \delta(R,t) \tag{3.43}$$

where γ and $g_0(t)$ are solutions of equations (3.31) and (3.34), respectively, and $g_0(0) = 1$.
When the perturbed solutions are plugged in equations (3.31) and (3.34) and only first order terms are retained, the following linear equations are found

$$\left(\rho' + 2\frac{\rho}{R}\right)' = \gamma \frac{3-\gamma^2}{\gamma^2+1}\, \delta', \tag{3.44}$$

$$\dot{\delta} = \left(1 + 2\frac{g_0}{\kappa} - 2\frac{g_0}{\alpha} - 4\frac{g_0}{\kappa\gamma^2}\right)\frac{\delta}{\tau} + \frac{2}{3}\frac{g_0}{\kappa\tau\gamma^3}\left(\rho' + 2\frac{\rho}{R}\right). \tag{3.45}$$

Derivation of the former equation in space, derivation of the latter in time and cross substitution yields

$$\dot{\delta}' = \left(1 + 2\frac{g_0}{\kappa} - 2\frac{g_0}{\alpha} - 4\frac{g_0}{\kappa\gamma^2} + \frac{2}{3}\frac{g_0}{\kappa\gamma^2}\frac{3-\gamma^2}{\gamma^2+1}\right)\frac{\delta'}{\tau} \tag{3.46}$$

which determines the evolution in time of the spatial perturbation in the growth $g(t)$. Instability shows up if

$$\alpha\kappa\gamma^2(\gamma^2+1) > 2g_0\left(\alpha\left(1 + \frac{4}{3}\gamma^2 - \gamma^4\right) + \kappa\gamma^2\left(\gamma^2+1\right)\right), \tag{3.47}$$

for some $1 < g_0(t) < g_e$, where $0 < \gamma(p_D) < 1$.
The result (3.47) is negative versus our conjecture: it predicts a stabilization of the system for large enough growth g_0 which is not in agreement with experiments. If the purely mechanical system is stable, the reported inhomogeneity (large proliferation near the boundary, smaller internally) should instead be explained accounting for the role of nutrients.

4 PATTERN FORMATION IN SOFT MATTER

The main focus of this Chapter is the study of pattern formation in soft bodies. Indeed, large stresses can induce topological transitions in elastic bodies as a result of the coupling of physical or geometrical non-linearities, leading to a partial release of the total elastic energy stored inside the bodies.

We first investigate the morphogenetic mechanism behind the tortuosity of tumour capillaries. In Section 4.1.1, we introduce the morpho-elastic model and we derive the basic axis-symmetric solution of the corresponding hyperelastic problem. In Section 4.1.2, we perform a linear stability analysis of the basic axis-symmetric solution using the method of incremental deformations superposed on a finite strain. In Section 4.1.3, we describe the mixed finite element method that we have implemented to perform the numerical simulations of the post-buckling behavior. The results of both the theoretical analysis and the numerical simulations are finally discussed in Section 4.1.4, together with some concluding remarks.

Then, in Section 4.2 we employ the theory of initially stressed materials to study the morphological stability of a sphere with an arbitrary, radially symmetric, distribution of the residual stress. Firstly in Section 4.2.1, we introduce the hyperelastic model for a pre-stressed material, defining the constitutive assumptions as a function of given distributions of residual stresses. Secondly, in Section 4.2.2 we apply the theory of incremental deformations in order to study the linear stability of a pre-stressed solid sphere with respect to the underlying residual stresses. Finally, in Section 4.2.3 we implement a numerical algorithm using the mixed finite element method in order to approximate the fully non-linear elastic solution. In the last Section we discuss the results of the linear and non-linear analysis, together with some concluding remarks.

Finally, we study the elastic equivalent of the Rayleigh-Taylor instability. In Section 4.3.1, we define the nonlinear elastic problem and identify its basic solution. In Section 4.3.2, we perform the linear stability analysis of the problem, deriving the marginal stability curves as a function of the elastic and geometric dimensionless parameters. In Section 4.3.3, we perform numerical simulations using finite elements for studying pattern formation in the fully nonlinear regime. In Section 4.3.4, we finally discuss the theoretical and numerical results, adding a few concluding remarks.
The results of this Section lead to the following publications:

D. Riccobelli and P. Ciarletta. Morpho–elastic model of the tortuous tumour vessels. *International Journal of Non-Linear Mechanics*, 107:1 – 9, 2018
D. Riccobelli and P. Ciarletta. Shape transitions in a soft incompressible sphere

with residual stresses. *Mathematics and Mechanics of Solids*, 23(12):1507–1524, 2018
D. Riccobelli and P. Ciarletta. Rayleigh–Taylor instability in soft elastic layers. *Philosophical Transactions of the Royal Society A: Mathematical, Physical and Engineering Sciences*, 375(2093):20160421, 2017

4.1 MORPHO–ELASTIC MODEL OF THE TORTUOUS TUMOUR VESSELS

In this Section, we aim at modelling the morphogenesis of the tumour vascular network. After an initial avascular phase, a solid tumour can activate a process known as angiogenesis, assembling its own vascular network for opening a new access to the vital nutrients [130, 3]. These new capillaries are morphologically different from normal physiological vessels. In particular, they have a much higher spatial tortuosity and an increased permeability [195, 42] forcing an impaired flow within the peritumoral area. These structural peculiarities represent a major obstacle for the efficient delivery of antitumoral drugs [117].

Recently, the irregular shape of tumour capillaries has been explained as a result of an elastic instability. More in general, several works have addressed the problem of the stability of cylindrical structures subjected to differential growth and geometrical constraints. In [148], Moulton and Goriely studied the buckling of an hollow cylindrical tube subjected to a radial and circumferential differential growth. Subsequently O'Keeffe et al. [158] addressed the problem of the stability of a solid cylinder growing along the axial direction, embedded into an elastic inert matrix and confined between two parallel, rigid planes. The stability of residually stressed cylindrical structures has been further studied by exploiting an alternative approach, prescribing the residual stress field instead of the growth tensor [140, 60].

In [15] Araujo and McElwain have proposed a model of the growth induced residual stress in solid tumors, assuming that the buckling of capillaries is induced by the stress applied by the tumor on the vessel. A seminal morpho–elastic model of this biological process has proved that an incompatible growth process of the tumor intertium can explain the buckling of capillaries [136] but not as easily their tortuosity. The aim of this work is to study the stability of a growing hyperelastic hollow cylinder taking into account for the linear elastic constraint of the surrounding interstitial matter. Contrarily to the work of MacLaurin et al. [136], here we assume that the buckling of the tumour capillary is not triggered by the growth of the surrounding tissue but by the growth of the vessel wall.

4.1.1 The elastic model

Let the reference configuration of the elastic body be the open set $\Omega_0 \subset \mathbb{R}^3$ such that

$$\Omega_0 = \{\boldsymbol{X} = (R\cos\Theta,\, R\sin\Theta,\, Z) \mid R_\text{i} < R < R_\text{o} \text{ and } 0 < Z < H)\}\,,$$

representing the wall of the tumor capillary, composed by the endothelium and the basement membrane [89], where R, Θ and Z are the cylindrical coordinates of the material point $\boldsymbol{X}$. We denote by $\boldsymbol{E}_R$, $\boldsymbol{E}_\Theta$ and $\boldsymbol{E}_Z$ the orthonormal vector basis in a cylindrical reference system.

We indicate by Ω the deformed configuration of the elastic tube and the mapping by

$$\boldsymbol{\varphi} : \Omega_0 \to \Omega$$

such that $\boldsymbol{u}(\boldsymbol{X}) = \boldsymbol{\varphi}(\boldsymbol{X}) - \boldsymbol{X}$ is the displacement vector and $\mathsf{F} = \operatorname{Grad}\boldsymbol{\varphi} = \frac{\partial\boldsymbol{\varphi}}{\partial\boldsymbol{X}}$ be the deformation gradient.

The volumetric growth of the body is enforced by introducing a multiplicative decomposition of the deformation gradient [126, 128, 181], as follows

$$\mathsf{F} = \mathsf{F}_\text{e}\mathsf{G}$$

so that G describes the metric distortion induced by the growth and F_e is the elastic deformation of the material restoring the geometrical compatibility of the current configuration.

We assume that the material is hyperelastic and incompressible, since the tissue constituents are mostly made of water. Denoting by ψ its strain energy density per unit volume, the first Piola–Kirchhoff and the Cauchy stress tensors read

$$\begin{cases} \mathsf{P} = \det\mathsf{G}\dfrac{\partial\psi(\mathsf{F}\mathsf{G}^{-1})}{\partial\mathsf{F}} - p\mathsf{F}^{-1} \\ \mathsf{T} = \dfrac{1}{\det\mathsf{F}}\mathsf{F}\mathsf{P} \end{cases} \tag{4.1}$$

where p is the Lagrangian multiplier that enforces the incompressibility constraint $\det\mathsf{F}_\text{e} = 1$.

Assuming quasi-static conditions in absence of external body forces, the balance of the linear and of the angular momentum reads

$$\operatorname{Div}\mathsf{P} = \mathbf{0} \text{ in } \Omega_0 \quad \text{or} \quad \operatorname{div}\mathsf{T} = \mathbf{0} \text{ in } \Omega \tag{4.2}$$

where Div and div denote the divergence operator in material and current coordinates, respectively.

The nonlinear system of equations (4.2) is complemented by the following boundary conditions

$$\begin{cases} \mathsf{P}^T\boldsymbol{N} = \mathbf{0} & \text{for } R = R_\mathrm{i} \\ \mathsf{P}^T\boldsymbol{N} = -\mu_k\boldsymbol{u} & \text{for } R = R_\mathrm{o} \\ \mathsf{P}^T\boldsymbol{N}\cdot\boldsymbol{E}_R = 0 & \text{for } Z = 0,\, H \\ \mathsf{P}^T\boldsymbol{N}\cdot\boldsymbol{E}_\Theta = 0 & \text{for } Z = 0,\, H \\ u_Z = 0 & \text{for } Z = 0,\, H \end{cases} \tag{4.3}$$

where $\boldsymbol{N}$ denotes the outer normal in the Lagrangian configuration and μ_k is the linear elastic stiffness of the outer peritumoral tissue. Since the intercapillary distance is much bigger than the characteristic diameter of the capillary, we indeed assume that the outer tissue exerts a linear elastic response that is simplified by an isotropic spring foundation.

4.1.1.1 *Constitutive assumptions and basic axis-symmetric solution*

We assume that the tube is composed of an incompressible neo–Hookean material, thus the strain energy ψ is given by

$$\psi(\mathsf{F}) = \frac{\mu}{2}\left(I_1 - 3\right) = \frac{\mu}{2}\left(\lambda_1^2 + \lambda_2^2 + \lambda_3^2 - 3\right) \tag{4.4}$$

where I_1 is the trace of the right Cauchy–Green tensor $\mathsf{C} = \mathsf{F}^T\mathsf{F}$ and λ_i are the eigenvalues of the deformation gradient. We can write the Cauchy stress tensor (4.1) as

$$\mathsf{T} = \mu\mathsf{F}\mathsf{G}^{-1}\mathsf{G}^{-T}\mathsf{F}^T - p\mathsf{I} \tag{4.5}$$

where I is the identity tensor. We further assume that the growth tensor G has the form

$$\mathsf{G} = \mathrm{diag}(1,\, 1,\, \gamma), \tag{4.6}$$

so that the elastic tube grows along the axial direction. We look for a solution of the form

$$\boldsymbol{\varphi}(\boldsymbol{X}) = r(R)\boldsymbol{E}_R + Z\boldsymbol{E}_Z.$$

We denote by $r_\mathrm{i} = r(R_\mathrm{i})$ and $r_\mathrm{o} = r(R_\mathrm{o})$. For the sake of simplicity, in the following we omit the explicit dependence of r on the variable R. The deformation gradient is given by

$$\mathsf{F} = \mathrm{diag}\left(r',\, \frac{r}{R},\, 1\right) \tag{4.7}$$

Considering the equations (4.6) and (4.7), the incompressibility constraint $\det\mathsf{F}_\mathrm{e} = 1$ leads to the following differential equation

$$r'r = \gamma R \tag{4.8}$$

so that

$$r = \sqrt{\gamma(R^2 - R_\mathrm{i}^2) + r_\mathrm{i}^2}. \tag{4.9}$$

By enforcing the global incompressibility constraint in Eq.(4.9), we get

$$r_{\mathrm{o}} = \sqrt{\gamma(R_{\mathrm{o}}^2 - R_{\mathrm{i}}^2) + r_{\mathrm{i}}^2}. \tag{4.10}$$

The inverse of Eq. (4.9) reads:

$$R = \sqrt{\frac{r^2 - r_{\mathrm{i}}^2}{\gamma} + R_{\mathrm{i}}^2},$$

so that, from (4.8), we get:

$$r' = \frac{\gamma R}{r} = \frac{\sqrt{\gamma\left(r^2 - r_{\mathrm{i}}^2\right) + \gamma^2 R_{\mathrm{i}}^2}}{r}. \tag{4.11}$$

From (4.5), (4.6) and (4.7) the Cauchy stress tensor reads

$$\mathsf{T} = T_{rr}\boldsymbol{e}_r \otimes \boldsymbol{e}_r + T_{\theta\theta}\boldsymbol{e}_\theta \otimes \boldsymbol{e}_\theta + T_{zz}\boldsymbol{e}_z \otimes \boldsymbol{e}_z$$

where $\boldsymbol{e}_r$, $\boldsymbol{e}_\theta$ and $\boldsymbol{e}_z$ constitute the local orthonormal vector basis of the actual configuration in cylidrical coordinates and

$$\begin{cases} T_{rr}(r) = \mu r'^2 - p, \\ T_{\theta\theta}(r) = \mu \dfrac{r^2}{R^2} - p, \\ T_{zz}(r) = \mu \dfrac{1}{\gamma^2} - p. \end{cases}$$

In cylindrical coordinates, the balance of the linear and angular momentum (4.2) reads

$$\frac{dT_{rr}}{dr} + \frac{T_{rr} - T_{\theta\theta}}{r} = 0; \tag{4.12}$$

with the following boundary conditions (4.3):

$$\begin{cases} T_{rr}(0) = 0 & \text{for } r = r_{\mathrm{i}} \\ T_{rr}(r_{\mathrm{o}}) = -\mu_k \dfrac{R_{\mathrm{o}}}{r_{\mathrm{o}}}(r_{\mathrm{o}} - R_{\mathrm{o}}) & \text{for } r = r_{\mathrm{o}} \end{cases} \tag{4.13}$$

Making use of (4.13), we can integrate the equation (4.12) from $r = r_{\mathrm{i}}$ to $r = r_{\mathrm{o}}$, obtaining

$$\mu_k \frac{R_{\mathrm{o}}}{r_{\mathrm{o}}}(r_{\mathrm{o}} - R_{\mathrm{o}}) = \int_{r_{\mathrm{i}}}^{r_{\mathrm{o}}} \frac{T_{rr}(r) - T_{\theta\theta}(r)}{r} dr,$$

so that, together with the equation (4.10), we obtain an equation for r_{i} which can be solved numerically if we fix the ratio $R_{\mathrm{o}}/R_{\mathrm{i}}$ and the axial growth parameter γ.

Finally, we integrate the equation (4.12) from r_i to r in order to determine the Lagrangian multiplier p, so that

$$p = \mu r'^2 + \int_{r_\mathrm{i}}^{r} \frac{T_{rr}(s) - T_{\theta\theta}(s)}{s} ds.$$

The latter integral can be computed analytically, obtaining

$$\begin{aligned} p(r) = \frac{1}{2}\gamma\mu \Bigg(& \frac{\gamma R_\mathrm{i}^2 - r_\mathrm{i}^2}{r^2} - \log\left(r^2 - r_\mathrm{i}^2 + \gamma R_\mathrm{i}^2\right) + 2\log(r) + \\ & + \frac{\gamma R_\mathrm{i}^2}{r_\mathrm{i}^2} - 2\log(r_\mathrm{i}) + \log\left(\gamma R_\mathrm{i}^2\right) + 1 \Bigg). \end{aligned} \tag{4.14}$$

Thus, we have found a basic axis-symmetric solution of the boundary value problem, that is given by Eqs.(4.9,4.14)

In the following, we study its marginal stability as a function of the control parameter γ denoting the local volumetric growth along the axial direction.

4.1.2 Linear stability analysis

In this Section we study the linear stability of the finitely deformed tube by using the method of incremental deformations superposed on a finite strain [156].

We rewrite the incremental boundary value problem into a more convenient form called Stroh formulation and we implement a numerical method based on the impedance matrix method to solve it.

4.1.2.1 *Incremental boundary value problem*

We denote the incremental displacement field $\delta\boldsymbol{u}$. Let $\Gamma = \mathrm{grad}\,\delta\boldsymbol{u}$, we introduce the push-forward of the incremental Piola–Kirchhoff stress in the finitely deformed configuration of the axis-symmetric solution, that is given by

$$\delta \mathsf{P}_0 = \mathcal{A}_0 : \Gamma + p\Gamma - \delta p \mathsf{I}, \qquad \text{where} \qquad (\mathcal{A}_0 : \Gamma)_{ij} = A_{0ijhk}\Gamma_{kh}, \tag{4.15}$$

where $\mathcal{A}_0$ is the fourth order tensor of instantaneous elastic moduli, δp is the increment of the Lagrangian multiplier that imposes the incompressibility constraint, and the convention of summation over repeated indices is adopted.

The components of the tensor $\mathcal{A}_0$ for a neo–Hookean material, are given by

$$A_{0ijhk} = \mu\delta_{jk}(B_\mathrm{e})_{ih} = \mu\delta_{jk}\delta_{ih}(\lambda_i^\mathrm{e})^2$$

where $\mathsf{B}_e = \mathsf{F}_e\mathsf{F}_e^T$, λ_i^e are the eigenvalues of the tensor $\mathsf{F}_e = \mathsf{F}\mathsf{G}^{-1}$. Considering the growth tensor (4.6),the deformation gradient (4.7) and the equation (4.11), such eigenvalues are given by

$$\begin{cases} \lambda_1^e = r' = \dfrac{\sqrt{\gamma\left(r^2 - r_i^2\right) + \gamma^2 R_i^2}}{r}, \\ \lambda_2^e = \dfrac{r}{R} = \dfrac{\gamma r}{\sqrt{\gamma\left(r^2 - r_i^2\right) + \gamma^2 R_i^2}}, \\ \lambda_3^e = \dfrac{1}{\gamma}. \end{cases}$$

The incremental form of the balance of the linear momentum and of the incompressibility constraint are given by

$$\begin{cases} \operatorname{div} \delta\mathsf{P}_0 = \mathbf{0}, & \text{in } \Omega, \\ \operatorname{tr} \Gamma = 0 & \text{in } \Omega. \end{cases} \tag{4.16}$$

This system of partial differential equations is complemented by the following boundary conditions

$$\begin{cases} \delta\mathsf{P}^T \boldsymbol{e}_r = \mathbf{0} & \text{for } r = r_i \\ \delta\mathsf{P}^T \boldsymbol{e}_r = -\mu_k \dfrac{R_o}{r_o} \delta\boldsymbol{u} & \text{for } r = r_o \\ \delta\mathsf{P}\boldsymbol{e}_r \cdot \boldsymbol{e}_r = 0 & \text{for } z = 0,\, H \\ \delta\mathsf{P}^T \boldsymbol{e}_r \cdot \boldsymbol{e}_\theta = 0 & \text{for } z = 0,\, H \\ \delta u_z = 0 & \text{for } z = 0,\, H. \end{cases} \tag{4.17}$$

where $\boldsymbol{e}_r$, $\boldsymbol{e}_\theta$ and $\boldsymbol{e}_z$ is the vector basis in cylindrical coordinates in the actual configuration.

To implement a robust numerical method, we employ a method which is different to the one used in [158] where the authors studied the stability of a growing solid cylinder surrounded by an elastic tube. We reformulate the boundary value problem given by the equations (4.16)–(4.17) by using the Stroh formulation.

4.1.2.2 *Stroh formulation*

We denote with u, v and w the components of $\delta\boldsymbol{u}$ in cylindrical coordinates.To reduce the system of partial differential equations (4.16) to a system of ordinary differential equations, we assume the following ansatz [136]:

$$\begin{aligned} u(r, \theta, z) &= U(r)\cos(m\theta)\cos(kz), \\ v(r, \theta, z) &= V(r)\sin(m\theta)\cos(kz), \\ w(r, \theta, z) &= W(r)\cos(m\theta)\sin(kz), \end{aligned}$$

where $m \in \mathbb{N}$ and $k \in \mathbb{R}$ with $k \geq 0$.

Following the method exposed in [22], we consider the components δP_{rr}, $\delta P_{r\theta}$ and δP_{rz} as additional unknowns. We assume then that

$$\delta P_{rr}(r, \theta, z) = p_{rr}(r) \cos(m\theta) \cos(kz), \tag{4.18}$$

$$\delta P_{r\theta}(r, \theta, z) = p_{r\theta}(r) \sin(m\theta) \cos(kz), \tag{4.19}$$

$$\delta P_{rz}(r, \theta, z) = p_{rz}(r) \cos(m\theta) \sin(kz). \tag{4.20}$$

We substitute (4.18) into (4.15) obtaining the following expression for δp:

$$\delta p = \frac{\gamma\mu U'(r) \left(\gamma R_\mathrm{i}^2 \left(r^2 + 3r_\mathrm{i}^2\right) + r^2 r_\mathrm{i}^2 \left(-\log\left(r^2 - r_\mathrm{i}^2 + \gamma R_\mathrm{i}^2\right) + 2\log(r) - 2\log(r_\mathrm{i}) + \log\left(\gamma R_\mathrm{i}^2\right)\right)\right)}{2r^2 r_\mathrm{i}^2} + \frac{3\gamma\mu U'(r)(r - r_\mathrm{i})(r + r_\mathrm{i})}{2r^2} - p_{rr}(r)$$

We introduce the displacement-traction vector $\boldsymbol{\eta}$ as

$$\boldsymbol{\eta} = [\boldsymbol{U}, r\boldsymbol{T}] \quad \text{where} \begin{cases} \boldsymbol{U} = [U, V, W], \\ \boldsymbol{T} = [p_{rr}, p_{r\theta}, p_{rz}]. \end{cases} \tag{4.21}$$

By using a well-established procedure [197], exploiting the incremental constitutive relations (4.15), we can rewrite the incremental system of partial differential equations (4.16) as

$$\frac{d\boldsymbol{\eta}}{dr} = \frac{1}{r} \mathsf{N} \boldsymbol{\eta} \tag{4.22}$$

where $\mathsf{N} \in \mathbb{R}^{6\times 6}$ is the Stroh matrix; the expressions of its components are reported in the appendix. In particular, we can identify four sub-blocks

$$\mathsf{N} = \begin{bmatrix} \mathsf{N}_1 & \mathsf{N}_2 \\ \mathsf{N}_3 & \mathsf{N}_4 \end{bmatrix}$$

such that $\mathsf{N}_i \in \mathbb{R}^{3\times 3}$ and $\mathsf{N}_1 = -\mathsf{N}_4^T, \quad \mathsf{N}_2 = \mathsf{N}_2^T, \quad \mathsf{N}_3 = \mathsf{N}_3^T$.

4.1.2.3 *Impedance matrix method*

The system of ordinary differential equations gien by Eq. (4.22) is numerically solved using the impedance matrix method [32, 33]. We introduce the matricant

$$\mathsf{M}(r, r_\mathrm{i}) = \begin{bmatrix} \mathsf{M}_1(r, r_\mathrm{i}) & \mathsf{M}_2(r, r_\mathrm{i}) \\ \mathsf{M}_3(r, r_\mathrm{i}) & \mathsf{M}_4(r, r_\mathrm{i}) \end{bmatrix}, \qquad \mathsf{M} \in \mathbb{R}^{6\times 6}$$

called conditional matrix. Such a matrix is a solution of the problem

$$\begin{cases} \dfrac{d}{dr} \mathsf{M}(r, r_\mathrm{i}) = \dfrac{1}{r} \mathsf{N} \mathsf{M}(r, r_\mathrm{i}), \\ \mathsf{M}(r_\mathrm{i}, r_\mathrm{i}) = \mathsf{I}. \end{cases} \tag{4.23}$$

It is easy to verify that the solution of the Stroh equation (4.22) is given by

$$\boldsymbol{\eta}(r) = \mathsf{M}(r, r_\mathrm{i}) \boldsymbol{\eta}(r_\mathrm{i}). \tag{4.24}$$

Since $\boldsymbol{T}(r_\mathrm{i}) = \mathbf{0}$, exploiting the relation (4.24), we can define the conditional impedance matrix $\mathsf{Z}(r, r_\mathrm{i})$ [155] as

$$\mathsf{Z}(r, r_\mathrm{i}) = \mathsf{M}_3(r, r_\mathrm{i})\mathsf{M}_1^{-1}(r, r_\mathrm{i}). \tag{4.25}$$

For the sake of simplicity we omit the explicit dependence of Z on r and r_i. Such a matrix satisfy the following relation

$$r\boldsymbol{T} = \mathsf{Z}\boldsymbol{U} \qquad \forall r \in (r_\mathrm{i}, r_\mathrm{o}).$$

Thus, we can observe that the Stroh system (4.22) can be written as

$$\frac{d\boldsymbol{U}}{dr} = \frac{1}{r}(\mathsf{N}_1 + \mathsf{N}_2\mathsf{Z})\boldsymbol{U}, \tag{4.26}$$

$$\frac{d\mathsf{Z}}{dr}\boldsymbol{U} + \mathsf{Z}\frac{d\boldsymbol{U}}{dr} = \frac{1}{r}(\mathsf{N}_3 + \mathsf{N}_4\mathsf{Z})\boldsymbol{U}. \tag{4.27}$$

We now can substitute (4.26) in (4.27) obtaining a Riccati differential equation

$$\frac{d\mathsf{Z}}{dr} = \frac{1}{r}(\mathsf{N}_3 + \mathsf{N}_4\mathsf{Z} - \mathsf{Z}\mathsf{N}_1 - \mathsf{Z}\mathsf{N}_2\mathsf{Z}); \tag{4.28}$$

As a starting condition, considering (4.23) and the definition of surface impedance matrix (4.25), we set

$$\mathsf{Z}(r_\mathrm{i}, r_\mathrm{i}) = 0.$$

The boundary condition in (4.17) linked to the presence of the springs at $r = r_\mathrm{o}$ can be written as

$$\boldsymbol{T} = -\mu_k\frac{R_\mathrm{o}}{r_\mathrm{o}}\boldsymbol{U}$$

so that

$$(\mathsf{Z} + \mu_k R_o \mathsf{I})\,\boldsymbol{U} = 0$$

Non-null solutions of the incremental problem exist if and only if

$$\det(\mathsf{Z} + \mu_k R_o \mathsf{I}) = 0. \tag{4.29}$$

For a fixed value of the control parameter γ we integrate the Riccati equation (4.28) from $r = r_\mathrm{i}$ up to $r = r_\mathrm{o}$ making use of the software MATHEMATICA (ver. 11.2, Wolfram Research, Champaign, IL, USA). We iteratively increase the control parameter γ until the stop condition (4.29) is satisfied.

4.1.2.4 *Marginal stability thresholds and critical modes*

In this Section we discuss the results of the linear stability analysis.
Setting $\mu_k = 0$, we neglect the elastic contribution of the surrounding matter, thus dealing with a classical problem of Euler buckling. The corresponding marginal stability curves are depicted in Fig. 4.1, in quantitative agreement with the results obtained by Goriely and co-workers [96]. As expected, the

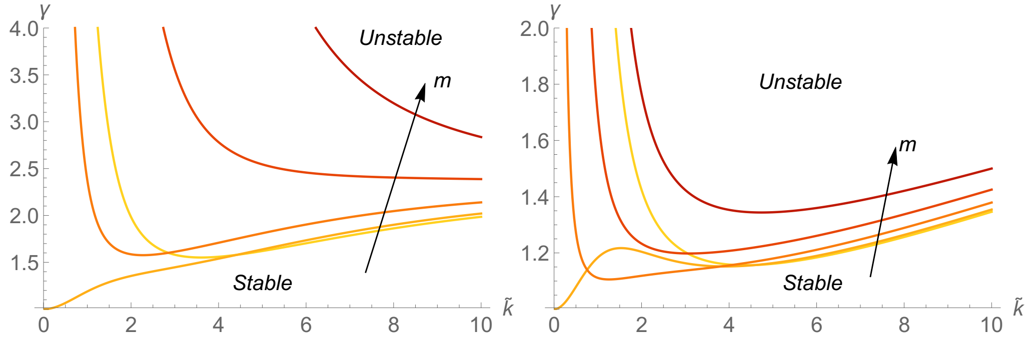

Figure 4.1: Marginal stability curves kR_o versus γ when the elastic constant of the springs is $\mu_k = 0$, the aspect ratio α_R is equal to 0.5 (top) and 0.8 (bottom). The circumferential wavenumber m varies from 0 (light line) up to 4 (dark line), the arrow denotes the direction in which m increases.

marginal stability threshold tends to $\gamma = 1$ for $m = 1$ and $\tilde{k}$ tends to zero, i.e. the critical mode is the one with infinite wavelength along the axial direction.

the presence of an elastic foundation at the outer surface of the capillary drastically changes this limiting behavior of Euler buckling. The elastic boundary value problem is governed by the following the dimensionless parameters:

$$\tilde{k} = kR_o, \qquad \alpha_k = \frac{\mu_k R_o}{\mu}, \qquad \alpha_R = \frac{R_i}{R_o},$$

where $\tilde{k}$ represents the dimensionless axial wavenumber, α_k is the ratio between the surface and bulk elastic energies, and α_R is the geometrical aspect ratio of the tube.

The radius of a tumour capillary measures $5.1 \pm 0.7\,\mu$m while its length $66.8 \pm 34.2\,\mu$m [129]. Thus, for a given length L, the admissible axial wavenumber $\tilde{k}$ are given by

$$\tilde{k} = n\pi\frac{R_o}{L} \qquad n \in \mathbb{N}$$

for the sake of simplicity, in the following we consider $\tilde{k}$ continuous since the slenderness ratio is small.

In Fig. 4.2 we report the marginal stability curves when $\alpha_k = 0.01$. These marginal stability curves tend to the ones plotted in Fig. 4.1 where kR_o is large. However, a different behavior arises in the limit where kR_o tends to zero, especially since the marginal stability threshold γ now goes to infinity for $m = 1$.

This effect is even more evident by setting $\alpha_k = 1$, as sketched in Fig. .

For each fixed value of the dimensionless parameter α_k, we define the critical value γ_{cr} as the minimum value of the marginal stability curves γ versus $\tilde{k}$ for all the circumferential wavenumber m. The corresponding axial and circumferential critical modes are denoted by $\tilde{k}_{cr}$ and m_{cr}, respectively.

We plot the critical modes in Fig. 4.4 for two different values of the aspect ratio, $\alpha_R = 0.5$ (left) and 0.8 (right). In both cases the critical axial wavenumber

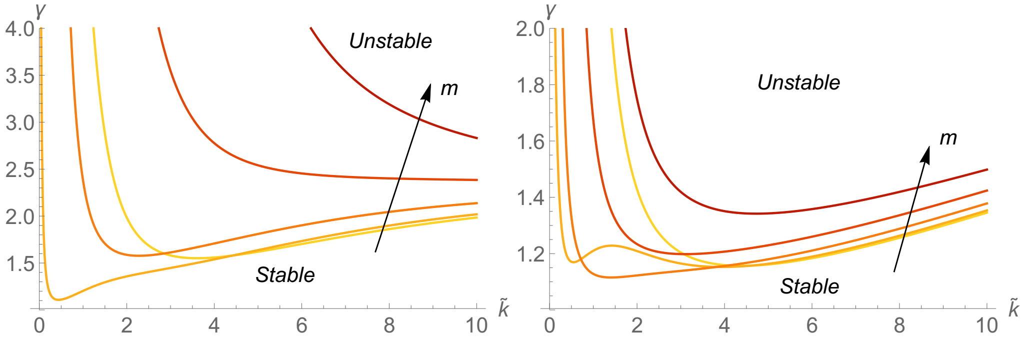

Figure 4.2: Marginal stability curves $\tilde{k}$ versus γ when $\alpha_k = 0.01$, the aspect ratio α_R is equal to 0.5 (top) and 0.8 (bottom). The circumferential wavenumber m varies from 0 (light line) up to 4 (dark line), the arrow denotes the direction in which m increases.

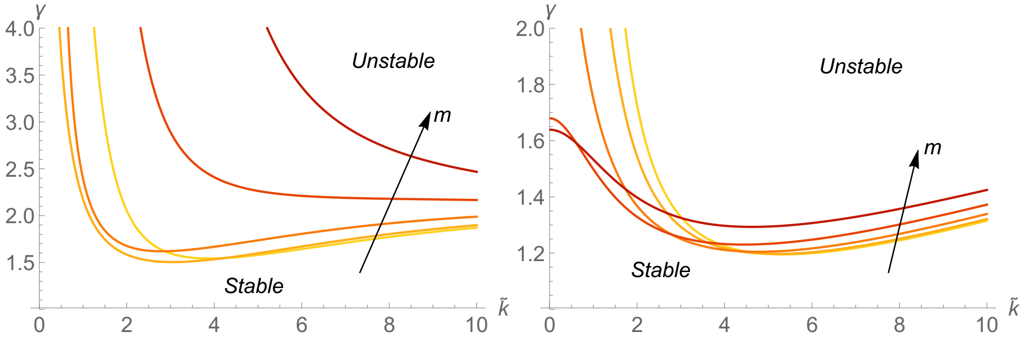

Figure 4.3: Marginal stability curves $\tilde{k}$ versus γ when $\alpha_k = 1$, the aspect ratio α_R is equal to 0.5 (top) and 0.8 (bottom). The circumferential wavenumber m varies from 0 (light line) up to 4 (dark line), the arrow denotes the direction in which m increases.

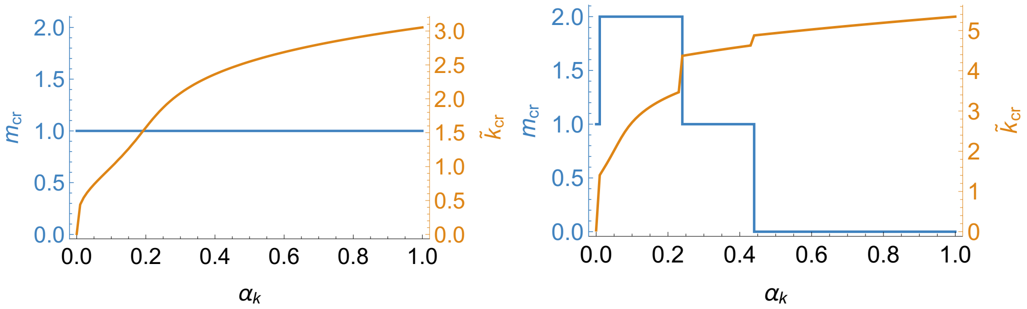

Figure 4.4: Plots of the critical wavenumbers m_{cr} and $\tilde{k}_{cr}$ versus α_k for $\alpha_R = 0.5$ (left) and $\alpha_R = 0.8$ (right).

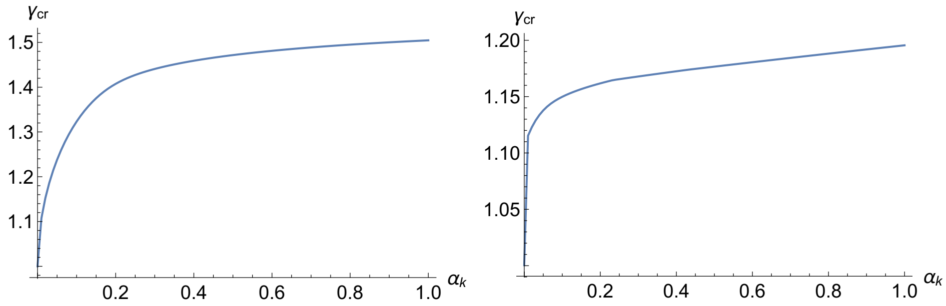

Figure 4.5: Plots of the critical values of the control parameter γ_{cr} versus α_k for $\alpha_R = 0.5$ (left) and $\alpha_R = 0.8$ (right).

$\tilde{k}_{cr}$ is increasing as α_k increases, highlighting discrete changes of the critical circumferential wavenumber.

Also the critical value of the control parameter γ_{cr} is an increasing function of the dimensionless parameter α_k as shown in the plots of Fig. 4.5.

We also compute the dimensionless critical load τ that is applied on the top surface in order to enforce the torsion through the application of a surface traction at the tube top and bottom ends. Let $\mathcal{S} = \{\boldsymbol{X} \in \Omega \mid Z = H\}$, this critical load is given by:

$$\tau = -\frac{1}{\mu R_o^2} \int_{\mathcal{S}} P_{ZZ} dS = -\frac{1}{\mu R_o^2} \int_{\mathcal{S}} \left(\frac{\mu}{\gamma^2} - p \right) dS.$$

where γ_{cr} is the marginal stability threshold and $L_{cr} = \pi R_o / \tilde{k}_{cr}$ is half of the critical wavelength.

In Fig. 4.6 we plot τ versus α_k for $\alpha_R = 0.5$ and 0.8. In both cases, the critical load is a decreasing function of α_k, so the presence of the outer elastic confinement has a stabilizing effect, whilst thinner tubes always require lower critical loads.

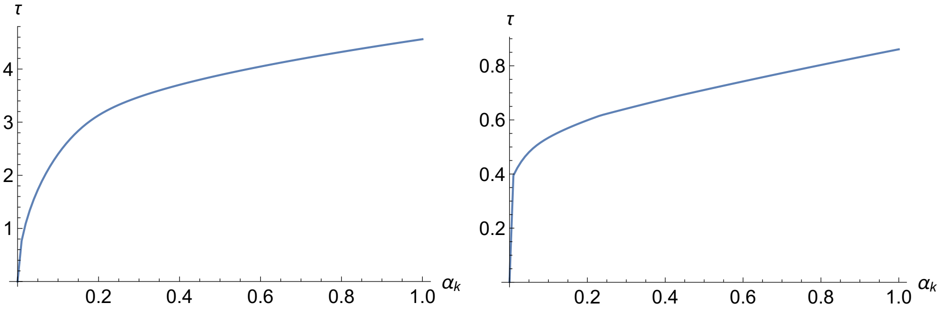

Figure 4.6: Plots of the dimensionless critical load τ vs α_k for $\alpha_R = 0.5$ (left) and $\alpha_R = 0.8$ (right).

4.1.3 Post-buckling behaviour

In order to study the behavior of the buckled configuration far beyond the marginal stability threshold, we have implemented a finite element code to discretize and numerically solve the fully nonlinear boundary value problem given by (4.2)–(4.3).

4.1.3.1 *Finite-element implementation*

To break the axial symmetry of the problem, we numerically solve the boundary value problem only on half cylinder whose height is half of the critical axial wavelength:

$$\Omega_c = \left\{ \boldsymbol{X} = (X, Y, Z) \;\middle|\; \frac{R_i}{R_o} < \sqrt{X^2 + Y^2} < 1 \cap 0 < Z < \frac{\pi}{\tilde{k}_{cr}} \cap Y > 0 \right\}.$$

where $\tilde{k}_{cr}$ is the critical dimensionless wave-number arising from the linear stability analysis presented in Section 4.1.2 and $(\boldsymbol{E}_X, \boldsymbol{E}_Y, \boldsymbol{E}_Z)$ is the cartesian orthonormal vector basis. We discretize this domain by using a tetrahedral mesh composed by 93398 elements. We used the Taylor–Hood $\boldsymbol{P}_2$–P_1 element, i.e. the displacement field is given by a continuous, piecewise quadratic function while the pressure field by a continuous, piecewise linear function. The choice of this particular element is motivated by its stability for non-linear elastic problems [18]. Since we have only considered a half tube, we complement the boundary conditions (4.3) by adding the following equations

$$\begin{cases} \mathsf{P}^T \boldsymbol{E}_Y \cdot \boldsymbol{E}_X = 0 & \text{for } Y = 0, \\ \mathsf{P}^T \boldsymbol{E}_Y \cdot \boldsymbol{E}_Z = 0 & \text{for } Y = 0, \\ u_Y = 0 & \text{for } Y = 0. \end{cases}$$

The numerical algorithm is based on a Newton continuation method [188], the control parameter γ being incremented starting from 1 with an automatic adaptation of step if the Newton method does not converge.

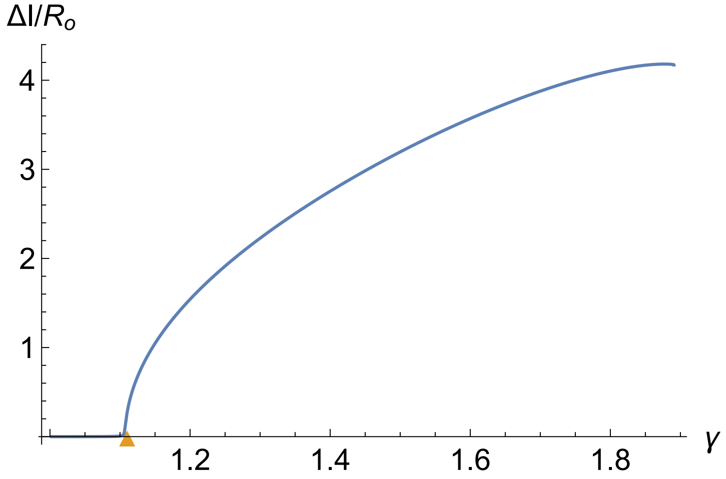

Figure 4.7: Bifurcation diagram where we show the dimensionless parameter $\Delta l / R_{\mathrm{o}}$ versus the control parameter γ when $\alpha_k = 0.01$, $\alpha_R = 0.5$. The numerical simulation is validated against the marginal stability threshold computed with the linear stability analysis (orange triangle, $\gamma_{\mathrm{cr}} = 1.1103$).

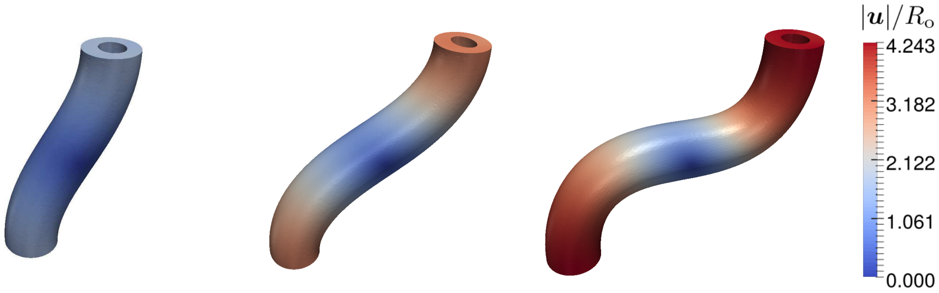

Figure 4.8: Actual configuration of the buckled tube for $\gamma = 1.2$ (left), $\gamma = 1.5$ (center), $\gamma = 1.89$ (right) when $\alpha_k = 0.01$, $\alpha_R = 0.5$. In such conditions $\gamma_{\mathrm{cr}} = 1.1103$.

In order to follow the bifurcated branch, a small perturbation is imposed at the outer boundary of the cylinder according to the critical mode arising from the linear stability analysis [41, 188]. The amplitude of such an imperfection is set to $0.005\,R_{\mathrm{o}}$.

The method is implemented in Python through the open source computing platform FEniCS [134]. As a linear algebra back–end we used PETSc [20], the linear Newton iteration is solved in parallel through MUMPS [13].

4.1.3.2 *Numerical results*

In this Section we show the results of the numerical simulations for $\alpha_R = 0.5$ and $\alpha_k = 0.01$. In this case, the critical mode is given by $\tilde{k}_{\mathrm{cr}} = 0.44$, $m_{\mathrm{cr}} = 1$ and the critical threshold is $\gamma_{\mathrm{cr}} = 1.1076$.

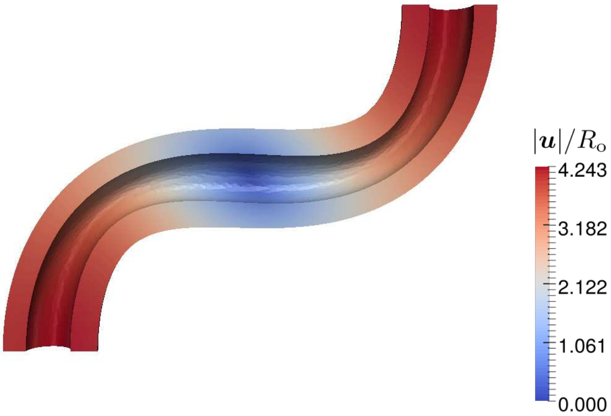

Figure 4.9: Actual configuration of the buckled tube for $\gamma = 1.89$. We can notice that the lumen is minimum where the tube has maximum curvature.

We define Δl as the average integral of the displacement along the direction $\boldsymbol{E}_X$ on the top surface $\mathcal{S}$, namely

$$\Delta l = \frac{\int_{\mathcal{S}} u_X \, dS}{\pi(R_\mathrm{o}^2 - R_\mathrm{i}^2)}.$$

Such a quantity represents a measure of the displacement of the top surface of the half-cylinder in the direction orthogonal to the axis of the cylinder and parallel to the plane $Y = 0$. Since we broke the axial symmetry of the problem by considering an half cylinder only, this is the only plane of symmetry.

In Fig. 4.7 we plot $\Delta l / R_\mathrm{o}$ versus γ. The numerical results are in agreement with the numerical outcomes, this bifurcation diagram highlights the presence of a supercritical pitchfork bifurcation.

We show the actual configuration of the elastic tube for several values of the control parameter γ in Fig. 4.8. In all the cases, there is a thinning of the tube and a reduction of the lumen in the regions where the curvature is higher as shown in Fig. 4.9.

The numerical method does not converge near the theoretical marginal stability threshold if α_k is large, probably because the bifurcation becomes subcritical. The improvement of the numerical algorithm is beyond the scope of this work; future works will aim at implementing an arclength continuation method which can also capture the behavior of subcritical bifurcations.

If we consider a tube of length $4\pi/\tilde{k}_\mathrm{cr} \simeq 28.55$ with $\alpha_k = 0.01$ we obtain a slenderness ratio which is compatible with the experimental measurements [129]. In Fig. 4.10 we plot the evolution of the tortuosity of the capillary, we observe again that the lumen is minimum in regions where the curvature of the cylinder wall is maximum.

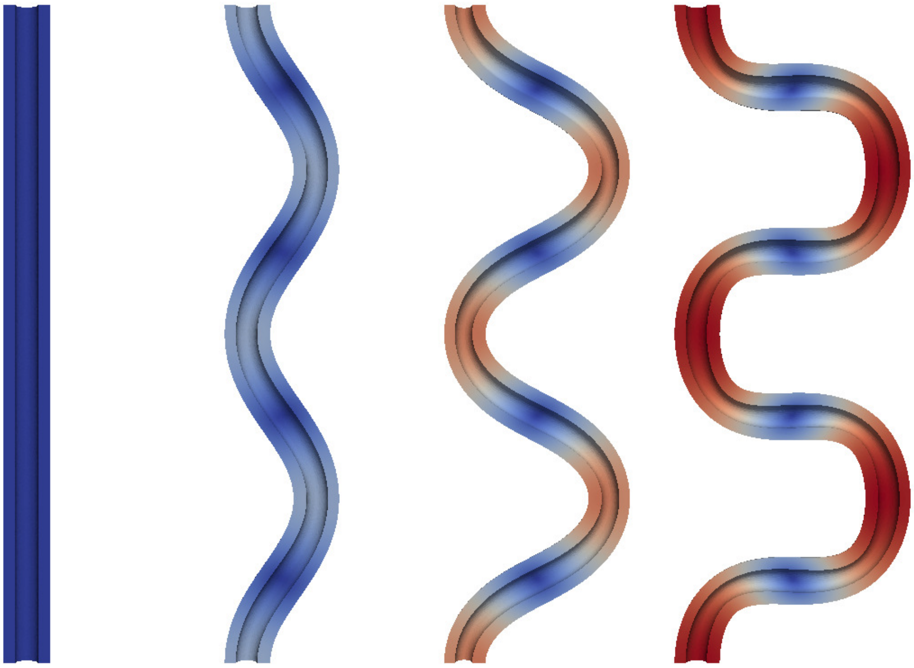

Figure 4.10: Deformed configuration when $\alpha_k = 0.01$, $H/R_o = 4\pi/\tilde{k}_{cr} \simeq 28.55$ and $\gamma = 1, 1.2, 1.5, 1.89$. The corresponding marginal stability threshold is given by $\gamma_{cr} = 1.1103$.

4.1.4 Discussion and concluding remarks

In this Section, we have proposed a morpho–elastic model of the tortuous shape of tumour vessels.

In Section 4.1.1, we have assumed that the tumour capillary is composed of a incompressible neo–Hookean material, and it behaves as a growing hyperelastic tube that is spatially constrained by a linear elastic environment, representing the surrounding interstitial matter. We have modeled the growth by using the multiplicative decomposition of the deformation gradient, assuming an incompatible growth along the axial direction, due to the spatial confinement applied at both ends.

In Section 4.1.2, we have derived a linear stability analysis on the basic axis–symmetric solution using the method of incremental deformations superposed on finite strains [156]. In order to build a robust numerical method, we exploited the Stroh formulation and the impedance matrix method in order to reduce the incremental boundary value problem to a differential Riccati equation (4.28).

The control parameter of the bifurcation is the axial growth rate γ, whose critical value is governed by two dimensionless parameters α_R and α_k, representing the geometrical aspect ratio and the ratio between the energy exerted by the surrounding matter and the bulk strain energy of the capillary, respectively.

The results of the linear stability analysis are collected in Figures 4.1–4.6. Slender capillaries are found having a lower threshold of marginal stability. On the contrary, when increasing α_k we find that the overall axial traction load exerted at the tube ends also increases, finding the Euler buckling as the limiting behavior for $\alpha_k \to 0$ [96]. Interestingly, we find that the linear elastic constraint of the surrounding matter favours the occurrence of short-wavelength critical modes, thus explaining the tortousity of the observed tumour vessels.

The post-buckling behavior is studied implementing numerical simulation using a mixed finite-element method. The numerical algorithm is based on a Newton based continuation method with an adaptive increment of the control parameter. We considered a physiological geometry for a tumour capillary from referenced literature. The corresponding numerical simulation is validated against the linear stability threshold, showing that the bifurcation is supercritical, as depicted in Fig. 4.7. The emerging morphology of the buckled vessel is illustrated in Figs. 4.8–4.10. The tortuousity of the capillary is also characterized by lumen restrictions in the localised regions where the capillary reaches its maximum curvature. This suggests that the elastic bifurcation triggers a significant change in the flow properties inside the vessel.

In summary, the results of this Section show that the tortuosity of the tumour vascular network is mainly driven by the elastic confinement of the interstitial matter where it is embedded. The emerging short-wavelength buckling is similar as the one observed for micro-tubules immersed in the cytosol [37] and for a growing solid cylinder surrounded by an inert elastic tube [158]. We remark that modelling the interstitial matter with linear springs is a very simplificative assumption. Thus, future developments will focus on taking into account for the nonlinear response of the tumour interstitium, possibly including the presence of residual stresses. Moreover, we will investigate the nonlinear effects of the simultaneous buckling of several neighboring capillaries in different spatial networks. The continuation method in numerical simulations shall also be improved in order to compute the full bifurcation diagram. [188, 82]. Finally, introducing an elastic-fluid coupling will allow us to quantify how the capillary tortuosity influences the inner fluid transport, possibly leading to new insights for optimizing drug delivery withing solid tumors [19, 47].

4.1.5 Appendix – Expressions of the components of the Stroh matrix

The expression of the sub-block N_1 of the Stroh matrix is given by

$$\mathsf{N}_1 = \begin{bmatrix} -1 & -m & -kr \\ \frac{1}{2} m v_1 & \frac{-r^2+2r'^2R^2+r_\mathrm{i}^2}{2r'^2R^2} + \log(r) - \log(r_\mathrm{i}) & 0 \\ \frac{1}{2} k r v_1 & 0 & 0 \end{bmatrix}$$

where

$$v_1 = \left(\frac{-r^2 + 2r'^2R^2 + r_\mathrm{i}^2}{r'^2R^2} + 2\log(r) - 2\log(r_\mathrm{i}) \right).$$

The sub-block N_2 reads

$$\mathsf{N}_2 = \begin{bmatrix} 0 & 0 & 0 \\ 0 & \frac{1}{r'^2\mu} & 0 \\ 0 & 0 & \frac{1}{r'^2\mu} \end{bmatrix}.$$

Finally the sub-block N_3 is given by

$$\mathsf{N}_3 = \begin{bmatrix} N_{41} & N_{42} & N_{43} \\ N_{42} & N_{52} & N_{53} \\ N_{43} & N_{53} & N_{63} \end{bmatrix}$$

where

$$\begin{aligned} N_{41} =& \frac{k^2\mu r^2}{\gamma^2} - \frac{\left(\left(r^4 - 2\left(4r'^2R^2 + r_{\mathrm{i}}^2\right)r^2 + \left(2r'^2R^2 + r_{\mathrm{i}}^2\right)^2\right)m^2\right)\mu}{4r'^2R^4} + \\ &+ \frac{\left(k^2r^2\left(-r^2 + 2r'^2R^2 + r_{\mathrm{i}}^2\right)^2 - 4r'^2R^2\left(3r'^2R^2 + r_{\mathrm{i}}^2\right)\right)\mu}{4r'^2R^4} + \\ &+ \frac{\mu\left(2r'^2R^2 - r'^2\left(m^2 + k^2r^2\right)(\log(r) - \log(r_{\mathrm{i}}))R^2\right)(\log(r) - \log(r_{\mathrm{i}}))}{R^2} + \\ &+ \frac{\mu\left(\left(m^2 + k^2r^2\right)\left(r^2 - 2r'^2R^2 - r_{\mathrm{i}}^2\right)\right)(\log(r) - \log(r_{\mathrm{i}}))}{R^2} \end{aligned}$$

$$\begin{aligned} N_{42} =& \frac{m\mu\left(-r^4 + 2\left(4r'^2R^2 + r_{\mathrm{i}}^2\right)r^2 + 8r'^4R^4 - r_{\mathrm{i}}^4\right)}{4r'^2R^4} + \\ &+ \frac{m\mu\left(4r'^2R^2(\log(r) - \log(r_{\mathrm{i}}))\left(r'^2(\log(r_{\mathrm{i}}) - \log(r))R^2 + (r - r_{\mathrm{i}})(r + r_{\mathrm{i}})\right)\right)}{4r'^2R^4} \end{aligned}$$

$$N_{43} = \frac{kr\mu\left(-r^2 + 4r'^2R^2 + r_{\mathrm{i}}^2 + 2r'^2R^2(\log(r) - \log(r_{\mathrm{i}}))\right)}{2R^2}$$

$$\begin{aligned} N_{52} =& \left(3m^2 - 1\right)\mu r'^2 + \frac{\left(2r^2 + \left(m^2 - 1\right)r_{\mathrm{i}}^2\right)\mu}{R^2} + \frac{k^2r^2\mu}{\gamma^2} + \\ &+ \frac{\mu(\log(r) - \log(r_{\mathrm{i}}))\left(r^2 + 2r'^2\left(m^2 - 1\right)R^2 - r_{\mathrm{i}}^2 + r'^2R^2(\log(r_{\mathrm{i}}) - \log(r))\right)}{R^2} + \\ &- \frac{\left(r^2 - r_{\mathrm{i}}^2\right)^2\mu}{4r'^2R^4} \end{aligned}$$

$$N_{53} = \frac{kmr\mu\left(-r^2 + 3r'^2R^2 + r_{\mathrm{i}}^2 + 2r'^2R^2(\log(r) - \log(r_{\mathrm{i}}))\right)}{R^2}$$

$$\begin{aligned} N_{63} =& \frac{r^2\mu\left(\left(R^2 + \left(-r^2 + 3r'^2R^2 + r_{\mathrm{i}}^2\right)\gamma^2\right)k^2\right)}{R^2\gamma^2} + \\ &+ \frac{r^2\mu\left(2r'^2R^2\gamma^2(\log(r) - \log(r_{\mathrm{i}}))k^2 + m^2\gamma^2\right)}{R^2\gamma^2} \end{aligned}$$

4.2 SHAPE TRANSITIONS IN A SOFT INCOMPRESSIBLE SPHERE WITH RESIDUAL STRESSES

As exposed in Section 3.2, inhomogeneous growth processes generate residual stresses in solid tumours. More in general, residual stresses result from the presence of microstructural misfits, for example after plastic deformations (e.g. in metals) or thermal processes (e.g. quick solidification in glass). Indeed, it is well acknowledged that there exists a mechanical feedback in many biological processes. Living tissues can adapt their structural response to the external mechanical stimuli by generating residual stresses either in physiological conditions (e.g. within arteries or the gastro-intestinal tract [53, 74, 213]) or pathological situations (e.g. solid tumors [198, 72, 10]). Moreover, residual stresses can accumulate reaching a critical threshold beyond which a morphological transition is triggered, possibly leading to complex pattern formation, such as wrinkling, creasing or folding [131, 57].

Several studies about mechanical instabilities in soft materials with a spherical shape have been carried out in the last decades. The stability of spherical elastic shells has been studied with respect to the application of an external [214, 211] or internal pressure [108, 103]. More recently, the influence of residual stresses on stability in growing spherical shells [26] as well as in spherical solid tumor [55] has been addressed.

Residual stresses are classically modeled by exploiting the theory of elastic distortions, i.e. decomposing multiplicatively the deformation gradient [181]. The main drawback of this method is the necessity of the *a priori* knowledge of the relaxed state, since it is not often physically accessible [75]. Indeed, from an experimental viewpoint, its determination would require several cuttings (ideally infinite) on the elastic body in order to release all the underlying residual stresses.

Instead, in this Section we employ the theory of initially stressed materials to study the morphological stability of a sphere with an arbitrary, radially symmetric, distribution of the residual stress.

4.2.1 The elastic model

Let us consider a soft residually-stressed solid sphere composed of an incompressible hyperelastic material in a reference configuration $\Omega \subset \mathbb{E}^3$, where $\mathbb{E}^3$ is the three-dimensional Euclidean space. We use a spherical coordinate system in the reference configuration so that the material position vector is given by

$$\boldsymbol{X} = (R\sin(\Theta)\cos(\Phi), R\sin(\Theta)\sin(\Phi), R\cos(\Theta))$$

where R is the radial coordinate, Θ is the polar angle and Φ is the azimuthal angle.

We define the domain Ω as the set such that

$$\Omega = \left\{ \boldsymbol{X} \in \mathbb{E}^3 \mid R < R_o \right\},$$

so that R_o is the radius of the solid sphere. We indicate with $\boldsymbol{e}_R$, $\boldsymbol{e}_\Theta$ and $\boldsymbol{e}_\Phi$ the local orthonormal vector basis.

4.2.1.1 *Constitutive assumptions*

Indicating with $\boldsymbol{x} = \boldsymbol{\varphi}(\boldsymbol{X})$ the spatial position vector, so that $\boldsymbol{\varphi}$ is the deformation field, we assume that the strain energy density of the body ψ is a function depending on both the deformation gradient $\mathsf{F} = \operatorname{Grad} \boldsymbol{\varphi}$ and the Cauchy stress Σ in the reference configuration (i.e. the residual stress [109]):

$$\psi = \psi(\mathsf{F}, \Sigma), \tag{4.30}$$

as previously proposed in [161, 189].

Hence, the first Piola–Kirchhoff stress tensor P and the Cauchy stress tensor T are given by

$$\mathsf{P}(\mathsf{F}, \Sigma) = \frac{\partial \psi}{\partial \mathsf{F}}(\mathsf{F}, \Sigma) - p\mathsf{F}^{-1}, \qquad \mathsf{T}(\mathsf{F}, \Sigma) = \mathsf{F}\mathsf{P} \tag{4.31}$$

where p is the Lagrangian multiplier that enforces the incompressibility constraint $\det \mathsf{F} = 1$.

Hence, the fully non-linear problem in the quasi-static case reads

$$\operatorname{Div} \mathsf{P} = \mathbf{0}. \tag{4.32}$$

where Div denotes the divergence operator in material coordinates; the boundary conditions are

$$\mathsf{P}^T \boldsymbol{e}_R = \mathbf{0} \qquad \text{when } R = R_o \tag{4.33}$$

where $\boldsymbol{u}(\boldsymbol{X}) = \boldsymbol{\varphi}(\boldsymbol{X}) - \boldsymbol{X}$ is the displacement vector field.

When we evaluate the Piola–Kirchhoff stress in the reference configuration, we obtain the residual stress Σ, i.e. setting F equal to the identity tensor I in Eq. (4.31), we get

$$\Sigma = \frac{\partial \psi}{\partial \mathsf{F}}(\mathsf{I}, \Sigma) - p_0\mathsf{I}; \tag{4.34}$$

this relation represents the *initial stress compatibility condition* [189, 97, 98], where p_0 is a scalar field corresponding to the pressure field in the unloaded case.

Moreover, since Σ is the Cauchy stress tensor in the reference configuration, the balance of the linear and the angular momentum impose

$$\operatorname{Div} \Sigma = \mathbf{0}, \qquad \Sigma = \Sigma^T \qquad \text{in } \Omega, \tag{4.35}$$

together with the following boundary conditions

$$\Sigma_{RR} = \Sigma_{\Theta R} = \Sigma_{\Phi R} = 0 \qquad \text{for } R = R_o. \tag{4.36}$$

From Eqs. (4.35)-(4.36), it is possible to prove that [110]

$$\int_{\Omega} \Sigma \, d\mathcal{L}^3(\boldsymbol{X}) = 0,$$

so that the residual stress field must be inhomogeneous, with zero mean value.

We also assume that the strain energy density depends on the choice of the reference configuration only through the functional dependence on Σ. Thus, we impose the *initial stress reference independence* (see [97, 98] for further details), reading

$$\psi\left(\mathsf{F}_1\mathsf{F}_2, \Sigma\right) = \psi\left(\mathsf{F}_1, \mathsf{T}\left(\mathsf{F}_2, \Sigma\right)\right). \tag{4.37}$$

The Eq. (4.37) must hold for all second order tensor F_1, F_2 with positive determinant and for all the symmetric tensors Σ.

The general material with a strain energy given by Eq. (4.30), such that the material behaviour is isotropic in absence of residual stress, i.e. for $\Sigma = 0$, may depend up to ten independent invariants [189].

A simple possible choice for the strain energy density which satisfies both the initial stress compatibility condition and the initial stress reference independence is the one corresponding to an *initially stressed neo–Hookean material*. The strain energy of such material is constructed so that if a virtual relaxed state exists [119], then it naturally behaves as a neo–Hookean material with a given shear modulus μ. In the following we briefly sketch how this strain energy is obtained (see [97] for a detailed derivation).

Let us introduce the following five invariants:

$$I_1 = \operatorname{tr}\mathsf{C}, \quad J_1 = \operatorname{tr}\left(\Sigma\mathsf{C}\right), \quad I_{\Sigma1} = \operatorname{tr}\Sigma, \quad I_{\Sigma2} = \frac{(\operatorname{tr}\Sigma)^2 - \operatorname{tr}\Sigma^2}{2}, \quad I_{\Sigma3} = \det\Sigma,$$

where $\mathsf{C} = \mathsf{F}^T\mathsf{F}$ is the right Cauchy–Green tensor.

Assuming that the material behaves as an incompressible neo-Hookean body, its strain energy density is given by

$$\psi(\mathsf{F}, \Sigma) = \frac{\mu}{2}(\operatorname{tr}(\widetilde{\mathsf{B}}\mathsf{C}) - 3), \tag{4.38}$$

here C is the right Cauchy-Green strain tensor, $\widetilde{\mathsf{F}}$ is the deformation gradient from the virtual unstressed state to the reference configuration, $\widetilde{\mathsf{B}} = \widetilde{\mathsf{F}}\widetilde{\mathsf{F}}^{\mathsf{T}}$ and μ is the shear modulus of the material in absence of residual stresses.

So, substituting Eq. (4.38) in Eq. (4.31), the initial stress Σ is given by

$$\Sigma = \mu\widetilde{\mathsf{B}} - \widetilde{p}\mathsf{I}. \tag{4.39}$$

Imposing the incompressibility constraint on the deformation gradient $\widetilde{\mathsf{F}}$, we get $\det(\mu\widetilde{\mathsf{B}}) = \mu^3 = \det(\Sigma + \widetilde{p}I)$. Thus, $\widetilde{p}$ is the real root of the following polynomial:

$$\tilde{p}^3 + \tilde{p}^2 I_{\Sigma1} + \tilde{p} I_{\Sigma2} + I_{\Sigma3} - \mu^3 = 0. \tag{4.40}$$

Hence, multiplying Eq. (4.39) by C on the right and taking the trace on both sides, we obtain

$$\mathrm{tr}(\widetilde{\mathsf{S}}\mathsf{C}) = \mu\,\mathrm{tr}(\widetilde{\mathsf{B}}\mathsf{C}) - \tilde{p} I_1. \tag{4.41}$$

Substituting Eq. (4.41) in Eq. (4.38), we obtain the strain energy of an initially stressed Neo–Hookean body:

$$\psi\,(I_1, J_1, I_{\Sigma 1}, I_{\Sigma 2}, I_{\Sigma 3}) = \frac{1}{2}(J_1 + \tilde{p} I_1 - 3\mu). \tag{4.42}$$

where $\tilde{p}$ is the only real root of Eq. (4.40). It is given by [97]

$$\tilde{p} = \frac{1}{3}\left[T_3 + \frac{T_1}{T_3} - I_{\Sigma 1}\right],$$

where

$$\begin{aligned} T_1 &= I_{\Sigma 1}^2 - 3 I_{\Sigma 2}, \\ T_2 &= I_{\Sigma 1}^3 - \frac{9}{2} I_{\Sigma 1} I_{\Sigma 2} + \frac{27}{2}\left(I_{\Sigma 3} - \mu^3\right), \\ T_3 &= \sqrt[3]{\sqrt{T_2^2 - T_1^3} - T_2}. \end{aligned}$$

In this setting, it is possible to prove that the pressure field in the reference configuration is given by $p = \tilde{p}$ [97].

In the following, we use symmetry arguments to discuss a few possible choices for the distribution of the residual stresses.

4.2.1.2 *Residual stress distribution*

We assume that the residual stress Σ depends only on the variable R. Hence the system of equations given by Eq. (4.35) reduces to

$$\begin{cases} \dfrac{\partial \Sigma_{RR}}{\partial R} + \dfrac{2}{R}(\Sigma_{RR} - \Sigma_{\Theta\Theta}) = 0, \\ \Sigma_{R\Theta} = \Sigma_{R\Phi} = \Sigma_{\Theta\Phi} = 0; \end{cases}. \tag{4.43}$$

Then, being $f(R)$ the radial component of the residual stress, the tensor Σ is given by

$$\Sigma = \mathrm{diag}\left(f(R), \frac{R}{2} f'(R) + f(R), \frac{R}{2} f'(R) + f(R),\right)$$

where $f : [0, R_o] \to \mathbb{R}$ is such that $f(R_o) = 0$ in order to satisfy automatically Eq. (4.43).

In the following, we will focus on two possible choices for the function f:

$$\textbf{case (a)} : f(R) = \alpha\mu \frac{R^\beta - R_o^\beta}{R_o^\beta}, \tag{4.44}$$

$$\textbf{case (b)} : f(R) = \alpha\mu \left(\frac{R}{R_o}\right)^\gamma \log\left(\frac{R}{R_o}\right), \tag{4.45}$$

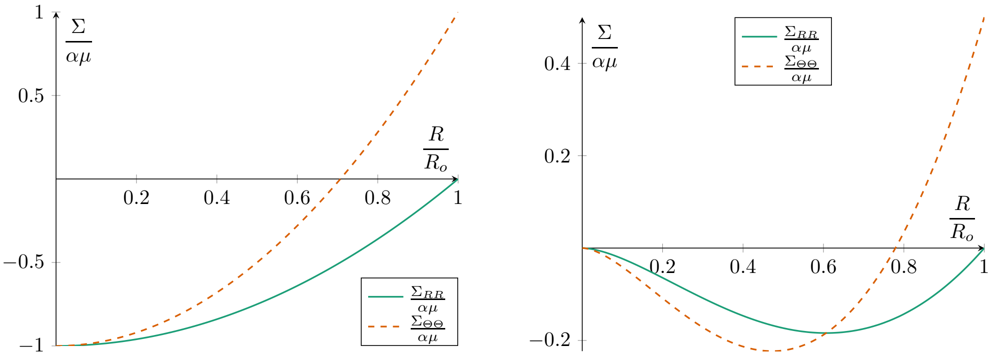

Figure 4.11: Plot of the radial (solid line) and hoop (dashed line) residual stress components normalized with respect to $\alpha\ \mu$ when $f(R)$ is given by Eq. (4.44) (left) $f(R)$ is given by Eq. (4.45) (right). Both the dimensionless parameters β and γ are set equal to 2.

where α, β and γ are real dimensionless parameters with $\beta, \gamma > 1$. The corresponding residual stress components are depicted in Fig. 4.11.

In the next Section we apply the theory of incremental deformations in order to study the stability of the residually stressed configuration with respect to the magnitude of the underlying residual stresses expressed by the dimensionless parameters α, β and γ.

4.2.2 Incremental problem and linear stability analysis

4.2.2.1 *Structure of the incremental equations*

In order to study the linear stability of the undeformed configuration with respect to the intensity of the residual stresses, we use the method of the incremental elastic deformations [156]. We denote with $\delta \boldsymbol{u}$ the incremental displacement vector and with $\mathsf{\Gamma}$ the gradient of the vector field $\delta \boldsymbol{u}$, namely $\mathsf{\Gamma} = \text{Grad}\,\delta \boldsymbol{u}$.

The linearized incremental Piola–Kirchhoff stress tensor reads

$$\delta \mathsf{P} = \mathcal{A}_0^1 : \mathsf{\Gamma} + p\mathsf{\Gamma} - q\mathsf{I} \tag{4.46}$$

where q is the increment of the Lagrangian multiplier p and

$$\left(\mathcal{A}_0^1 : \mathsf{\Gamma}\right)_{ij} := A^1_{0ijhk}\Gamma_{kh} = \left.\frac{\partial^2 \psi}{\partial F_{ji} \partial F_{kh}}\right|_{\mathsf{F}=\mathsf{I}} \Gamma_{kh},$$

with $\mathcal{A}_0$ being the fourth order tensor of the elastic moduli, and summation over repeated subscripts is assumed.

From Eq. (4.42) and following [189], we get

$$A^1_{0ijhk} = \delta_{jk}(2\psi_{,I_1}\,\delta_{ih} + \Sigma_{ih}),$$

where δ_{ij} is the Kronecker delta the comma denotes the partial derivative.

Hence, the incremental equilibrium equation is given by

$$\operatorname{Div} \delta \mathsf{P} = \mathbf{0}, \tag{4.47}$$

and the boundary conditions read

$$\delta \mathsf{P}^T \boldsymbol{e}_R = \mathbf{0} \qquad \text{at } R = R_o. \tag{4.48}$$

The incompressibility of the incremental deformation is given by the constraint

$$\operatorname{tr} \Gamma = 0. \tag{4.49}$$

We assume an axis-symmetric incremental displacement vector given by

$$\delta \boldsymbol{u} = u(R, \Theta)\boldsymbol{e}_R + v(R, \Theta)\boldsymbol{e}_\Theta.$$

This choice is motivated by the fact that, imposing a general incremental displacement vector, the resulting governing equations in the azimuthal direction decouple [214, 211], thus not influencing the linearized bifurcation analysis.

Hence, the incremental displacement gradient is given by

$$\Gamma = \begin{bmatrix} u_{,R} & \dfrac{u_{,\Theta} - v}{R} & 0 \\ v_{,R} & \dfrac{u + v_{,\Theta}}{R} & 0 \\ 0 & 0 & \dfrac{u + \cot(\Theta) v}{R} \end{bmatrix}.$$

In order to build a robust numerical procedure to solve the incremental boundary value problem, we first rewrite Eqs. (4.47)-(4.49) using a more convenient form, known as Stroh formulation.

4.2.2.2 *Stroh formulation*

Since the residually stressed material is inhomogeneous only in the radial direction, we study the bifurcation problem by assuming variable separation for the incremental fields [154], namely

$$u(R, \Theta) = U(R) P_m(\cos\Theta), \tag{4.50}$$

$$v(R, \Theta) = V(R) \frac{1}{\sqrt{m(m+1)}} \frac{dP_m(\cos\Theta)}{d\Theta}, \tag{4.51}$$

$$\delta P_{RR}(R, \Theta) = s_{RR}(R) P_m(\cos\Theta), \tag{4.52}$$

$$\delta P_{R\Theta}(R, \Theta) = s_{R\Theta}(R) \frac{1}{\sqrt{m(m+1)}} \frac{dP_m(\cos\Theta)}{d\Theta}, \tag{4.53}$$

where $P_m(\Theta)$ denotes the Legendre polynomial of order m.

In order to write the incremental boundary value problem Eqs. (4.47)-(4.49) in the Stroh formulation, we introduce the displacement-traction vector $\boldsymbol{\eta}$, defined as

$$\boldsymbol{\eta}(R) = \begin{bmatrix} \boldsymbol{U}(R) \\ R^2\boldsymbol{T}(R) \end{bmatrix}, \qquad \text{where} \quad \boldsymbol{U}(R) = \begin{bmatrix} U(R) \\ V(R) \end{bmatrix}, \quad \boldsymbol{T}(R) = \begin{bmatrix} s_{RR}(R) \\ s_{R\Theta}(R) \end{bmatrix}.$$

An expression for q is found by substituting Eq. (4.46) in Eq. (4.52), so that

$$q = P_m(\cos(\Theta)) \left(U'(R) \left(2\psi,_{I_1} + f(R) + p \right) - \delta P_{RR}(R) \right). \tag{4.54}$$

Thus, using a well established procedure [197], we can use the definition of the linearized incremental Piola–Kirchhoff given by Eq. (4.46), the incremental equilibrium equations given by Eq. (4.47) and the linearized incompressibility constraint Eq. (4.49) to obtain a first order system of ordinary differential equations, namely

$$\frac{d\boldsymbol{\eta}}{dR} = \frac{1}{R^2}\mathsf{N}\boldsymbol{\eta}, \tag{4.55}$$

where $\mathsf{N}(R)$ is the *Stroh matrix* which has the following structure

$$\mathsf{N} = \begin{pmatrix} \mathsf{N}_1 & \mathsf{N}_2 \\ \mathsf{N}_3 & -\mathsf{N}_1^{\mathsf{T}} \end{pmatrix},$$

where the sub-blocks read:

$$\mathsf{N}_1 = \begin{pmatrix} -2R & \sqrt{m(m+1)}R \\ -\frac{\sqrt{m(m+1)}pR}{f(R)+2\psi,_{I_1}} & \frac{pR}{f(R)+2\psi,_{I_1}} \end{pmatrix}, \quad \mathsf{N}_2 = \begin{pmatrix} 0 & 0 \\ 0 & \frac{1}{f(R)+2\psi,_{I_1}} \end{pmatrix},$$
$$\mathsf{N}_3 = \begin{pmatrix} \nu_1 & \nu_2 \\ \nu_2 & \nu_3 \end{pmatrix}.$$

The expressions for the coefficients ν_1, ν_2 and ν_3 are given by:

$$\begin{aligned}
\nu_1 = {} & \frac{R^2((2\psi,_{I_1} + f(R))(4(m^2+m+6)\psi,_{I_1} + (m^2+m+2)Rf'(R)}{2(2\psi,_{I_1} + f(R))} + \\
& + \frac{2(m^2+m+6)f(R) + 12p) - 2m(m+1)p^2)}{2(2\psi,_{I_1} + f(R))}, \\
\nu_2 = {} & \frac{R^2\sqrt{m(m+1)}\left(p^2 - (2\psi,_{I_1} + f(R))\left(8\psi,_{I_1} + Rf'(R) + 4f(R) + 3p\right)\right)}{2\psi,_{I_1} + f(R)}, \\
\nu_3 = {} & \frac{R^2\left(2\psi,_{I_1} + f(R)\right)\left(m(m+1)\left(8\psi,_{I_1} + Rf'(R) + 4f(R)\right) + 2(2m(m+1)-1)p\right)}{2\left(2\psi,_{I_1} + f(R)\right)} + \\
& - \frac{2R^2p^2}{2\left(2\psi,_{I_1} + f(R)\right)}.
\end{aligned}$$

In the next Section, we solve the Eq. (4.55) by using the impedance matrix method.

4.2.2.3 *Impedance matrix method*

Let us briefly sketch the main theoretical aspects of this method [32, 33]. We define a linear functional relation between $\boldsymbol{U}$ and $\boldsymbol{T}$, namely

$$R^2\boldsymbol{T} = \mathsf{Z}\boldsymbol{U}. \tag{4.56}$$

where Z is the so called *surface impedance matrix*.

By substituting Eq. (4.56) in Eq. (4.55), we obtain

$$\frac{d\boldsymbol{U}}{dR} = \frac{1}{R^2}(\mathsf{N}_1\boldsymbol{U} + \mathsf{N}_2\mathsf{Z}\boldsymbol{U}), \tag{4.57}$$

$$\frac{d\mathsf{Z}}{dR}\boldsymbol{U} + \mathsf{Z}\frac{d\boldsymbol{U}}{dR} = \frac{1}{R^2}(\mathsf{N}_3\boldsymbol{U} + \mathsf{N}_4\mathsf{Z}\boldsymbol{U}). \tag{4.58}$$

Thus, by substituting Eq. (4.57) in Eq. (4.58), a Riccati differential equation is found for Z, being

$$\frac{d\mathsf{Z}}{dR} = \frac{1}{R^2}\left(\mathsf{N}_3 - \mathsf{N}_1^T\mathsf{Z} - \mathsf{Z}\mathsf{N}_1 - \mathsf{Z}\mathsf{N}_2\mathsf{Z}\right). \tag{4.59}$$

Let now us define M as the solution to the following problem

$$\begin{cases} \dfrac{d}{dR}\mathsf{M}(R, R_o) - \dfrac{\mathsf{N}}{R^2}\mathsf{M}(R, R_o) = 0 \\ \mathsf{M}(R_o, R_o) = \mathsf{I}. \end{cases} \tag{4.60}$$

where the matricant $\mathsf{M}(R, R_o)$ is a 4×4 matrix, called the *conditional matrix*.

Since M is the solution of the problem given in Eq. (4.60), from Eq. (4.55) it is straightforward to show that

$$\boldsymbol{\eta}(R) = \mathsf{M}(R, R_o)\boldsymbol{\eta}(R_o). \tag{4.61}$$

Let us split the conditional matrix into four blocks as

$$\mathsf{M} = \begin{bmatrix} \mathsf{M}_1(R, R_o) & \mathsf{M}_2(R, R_o) \\ \mathsf{M}_3(R, R_o) & \mathsf{M}_4(R, R_o) \end{bmatrix}. \tag{4.62}$$

We can use two possible ways to construct the surface impedance matrix, either the *conditional impedance matrix* $\mathsf{Z}^c(R, R_o)$ or the *solid impedance matrix* $\mathsf{Z}^s(R)$ [155].

In fact, considering that $\boldsymbol{T}(R_o) = \mathbf{0}$ and by using the Eqs. (4.61)-(4.62), we can define the conditional impedance matrix as $\mathsf{Z}^c(R, R_o) := \mathsf{M}_3(R, R_o)\mathsf{M}_1^{-1}(R, R_o)$. Such a matrix is called conditional since it depends explicitly on its value at $R = R_o$.

Conversely, the solid impedance matrix does not depend explicitly on its value at one point, but instead it ensures that the surface impedance matrix is well posed at the origin.

Following [155], we consider a Taylor series expansion of the solid impedance matrix $\mathsf{Z}^s(R)$ around $R = 0$, namely

$$\mathsf{Z}^s(R) = \mathsf{Z}_0 + \mathsf{Z}_1 R + o(R), \tag{4.63}$$

where Z_0 is called *central impedance matrix*.

From the Eq. (4.59), the solid impedance matrix is well posed at the origin only if the central impedance matrix satisfies the following algebraic Riccati equation:

$$\mathsf{N}_3(0) - \mathsf{N}_1^T(0)\mathsf{Z}_0 - \mathsf{Z}_0\mathsf{N}_1(0) - \mathsf{Z}_0\mathsf{N}_2(0)\mathsf{Z}_0 = 0;$$

whose general solution is given by

$$\mathsf{Z}_0 = \delta \boldsymbol{e}_1 \otimes \boldsymbol{e}_1, \qquad \delta \in \mathbb{R}. \tag{4.64}$$

By substituting Eq. (4.63) in Eq. (4.59) and setting $R = R_c \ll 1$, we obtain the following algebraic Riccati equation

$$\begin{aligned} 0 = \mathsf{N}_3(R_c) - \mathsf{N}_1^T(R_c)\mathsf{Z}_0 - \mathsf{Z}_0\mathsf{N}_1(R_c) - \mathsf{Z}_0\mathsf{N}_2(R_c)\mathsf{Z}_0 - R_c^2\mathsf{Z}_1\mathsf{N}_2(R_c)\mathsf{Z}_1 + \\ -R_c\mathsf{Z}_1\left(\mathsf{N}_1(R_c) + \mathsf{N}_2(R_c)\mathsf{Z}_0 + \frac{R_c}{2}\mathsf{I}\right) - R_c\left(\mathsf{N}_1^T(R_c) + \mathsf{Z}_0\mathsf{N}_2(R_c) + \frac{R_c}{2}\mathsf{I}\right)\mathsf{Z}_1 \end{aligned} \tag{4.65}$$

whose stable solution is the only one such that the eigenvalues of

$$-R_c\left(\mathsf{N}_1(R_c) + \mathsf{N}_2(R_c)\mathsf{Z}_0 + \frac{R_c}{2}\mathsf{I}\right) - R_c^2\mathsf{N}_2(R_c)\mathsf{Z}_1$$

are all negative [58].

In summary, the surface impedance method allows us to avoid the direct resolution of the boundary value problem given by Eqs. (4.47)-(4.49) by using a numerical integration of the Riccati equation given by Eq. (4.59).

4.2.2.4 *Numerical procedure and results of the linear stability analysis*

The aim of this Section is to implement a robust numerical procedure to analyze the onset of a morphological transition as a function of the dimensionless parameters α, β and γ representing the magnitude and the spatial distribution of the residual stresses.

The solution of the incremental boundary value problem can be obtained by a numerical integration of the differential Riccati equation (4.59) using two different procedures.

First, the differential Riccati equation in Eq. (4.59) can be integrated from R_c to R_o with starting value

$$\mathsf{Z}^s(R_c) = \mathsf{Z}_0 + R_c\mathsf{Z}_1, \tag{4.66}$$

given by the solid impedance matrix in Eq. (4.63).

Using Eq. (4.66), we numerically solve Eq. (4.59) by iterating on the value α in Eqs. (4.44)-(4.45), starting from 0 until the stop condition

$$\det \mathsf{Z}^s(R_o) = 0, \tag{4.67}$$

is reached, namely when the impedance matrix is singular and the incremental Eqs. (4.47) and (4.49) admit a non-null solution that satisfies Eq. (4.48).

A second approach consists in integrating Eq. (4.59) by using the conditional impedance matrix $\mathsf{Z}^c(R, R_o)$. Since from Eq. (4.61) it can be shown that $\mathsf{M}(R_o, R_o) = \mathsf{I}$, the definition of the conditional impedance matrix given by Eq. (4.60) allows us to set the following initial condition:

$$\mathsf{Z}^c(R_o, R_o) = 0. \tag{4.68}$$

Analogously, we iteratively integrate Eq. (4.59) until the stop condition

$$\det(\mathsf{Z}^c(R_c, R_o) - \mathsf{Z}_0 - \mathsf{Z}_1 R_c) = 0 \tag{4.69}$$

is reached. This condition corresponds to the existence of non-null solutions for the variable $\boldsymbol{U}$ by imposing the continuity of the incremental stress vector $\boldsymbol{T}$ at $R = R_c$.

In both cases, in order to find the incremental displacement field, we perform a further integration of Eq. (4.57) using the procedure described in [69].

The two numerical schemes were implemented by using the software *Mathematica 11.0* (Wolfram Research, Champaign, IL, USA) in order to identify the marginal stability curves as function of the dimensionless parameters α, β and γ.

CASE (A): EXPONENTIAL POLYNOMIAL CASE Let us first consider the case in which the expression of $f(R)$ is the exponential polynomial given by Eq. (4.44). We use the initial condition given by Eq. (4.66).

We find out that the stop condition given by Eq. (4.67) is satisfied only for negative values of α, namely we can find an instability only if the hoop residual stress is tensile close to the center and compressive near the boundary of the sphere. Moreover, the results are independent on the choice of the δ in Eq. (4.64).

For fixed β and m, let α_m be the first value such that the stop condition Eq. (4.67) is satisfied, we define the critical wavenumber m_{cr} as the wavenumber with minimum $|\alpha_m|$ and we denote such a critical value with α_{cr}. In Fig. 4.12 (left) we depict several marginal stability curves for various β whilst in Fig. 4.12 (right) we plot the critical wavenumber vs. β. We highlight that, as we increase the parameter β, the critical wavenumber m_{cr} also increases with a nearly linear behavior.

In Fig. 4.13 we plot the solution of the linearized incremental problem for $\beta = 3$ where $m = m_{cr} = 7$ (see Fig. 4.12 (right)) and we observe that wrinkles appear in the outer shell of the sphere, where the hoop residual stress is compressive.

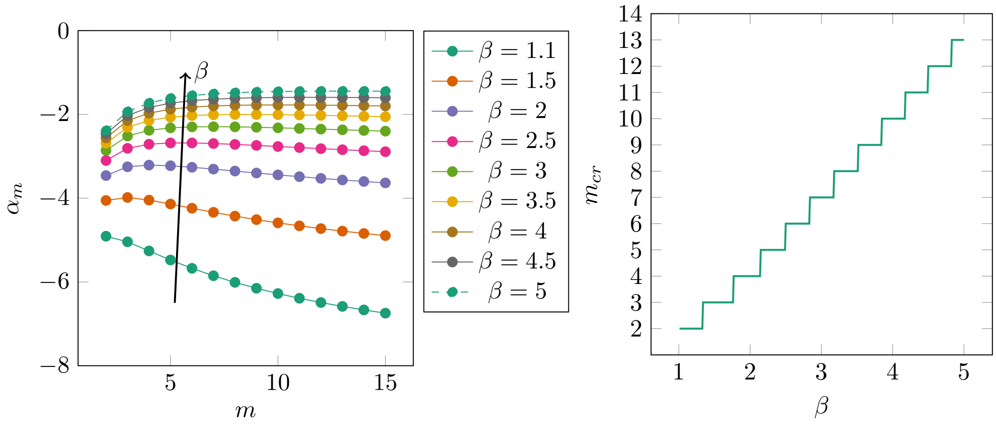

Figure 4.12: Marginal stability curves for the residually stressed sphere where $f(R)$ is given by the Eq. (4.44), showing the critical α vs. the wavenumber m (left) and the critical wavenumber m_{cr} vs. β (right).

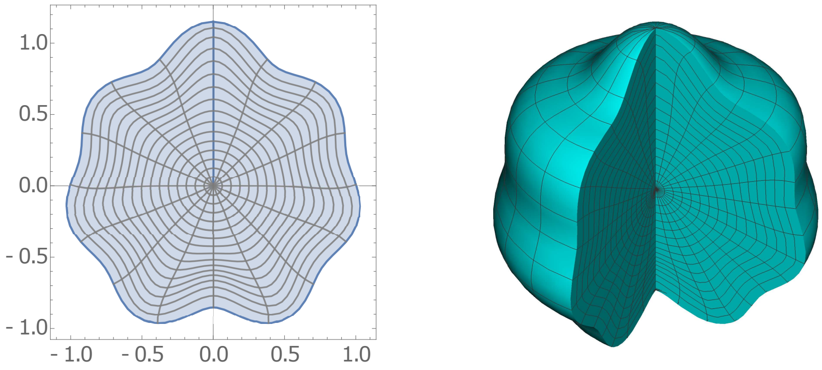

Figure 4.13: Solution of the linearized incremental problem for $\beta = 3$ and $m = m_{cr} = 7$ where $f(R)$ is given by the Eq. (4.44). The amplitude of the incremental deformation has been arbitrarily set $0.15\,R_o$ for the sake of graphical clarity.

CASE (B): LOGARITHMIC CASE Let us now consider the case in which $f(R)$ is given by Eq. (4.45). We find that the residually stressed sphere is unstable for both positive and negative values of α.

When we consider positive values for the control parameter α, we integrate the differential Riccati equation given by Eq. (4.59) from $R = R_o$, using the initial condition given by Eq. (4.68), and using the stop condition at $R = R_c$ given by Eq. (4.69).

On the other hand, when α is negative, we use as the initial condition the Eq. (4.66) and as stop condtion the Eq. (4.67). This means that we integrate the Riccati equation from the interior to the exterior.

Let us first consider the case in which α is negative, namely when the hoop stress is compressive at the boundary (see Fig. 4.11). In this framework in Fig. 4.14 (left), we depict several marginal stability curves for various γ, whereas

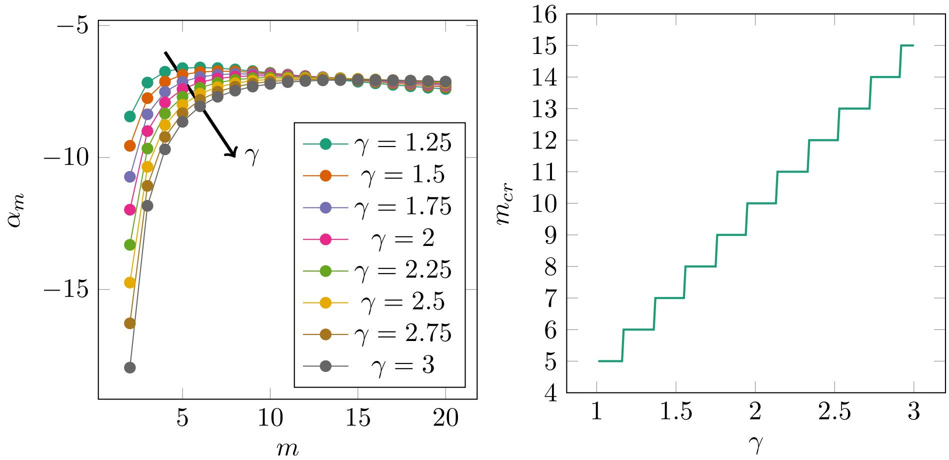

Figure 4.14: Marginal stability curves for the residually stressed sphere where $f(R)$ is given by the Eq. (4.45), showing the critical positive α vs. the wavenumber m (left) and the critical wavenumber m_{cr} vs. γ (right).

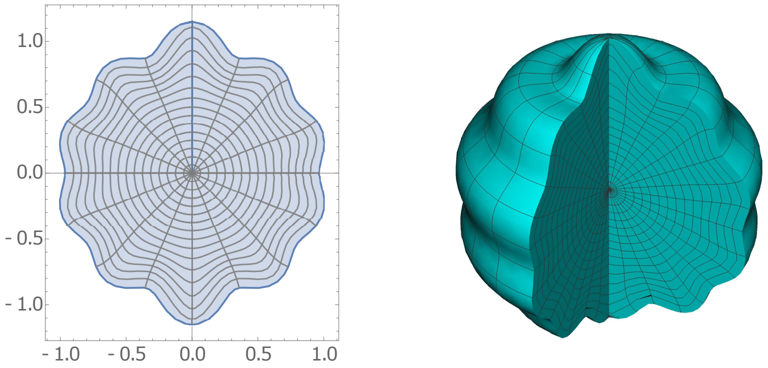

Figure 4.15: Solution of the linearized incremental problem for $\gamma = 2$ and $m = m_{cr} = 10$ where $f(R)$ is given by the Eq. (4.45). The amplitude of the incremental deformation has been arbitrarily set $0.15\,R_o$ for the sake of graphical clarity.

in Fig. 4.14 (right) we plot the values of the critical wavenumber vs. the parameter γ. As previously observed, by increasing γ, also the critical wavenumber m_{cr} increases with a nearly linear dependence.

In Fig. 4.15 we plot the solution of the linearized incremental for $\gamma = 2$, where $m = m_{cr} = 7$ (see Fig. 4.14, right); as in the polynomial case, we can notice how wrinkles appear in the outer rim of the domain, where the hoop residual stress is compressive.

We perform the same calculations for the case in which α is positive. In Fig. 4.16 we depict the resulting marginal stability curves for various γ and m.

In Fig. 4.17 we plot the solution of the linearized incremental problem for $\gamma = 2$ and $m = m_{cr} = 3$. We highlight that the displacement is localized in the center of the sphere whereas the exterior part remains almost undeformed.

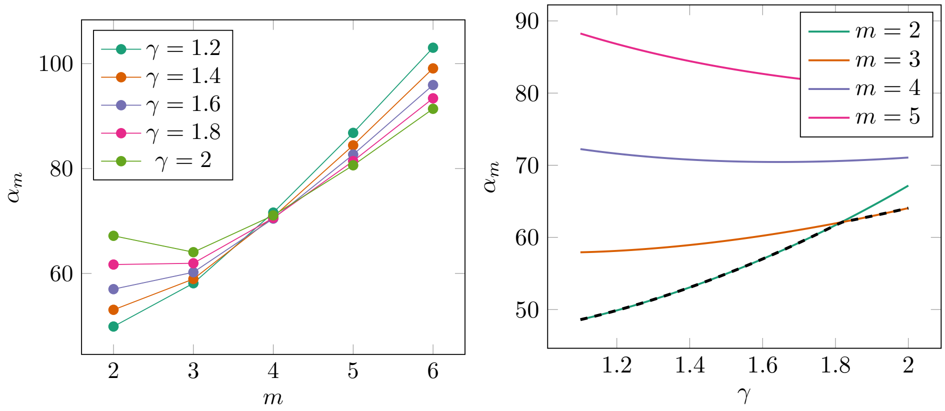

Figure 4.16: Marginal stability curves for the residually stressed sphere where $f(R)$ is given by the Eq. (4.45), showing α_m vs. the wavenumber m (left) and γ (right). The black dashed curves on the right is the plot of the α_{cr} vs. γ.

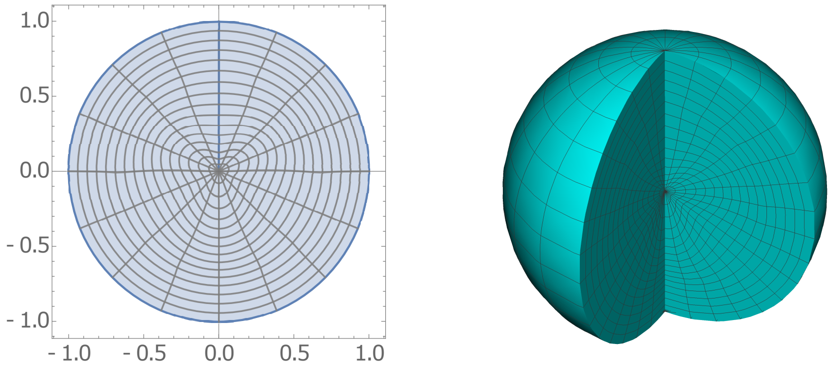

Figure 4.17: Solution of the linearized incremental problem for $\gamma = 2$ and $m = m_{cr} = 3$ where $f(R)$ is given by the Eq. (4.45). The amplitude of the incremental deformation has been arbitrarily set $0.15\, R_o$ for the sake of graphical clarity.

Also in this case, we found that all the results exposed are independent of the chosen value of δ in Eq. (4.64).

In the next Section, we implement a finite element code in order to investigate the fully non-linear evolution of the morphological instability.

4.2.3 Finite element implementation and post-buckling analysis

4.2.3.1 *Mixed finite element implementation*

We use a mixed variational formulation of the problem implemented with the open source project FEniCS [134]. Let $\mathcal{B}$ be a semicircle and $\hat{\mathcal{B}} = (0,1) \times (0, \pi)$ as depicted in Fig. 4.18. We define $g : \mathcal{B} \to \hat{\mathcal{B}}$ as the mapping that associates each point in $\mathcal{B}$ with the point in $\mathbb{R}^2$ such that the two components are the normalized radial distance R/R_o and the polar angle Θ. Hence, denoting by

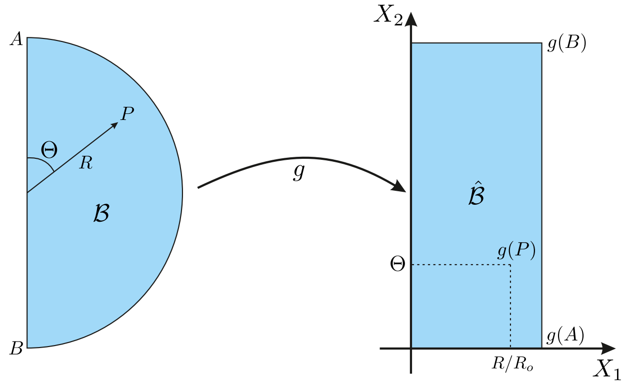

Figure 4.18: Representation of the conformal mapping between the physical domain $\mathcal{B}$ and its conformal image $\hat{\mathcal{B}}$, defined through the coordinate transformation in Eq. (4.70).

X_1 and X_2 the first and the second coordinates respectively and by $\boldsymbol{e}_1$ and $\boldsymbol{e}_2$ the canonical unit basis vectors, we get that

$$X_1 = \frac{R}{R_o}, \qquad X_2 = \Theta. \tag{4.70}$$

We solve the nonlinear problem using a triangular mesh $\hat{\mathcal{B}}_h$ obtained through the discretization of the set $\hat{\mathcal{B}}$. The mesh is composed of 14677 elements, 7519 vertices and the maximum diameter of the cells is 0.033.

We use the Taylor–Hood elements $\boldsymbol{P}_2$-P_1, discretizing the displacement field by using piecewise quadratic functions and the pressure field by piecewise linear functions. The Taylor-Hood element is numerically stable for linear elasticity problems [34] and has been used in several applications of non-linear elasticity [16].

In order to study the behavior of the bifurcated solution in the post-buckling regime, we impose a small imperfection on the mesh at the boundary [60] with the form given by Eqs. (4.50)-(4.51), where m is the critical wavenumber obtained from the linear stability analysis and the amplitude is of the order of 10^{-4}.

We impose as boundary conditions

$$\begin{cases} \boldsymbol{u}_h = \boldsymbol{0} & \text{if } X_1 = 0, \\ \boldsymbol{u}_h \cdot \boldsymbol{e}_2 = 0 \text{ and } \boldsymbol{e}_1 \cdot \mathsf{P}_h^T \boldsymbol{e}_2 = 0 & \text{if } X_2 = 0 \text{ or } X_2 = \pi, \\ \mathsf{P}_h^T \boldsymbol{e}_1 = \boldsymbol{0} & \text{if } X_1 = 1; \end{cases} \tag{4.71}$$

where $\boldsymbol{u}_h$ is the discretized displacement field and P_h the discretized first Piola–Kirchhoff stress tensor.

The problem is solved by using an iterative Newton–Raphson method whilst adaptively incrementing the control parameter α. The code automatically adjusts the increment of this parameter either near the marginal stability threshold or when the Newton method does not converge.

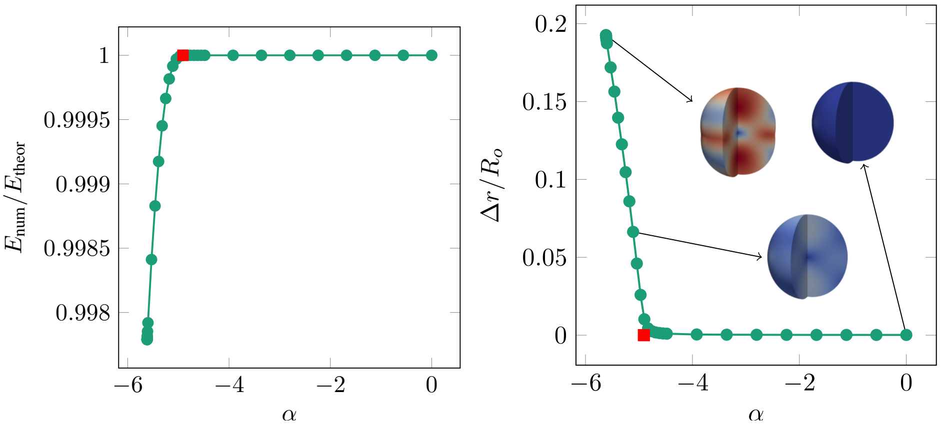

Figure 4.19: Plots of the ratio $E_{\text{num}}/E_{\text{theor}}$ (left) and the normalized buckling amplitude $\Delta r/R_o$ (right) versus the control parameter α. The numerical results are in good agreement with the theoretical instability threshold $\alpha_{cr} = -4.9084$ (red square marker).

Each step of the Newton–Raphson method is performed using PETSc as a linear algebra back-end and then the linear system is solved through an LU decomposition.

4.2.3.2 *Results of the finite element simulations*

CASE (A): EXPONENTIAL POLYNOMIAL CASE We first show the results for the case in which $f(R)$ is given by Eq. (4.44). We denote by E_{num} the total strain energy of the deformed material, and by E_{theor} the theoretically computed strain energy of the undeformed sphere, namely in the reference configuration. We remark that the strain energy density in the undeformed reference configuration may not be zero. Indeed, setting $\mathsf{F} = \mathsf{I}$ in (4.42), it is easy to check that the energy density vanishes only if $\Sigma = 0$. Thus, the presence of pre–stresses is physically related to the fact that some mechanical energy is already stored inside the material.

In Fig. 4.19 (left) we plot the ratio between E_{num} and E_{theor} vs. α when $\beta = 1.1$; the mode of the imperfection applied on the mesh is the critical one $m_{\text{cr}} = 2$, we also computed the amplitude of the pattern, defined as

$$\Delta r := \max_{\Theta \in [0,\pi]} r_h(R_o, \Theta) - \min_{\Theta \in [0,\pi]} r_h(R_o, \Theta),$$

where r_h is the discretized deformation field in the radial direction (Fig. 4.19 (right)). We observe that there is a smooth increase of such an amplitude when the control parameter is lower than α_{cr}. When performing a cyclic variation of the control parameter, decreasing α first and then increasing it to zero, both the amplitude of the wrinkling and the energy ratio do not encounter any discontinuity and they both follow the same curve in both directions.

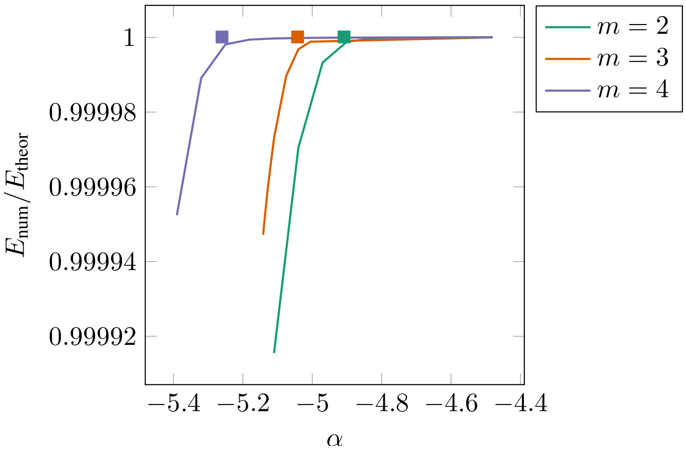

Figure 4.20: Comparison between the ratios $E_{\mathrm{num}}/E_{\mathrm{theor}}$ vs. the wavenumber m. The squares denote the thresholds α_m computed in the previous Section.

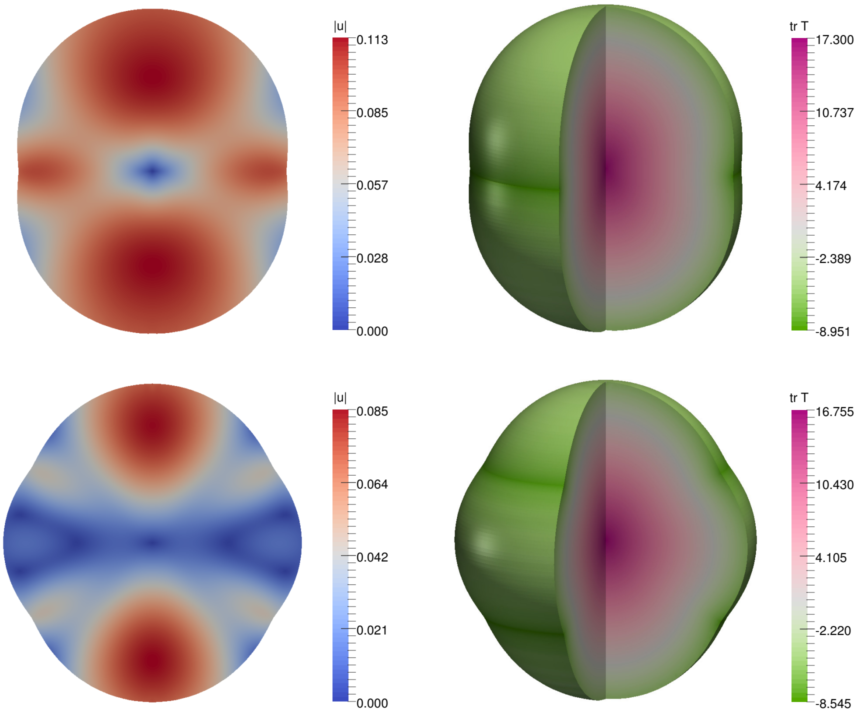

Figure 4.21: Plot of the deformed configuration when $f(R)$ is given by Eq. (4.44), $\beta = 1.1$, $\alpha = -5.62$ and $m = m_{\mathrm{cr}} = 2$ (top); $\alpha = -5.55$ and $m = 4$ (bottom). The color bars indicate the norm of the displacement $\|\boldsymbol{u}_h\|$ (left) and the trace of the Cauchy stress tensor normalized with respect to the shear modulus μ (right). On the right we depict a 3D representation of the deformed sphere.

Since α_{cr} is very close to the other values α_m, in Fig. 4.20 we compare the energy ratio also for the cases in which the wavenumber of the imperfection is

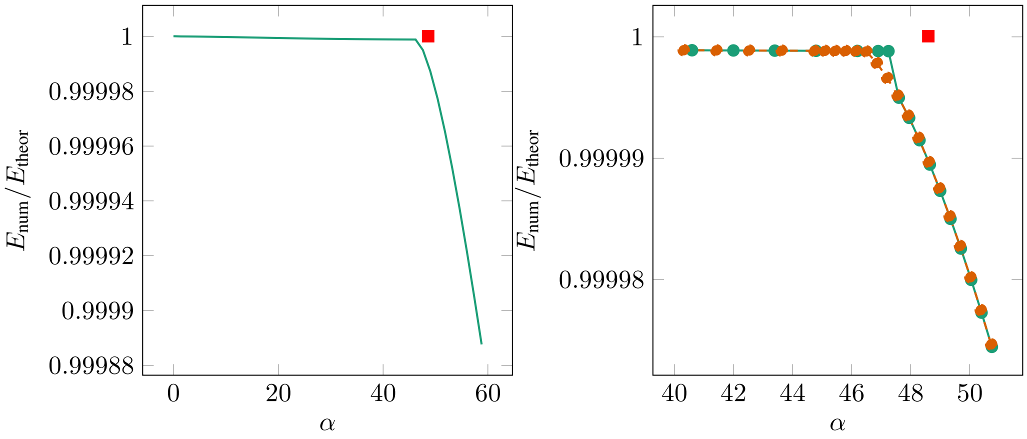

Figure 4.22: Ratio between $E_{\mathrm{num}}/E_{\mathrm{theor}}$ versus the control parameter α(Left) when $f(R)$ is given by Eq. (4.45) for $\gamma = 1.1$ and $m = m_{cr} = 2$. We performed a cyclic variation of the control parameter α (right), first increasing it beyond the linear stability threshold (green solid line) and then decreasing it down to the initial value (orange dashed line). In both plots, the red squares denote the threshold $\alpha_2 = 48.60$ computed in the previous Section.

not the critical one, specifically $m = 3$ and $m = 4$. We can observe that there is a continuous decrease of such a ratio when the threshold α_m is reached. From the picture we can also notice that there is no intersection of the curves that represent the ratio of the energies, thus suggesting the absence of secondary bifurcations.

Setting $\beta = 1.1$, in Fig. 4.21 we depict the deformed configuration of the sphere when $\alpha = -5.62$, when $m = m_{\mathrm{cr}} = 2$ (top) and $\alpha = -5.55$ when $m = 4$ (bottom), with the color bar we indicate the norm of the displacement $\|\boldsymbol{u}_h\|$ (left) and the trace of the Cauchy stress tensor T_h normalized with respect to the shear modulus μ (right).

CASE (B): LOGARITHMIC CASE We performed the same numerical procedure for simulating the logarithmic case.

We considered the case in which α is positive. From the linear stability analysis we expect that the instability is localized in the interior part of the sphere (Fig. 4.17).

Let $\gamma = 1.1$, in Fig. 4.22 we plot the ratio $E_{\mathrm{num}}/E_{\mathrm{theor}}$ at varying α. We performed a cyclic variation of the control parameter α, first increasing it and then decreasing it down to zero Fig. 4.22 (right). We highlight the presence of both a jump across the linear threshold and hysteresis, thus highlighting the presence of a subcritical bifurcation. The linear stability threshold is in good agreement with the theoretical prediction, given that subcritical bifurcations have a higher sensitivity to imperfection than supercritical ones.

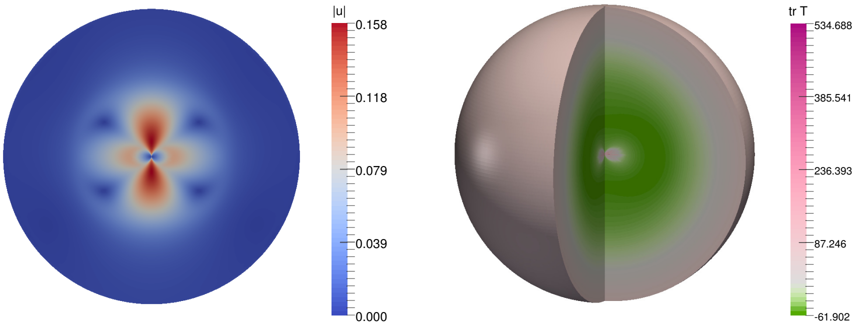

Figure 4.23: Plot of the deformed configuration when $f(R)$ is given by Eq. (4.45), $\gamma = 1.1$, $\alpha = 58.8$ and $m = m_{\mathrm{cr}} = 2$. The color bars indicate the norm of the displacement $\|\boldsymbol{u}_h\|$ (left) and the trace of the Cauchy stress tensor (right). On the right we depict a 3D representation of the deformed sphere.

In Fig. 4.23 we show the deformed configuration of the sphere when $\alpha = 58.8$ for $\gamma = 1.1$, where the color bars indicate the norm of the displacement $\|\boldsymbol{u}_h\|$ and the trace the Cauchy stress tensor T_h normalized with respect to the shear modulus μ.

We remark that we obtain small numerical oscillations of the displacement field near the center of the sphere in the fully nonlinear post-buckling regime. These errors eventually get amplified during the computation of the stress field, and the numerical solution no longer converges. In some cases, we observed that the Newton method failed to converge for some different values of the parameter γ when α is just beyond the marginal stability threshold α_{cr}. The improvement of the numerical continuation method is outside the scope of this work, but we acknowledge that a different approach, e.g. using scalable iterative solvers and preconditioners [83], could improve the stability of the numerical solution in the post-buckling regime.

4.2.4 Discussion and concluding remarks

This Section investigated the morphological stability of a soft elastic sphere subjected to residual stresses.

In the first part, we modeled the sphere as a hyperelastic material by introducing a strain energy depending explicitly on the deformation gradient and on the initial stress [97, 98]. In this way, we can avoid the classical deformation gradient decomposition [181] which has the drawback of requiring the a priori knowledge of a virtual relaxed state.

Secondly, we described the residual stress fields by using a function $f(R)$ that denotes the radial component of the residual stress. This function depends on the dimensionless parameters α, β and γ, where α is the normalized intensity of the residual stress whereas β and γ describe the spatial distribution of the residual stress components within the sphere.

We investigate two possible distributions of the radial residual stress $f(R)$, one based on a polynomial function, the other on a logarithmic one. We denote these two choices as case (a) and (b) respectively.

We performed the linear stability analysis in both cases by using the theory of incremental deformations superposed on the undeformed, pre-stressed configuration. In order to solve the incremental boundary value problem, we used the Stroh formulation and the surface impedance matrix method to transform it into the differential Riccati equation given by Eq. (4.59) [154] .

We integrated numerically the resulting incremental initial value problem by iterating the control parameter until a stop condition is reached, in order to find the marginal stability thresholds. We found out that the morphological transition occurs in the region where the hoop residual stress reaches its maximum magnitude in compression.

In the case (a) we find an instability only for $\alpha < 0$, whilst in case (b) we find an instability for both α positive and negative. In this latter case, when α is positive the instability occurs in the inner region of the sphere whereas if α is negative it is localized in the external region. The results of such analysis are reported in Figures 4.12-4.17.

Finally, we implemented a numerical procedure by using the mixed finite element method in order to approximate the fully non-linear problem. After the validation of the numerical simulations obtained by the comparison with the results of the linear stability analysis, we analyzed the resulting morphology in the fully non-linear regime.

In the case (a), the instability is localized in the external part of the sphere where the hoop residual stress is compressive. The continuous transition from the initial configuration to the buckled state indicates that the bifurcation is supercritical.

In the case (b), the instability is localized near the center of the sphere when the parameter $\alpha > 0$. In contrast to the previous case, the bifurcation is found to be subcritical, thus suffering a jump across the linear stability threshold. The results of these simulations are reported in Figures 4.19-4.23.

Future efforts will be directed to improve the proposed analysis either by implementing of a fully 3D numerical model in order to study the secondary bifurcation that might appear in the azimuthal direction or by accounting for the presence of material anisotropy, a major determinant for the residual stress distribution in living matter, e.g. tumor spheroids [72].

In summary, this Section proposes a novel approach that may provide useful guidelines for engineering applications. For example, it may be of interest for achieving a nondestructive determination of the pre–stresses in soft spheres. Whilst the currently used method consists in cutting the material and inferring the residual stresses through the resulting deformation [198], the proposed model explicitly correlates both the mechanical response of the material and its morphology with the underlying distribution of pre-stresses. Moreover, the proposed static analysis based on the Stroh formulation can be easily adapted to solve the corresponding elasto–dynamic problem in a solid sphere [154, 59]. Thus, we will derive the dispersion curves governing the propagation of time-harmonic spherical waves of small amplitude as a function of the residual stress components. This theoretical prediction will be used to feed a nonlinear inverse analysis for determining the pre–stress distribution using elastic waves, e.g. by ultrasound elastography [137, 132].

Furthermore, our results may provide useful insights for designing mechanical meta-materials with adaptive morphology. Indeed, it would be possible to fabricate soft spheres in which the magnitude of the pre-stresses can be controlled by external stimuli, such as voltage in dielectic elastomers [38] or solvent concentration in soft gels [205]. Digital fabrication techniques offer a low cost alternative for printing materials with a targeted distribution of residual stresses [219]. Thus, morphable spheres can be obtained by modulating the residual stresses around the critical value of marginal stability. Dealing with pre–stressed neo-Hookean materials, the results of this Section are particularly relevant for controlling the transient wrinkles that form and then vanish during the drying and swelling of hydrogels [135, 27]. Other applications range from adaptive drag reduction [204] to the pattern fabrication on spherical surfaces [196, 39].

4.3 RAYLEIGH–TAYLOR INSTABILITY IN SOFT ELASTIC LAYERS

The study of pattern formation in soft solids has highlighted some similarities, yet several relevant differences, with the instability characteristics of hydrodynamic systems, although their boundary value problems are intrinsically different. For example, if the surface tension in a thin fluid filament triggers the formation of droplets, which spontaneously break down [171], such a dynamics can be stabilised by elastic effects in soft solid cylinders [145], thus driving the emergence of stable beads-on-a-string patterns [201]. Similarly, whilst fingering at the interface of two immiscible viscous fluids is an unstable process [185], stable digitations may occur after a subcritical bifurcation for a fluid pushing against an elastic surface [187] and at the interface between a thin elastic layer adhering to a glass plate [92]. A compressible hyperelastic tube subjected to a circular shear can exhibit bifurcations reminescent to the classical Taylor-Couette patterns appearing in the motion of viscous fluids [88].

Another interesting example is the gravity-induced instability in an elastic layer attached to a rigid substrate with a traction-free surface facing downwards. Contrarily to gravity waves in a fluid layer, the free surface experiences fluctuations that eventually saturate when the large deformations store an elastic free energy of the same order as the corresponding variation of the potential energy. Piriz et al. studied the problem for a linear elastic material [166]. The linear stability analysis of this problem for a nonlinear elastic solid has been recently performed [146], then refined to consider the effect of an applied strain on the elastic layer [133]. Nonetheless, this problem had been previously solved using numerical techniques [18], often being used as a test case to study the stability of discrete solutions, obtained by means of mixed finite element techniques [16, 17]. More recently, also the weakly non-linear and the 3D numerical post-buckling analysis have been performed [49].

Since Rayleigh [172] and Taylor [203], it is well known that the horizontal interface between one fluid layer put on top of a lighter one is unstable to perturbation of long wavelength, i.e. bigger than the capillary length, forming protrusions growing with a characteristic time. However, if one takes surface tension into account, the growth of small wavelength protrusions is inhibited by capillary effects, thus larger wavelength drops grow and eventually drip [84]. In Chapter 4.3, we aim at studying this kind of gravity instability in a soft system made of two heavy elastic layers attached on one end to a rigid surface. In particular, we are interested in characterizing both pattern formation and its nonlinear evolution, determining the interplay between elastic and geometric effects for the emergence of a given pattern.

4.3.1 The non-linear elastic problem and its basic solution

In a Cartesian coordinate system with unit base vectors $\boldsymbol{E}_i$, with $i = (X, Y, Z)$, we consider a soft body made of two hyperelastic layers, as sketched in Figure 4.24.

Let $\mathbb{E}^3$ be the three-dimensional Euclidean space, the body occupies a domain $\Omega \subset \mathbb{E}^3$, having a thickness H along the Y axis and a length L along the X axis, with $L \gg H$. We also consider that the body is infinitely long along the Z direction, so that a plane strain assumption can be made, hence

$$\Omega = (0,\, L) \times (0,\, H) \times \mathbb{R}.$$

The body is clamped to a rigid substrate at $Y = 0$, so that its volume Ω can be split in the two subdomains Ω_a and Ω_b occupied by the constituting layers, such that:

$$\begin{aligned} \Omega_a &= \{\boldsymbol{X} \in \Omega \mid 0 < Y < H_a\}\,, \\ \Omega_b &= \{\boldsymbol{X} \in \Omega \mid H_a < Y < H\}\,, \end{aligned}$$

where $\boldsymbol{X}$ is the material position vector, H_a and H_b are the thicknesses of the layers.

Indicating $\boldsymbol{x} = \boldsymbol{x}(X, Y)$ the spatial position vector, the kinematics is described by the geometrical deformation tensor $\mathsf{F} = \operatorname{Grad} \boldsymbol{x}$. We also assume that the layers behave as incompressible neo-Hookean materials and the strain energy density of each layer is given by

$$W_\beta(\mathsf{F}) = \frac{\mu_\beta}{2}(I_1 - 2) - p(\det \mathsf{F} - 1), \qquad \beta = (a,\, b); \tag{4.72}$$

where I_1 is the trace of the right Cauchy–Green tensor $\mathsf{C} = \mathsf{F}^T\mathsf{F}$ and p is the Lagrangian multiplier enforcing the internal constraint of incompressibility.

Using the constitutive assumption in Eq. (4.72), the first Piola-Kirchhoff stress tensor P reads:

$$\mathsf{P}_\beta = \frac{\partial W_\beta}{\partial \mathsf{F}} = \mu_\beta \mathsf{F}^T - p\mathsf{F}^{-1}, \qquad \beta = (a,\, b).$$

Assuming quasi-static conditions, the balance of linear momentum for the elastic body subjected to its own weight reads:

$$\mathrm{Div}\, \mathsf{P}_\beta + \rho_\beta \boldsymbol{g} = 0 \qquad \text{in } \Omega_\beta, \quad \text{where } \beta = (a,\, b); \tag{4.73}$$

where Div is the material divergence, ρ_a and ρ_b are the densities of the layers, $\boldsymbol{g} = g\boldsymbol{E}_Y$, is the gravity acceleration vector.

In the following we aim to provide a unified analysis of the two configurations depicted in Figure 4.24. For the sake of notational compactness, we consider that a positive g represents the body hanging down a rigid wall (Figure 4.24a), and a negative g the body placed on top of a rigid substrate (Figure 4.24b).

The two boundary conditions at the fixed substrate and at the free surface read

$$\begin{cases} \mathsf{P}_b^T \boldsymbol{E}_Y = \boldsymbol{0} & \text{for } Y = H, \\ \boldsymbol{E}_Y \cdot \mathsf{P}_\beta^T \boldsymbol{E}_X = 0 & \text{for } X = (0,\, L), \beta = (a,\, b) \\ \boldsymbol{u} = \boldsymbol{0} & \text{for } Y = 0, \\ \boldsymbol{u} \cdot \boldsymbol{E}_X = 0 & \text{for } X = (0,\, L); \end{cases} \tag{4.74}$$

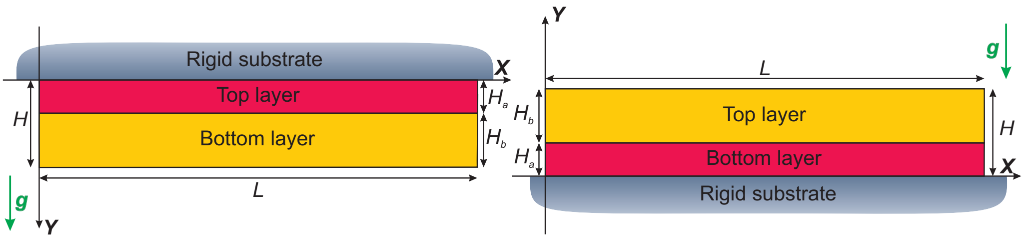

(a) $g > 0$ (b) $g < 0$

Figure 4.24: Sketch of the material setting in two different configurations. Case (a): the body hangs below on a fixed rigid wall, thus being subjected to a tensile gravity force along Y (left). Case (b): the body is placed on top of a rigid substrate, thus being subjected to a compressive gravity force along Y (right).

where $\boldsymbol{u} = (\boldsymbol{x} - \boldsymbol{X})$ is the displacement vector field. The elastic boundary value problem is finally complemented by the following displacement and stress continuity conditions at the interface between the two layers, respectively

$$\begin{cases} \lim\limits_{Y \to H_a^-} \boldsymbol{u} = \lim\limits_{Y \to H_a^+} \boldsymbol{u}, \\ \lim\limits_{Y \to H_a^-} \mathsf{P}_a^T \boldsymbol{E}_Y = \lim\limits_{Y \to H_a^+} \mathsf{P}_b^T \boldsymbol{E}_Y. \end{cases} \tag{4.75}$$

The boundary value problem Eqs. (4.73)–(4.75) admits a basic solution given by

$$\boldsymbol{u} = \boldsymbol{0}, \qquad p = \begin{cases} \mu_a + \rho_a g(Y - H_a) - \rho_b g H_b & \text{for } 0 < Y < H_a, \\ \mu_b + \rho_b g(Y - H) & \text{for } H_a < Y < H; \end{cases} \tag{4.76}$$

so that no basic deformation is allowed by the incompressibility constraint, and the body is subjected to a hydrostatic pressure linearly dependent on Y. We also highlight that the pressure field in Eq. (4.76) is discontinuous if $\mu_a \neq \mu_b$ or $\rho_a \neq \rho_b$.

4.3.2 Linear stability analysis of the basic solution

4.3.2.1 *Incremental equations*

We now aim at investigating the stability of the basic elastic solution Eq. (4.76) using the method of incremental deformations superposed on a finite strain [156].

Let us perturb the basic configuration by applying an incremental displacement $\delta\boldsymbol{u}$, if we set $\delta\mathsf{F} = \operatorname{Grad}\delta\boldsymbol{u}$, the linearised incremental Piola-Kirchhoff stress tensor is

$$\delta\mathsf{P}_\beta = \mathcal{A}_0^\beta : \delta\mathsf{F} + p\,\delta\mathsf{F} - \delta p\,\mathsf{I} \quad \text{for } \beta = (a, b);$$

where

$$\mathcal{A}_0^\beta = \frac{\partial^2 W_\beta}{\partial\mathsf{F}\partial\mathsf{F}}; \quad \text{with} \quad \mathcal{A}_{0ijhk}^\beta = \frac{\partial^2 W_\beta}{\partial F_{ji}\partial F_{kh}}$$

is the tensor of instantaneous elastic moduli, I is the identity tensor, δp is the increment of the Lagrangian multiplier p and the two dots operator (:) denotes the double contraction of the indices, namely

$$(\mathcal{A}_0^\beta : \delta\mathsf{F})_{ij} = \mathcal{A}_{0ijhk}^\beta \delta F_{kh}.$$

Recalling that the basic solution is undeformed, the incremental incompressibility and equilibrium equations read, respectively

$$\operatorname{Div}\delta\mathsf{P}_\beta = \boldsymbol{0} \quad \text{in } \Omega_\beta, \text{ with } \beta = (a, b), \tag{4.77}$$

$$\operatorname{Div}\delta\boldsymbol{u} = 0 \qquad \text{in } \Omega. \tag{4.78}$$

The incremental counterparts of two boundary conditions at the fixed substrate and at the free surface may be rewritten as, respectively

$$\begin{cases} \delta \mathsf{P}_b^T \boldsymbol{E}_Y = \boldsymbol{0} & \text{for } Y = H, \quad (4.79) \\ \boldsymbol{E}_Y \cdot \delta \mathsf{P}_\beta^T \boldsymbol{E}_X = \boldsymbol{0} & \text{for } X = (0,\, L),\ \beta = (a,\, b), \quad (4.80) \\ \delta \boldsymbol{u} = \boldsymbol{0} & \text{for } Y = 0, \quad (4.81) \\ \delta \boldsymbol{u} \cdot \boldsymbol{E}_X = 0 & \text{for } X = (0,\, L). \quad (4.82) \end{cases}$$

Similarly, the incremental versions of the displacement and stress continuity conditions at the interface read:

$$\begin{cases} \lim\limits_{Y \to H_a^-} \delta \boldsymbol{u} = \lim\limits_{Y \to H_a^+} \delta \boldsymbol{u}, & (4.83) \\ \lim\limits_{Y \to H_a^-} \delta \mathsf{P}_a^T \boldsymbol{E}_Y = \lim\limits_{Y \to H_a^+} \delta \mathsf{P}_b^T \boldsymbol{E}_Y. & (4.84) \end{cases}$$

In the following, we derive the solution of the incremental boundary value problem given by Eqs. (4.77)-(4.84).

4.3.2.2 *Solution of the incremental boundary value problem*

Let us now assume an ansatz by variable separation in the expression of the incremental displacement, namely

$$\delta \boldsymbol{u} = U(Y) \sin(kX) \boldsymbol{E}_X + V(Y) \cos(kX) \boldsymbol{E}_Y, \tag{4.85}$$

where k is the horizontal spatial wavenumber. We recall that such a functional dependence along the X direction suitably describes both the infinite geometry, for which k is a continuous variable, and a finite length L, so that $k = 2\pi n / L$ with integer mode n.

From Eq. (4.78) we get that

$$kU(Y) = -V'(Y). \tag{4.86}$$

From the first component of Eq. (4.77) we obtain the expression for δp as

$$\delta p = \cos(kX) \left(\rho_\beta g V(Y) - \mu_\beta V'(Y) + k^{-2} \mu_\beta V'''(Y) \right) \quad \text{in } \Omega_\beta \text{ with } \beta = (a,\, b). \tag{4.87}$$

By substituting Eqs. (4.86) and (4.87) in the second component of Eq. (4.77), we obtain the following ordinary differential equation:

$$V''''(Y) - 2k^2 V''(Y) + k^4 V(Y) = 0, \tag{4.88}$$

which is valid for both layers and whose solution is given by:

$$V(Y) = C_{1\beta} e^{-kY} + C_{2\beta} Y e^{-kY} + C_{3\beta} e^{kY} + C_{4\beta} Y e^{kY} \quad \text{in } \Omega_\beta,\ \beta = (a,\, b). \tag{4.89}$$

Hence, setting

$$v = \left[\frac{C_{1a}}{H_a}, C_{2a}, \frac{C_{3a}}{H_a}, C_{4a}, \frac{C_{1b}}{H_a}, C_{2b}, e^{2kH_a}\frac{C_{3b}}{H_a}, e^{2kH_a}C_{4b}\right]^T$$

we impose the conditions given in Eqs. (4.79)–(4.84), we find 8 linear algebraic equations in the unknowns v_j, $j = (1, \dots, 8)$, so that we can write such system in the compact form $\mathsf{M}v = \mathbf{0}$ where M is the 8×8 coefficients' matrix. Hence, we find that a non-null solution of such linear system exists if and only if

$$\det \mathsf{M} = 0; \tag{4.90}$$

The full form of M is reported in the Appendix 4.3.5.

4.3.2.3 *Results of the linear stability analysis*

Let us now discuss the results of the linear stability analysis by making use of the following dimensionless parameters:

$$\gamma = \frac{\rho_a g H_a}{\mu_a}, \qquad \alpha_H = \frac{H_b}{H_a}, \qquad \alpha_\mu = \frac{\mu_b}{\mu_a}, \qquad \alpha_\rho = \frac{\rho_b}{\rho_a}, \qquad \tilde{k} = H_a k.$$

A great simplification arises if we set both $\alpha_\rho = 1$ and $\alpha_\mu = 1$ or if we impose $\alpha_H = 0$ in Eq. (4.90), so that the body is made of a single homogeneous slab. In particular, we recover the same expression reported in [146]:

$$\frac{\rho g H}{\mu_a} = \frac{2kH\left(2\,(kH)^2 + \cosh(2kH) + 1\right)}{\sinh(2kH) - 2kH};$$

highlighting that an elastic bifurcation occurs for the critical value $\frac{\rho g H}{\mu_a} \simeq 6.22$ with critical wavenumber $kH \simeq 2.11$.

Let us now analyse the resulting solutions when $\alpha_\rho = 1$, namely assuming that the body force is the same for both layers. In the case in which $\alpha_\mu \neq 1$ or $\alpha_H \neq 1$, we find only one root of equation Eq. (4.90). In Figure 4.25 we depict the resulting marginal stability curves varying the parameters α_μ and α_H.

We denote by γ_{cr} the critical value of γ, i.e. the minimum value of the marginal stability curve obtained fixing α_H and α_μ. We denote by $\tilde{k}_{cr}$ the critical wavenumber, namely the value of $\tilde{k}$ for which the marginal stability curve has a minimum. All the critical values of the marginal stability curves have been found by using the Newton's method with the software *Mathematica* 11.0 (Wolfram Research,Champaign,IL, USA).

In Figure 4.26 we plot the critical values γ_{cr} and $\tilde{k}_{cr}$ when varying α_H and α_μ. We find that γ_{cr} strongly depends on α_μ and α_H. In Figure 4.26a we find that if we increase the parameter α_μ the critical value γ_{cr} also increases, so that high values of α_μ have a stabilizing effect. On the contrary, in Figure 4.26c we find that if we increase α_H the critical value γ_{cr} decreases. We highlight that, if α_H

tends to zero we obtain that $\gamma_{cr} \simeq 6.22$, which is the single layer limit discussed

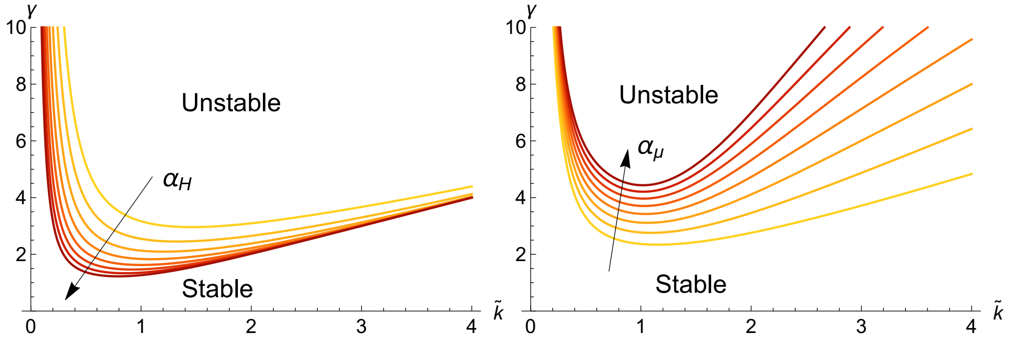

(a) $\alpha_\mu = 0.5$ **(b)** $\alpha_H = 1$

Figure 4.25: Marginal stability curves showing the order parameter γ versus the horizontal wavenumber $\tilde{k}$ for $\rho_a = \rho_b$ and: (a) $\alpha_\mu = 0.5$, (b) $\alpha_H = 1$. The curves are shown at varying α_H (a) and α_μ (b) from 0.6 to 2 by steps of 0.2, the arrow indicates the direction in which the parameter grows.

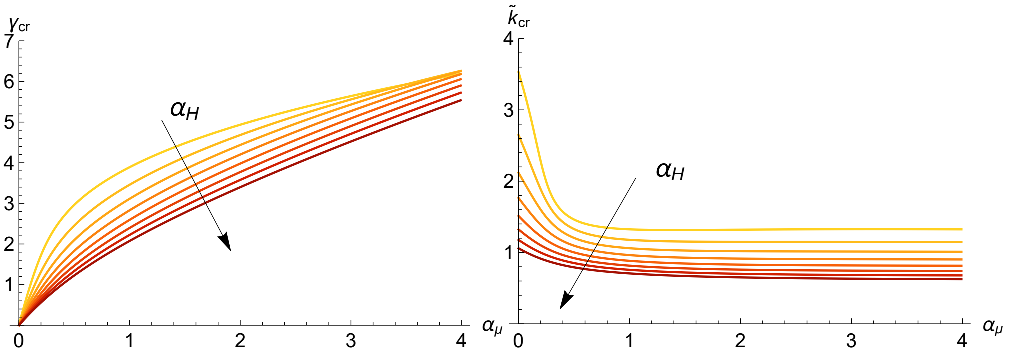

(a) γ_{cr} vs α_μ **(b)** k_{cr} vs α_μ

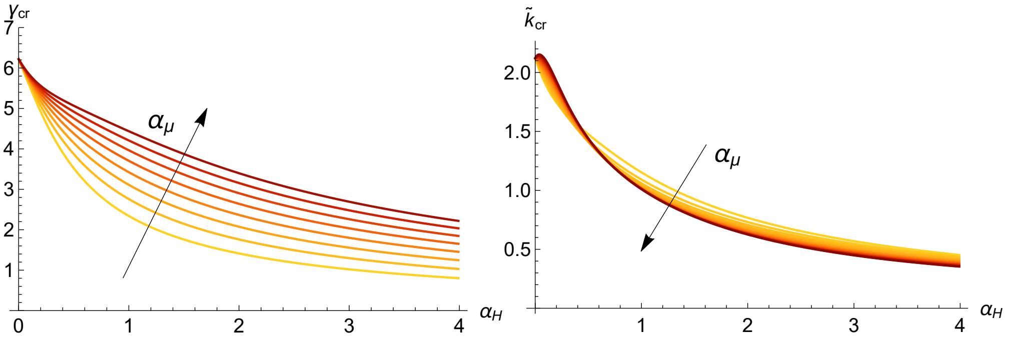

(c) γ_{cr} vs α_H **(d)** k_{cr} vs α_H

Figure 4.26: Plot of the critical values of (a) γ_{cr} versus α_μ at varying α_H; (b) γ_{cr} versus α_H at varying α_μ; (c) $\tilde{k}_{cr}$ versus α_μ at varying α_H; (d) $\tilde{k}_{cr}$ versus α_H at varying α_μ. The arrows indicate the direction in which the parameters α_H (a,b) and α_μ (c,d) grow from 0.6 to 2 by steps of 0.2.

before. The same limit is found for α_μ tending to zero, since it represents the case in which the bottom layer in Figure 4.24a becomes infinitely soft. The critical wavelength is always of the same order of the body thickness, resulting to be more influenced by the parameter α_H if $\alpha_\mu > 1$, as we can notice from Figures 4.26b and 4.26d.

The case in which $\alpha_\rho = 1$ is of particular interest in the applications because it is reproducible in experiments using hydrogels. In fact, these soft materials are mainly composed of water, thus having a density which is of the order of 10^3 kg/m^3. Nonetheless, by small variation of the crosslink concentration, it is possible to obtain a shear modulus μ ranging from 100 Pa to 10 kPa. For example, if we consider two hydrogel layers with $H_a = H_b$ (Figure 4.25b), where the clamped one has $\mu_a = 300$ Pa and the other $\mu_b = 600$ Pa, we find that $\gamma_{cr} \simeq 4.4366$. Accordingly, an instability would appear at $H_a \geq \mu_a \gamma_{cr}/(\rho g) \simeq$ 13.57 cm.

The general case in which $\alpha_\rho \neq 1$ is a bit more complex, in fact Eq. (4.90) can be written in the following compact form

$$c_1\gamma^2 + c_2\gamma + c_3 = 0 \tag{4.91}$$

where the coefficients c_1, c_2 and c_3 depend on α_H, α_μ, α_ρ and $\tilde{k}$, as reported in the Appendix 4.3.6.

Even if their expressions are very cumbersome, we can still make some general observations. In fact we observe that c_1 does not depend on α_ρ whereas, if we fix the other variables, c_3 has a different sign if $\alpha_\rho > 1$ or if $0 < \alpha_\rho < 1$. Hence, one of the two real roots of Eq. (4.91) changes sign if we consider $\alpha_\rho > 1$ or $0 < \alpha_\rho < 1$.

Thus, we make a distinction in the following between these two cases, which physically correspond to the two configurations depicted in Figure 4.24.

CASE (A): FREE SURFACE INSTABILITY ($\gamma > 0$) The configuration shown in Figure 4.24a undergoes a morphological transition if Eq. (4.91) possesses at least a positive root for γ, since we assume $g > 0$.

In Figures 4.27 and 4.28 we depict the marginal stability curves $\gamma(\tilde{k})$ when we vary the parameters α_H, α_ρ and α_μ in Eq. (4.91). In this case, we find that the instability is localised at the free boundary of the slab, i.e. at $Y = H$.

We can observe that we have the same behaviour discussed for the case $\alpha_\rho =$ 1: if we increase the parameter α_μ we obtain a stabilization of the system (i.e. γ_{cr} increases) whereas if we decrease α_H we have instability for lower values of γ.

CASE (B): INTERFACIAL INSTABILITY ($\gamma < 0$) Conversely, the configuration shown in Figure 4.24b undergoes a morphological transition if Eq. (4.91) possesses a negative root for γ, since we assume $g < 0$. As previously discussed, this happens only if $\alpha_\rho > 1$, meaning that the top layer is heavier than the bottom one. Thus, this case is the elastic analog of the Rayleigh-Taylor instability.

As found in fluids, the instability is concentrated at the interface between the layers and decays away from it.

In this configuration, we define the critical value γ_{cr} as the maximum of the marginal stability curve $\gamma(\tilde{k})$ for fixed α_H, α_μ, and α_ρ.

In Figure 4.29 we set $\alpha_\rho = 2$ and we plot the marginal stability curves for several values of the parameters α_H and α_μ. Also in this case we highlight that increasing the parameter α_μ stabilizes the system, whereas an increase of the parameter α_H favours the onset of the interfacial instability.

In the next Section, based on the results of the linear stability analysis, we build the simulation tools for studying the fully nonlinear morphological transition.

4.3.3 Post-buckling analysis

In this Section we numerically implement the fully non-linear problem given by Eqs. (4.73)-(4.75). We finally report the results of numerical simulations for the two cases under considerations, highlighting the morphological evolution of the emerging patterns in the fully nonlinear regime.

4.3.3.1 *Finite element implementation*

The boundary value problem is implemented by using the open source tool for solving partial differential equations FEniCS [134]. In order to enforce the incompressibility constraint, a mixed formulation has been chosen. If the two layers have different stiffness or mass density, the pressure field may present a discontinuity at the interface between the two layers, according to the basic

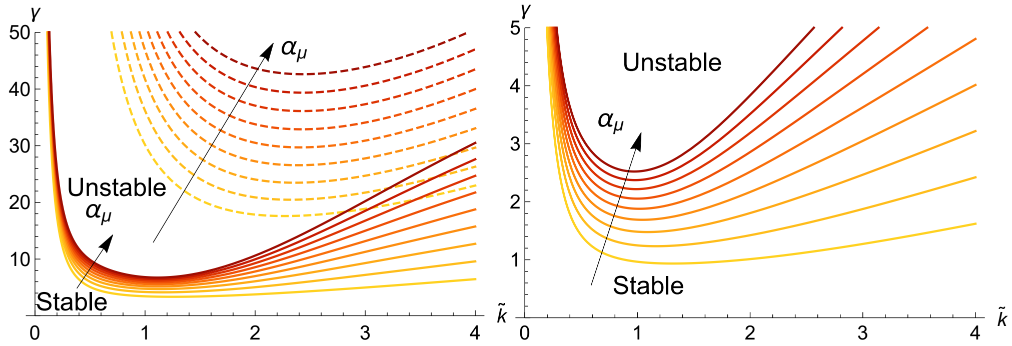

(a) $\alpha_H = 1, \alpha_\rho = 0.5$ **(b)** $\alpha_H = 1, \alpha_\rho = 2$

Figure 4.27: Marginal stability curves showing the order parameter γ versus the horizontal wavenumber $\tilde{k}$ for $\alpha_H = 1$ and: (a) $\alpha_\rho = 0.5$, (b) $\alpha_\rho = 2$ where α_μ varies from 0.4 to 2 by steps of 0.2. In (a) we find two positive solutions (solid and dashed lines) of equation Eq. (4.91) whereas in Figure (b) we only find one positive solution.

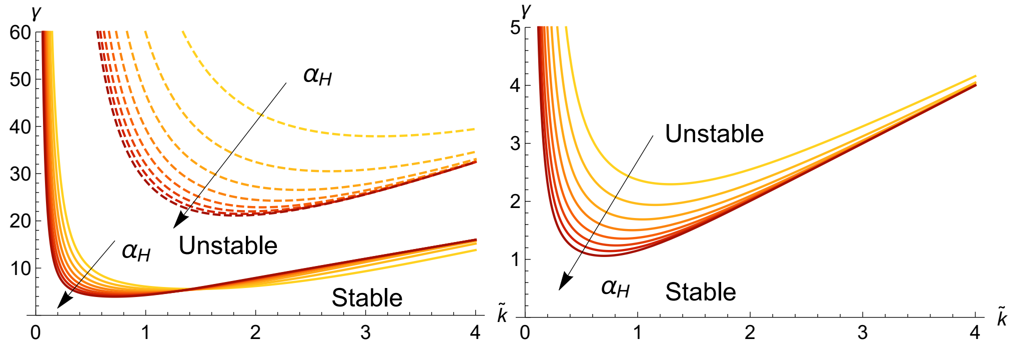

(a) $\alpha_\mu = 1$, $\alpha_\rho = 0.5$ **(b)** $\alpha_\mu = 1$, $\alpha_\rho = 2$

Figure 4.28: Marginal stability curves showing the order parameter γ versus the horizontal wavenumber $\tilde{k}$ for $\alpha_\mu = 1$ and: (a) $\alpha_\rho = 0.5$, (b) $\alpha_\rho = 2$ with α_H varying from 0.6 to 2 by steps of 0.2. In (a) we find two positive solutions (solid and dashed lines) of equation Eq. (4.91) whereas in Figure (b) we only find one positive solution.

solution Eq. (4.76). Accordingly, we used the element P_2–P_0 [34] in numerical simulations.

This element discretizes the displacement with piecewise quadratic functions and the pressure field with piecewise constant functions, so that we can correctly account for a discontinuous pressure field. It is also numerically stable in linear elasticity [34] and it has been successfully used in several non-linear applications [16, 18].

We use a rectangular mesh whose height is $H = 1$ and whose length is the critical wavelength $\lambda = 2\pi H_a/\tilde{k}_{cr}$, where $\tilde{k}_{cr}$ is the critical value arising from the previous linear stability analysis and depending on α_ρ, α_H and α_μ. We set $\boldsymbol{u} = \boldsymbol{0}$ at $Y = 0$ and we impose periodic boundary conditions at $X = 0$ and

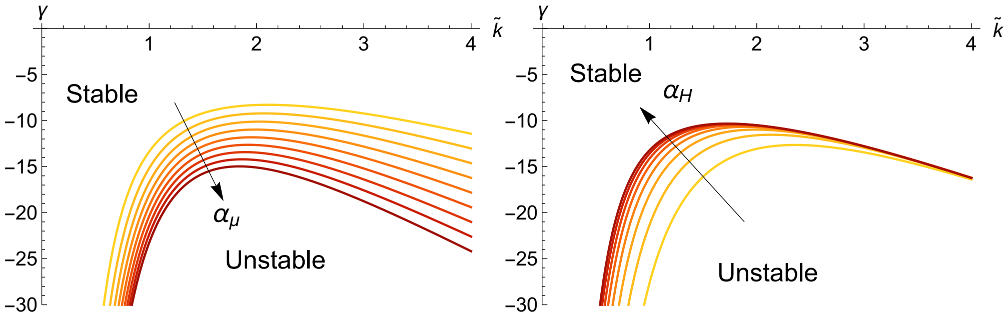

(a) $\alpha_H = 1$, $\alpha_\rho = 2$ **(b)** $\alpha_\mu = 1$, $\alpha_\rho = 2$

Figure 4.29: Marginal stability curves showing the negative root of the order parameter γ versus the horizontal wavenumber $\tilde{k}$ for $\alpha_\rho = 2$ and: (a) $\alpha_H = 1$ with α_μ varying from 0.4 to 2 by steps of 0.2; (b) $\alpha_\mu = 1$ with α_H varying from 0.6 to 2 by steps of 0.2.

$X = \lambda$. The number of elements used depends on the length of the mesh, the maximum number of elements used is 30000.

In order to investigate the post-buckling regime, we impose a sinusoidal imperfection at the top boundary of the mesh with a wavenumber k_{cr} and an amplitude $h = 10^{-4}H$ as done in [57, 60].

The solution is found by using an incremental iterative Newton–Raphson method increasing (or decreasing in the fluid analogue case) the control parameter γ. In each iteration, the calculation is performed by using the linear algebra back-end PETSc (Portable, Extensible Toolkit for Scientific Computation) and the linear system is solved through a LU (Lower-Upper) decomposition. The code automatically adjust the increment of the control parameter if γ is near the critical value γ_{cr} or when the Newton–Raphson method fails to converge.

Since secondary bifurcations may appear in such a dispersive problem, due to subharmonic resonance phenomena in the fully nonlinear regime, we performed further simulations using the approach proposed in [40]. Accordingly, we looked for period-doubling and period-tripling secondary bifurcations by using as computational domain the sets $[0, 2m\pi/k_{cr}] \times [0, 1]$ with $m = 2$ and $m = 3$, respectively. However, we did not find any further bifurcation in the parameters' range considered in the manuscript, in agreement with the experimental observations performed in the single layer case [146].

4.3.3.2 *Numerical results*

In the following, we report the results of the numerical simulation for the two cases under considerations.

CASE (A): FREE SURFACE INSTABILITY ($\gamma > 0$) We first implement the case described in Figure 4.24a, setting $\alpha_\rho = 1$ in order to mimic the behaviour of a slab made of two hydrogel layers. In Figure 4.30, we depict the results of the numerical simulations for two different values of α_μ. In particular, we highlight that the deformation is localised at the free boundary of the body, and it evolves towards the formation of stable hanging digitations. Let Δh be the maximum vertical distance of the points on the free surface whilst Δl be the horizontal distance between the points which have initial coordinates $(\lambda/4, H)$ and $(3/4\lambda, H)$, so that $\Delta l/\lambda = 0.5$ if $\gamma < \gamma_{cr}$. Thus, we employ Δh and Δl to study the nonlinear evolution of the fingers' morphology.

As shown in Figure 4.31a, we find that the fingering height Δh continuously increases as the control parameter γ goes beyond its critical value. When performing a cyclic variation of the order parameter, where we first incremented γ until a value $\gamma_{\max} > \gamma_{cr}$ and later decreased it back to the initial value, we found that both Δh and Δl did not encounter any discontinuity, always following the same curve in both directions. Moreover, in the weakly nonlinear regime Δh increases as the square root of the distance to threshold of the order parameter, thus highlighting the presence of a supercritical pitchfork bifurcation.

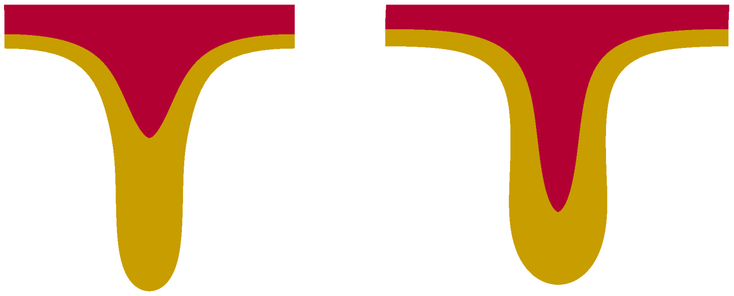

(a) $\alpha_\mu = 0.5$ **(b)** $\alpha_\mu = 2$

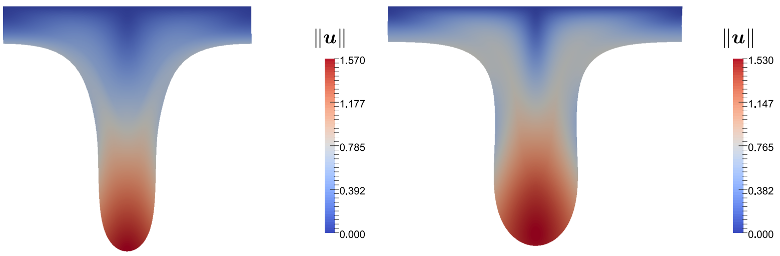

(c) $\alpha_\mu = 0.5$ **(d)** $\alpha_\mu = 2$

Figure 4.30: Resulting fingering morphology and displacement fields setting $\alpha_H = 1$, $\alpha_\rho = 1$ and (a, c) $\alpha_\mu = 0.5$ and $\gamma = 3.14$; (b, d) $\alpha_\mu = 2$ and $\gamma = 5.5$. In (c, d) the colorbars indicate the norm of the displacement.

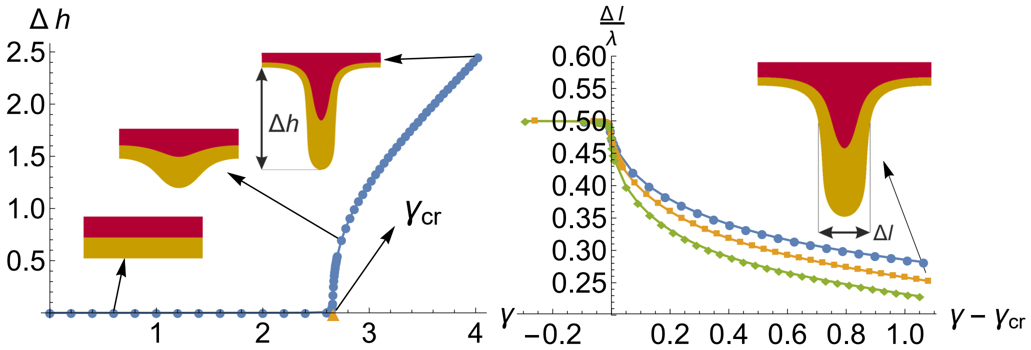

(a) Plot of Δh vs. γ **(b)** Plot of $\Delta l/\lambda$ vs. $\gamma - \gamma_{cr}$

Figure 4.31: (a) Numerical results showing the height of the fingers Δh versus the order parameter γ, setting $\alpha_\rho = 1$, $\alpha_H = 1$, $\alpha_\mu = 0.75$. The simulations validate the marginal stability threshold $\gamma_{cr} \simeq 2.66$ predicted by the linear stability analysis. (b) Plot of the normalized fingers' thickness $\Delta l/\lambda$ for $\alpha_\mu = 0.5$ (green), 0.75 (orange) and 2 (blue).

The shape and the thickness of these fingers strongly depend on the stiffness and the thickness of the two layers. As shown in Figure 4.31b, the fingers become thicker as we increase α_μ.

We remark that the maximum diameter h of the mesh elements is chosen as the maximum value such that the resulting Δh and $\Delta l/\lambda$ differ by less than 10^{-3} from the corresponding values obtained using a refined mesh with $h/2$.

CASE (B): INTERFACIAL INSTABILITY ($\gamma < 0$) We now focus on the elastic analogue of the Rayleigh Taylor instability, occurring in the configuration depicted in Figure 4.24b. Here we set $\alpha_\rho = 2$, so the top layer is heavier than the bottom one.

The simulation results are depicted in Figure 4.32 for two different values of α_H. In particular, we find a behavior similar to the Rayleigh–Taylor instability in fluids: the displacement is concentrated at the interface of the two layers forming a marginally stable undulation.

Let Δh denote here the maximum vertical distance of the points on the interface between the two layers whilst let Δl be the horizontal distance between the points which have initial coordinates $(\lambda/4, H_a)$ and $(3/4\,\lambda, H_a)$, so that $\Delta l/\lambda = 0.5$ if $\gamma > \gamma_{cr}$. In Figure 4.33, we show the nonlinear evolution of such morphological parameters as a function of γ. As in the previous case, we measured the quantity Δh decreasing the parameter γ finding a continuous increase of the height of the undulation, as reported in Figure 4.33a. We highlight that the normalized thickness $\Delta l/\lambda$ strongly depends on the parameter α_H, as we can see from Figure 4.33b.

In fact, for thin soft layers the undulation decreases its width whilst decreasing γ beyond its critical value, thus forming a digitation. Conversely, the un-

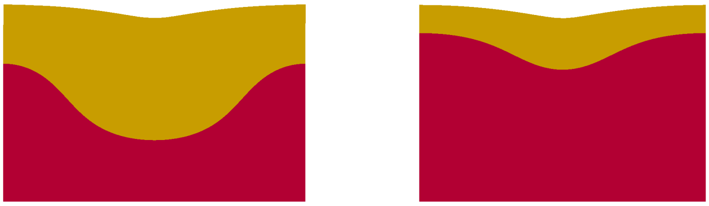

(a) $\alpha_H = 1$ (b) $\alpha_H = 0.25$

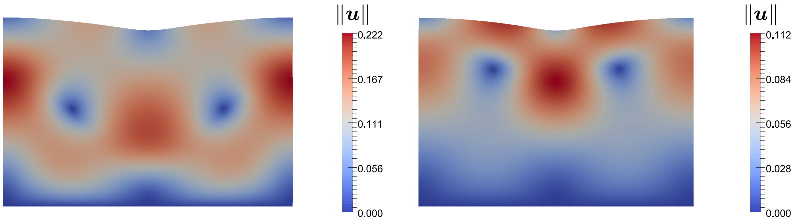

(c) $\alpha_H = 1$ (d) $\alpha_H = 0.25$

Figure 4.32: Resulting morphology and displacement fields setting $\alpha_\mu = 1$, $\alpha_\rho = 2$ and (a, c) $\alpha_H = 1$ and $\gamma = -12.36$, (b, d) $\alpha_H = 0.25$ and $\gamma = -21.12$. In (c, d) the colorbars indicate the norm of the displacement.

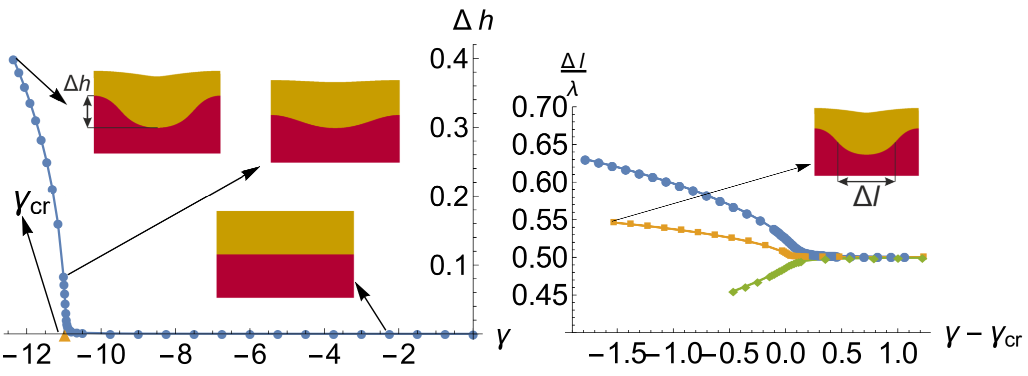

(a) Plot of Δh vs. γ

(b) Plot of $\Delta l/\lambda$ vs. $\gamma - \gamma_{cr}$

Figure 4.33: (a) Numerical results showing the height Δh of the undulation versus the order parameter γ, setting $\alpha_\rho = 2$, $\alpha_H = 1$, $\alpha_\mu = 1$. The simulations validate the marginal stability threshold $\gamma_{cr} \simeq -10.97$ predicted by the linear stability analysis. (b) Plot of the normalized undulation thickness $\Delta l/\lambda$ for $\alpha_H = 0.25$ (green), 1 (orange) and 4 (blue).

dulation width increases for thick top layers, thus forming a stable wrinkle. In summary, $\Delta l/\lambda$ increases if the top layer is sufficiently thin, whilst it decreases if the top layer is above a critical thickness. In both cases, the resulting morphology is perfectly reversible after cyclic variations of the order parameters, highlighting the presence of a supercritical pitchfork bifurcation.

4.3.4 Discussion and concluding remarks

In this Section, we used theoretical and computational tools to investigate the stability of a soft elastic bilayer subjected only to the bulk gravity force.

Assuming that both layers are made of incompressible neo-Hookean materials, we have first formulated the boundary value problem in nonlinear elasticity considering that the slab attached on one end to a rigid substrate and it is traction-free at the other end. Considering the two configurations depicted in Figure 4.24, we have identified their basic undeformed solutions in Eq. (4.76), characterized by an hydrostatic pressure linearly varying on the thickness direction.

Secondly, we have studied the linear stability by the means of the method of incremental deformations superposed on the basic elastic solution. We found that both configurations can undergo a morphological transition governed by the order parameter γ, representing the ratio between potential and elastic energies of the top layer. In particular, its critical value depends on three dimensionless parameters: α_H, α_μ, α_ρ representing the thickness, shear moduli and density ratios between the layers, respectively.

Thirdly, we have implemented a finite element code to solve the boundary value problem in the fully nonlinear instability regime. Other than validating the predictions of the linear stability analysis, the simulations have highlighted the nonlinear evolution of the characteristic patterns.

Compared to the classic Rayleigh-Taylor hydrodynamic instability, not surprisingly we have found that elastic effects tend to stabilize the dynamics of the surface undulations forming beyond the linear stability threshold. Nonetheless, we obtained a rich morphological diagram with respect to both geometric and elastic parameters. In the following, we briefly discuss the main results for the two cases under consideration.

If the body hangs below a rigid wall, as depicted in Figure 4.24a, we find that there always exists a critical value for the order parameter, driving a morphological transition localised at the free surface. Such an shape instability is favoured if the bottom layer is softer and thicker than the top one, having a critical horizontal wavelength of the same order as the body thickness. In the nonlinear regime, this critical undulation evolves towards forming a digitation, whose characteristic penetration length continuously increases beyond the linear stability threshold, highlighting the existence of a supercritical pitchfork bifurcation.

If the body is attached to a rigid substrate at the bottom surface, as depicted in Figure 4.24b, a morphological transition can occur if and only if the top layer has a higher density than the bottom one. Similarly to the previous case, the onset of an elastic bifurcation is favoured by a softer and thicker bottom layer compared to the top one, with a critical wavelength of the same order as the body thickness. However, an important difference is that the shape instability is localised at the interface between the two layers, displaying two characteristic nonlinear patterns. If the top layer is thinner than the bottom one, the undulation evolves towards forming finger-like protrusions, whilst in the opposite geometrical limit a stable wrinkling occurs.

In summary, we have characterized the shape instabilities occurring in a soft elastic bilayer subjected only to the action of the gravity bulk force. Unlike the Rayleigh-Taylor instabilities in fluids, we have demonstrated that the nonlinear elastic effects saturate the dynamic instability of the bifurcated solutions, displaying a rich morphological diagram where both digitations and stable wrinkling can emerge. The results of this Section provide important guidelines for the design of novel soft systems with tunable shapes. In fact, the possibility to control by external stimuli both the geometric and the elastic properties in smart materials, such as hydrogels or dielectric elastomers [164], can be used to provoke morphological transitions on demand [199]. Morphological changes in such soft devices may be used, for example, to selectively change the surface roughness (e.g. to perform drag reduction in fluid-structure interactions [64]) or to fabricate tailor-made patterns (e.g. to design adaptive material scaffolds [186]).

4.3.5 Appendix – Structure of the matrix M

We report the matrix M we used in the equation Eq. (4.90). We split it into 16 blocks:

$$\mathsf{M} = \begin{bmatrix} 0 & 0 & \mathsf{M}_{13} & \mathsf{M}_{14} \\ \mathsf{M}_{21} & \mathsf{M}_{22} & 0 & 0 \\ \mathsf{M}_{31} & \mathsf{M}_{32} & \mathsf{M}_{33} & \mathsf{M}_{34} \\ \mathsf{M}_{41} & \mathsf{M}_{42} & \mathsf{M}_{43} & \mathsf{M}_{44} \end{bmatrix},$$

where 0 is the null 2×2 matrix and:

$$\mathsf{M}_{13} = \begin{bmatrix} \tilde{k} & \alpha_H\tilde{k}+\tilde{k}-1 \\ -2\tilde{k}\alpha_\mu-\alpha_\rho\gamma & -(\alpha_H+1)(2\tilde{k}\alpha_\mu+\alpha_\rho\gamma) \end{bmatrix},$$

$$\mathsf{M}_{14} = \begin{bmatrix} e^{2\alpha_H\tilde{k}}\tilde{k} & e^{2\alpha_H\tilde{k}}(\alpha_H\tilde{k}+\tilde{k}+1) \\ e^{2\alpha_H\tilde{k}}(2\tilde{k}\alpha_\mu-\alpha_\rho\gamma) & e^{2\alpha_H\tilde{k}}(\alpha_H+1)(2\tilde{k}\alpha_\mu-\alpha_\rho\gamma) \end{bmatrix}, \quad \mathsf{M}_{21} = \begin{bmatrix} 1 & 0 \\ -\tilde{k} & 1 \end{bmatrix},$$

$$\mathsf{M}_{22} = \begin{bmatrix} 1 & 0 \\ \tilde{k} & 1 \end{bmatrix}, \quad \mathsf{M}_{31} = \begin{bmatrix} 1 & 1 \\ -\tilde{k} & 1-\tilde{k} \end{bmatrix}, \quad \mathsf{M}_{32} = \begin{bmatrix} e^{2\tilde{k}} & e^{2\tilde{k}} \\ e^{2\tilde{k}}\tilde{k} & e^{2\tilde{k}}(\tilde{k}+1) \end{bmatrix}, \quad \mathsf{M}_{33} = \begin{bmatrix} -1 & -1 \\ \tilde{k} & \tilde{k}-1 \end{bmatrix},$$

$$\mathsf{M}_{34} = \begin{bmatrix} -1 & -1 \\ -\tilde{k} & -\tilde{k}-1 \end{bmatrix}, \quad \mathsf{M}_{41} = \begin{bmatrix} -\tilde{k}(\alpha_H\alpha_\rho\gamma-2) & \tilde{k}(2-\alpha_H\alpha_\rho\gamma)-2 \\ \tilde{k}(\alpha_H\alpha_\rho\gamma-2)-\gamma & \tilde{k}(\alpha_H\alpha_\rho\gamma-2)-(\alpha_H\alpha_\rho+1)\gamma \end{bmatrix},$$

$$\mathsf{M}_{42} = \begin{bmatrix} -e^{2\tilde{k}}\tilde{k}(\alpha_H\alpha_\rho\gamma-2) & e^{2\tilde{k}}(\tilde{k}(2-\alpha_H\alpha_\rho\gamma)+2) \\ -e^{2\tilde{k}}(\gamma+\tilde{k}(\alpha_H\alpha_\rho\gamma-2)) & -e^{2\tilde{k}}(\alpha_H\alpha_\rho\gamma+\gamma+\tilde{k}(\alpha_H\alpha_\rho\gamma-2)) \end{bmatrix},$$

$$\mathsf{M}_{43} = \begin{bmatrix} \tilde{k}(\alpha_H\alpha_\rho\gamma-2\alpha_\mu) & \alpha_H\tilde{k}\alpha_\rho\gamma-2(\tilde{k}-1)\alpha_\mu \\ 2\tilde{k}\alpha_\mu-\alpha_H\tilde{k}\alpha_\rho\gamma+\alpha_\rho\gamma & (\alpha_H+1)\alpha_\rho\gamma+\tilde{k}(2\alpha_\mu-\alpha_H\alpha_\rho\gamma) \end{bmatrix},$$

$$\mathsf{M}_{44} = \begin{bmatrix} \tilde{k}(\alpha_H\alpha_\rho\gamma-2\alpha_\mu) & \alpha_H\tilde{k}\alpha_\rho\gamma-2(\tilde{k}+1)\alpha_\mu \\ -2\tilde{k}\alpha_\mu+\alpha_H\tilde{k}\alpha_\rho\gamma+\alpha_\rho\gamma & (\tilde{k}\alpha_H+\alpha_H+1)\alpha_\rho\gamma-2\tilde{k}\alpha_\mu \end{bmatrix}.$$

4.3.6 Appendix – Expressions of the coefficients c_j

The coefficient c_1 of equation Eq. (4.91) is given by

$$\begin{aligned} c_1 = {} & 2\tilde{k}^2\alpha_\mu\Big(-2\big(\alpha_\mu^2-1\big)\big(2\alpha_H^2\tilde{k}^2+1\big)\cosh(2\tilde{k})+2\Big(4\alpha_H^2\tilde{k}^4(\alpha_\mu-1)^2+2\tilde{k}^2\Big(\alpha_H^2\big(\alpha_\mu^2+1\big)+4\alpha_H\alpha_\mu+\alpha_\mu^2+1\Big)+ \\ & -\big(2\tilde{k}^2+1\big)\big(\alpha_\mu^2-1\big)\cosh(2\alpha_H\tilde{k})+\alpha_\mu^2+1\Big)+(\alpha_\mu-1)^2\cosh(2(\alpha_H-1)\tilde{k})+(\alpha_\mu+1)^2\cosh(2(\alpha_H+1)\tilde{k})\Big), \end{aligned}$$

whereas c_2 is

$$\begin{aligned} c_2 = {} & \tilde{k}\Big(4\alpha_H^2\tilde{k}^2\alpha_\rho\alpha_\mu\sinh(2\tilde{k})-4\alpha_H^2\tilde{k}^2\alpha_\mu\sinh(2\tilde{k})+4\tilde{k}\Big(\alpha_\mu\Big(2\alpha_H\tilde{k}^2(\alpha_H-(\alpha_H+2)\alpha_\rho)+\alpha_\rho+1\Big)+ \\ & +\alpha_H\big(2\tilde{k}^2+1\big)\alpha_\rho+\alpha_\mu^2\big(2\alpha_H\tilde{k}^2+\alpha_H\big)\Big)-4\tilde{k}^2\alpha_\rho\sinh(2\alpha_H\tilde{k})+4\tilde{k}^2\alpha_\mu^2\sinh(2\alpha_H\tilde{k})+4\alpha_H\tilde{k}\cosh(2\tilde{k})\big(\alpha_\rho-\alpha_\mu^2\big)+ \\ & -2\alpha_\mu\cosh(2\alpha_H\tilde{k})(2\tilde{k}(\alpha_\rho-1)+(\alpha_\rho+1)\sinh(2\tilde{k}))-2\alpha_\rho\sinh(2\alpha_H\tilde{k})-\alpha_\rho\sinh(2(\alpha_H+1)\tilde{k})+ \\ & +\alpha_\rho\sinh(2\tilde{k}-2\alpha_H\tilde{k})-4\alpha_\mu^2\sinh^2(\tilde{k})\sinh(2\alpha_H\tilde{k})+4\alpha_\rho\alpha_\mu\sinh(\tilde{k})\cosh(\tilde{k})-4\alpha_\mu\sinh(\tilde{k})\cosh(\tilde{k})\Big), \end{aligned}$$

and the expression of c_3 is

$$\begin{aligned} c3 = {} & -\tfrac{1}{2}(\alpha_\rho-1)\alpha_\rho\Big(2\Big(2\tilde{k}^2(2\alpha_H+\alpha_\mu)-\big(2\tilde{k}^2+1\big)\alpha_\mu\cosh(2\alpha_H\tilde{k})-2\tilde{k}(\alpha_H\sinh(2\tilde{k})+\sinh(2\alpha_H\tilde{k}))+\alpha_\mu\Big)+ \\ & +(\alpha_\mu-1)\cosh(2(\alpha_H-1)\tilde{k})+(\alpha_\mu+1)\cosh(2(\alpha_H+1)\tilde{k})-2\alpha_\mu\cosh(2\tilde{k})\Big). \end{aligned}$$

5 CONCLUSIONS AND PERSPECTIVES

This thesis deals with the mathematical modelling of soft and active solids using continuum mechanics. The results provide useful insights for understanding the emerging non-standard behaviour of such materials, with application ranging from biology to engineering science.

The research activities concerned both analytical and numerical tasks that have been developed in order to solve few relevant problems in this field. In particular, we focused on:

- the well posedness of the constitutive theory of non-linear elastic materials with initial stresses,
- the mathematical description of active phenomena in living matter,
- the pattern formation in soft solids after a mechanical instability.

The main results are briefly summarized in the following.

WELL POSEDNESS OF THE NON-LINEAR MODEL In Chapter 2, we have studied the mathematical description of elastic bodies in presence of initial stress, i.e. the tensor field Σ therein corresponding to the Cauchy stress in the reference configuration.

The classical approach to model initially stressed bodies relies is the theory of elastic distortions. It is based on the Kröner-Lee multiplicative decomposition of the deformation gradient $\mathsf{F} = \mathsf{F}_e\mathsf{G}$, where G is the tensor field describing the inelastic distortion that locally maps the reference configuration to its relaxed state, while F_e describes the elastic distortion of the body. In this context, the strain energy density reads

$$\psi = \psi(\mathsf{F}, \mathsf{G}) = \det \mathsf{G}\psi_0(\mathsf{F}\mathsf{G}^{-1}),$$

where ψ_0 is the strain energy density in absence of initial stress. The main drawback of this approach is that the tensor field G should be constitutively provided. Indeed, the virtual relaxed configuration is usually not accessible experimentally due to the necessity of cutting the body to release all the residual stress.

To overcome these difficulties, we used an alternative approach, known as theory of initially stressed materials. It is based on the assumption that the strain energy density constitutively depends on both the deformation gradient and the initial stress field, namely

$$\psi = \psi(\mathsf{F}; \Sigma).$$

While the theory of distortions is quite well studied, this latter approach is relatively new and few results on the well posedness of the elastic problem exist. In particular, we investigate the influence of constitutive restrictions on the existence of elastic minimizers. In the framework of the theory of initially stressed materials, Johnson and Hoger [119] proved that a virtual relaxed configuration exists requiring that $\Sigma \in C^1(\Omega_0, \mathcal{S}(\mathbb{R}^3))$, being $\psi = \psi(\mathsf{F}; \Sigma(\boldsymbol{X}))$ twice differentiable with respect to both arguments, and the distortion from the neighbourhood of each point to the free state to be once differentiable in space. In Theorem 2.3.1 we have weaken the hypotheses of Johnson and Hoger, proving the existence of a relaxed state locally mapped by a tensor $\mathsf{G}_{\Sigma(\boldsymbol{X})}$ about a material point $\boldsymbol{X}$ assuming only a C^1 regularity on the dependence of the strain energy on F, performing a local minimization of the strain energy density. The collection of the local maps from the reference configuration to the virtual relaxed state is denoted by $\widehat{\mathsf{G}}[\Sigma]$.

Furthermore, in Theorem 2.4.1 we have proved that imposing constitutive assumptions based on the independence on the chosen reference configuration, known as initial stress reference independence (ISRI), is equivalent to assume that

$$\psi(\mathsf{F}, \Sigma) = \det \widehat{\mathsf{G}}[\Sigma] \psi(\mathsf{F}\widehat{\mathsf{G}}[\Sigma]^{-1}; 0),$$

so that the initial stress Σ is generated by an elastic distortion. This Theorem has important consequences also on the mechanical properties. For example, the material symmetry group and the elastic moduli of the medium are preserved for any initial stress field Σ if the ISRI is assumed.
Moreover, in Lemma 2.4.1 we have shown that the polyconvexity of the strain energy density in the relaxed case is automatically inherited when the body is initially stressed, if the ISRI is assumed. This has allowed us to extend Ball's existence Theorem 1.1.2 to the case of initially stressed materials (see Theorem 2.4.2).

The results of this chapter also allowed us to provide a new mechanical interpretation of the initial stress reference independence. Indeed, in view of Theorem 2.4.1, the ISRI should be imposed when the initial stress field is provoked only by an elastic distortion of the elastic body and not by a change of the material properties at the microstructural level. It is well suited to model the response of bodies with residual stressed caused by volumetric growth or remodelling. For example, it is too restrictive to describe complex active phenomena, such as the contraction of muscles, due to the change of the mechanical properties of the elastic body induced by the continuous formation and disruption of crossbridges.

MATHEMATICAL MODELLING OF ACTIVE PHENOMENA In Chapter 3, we have developed a mathematical framework for modelling active processes in soft biological matter. In particular, we have focused on both the active generation of force in muscles and the growth of a solid tumour.

Understanding the constitutive laws describing muscle contraction is crucial for many applications in biomechanics and several different models of muscle activation exist in the literature. A possible approach to model the contraction process is the *active strain*. As exposed previously, it is based on the multiplicative decomposition of the deformation gradient into an active contribution, due to the muscle activation, and an elastic one, due to the passive deformation of the body.
We have shown that it is not possible to recover the experimental stress-stretch curve corresponding to a uniaxial deformation of a skeletal muscle by simply assuming the active strain approach, whatever the functional form of the strain energy. Therefore, we have proposed an alternative model based on a mixture approach. We have proved that this model, called decoupled active strain, allows us to overcome these difficulties.

We have also focused on the mathematical description of growth in solid tumours, which is useful to target novel therapeutic actions for a more efficient drug delivery. We have shown that tumours exhibit several mechanical features of a poroelastic material, where the cellular component behaves like an elastic solid. In the *in-vitro* experiments, when the solid component of the cellular aggregate, known as multicellular tumour spheroid, is loaded at the boundary, it grows up to an asymptotic volume that depends on the exerted compression. Residual stress are evidenced by the tumour opening after the tumour is cut radially, highlighting a peculiar pattern. Introducing a novel numerical approach, we have correlated the measured opening angle and the underlying residual stress in a sphere. The features of the mechanobiological system can be explained in terms of the existence of an underlying feedback between mechanical forces and the cell proliferation rate. This feedback is modulated by the availability of nutrient, that is radially damped by the balance between diffusion and consumption. The volumetric growth profiles and the pattern of residual stress have been reproduced quantitatively assuming a dependence of the target stress on the concentration of nutrient which is specific of the malignant tissue.

PATTERN FORMATION AND MORPHO–ELASTICITY In Chapter 4 we investigated how elastic instabilities can generate patterns in both inert and active soft matter. The coupling between physical and geometrical non-linearities leads to non-convex energies that admit multiple local minimizers. Thus, a morphological transition may occur as the result of the accumulation of mechanical stress in the elastic body.

First, we studied the mechanics of growing capillaries in tumours. Indeed, solid tumours have the ability to assemble their own vascular network for optimizing their access to the vital nutrients. These new capillaries are morphologically different from normal physiological vessels. In particular, they have a much higher spatial tortuosity forcing an impaired flow within the peritumoural area. This is a major obstacle for the efficient delivery of antitumoural drugs. We proposed a morpho–elastic model of the tumour vessels, in which a tumour capillary is considered as a growing hyperelastic tube that is spatially constrained by a linear elastic environment, representing the interstitial matter. We assumed that the capillary is an incompressible neo–Hookean material, whose growth is modelled using a multiplicative decomposition of the deformation gradient. We studied the morphological stability of the capillary by means of the method of incremental deformations superposed on finite strains, solving the corresponding incremental problem using the Stroh formulation and the impedance matrix method. The incompatible axial growth of the straight capillary is found to control the onset of a bifurcation towards a tortuous shape. The post-buckling morphology is studied using a mixed finite element formulation in the fully non-linear regime. The proposed model highlights how the geometrical and the elastic properties of the capillary and the surrounding medium concur to trigger the loss of marginal stability of the straight capillary and the non-linear development of its spatial tortuosity.

Second, we have exploited the theory of initially stressed materials to study the morphological stability of a soft incompressible sphere, composed of a neo–Hookean material and subjected to two different distributions of residual stresses. The boundary value elastic problem has been studied with analytic and numerical tools. We have performed a linear stability analysis on the pre-stressed solid sphere using the method of incremental deformations. The marginal stability conditions are given as a function of a control parameter, that is the dimensionless variable representing the characteristic intensity of the spatial distribution of residual stress. We have also performed finite element simulations using a mixed formulation in order to investigate the post-buckling morphology in the fully non-linear regime. Considering different distributions of the residual stresses, we have found that morphological transitions occur where the hoop residual stress reaches its maximum compressive value. The loss of spherical symmetry is found to be controlled by the mechanical and geometrical properties of the sphere, as well as on the spatial distribution of the residual stress.

The results provide useful guidelines in order to design morphable soft spheres, for example by controlling the residual stresses through active deformations. They finally suggest a viable solution for the nondestructive characterization of residual stresses in soft tissues, such as solid tumors by the means of an inverse analysis based on wave propagation in soft solids [132].

Finally, we have investigated a new morphological transition in soft solids that we call elastic Rayleigh–Taylor instability. It concerns a soft body composed of two heavy elastic layers, attached to a rigid surface and subjected only to the bulk gravity force. An elastic instability is triggered in very soft solids, so that the increment of the elastic energy is compensated by the reduction of the gravitational potential energy.

Using theoretical and computational tools, we have characterized the selection of different patterns as well as their non-linear evolution, unveiling the interplay between elastic and geometric effects for their formation. Unlike similar gravity-induced shape transitions in fluids, we have proved that the non-linear elastic effects saturate the dynamic instability of the bifurcated solutions, displaying a rich morphological diagram where both digitations and stable wrinkling can emerge. The results of this work provided important guidelines for the design of novel soft systems with tunable shapes. Indeed, the possibility to trigger topological transitions exploiting a controllable bulk force or modulating the geometric and the elastic properties in smart materials, may be used to selectively change the surface roughness or to fabricate tailor-made patterns.

OPEN CHALLENGES AND FUTURE DEVELOPMENTS The research field concerning the mathematical modelling of soft and active matter is rapidly expanding and several open challenges have to be tackled. Beyond the few advances provided in this thesis, there are several improvements that will be addressed in future works.

Without pretending to give a full overview of the many open problems in the field, in the following I summarize some questions that are more directly related to the main object of this thesis.

For what concerns the mathematical framework of initially stressed materials, the strain energies developed so far are based on an isotropic response in the unstressed configuration [97, 98, 2]. Even if the anisotropic may result from an elastic distortion, these strain energies do not incorporate structural anisotropy, e.g. due to the presence of fibres.

In order to do so, we should exploit the theory of invariants to write

$$\psi(\boldsymbol{X}, \mathsf{F}; \Sigma, \mathsf{M}_1, \mathsf{M}_2, \dots)$$

where $\mathsf{M}_j = \boldsymbol{M}_j \otimes \boldsymbol{M}_j$ is the structural tensor related to the family of fibres with direction $\boldsymbol{M}_j$. However, in presence of only one family of fibre, we need to take into account eighteen independent invariants of [111, 157], leading to an involved expression of the strain energy. The main challenge is to understand if further restrictions can be assumed to constrain the functional dependence of the strain energy on such a large number of invariants.

For what concerns the modelling of active phenomena in biological media, in this thesis we have presented models based on a macroscopic description of the physical phenomena. However, the multiphysical exchanges of energy take place at the micro-scale, as happens for the conversion of chemical and electrical energy into mechanical stress taking place in sarcomeres. There is the need to develop a connection between these two scales, obtaining the continuum macroscopic model starting from the microscopic description of the active processes.

Moreover, the termodynamical description of these processes should be taken into account, since these systems produce dissipation during activation and usually operate in out-of-equilibrium conditions.

Finally, there is the necessity of further developing perturbative theories in a weakly non-linear regime in solid mechanics for a deeper theoretical understanding of pattern formations in soft solids. Moreover, the bifurcation diagram is usually very complex, with secondary and tertiary branches possibly detaching from the primary bifurcation curve not far from the linear stability threshold [40]. In this perspective, the numerical approximations of the non-linear problem can be exploited. Whenever the bifurcated branch is connected to the principal one, continuation algorithms such as the pesudo-arclength method can be used; otherwise, the deflated continuation method is useful [82]. Another big challenge is the study of material instabilities, such as cavitation, fracture, and creasing, since they exhibit an infinite scalable localization in space. In such a strong topology, very few mathematical tools are available, whilst numerical results heavily rely on the implementation of regularization techniques that must be validated using homogenization methods.

In conclusion, the description of these materials requires the developing of advanced mathematical tools. As shown in the thesis, their behaviour is non-standard, due to the constitutive geometrical and physical non-linearities, the non-convexity of the energy functional and the multi-physical nature of active processes.

It is my personal belief that the next progresses in this multidisciplinary research branch will be driven by the development of new mathematical tools, both to prove basic science insights and to drive engineering applications. Understanding the behaviours of soft active matter and the related non-linear partial differential systems is a formidable challenge that will require advancements in different fields of pure and applied mathematics, ranging from the calculus of variations to the application of differential geometry in continuum mechanics, from the development of new perturbation methods to the improvement of numerical schemes for computational mechanics.

BIBLIOGRAPHY

[1] E. Acerbi and N. Fusco. Semicontinuity problems in the calculus of variations. *Archive for Rational Mechanics and Analysis*, 86(2):125–145, 1984.

[2] A. Agosti, A. L. Gower, and P. Ciarletta. The constitutive relations of initially stressed incompressible mooney-rivlin materials. *Mechanics Research Communications*, 93:4–10, 2018.

[3] T. Alarcon, H. Byrne, P. Maini, and J. Panovska. 20 mathematical modelling of angiogenesis and vascular adaptation. In R. Paton and L. A. McNamara, editors, *Multidisciplinary Approaches to Theory in Medicine*, volume 3 of *Studies in Multidisciplinarity*, pages 369 – 387. Elsevier, 2005.

[4] M. Alnæs, J. Blechta, J. Hake, A. Johansson, B. Kehlet, A. Logg, C. Richardson, J. Ring, M. E. Rognes, and G. N. Wells. The FEniCS project version 1.5. *Archive of Numerical Software*, 3(100), 2015.

[5] D. Ambrosi, G. Ateshian, E. Arruda, S. Cowin, J. Dumais, A. Goriely, G. A. Holzapfel, J. Humphrey, R. Kemkemer, E. Kuhl, et al. Perspectives on biological growth and remodeling. *Journal of the Mechanics and Physics of Solids*, 59(4):863–883, 2011.

[6] D. Ambrosi and F. Guana. Stress-modulated growth. *Mathematics and Mechanics of Solids*, 12(3):319–342, 2007.

[7] D. Ambrosi and F. Mollica. On the mechanics of a growing tumor. *International Journal of Engineering Science*, 40(12):1297–1316, 2002.

[8] D. Ambrosi and F. Mollica. The role of stress in the growth of a multicell spheroid. *Journal of Mathematical Biology*, 48(5):477–499, 2004.

[9] D. Ambrosi and S. Pezzuto. Active stress vs. active strain in mechanobiology: constitutive issues. *Journal of Elasticity*, 107(2):199–212, 2012.

[10] D. Ambrosi, S. Pezzuto, D. Riccobelli, T. Stylianopoulos, and P. Ciarletta. Solid tumors are poroelastic solids with a chemo-mechanical feedback on growth. *Journal of Elasticity*, 129(1-2):107–124, 2017.

[11] D. Ambrosi and L. Preziosi. On the closure of mass balance models for tumor growth. *Mathematical Models and Methods in Applied Sciences*, 12(05):737–754, 2002.

[12] D. Ambrosi and L. Preziosi. Cell adhesion mechanisms and stress relaxation in the mechanics of tumours. *Biomechanics and Modeling in Mechanobiology*, 8(5):397–413, 2009.

[13] P. R. Amestoy, I. S. Duff, and J.-Y. L'Excellent. Multifrontal parallel distributed symmetric and unsymmetric solvers. *Computer Methods in Applied Mechanics and Engineering*, 184(2-4):501–520, 2000.

[14] P. R. Amestoy, I. S. Duff, J.-Y. L'Excellent, and J. Koster. A fully asynchronous multifrontal solver using distributed dynamic scheduling. *SIAM Journal on Matrix Analysis and Applications*, 23(1):15–41, 2001.

[15] R. P. Araujo and D. L. S. McElwain. New insights into vascular collapse and growth dynamics in solid tumors. *Journal of Theoretical Biology*, 228(3):335–346, 2004.

[16] F. Auricchio, L. B. da Veiga, C. Lovadina, and A. Reali. A stability study of some mixed finite elements for large deformation elasticity problems. *Computer Methods in Applied Mechanics and Engineering*, 194(9):1075–1092, 2005.

[17] F. Auricchio, L. B. da Veiga, C. Lovadina, and A. Reali. The importance of the exact satisfaction of the incompressibility constraint in nonlinear elasticity: Mixed FEMs versus NURBS-based approximations. *Computer Methods in Applied Mechanics and Engineering*, 199(5):314–323, 2010.

[18] F. Auricchio, L. B. da Veiga, C. Lovadina, A. Reali, R. L. Taylor, and P. Wriggers. Approximation of incompressible large deformation elastic problems: some unresolved issues. *Computational Mechanics*, 52(5):1153–1167, 2013.

[19] J. W. Baish, T. Stylianopoulos, R. M. Lanning, W. S. Kamoun, D. Fukumura, L. L. Munn, and R. K. Jain. Scaling rules for diffusive drug delivery in tumor and normal tissues. *Proceedings of the National Academy of Sciences*, 108(5):1799–1803, 2011.

[20] S. Balay, S. Abhyankar, M. Adams, J. Brown, P. Brune, K. Buschelman, L. Dalcin, V. Eijkhout, W. Gropp, D. Kaushik, et al. PETSc Users Manual Revision 3.8. Technical report, Argonne National Lab.(ANL), Argonne, IL (United States), 2017.

[21] S. Balay, S. Abhyankar, M. F. Adams, J. Brown, P. Brune, K. Buschelman, L. Dalcin, V. Eijkhout, W. D. Gropp, D. Kaushik, M. G. Knepley, L. C. McInnes, K. Rupp, B. F. Smith, S. Zampini, and H. Zhang. PETSc users manual. Technical Report ANL-95/11 - Revision 3.6, Argonne National Laboratory, 2015.

[22] V. Balbi and P. Ciarletta. Morpho-elasticity of intestinal villi. *Journal of the Royal Society Interface*, 10(82):20130109, 2013.

[23] J. M. Ball. Convexity conditions and existence theorems in nonlinear elasticity. *Archive for Rational Mechanics and Analysis*, 63(4):337–403, 1976.

[24] P. V. Bayly, L. A. Taber, and C. D. Kroenke. Mechanical forces in cerebral cortical folding: A review of measurements and models. *Journal of the Mechanical Behavior of Biomedical Materials*, 29:568–581, 2014.

[25] M. Ben Amar and P. Ciarletta. Swelling instability of surface-attached gels as a model of soft tissue growth under geometric constraints. *Journal of the Mechanics and Physics of Solids*, 58(7):935–954, 2010.

[26] M. Ben Amar and A. Goriely. Growth and instability in elastic tissues. *Journal of the Mechanics and Physics of Solids*, 53(10):2284–2319, 2005.

[27] T. Bertrand, J. Peixinho, S. Mukhopadhyay, and C. W. MacMinn. Dynamics of swelling and drying in a spherical gel. *Physical Review Applied*, 6(6):064010, 2016.

[28] B. Bilby, R. Bullough, and E. Smith. Continuous distributions of dislocations: A new application of the methods of non-Riemannian geometry. *Proceedings of the Royal Society of London. Series A. Mathematical and Physical Sciences*, 231(1185):263–273, 1955.

[29] M. A. Biot. Theory of elasticity with large displacements and rotations. In *Proceedings of the Fifth International Congress of Applied Mechanics*, pages 117–122, 1938.

[30] M. A. Biot. Surface instability of rubber in compression. *Applied Scientific Research, Section A*, 12(2):168–182, 1963.

[31] M. A. Biot. *Mechanics of Incremental Deformations*. Wiley, 1964.

[32] S. V. Biryukov. Impedance method in the theory of elastic surface waves. *Soviet Physics. Acoustics*, 31:350–354, 1985.

[33] S. V. Biryukov, Y. V. Gulyaev, V. V. Krylov, and V. P. Plessky. *Surface Acoustic Waves in Inhomogeneous Media*, volume 20. Springer, 1995.

[34] D. Boffi, F. Brezzi, M. Fortin, et al. *Mixed Finite Element Methods and Applications*, volume 44. Springer, 2013.

[35] E. M. H. Bosboom, M. K. C. Hesselink, C. W. J. Oomens, C. V. C. Bouten, M. R. Drost, and F. P. T. Baaijens. Passive transverse mechanical properties of skeletal muscle under in vivo compression. *Journal of Biomechanics*, 34(10):1365–1368, 2001.

[36] E. M. H. Bosboom, J. A. M. Thomassen, C. W. J. Oomens, C. V. C. Bouten, F. P. T. Baaijens, J. Middleton, M. L. Jones, N. G. Shrive, and G. N. Pande. A numerical-experimental approach to determine the transverse mechanical properties of skeletal muscle. *Computer Methods in Biomechanics and Biomedical Engineering-3*, pages 187–192, 2001.

[37] C. P. Brangwynne, F. C. MacKintosh, S. Kumar, N. A. Geisse, J. Talbot, L. Mahadevan, K. K. Parker, D. E. Ingber, and D. A. Weitz. Microtubules can bear enhanced compressive loads in living cells because of lateral reinforcement. *Journal of Cell Biology*, 173(5):733–741, 2006.

[38] P. Brochu and Q. Pei. Advances in dielectric elastomers for actuators and artificial muscles. *Macromolecular Rapid Communications*, 31(1):10–36, 2010.

[39] M. Brojan, D. Terwagne, R. Lagrange, and P. M. Reis. Wrinkling crystallography on spherical surfaces. *Proceedings of the National Academy of Sciences*, 112(1):14–19, 2015.

[40] S. Budday, E. Kuhl, and J. W. Hutchinson. Period-doubling and period-tripling in growing bilayered systems. *Philosophical Magazine*, 95(28-30):3208–3224, 2015.

[41] B. Budiansky. Theory of buckling and post-buckling behavior of elastic structures. In *Advances in Applied Mechanics*, volume 14, pages 1–65. Elsevier, 1974.

[42] E. Bullitt, D. Zeng, G. Gerig, S. Aylward, S. Joshi, J. K. Smith, W. Lin, and M. G. Ewend. Vessel tortuosity and brain tumor malignancy: A blinded study. *Academic Radiology*, 12(10):1232–1240, 2005.

[43] H. Byrne and L. Preziosi. Modelling solid tumour growth using the theory of mixtures. *Mathematical Medicine and Biology*, 20(4):341–366, 2003.

[44] Y. Cao and J. W. Hutchinson. From wrinkles to creases in elastomers: The instability and imperfection-sensitivity of wrinkling. *Proceedings of the Royal Society A: Mathematical, Physical and Engineering Sciences*, 468(2137):94–115, 2012.

[45] M. Carroll. Controllable states of stress for incompressible elastic solids. *Journal of Elasticity*, 3(2):147–153, 1973.

[46] M. Caruel and L. Truskinovsky. Physics of muscle contraction. *Reports on Progress in Physics*, 81(3):036602, 2018.

[47] L. Cattaneo and P. Zunino. A computational model of drug delivery through microcirculation to compare different tumor treatments. *International Journal for Numerical Methods in Biomedical Engineering*, 30(11):1347–1371, 2014.

[48] G. Chagnon, M. Rebouah, and D. Favier. Hyperelastic energy densities for soft biological tissues: A review. *Journal of Elasticity*, 120(2):129–160, 2014.

[49] A. Chakrabarti, S. Mora, F. Richard, T. Phou, J.-M. Fromental, Y. Pomeau, and B. Audoly. Selection of hexagonal buckling patterns by the elastic Rayleigh-Taylor instability. *Journal of the Mechanics and Physics of Solids*, 121:234–257, 2018.

[50] S. Chanet and A. C. Martin. Mechanical force sensing in tissues. *Progress in Molecular Biology and Translational Science*, 126:317, 2014.

[51] G. Cheng, J. Tse, R. K. Jain, and L. L. Munn. Micro-environmental mechanical stress controls tumor spheroid size and morphology by suppressing proliferation and inducing apoptosis in cancer cells. *PLOS ONE*, 4(2):e4632, 2009.

[52] C. Cherubini, S. Filippi, P. Nardinocchi, and L. Teresi. An electromechanical model of cardiac tissue: Constitutive issues and electrophysiological effects. *Progress in Biophysics and Molecular Biology*, 97(2-3):562–573, 2008.

[53] C.-J. Chuong and Y.-C. Fung. Residual stress in arteries. In *Frontiers in Biomechanics*, pages 117–129. Springer, 1986.

[54] P. G. Ciarlet. *Three-Dimensional Elasticity*, volume 20. Elsevier, 1988.

[55] P. Ciarletta. Buckling instability in growing tumor spheroids. *Physical Review Letters*, 110(15):158102, 2013.

[56] P. Ciarletta. Matched asymptotic solution for crease nucleation in soft solids. *Nature Communications*, 9(1):496, 2018.

[57] P. Ciarletta, V. Balbi, and E. Kuhl. Pattern selection in growing tubular tissues. *Physical Review Letters*, 113(24):248101, 2014.

[58] P. Ciarletta and M. Destrade. Torsion instability of soft solid cylinders. *IMA Journal of Applied Mathematics*, 79(5):804–819, 2014.

[59] P. Ciarletta, M. Destrade, and A. L. Gower. On residual stresses and homeostasis: an elastic theory of functional adaptation in living matter. *Scientific Reports*, 6, 2016.

[60] P. Ciarletta, M. Destrade, A. L. Gower, and M. Taffetani. Morphology of residually stressed tubular tissues: Beyond the elastic multiplicative decomposition. *Journal of the Mechanics and Physics of Solids*, 90:242–253, 2016.

[61] B. D. Coleman and W. Noll. On the thermostatics of continuous media. *Archive for Rational Mechanics and Analysis*, 4(1):97–128, 1959.

[62] R. De Pascalis, M. Destrade, and A. Goriely. Nonlinear correction to the Euler buckling formula for compressed cylinders with guided-guided end conditions. *Journal of Elasticity*, 102(2):191–200, 2011.

[63] D. De Tommasi, G. Puglisi, G. Saccomandi, and G. Zurlo. Pull-in and wrinkling instabilities of electroactive dielectric actuators. *Journal of Physics D: Applied Physics*, 43(32):325501, 2010.

[64] B. Dean and B. Bhushan. Shark-skin surfaces for fluid-drag reduction in turbulent flow: A review. *Philosophical Transactions of the Royal Society of London A: Mathematical, Physical and Engineering Sciences*, 368(1929):4775–4806, 2010.

[65] M. Delarue, F. Montel, O. Caen, J. Elgeti, J.-M. Siaugue, D. Vignjevic, J. Prost, J.-F. Joanny, and G. Cappello. Mechanical control of cell flow in multicellular spheroids. *Physical Review Letters*, 110(13):138103, 2013.

[66] J. Dervaux and M. Ben Amar. Mechanical instabilities of gels. *Annual Review of Condensed Matter Physics*, 3(1):311–332, 2012.

[67] M. Destrade, I. Lusetti, R. Mangan, and T. Sigaeva. Wrinkles in the opening angle method. *International Journal of Solids and Structures*, 122:189–195, 2017.

[68] M. Destrade, J. G. Murphy, and R. W. Ogden. On deforming a sector of a circular cylindrical tube into an intact tube: Existence, uniqueness, and stability. *International Journal of Engineering Science*, 48(11):1212–1224, 2010.

[69] M. Destrade, A. Ní Annaidh, and C. D. Coman. Bending instabilities of soft biological tissues. *International Journal of Solids and Structures*, 46(25):4322–4330, 2009.

[70] A. DiCarlo and S. Quiligotti. Growth and balance. *Mechanics Research Communications*, 29(6):449–456, 2002.

[71] P. M. Dixit, A. Narain, and D. D. Joseph. Free surface problems induced by motions perturbing the natural state of simple solids. *Archive for Rational Mechanics and Analysis*, 77(3):199–261, 1981.

[72] M. Dolega, M. Delarue, F. Ingremeau, J. Prost, A. Delon, and G. Cappello. Cell-like pressure sensors reveal increase of mechanical stress towards the core of multicellular spheroids under compression. *Nature Communications*, 8, 2017.

[73] M. J. Dorie, R. F. Kallman, D. F. Rapacchietta, D. Van Antwerp, and Y. R. Huang. Migration and internalization of cells and polystyrene microspheres in tumor cell spheroids. *Experimental Cell Research*, 141(1):201–209, 1982.

[74] Y. Dou, Y. Fan, J. Zhao, and H. Gregersen. Longitudinal residual strain and stress-strain relationship in rat small intestine. *BioMedical Engineering OnLine*, 5(1):37, 2006.

[75] Y. Du, C. Lü, W. Chen, and M. Destrade. Modified multiplicative decomposition model for tissue growth: Beyond the initial stress-free state. *Journal of the Mechanics and Physics of Solids*, 2018.

[76] I. Ekeland and R. Temam. *Convex Analysis and Variational Problems*, volume 28. Siam, 1999.

[77] M. Epstein. *The elements of continuum biomechanics*. John Wiley & Sons, 2012.

[78] M. Epstein. Mathematical characterization and identification of remodeling, growth, aging and morphogenesis. *Journal of the Mechanics and Physics of Solids*, 84:72–84, 2015.

[79] M. Epstein and G. A. Maugin. Thermomechanics of volumetric growth in uniform bodies. *International Journal of Plasticity*, 16(7-8):951–978, 2000.

[80] L. Euler. Methodus inveniendi lineas curvas maximi minimive proprietate gaudentes, sive solutio problematis isoperimetrici lattissimo sensu accepti. 1744.

[81] L. C. Evans. *Partial Differential Equations*. American Mathematical Society, 2010.

[82] P. E. Farrell, C. H. Beentjes, and Á. Birkisson. The computation of disconnected bifurcation diagrams. *arXiv preprint arXiv:1603.00809*, 2016.

[83] P. E. Farrell and C. Maurini. Linear and nonlinear solvers for variational phase-field models of brittle fracture. *International Journal for Numerical Methods in Engineering*, 109(5):648–667, 2017.

[84] M. Fermigier, L. Limat, J. Wesfreid, P. Boudinet, and C. Quilliet. Two-dimensional patterns in Rayleigh-Taylor instability of a thin layer. *Journal of Fluid Mechanics*, 236:349–383, 1992.

[85] G. Fichera. Existence theorems in elasticity. In *Linear Theories of Elasticity and Thermoelasticity*, pages 347–389. Springer, 1973.

[86] J. Folkman and M. Hochberg. Self-regulation of growth in three dimensions. *The Journal of Experimental Medicine*, 138(4):745–753, 1973.

[87] G. Forgacs, R. A. Foty, Y. Shafrir, and M. S. Steinberg. Viscoelastic properties of living embryonic tissues: A quantitative study. *Biophysical Journal*, 74(5):2227–2234, 1998.

[88] R. Fosdick, P. Foti, A. Fraddosio, S. Marzano, and M. D. Piccioni. Taylor-like bifurcations for a compressible isotropic elastic tube. *Mathematics and Mechanics of Solids*, 19(8):966–987, 2014.

[89] Y.-C. Fung. *Biomechanics: Mechanical Properties of Living Tissues*. Springer Science & Business Media, 2013.

[90] A. N. Gent. A new constitutive relation for rubber. *Rubber Chemistry and Technology*, 69(1):59–61, 1996.

[91] C. Geuzaine and J.-F. Remacle. Gmsh: A 3-d finite element mesh generator with built-in pre-and post-processing facilities. *International Journal for Numerical Methods in Engineering*, 79(11):1309–1331, 2009.

[92] A. Ghatak, M. K. Chaudhury, V. Shenoy, and A. Sharma. Meniscus instability in a thin elastic film. *Physical Review Letters*, 85(20):4329, 2000.

[93] G. Giantesio, A. Musesti, and D. Riccobelli. A comparison between active strain and active stress in transversely isotropic hyperelastic materials. *Journal of Elasticity*, 2018.

[94] S. Göktepe, A. Menzel, and E. Kuhl. The generalized hill model: A kinematic approach towards active muscle contraction. *Journal of the Mechanics and Physics of Solids*, 72:20–39, 2014.

[95] A. Goriely. *The Mathematics and Mechanics of Biological Growth*. Springer, 2017.

[96] A. Goriely, R. Vandiver, and M. Destrade. Nonlinear Euler Buckling. *Proceedings of the Royal Society of London A: Mathematical, Physical and Engineering Sciences*, 464(2099):3003–3019, 2008.

[97] A. L. Gower, P. Ciarletta, and M. Destrade. Initial stress symmetry and its applications in elasticity. *Proceedings of the Royal Society A: Mathematical, Physical and Engineering Sciences*, 471(2183):20150448, 2015.

[98] A. L. Gower, T. Shearer, and P. Ciarletta. A new restriction for initially stressed elastic solids. *Quarterly Journal of Mechanics and Applied Mathematics*, 70(4):455–478, 2017.

[99] Y. Grabovsky and L. Truskinovsky. Marginal material stability. *Journal of Nonlinear science*, 23(5):891–969, 2013.

[100] H. P. Greenspan. Models for the growth of a solid tumor by diffusion. *Studies in Applied Mathematics*, 51(4):317–340, 1972.

[101] M. E. Gurtin. The linear theory of elasticity. In *Linear theories of elasticity and thermoelasticity*, pages 1–295. Springer, 1973.

[102] M. E. Gurtin. *An Introduction to Continuum Mechanics*, volume 158. Academic press, 1982.

[103] D. M. Haughton and R. W. Ogden. On the incremental equations in non-linear elasticity—ii. bifurcation of pressurized spherical shells. *Journal of the Mechanics and Physics of Solids*, 26(2):111–138, 1978.

[104] D. Hawkins and M. Bey. A comprehensive approach for studying muscle-tendon mechanics. *Journal of Biomechanical Engineering*, 116(1):51–55, 1994.

[105] T. Heidlauf and O. Röhrle. On the treatment of active behaviour in continuum muscle mechanics. *PAMM*, 13(1):71–72, 2013.

[106] G. Helmlinger, P. A. Netti, H. C. Lichtenbeld, R. J. Melder, and R. K. Jain. Solid stress inhibits the growth of multicellular tumor spheroids. *Nature Biotechnology*, 15(8):778–783, 1997.

[107] B. Hernández-Gascón, J. Grasa, B. Calvo, and J. F. Rodríguez. A 3d electro-mechanical continuum model for simulating skeletal muscle contraction. *Journal of Theoretical Biology*, 335:108–118, 2013.

[108] J. M. Hill. Closed form solutions for small deformations superimposed upon the symmetrical expansion of a spherical shell. *Journal of Elasticity*, 6(2):125–136, 1976.

[109] A. Hoger. On the residual stress possible in an elastic body with material symmetry. *Archive for Rational Mechanics and Analysis*, 88(3):271–289, 1985.

[110] A. Hoger. On the determination of residual stress in an elastic body. *Journal of Elasticity*, 16(3):303–324, 1986.

[111] A. Hoger. The constitutive equation for finite deformations of a transversely isotropic hyperelastic material with residual stress. *Journal of Elasticity*, 33(2):107–118, 1993.

[112] E. Hohlfeld and L. Mahadevan. Unfolding the sulcus. *Physical Review Letters*, 106(10):105702, 2011.

[113] G. A. Holzapfel. *Nonlinear Solid Mechanics: A Continuum Approach for Engineering*. Wiley, 2000.

[114] C. O. Horgan. Korn's inequalities and their applications in continuum mechanics. *SIAM review*, 37(4):491–511, 1995.

[115] C. O. Horgan and G. Saccomandi. Constitutive modelling of rubber-like and biological materials with limiting chain extensibility. *Mathematics and Mechanics of Solids*, 7(4):353–371, 2002.

[116] C. O. Horgan and G. Saccomandi. A description of arterial wall mechanics using limiting chain extensibility constitutive models. *Biomechanics and Modeling in Mechanobiology*, 1(4):251–266, 2003.

[117] R. K. Jain. Barriers to drug delivery in solid tumors. *Scientific American*, 271(1):58–65, 1994.

[118] B. E. Johnson and A. Hoger. The dependence of the elasticity tensor on residual stress. *Journal of Elasticity*, 33(2):145–165, 1993.

[119] B. E. Johnson and A. Hoger. The use of a virtual configuration in formulating constitutive equations for residually stressed elastic materials. *Journal of Elasticity*, 41(3):177–215, 1995.

[120] B. E. Johnson and A. Hoger. The use of strain energy to quantify the effect of residual stress on mechanical behavior. *Mathematics and Mechanics of Solids*, 3(4):447–470, 1998.

[121] C. Keplinger, T. Li, R. Baumgartner, Z. Suo, and S. Bauer. Harnessing snap-through instability in soft dielectrics to achieve giant voltage-triggered deformation. *Soft Matter*, 8(2):285–288, 2012.

[122] J. Kim, J. A. Hanna, M. Byun, C. D. Santangelo, and R. C. Hayward. Designing responsive buckled surfaces by halftone gel lithography. *Science*, 335(6073):1201–1205, 2012.

[123] R. J. Knops and L. E. Payne. *Uniqueness Theorems in Linear Elasticity*, volume 19. Springer Science & Business Media, 2012.

[124] R. J. Knops and E. W. Wilkes. Theory of Elastic Stability. In *Handbuch der Physik*, volume VIa/3 (Ed. C. A. Truesdell), pages 117–129. Springer, 1973.

[125] V. Kondaurov and L. Nikitin. Finite strains of viscoelastic muscle tissue. *Journal of Applied Mathematics and Mechanics*, 51(3):346–353, 1987.

[126] E. Kröner. Allgemeine kontinuumstheorie der versetzungen und eigenspannungen. *Archive for Rational Mechanics and Analysis*, 4(1):273–334, 1959.

[127] T. G. Kuznetsova, M. N. Starodubtseva, N. I. Yegorenkov, S. A. Chizhik, and R. I. Zhdanov. Atomic force microscopy probing of cell elasticity. *Micron*, 38(8):824–833, 2007.

[128] E. H. Lee. Elastic-plastic deformation at finite strains. *Journal of Applied Mechanics*, 36(1):1–6, 1969.

[129] J. R. Less, T. C. Skalak, E. M. Sevick, and R. K. Jain. Microvascular architecture in a mammary carcinoma: Branching patterns and vessel dimensions. *Cancer Research*, 51(1):265–273, 1991.

[130] H. A. Levine, S. Pamuk, B. D. Sleeman, and M. Nilsen-Hamilton. Mathematical modeling of capillary formation and development in tumor angiogenesis: Penetration into the stroma. *Bulletin of Mathematical Biology*, 63(5):801–863, 2001.

[131] B. Li, Y.-P. Cao, X.-Q. Feng, and H. Gao. Mechanics of morphological instabilities and surface wrinkling in soft materials: A review. *Soft Matter*, 8(21):5728–5745, 2012.

[132] G.-Y. Li, Q. He, R. Mangan, G. Xu, C. Mo, J. Luo, M. Destrade, and Y. Cao. Guided waves in pre-stressed hyperelastic plates and tubes: Application to the ultrasound elastography of thin-walled soft materials. *Journal of the Mechanics and Physics of Solids*, 102:67–79, 2017.

[133] X. Liang and S. Cai. Gravity induced crease-to-wrinkle transition in soft materials. *Applied Physics Letters*, 106(4):041907, 2015.

[134] A. Logg, K.-A. Mardal, and G. Wells. *Automated solution of differential equations by the finite element method: The FEniCS book*, volume 84. Springer Science & Business Media, 2012.

[135] A. Lucantonio, P. Nardinocchi, and L. Teresi. Transient analysis of swelling-induced large deformations in polymer gels. *Journal of the Mechanics and Physics of Solids*, 61(1):205–218, 2013.

[136] J. MacLaurin, J. Chapman, G. W. Jones, and T. Roose. The buckling of capillaries in solid tumours. *Proceedings of the Royal Society A: Mathematical, Physical and Engineering Sciences*, 468(2148):4123–4145, 2012.

[137] C.-S. Man and W. Y. Lu. Towards an acoustoelastic theory for measurement of residual stress. *Journal of Elasticity*, 17(2):159–182, 1987.

[138] P. Mascheroni, C. Stigliano, M. Carfagna, D. P. Boso, L. Preziosi, P. Decuzzi, and B. A. Schrefler. Predicting the growth of glioblastoma multiforme spheroids using a multiphase porous media model. *Biomechanics and Modeling in Mechanobiology*, pages 1–14, 2016.

[139] J. Merodio and R. W. Ogden. Extension, inflation and torsion of a residually stressed circular cylindrical tube. *Continuum Mechanics and Thermodynamics*, 28(1-2):157–174, 2016.

[140] J. Merodio, R. W. Ogden, and J. Rodríguez. The influence of residual stress on finite deformation elastic response. *International Journal of Non-Linear Mechanics*, 56:43–49, 2013.

[141] S. Monnier, M. Delarue, B. Brunel, M. E. Dolega, A. Delon, and G. Cappello. Effect of an osmotic stress on multicellular aggregates. *Methods*, 94:114–119, 2016.

[142] F. Montel, M. Delarue, J. Elgeti, L. Malaquin, M. Basan, T. Risler, B. Cabane, D. Vignjevic, J. Prost, G. Cappello, et al. Stress clamp experiments on multicellular tumor spheroids. *Physical Review Letters*, 107(18):188102, 2011.

[143] F. Montel, M. Delarue, J. Elgeti, D. Vignjevic, G. Cappello, and J. Prost. Isotropic stress reduces cell proliferation in tumor spheroids. *New Journal of Physics*, 14(5):055008, 2012.

[144] M. Mooney. A theory of large elastic deformation. *Journal of Applied Physics*, 11(9):582–592, 1940.

[145] S. Mora, T. Phou, J.-M. Fromental, L. M. Pismen, and Y. Pomeau. Capillarity driven instability of a soft solid. *Physical Review Letters*, 105(21):214301, 2010.

[146] S. Mora, T. Phou, J.-M. Fromental, and Y. Pomeau. Gravity driven instability in elastic solid layers. *Physical Review Letters*, 113(17):178301, 2014.

[147] C. B. Morrey. Quasi-convexity and the lower semicontinuity of multiple integrals. *Pacific Journal of Mathematics*, 2(1):25–53, 1952.

[148] D. E. Moulton and A. Goriely. Circumferential buckling instability of a growing cylindrical tube. *Journal of the Mechanics and Physics of Solids*, 59(3):525–537, 2011.

[149] P. Nardinocchi and L. Teresi. On the active response of soft living tissues. *Journal of Elasticity*, 88(1):27–39, 2007.

[150] P. Neff. *Some Results Concerning the Mathematical Treatment of Finite Plasticity*, volume 10. Springer Lecture Notes in Applied and Computational Mechanics, Eds. K. Hutter and H. Baaser, Deformation and Failure in Metallic Materials, 2013.

[151] P. A. Netti, D. A. Berk, M. A. Swartz, A. J. Grodzinsky, and R. K. Jain. Role of extracellular matrix assembly in interstitial transport in solid tumors. *Cancer Research*, 60(9):2497–2503, 2000.

[152] S. A. Niederer and N. P. Smith. An improved numerical method for strong coupling of excitation and contraction models in the heart. *Progress in Biophysics and Molecular Biology*, 96(1-3):90–111, 2008.

[153] F. Nobile, A. Quarteroni, and R. Ruiz-Baier. An active strain electromechanical model for cardiac tissue. *International Journal for Numerical Methods in Biomedical Engineering*, 28(1):52–71, 2012.

[154] A. N. Norris and A. Shuvalov. Elastodynamics of radially inhomogeneous spherically anisotropic elastic materials in the stroh formalism. *Proceedings of the Royal Society A: Mathematical, Physical and Engineering Sciences*, 468(2138):467–484, 2012.

[155] A. N. Norris and A. L. Shuvalov. Wave impedance matrices for cylindrically anisotropic radially inhomogeneous elastic solids. *Quarterly Journal of Mechanics and Applied Mathematics*, 63:401–435, 2010.

[156] R. W. Ogden. *Non-linear Elastic Deformations*. Courier Corporation, 1997.

[157] R. W. Ogden and B. Singh. Propagation of waves in an incompressible transversely isotropic elastic solid with initial stress: Biot revisited. *Journal of Mechanics of Materials and Structures*, 6(1):453–477, 2011.

[158] S. G. O'Keeffe, D. E. Moulton, S. L. Waters, and A. Goriely. Growth-induced axial buckling of a slender elastic filament embedded in an isotropic elastic matrix. *International Journal of Non-Linear Mechanics*, 56:94–104, 2013.

[159] C. Paetsch and L. Dorfmann. Stability of active muscle tissue. *Journal of Engineering Mathematics*, 95(1):193–216, 2015.

[160] A. V. Panfilov, R. H. Keldermann, and M. P. Nash. Self-organized pacemakers in a coupled reaction-diffusion-mechanics system. *Physical Review Letters*, 95(25):258104, 2005.

[161] R. Paroni and C.-S. Man. Constitutive equations of elastic polycrystalline materials. *Archive for Rational Mechanics and Analysis*, 150(2):153–177, 1999.

[162] P. Pathmanathan, S. J. Chapman, D. J. Gavaghan, and J. P. Whiteley. Cardiac electromechanics: the effect of contraction model on the mathematical problem and accuracy of the numerical scheme. *Quarterly Journal of Mechanics and Applied Mathematics*, 63(3):375–399, 2010.

[163] R. Pelrine, R. Kornbluh, Q. Pei, and J. Joseph. High-speed electrically actuated elastomers with strain greater than 100%. *Science*, 287(5454):836–839, 2000.

[164] R. Pelrine, R. D. Kornbluh, J. Eckerle, P. Jeuck, S. Oh, Q. Pei, and S. Stanford. Dielectric elastomers: generator mode fundamentals and applications. In *SPIE's 8th Annual International Symposium on Smart Structures and Materials*, pages 148–156. International Society for Optics and Photonics, 2001.

[165] S. Pezzuto, D. Ambrosi, and A. Quarteroni. An orthotropic active–strain model for the myocardium mechanics and its numerical approximation. *European Journal of Mechanics-A/Solids*, 48:83–96, 2014.

[166] A. R. Piriz, J. J. L. Cela, O. D. Cortazar, N. A. Tahir, and D. H. H. Hoffmann. Rayleigh-Taylor instability in elastic solids. *Physical Review E*, 72(5):056313, 2005.

[167] K. R. Rajagopal. On implicit constitutive theories. *Applications of Mathematics*, 48(4):279–319, 2003.

[168] K. R. Rajagopal and A. R. Srinivasa. On the response of non-dissipative solids. *Proceedings of the Royal Society of London A: Mathematical, Physical and Engineering Sciences*, 463(2078):357–367, 2007.

[169] B. Rashid, M. Destrade, and M. D. Gilchrist. Mechanical characterization of brain tissue in compression at dynamic strain rates. *Journal of the Mechanical Behavior of Biomedical Materials*, 10:23–38, 2012.

[170] B. Rashid, M. Destrade, and M. D. Gilchrist. Mechanical characterization of brain tissue in tension at dynamic strain rates. *Journal of the Mechanical Behavior of Biomedical Materials*, 33:43–54, 2014.

[171] L. Rayleigh. On the capillary phenomena of jets. *Proceedings of the Royal Society of London*, 29(196-199):71–97, 1879.

[172] L. Rayleigh. Investigation of the character of the equilibrium of an incompressible heavy fluid of variable density. *Proceedings of the London Mathematical Society*, 14(1):8, 1883.

[173] F. Regazzoni, L. Dedè, and A. Quarteroni. Active contraction of cardiac cells: a reduced model for sarcomere dynamics with cooperative interactions. *Biomechanics and Modeling in Mechanobiology*, pages 1–24, 2018.

[174] C. Reina and S. Conti. Kinematic description of crystal plasticity in the finite kinematic framework: A micromechanical understanding of $\mathsf{F} = \mathsf{F}_e\mathsf{F}_p$. *Journal of the Mechanics and Physics of Solids*, 67:40–61, 2014.

[175] D. Riccobelli, A. Agosti, and P. Ciarletta. On the existence of elastic minimizers for initially stressed materials. *Philosophical Transactions of the Royal Society A: Mathematical, Physical and Engineering Sciences*, in press.

[176] D. Riccobelli and D. Ambrosi. Activation of a muscle as a mapping of stress strain curves. *Submitted*.

[177] D. Riccobelli and P. Ciarletta. Rayleigh–Taylor instability in soft elastic layers. *Philosophical Transactions of the Royal Society A: Mathematical, Physical and Engineering Sciences*, 375(2093):20160421, 2017.

[178] D. Riccobelli and P. Ciarletta. Morpho–elastic model of the tortuous tumour vessels. *International Journal of Non-Linear Mechanics*, 107:1 – 9, 2018.

[179] D. Riccobelli and P. Ciarletta. Shape transitions in a soft incompressible sphere with residual stresses. *Mathematics and Mechanics of Solids*, 23(12):1507–1524, 2018.

[180] R. S. Rivlin. Large elastic deformations of isotropic materials IV. Further developments of the general theory. *Philosophical Transactions of the Royal Society A: Mathematical, Physical and Engineering Sciences*, 241(835):379–397, 1948.

[181] E. K. Rodriguez, A. Hoger, and A. D. McCulloch. Stress-dependent finite growth in soft elastic tissues. *Journal of Biomechanics*, 27(4):455–467, 1994.

[182] J. Rodríguez and J. Merodio. Helical buckling and postbuckling of pre-stressed cylindrical tubes under finite torsion. *Finite Elements in Analysis and Design*, 112:1–10, 2016.

[183] T. Roose, P. A. Netti, L. L. Munn, Y. Boucher, and R. K. Jain. Solid stress generated by spheroid growth estimated using a linear poroelasticity model. *Microvascular Research*, 66(3):204–212, 2003.

[184] S. Rossi, R. Ruiz-Baier, L. F. Pavarino, and A. Quarteroni. Orthotropic active strain models for the numerical simulation of cardiac biomechanics. *International Journal for Numerical Methods in Biomedical Engineering*, 28(6-7):761–788, 2012.

[185] P. G. Saffman and G. I. Taylor. The penetration of a fluid into a porous medium or Hele-Shaw cell containing a more viscous liquid. *Proceedings of the Royal Society of London A: Mathematical, Physical and Engineering Sciences*, 245(1242):312–329, 1958.

[186] K. Saha, J. Kim, E. Irwin, J. Yoon, F. Momin, V. Trujillo, D. V. Schaffer, K. E. Healy, and R. C. Hayward. Surface creasing instability of soft polyacrylamide cell culture substrates. *Biophysical Journal*, 99(12):L94–L96, 2010.

[187] B. Saintyves, O. Dauchot, and E. Bouchaud. Bulk elastic fingering instability in hele-shaw cells. *Physical Review Letters*, 111(4):047801, 2013.

[188] R. Seydel. *Practical bifurcation and stability analysis*, volume 5. Springer Science & Business Media, 2009.

[189] M. Shams, M. Destrade, and R. W. Ogden. Initial stresses in elastic solids: Constitutive laws and acoustoelasticity. *Wave Motion*, 48(7):552–567, 2011.

[190] M. Shams and R. W. Ogden. On Rayleigh-type surface waves in an initially stressed incompressible elastic solid. *IMA Journal of Applied Mathematics*, 79(2):360–376, 2012.

[191] M. Shariff, R. Bustamante, and J. Merodio. On the spectral analysis of residual stress in finite elasticity. *IMA Journal of Applied Mathematics*, 82(3):656–680, 2017.

[192] S. Silling. Creasing singularities in compressible elastic materials. *Journal of Applied Mechanics*, 58(1):70–74, 1991.

[193] M. Singh and A. C. Pipkin. Note on Ericksen's problem. *Zeitschrift für angewandte Mathematik und Physik*, 16(5):706–709, 1965.

[194] N. P. Smith, D. P. Nickerson, E. J. Crampin, and P. J. Hunter. Multiscale computational modelling of the heart. *Acta Numerica*, 13:371–431, 2004.

[195] B. R. Stoll. *A quantitative analysis of the development and remodeling of blood vessels in tumors: Contribution of endothelial progenitor cells to angiogenesis and effect of solid stress on blood vessel morphology*. PhD thesis, Massachusetts Institute of Technology, 2003.

[196] N. Stoop, R. Lagrange, D. Terwagne, P. M. Reis, and J. Dunkel. Curvature-induced symmetry breaking determines elastic surface patterns. *Nature Materials*, 14(3):337–342, 2015.

[197] A. N. Stroh. Steady state problems in anisotropic elasticity. *Studies in Applied Mathematics*, 41(1-4):77–103, 1962.

[198] T. Stylianopoulos, J. D. Martin, V. P. Chauhan, S. R. Jain, B. Diop-Frimpong, N. Bardeesy, B. L. Smith, C. R. Ferrone, F. J. Hornicek, Y. Boucher, et al. Causes, consequences, and remedies for growth-induced solid stress in murine and human tumors. *Proceedings of the National Academy of Sciences*, 109(38):15101–15108, 2012.

[199] A. Sydney Gladman, E. A. Matsumoto, R. G. Nuzzo, L. Mahadevan, and J. A. Lewis. Biomimetic 4D printing. *Nature Materials*, 15(4):413–418, 2016.

[200] L. A. Taber and R. Perucchio. Modeling heart development. *Journal of Elasticity*, 61(1):165–198, 2000.

[201] M. Taffetani and P. Ciarletta. Beading instability in soft cylindrical gels with capillary energy: Weakly non-linear analysis and numerical simulations. *Journal of the Mechanics and Physics of Solids*, 81:91–120, 2015.

[202] T. Tanaka, S.-T. Sun, Y. Hirokawa, S. Katayama, J. Kucera, Y. Hirose, and T. Amiya. Mechanical instability of gels at the phase transition. *Nature*, 325(6107):796–798, 1987.

[203] G. Taylor. The instability of liquid surfaces when accelerated in a direction perpendicular to their planes. I. *Proceedings of the Royal Society of London A: Mathematical, Physical and Engineering Sciences*, 201(1065):192–196, 1950.

[204] D. Terwagne, M. Brojan, and P. M. Reis. Smart morphable surfaces for aerodynamic drag control. *Advanced Materials*, 26(38):6608–6611, 2014.

[205] I. Tokarev and S. Minko. Stimuli-responsive hydrogel thin films. *Soft Matter*, 5(3):511–524, 2009.

[206] L. Treloar. The elasticity of a network of long-chain molecules. I. *Transactions of the Faraday Society*, 39:36–41, 1943.

[207] L. Treloar. The elasticity of a network of long-chain molecules. II. *Transactions of the Faraday Society*, 39:241–246, 1943.

[208] L. Treloar. Stress-strain data for vulcanized rubber under various types of deformation. *Rubber Chemistry and Technology*, 17(4):813–825, 1944.

[209] C. Truesdell and W. Noll. The Non-Linear Field Theories of Mechanics. *Handbuch der Physik*, 2:1–541, 1965.

[210] M. Van Loocke, C. G. Lyons, and C. K. Simms. A validated model of passive muscle in compression. *Journal of Biomechanics*, 39(16):2999–3009, 2006.

[211] A. Wang and A. Ertepinar. Stability and vibrations of elastic thick-walled cylindrical and spherical shells subjected to pressure. *International Journal of Non-Linear Mechanics*, 7(5):539–555, 1972.

[212] H. M. Wang, X. Y. Luo, H. Gao, R. W. Ogden, B. E. Griffith, C. Berry, and T. Wang. A modified Holzapfel-Ogden law for a residually stressed finite strain model of the human left ventricle in diastole. *Biomechanics and Modeling in Mechanobiology*, 13(1):99–113, 2014.

[213] R. Wang and R. L. Gleason. Residual shear deformations in the coronary artery. *Journal of Biomechanical Engineering*, 136(6):061004, 2014.

[214] Z. Wesolowski. Stability of an elastic, thick-walled spherical shell loaded by an external pressure. *Archiwum Mechaniki Stosowanej*, 19:3–23, 1967.

[215] D. R. Wilkie. The mechanical properties of muscle. *British Medical Bulletin*, 12(3):177–182, 1956.

[216] E. Yamamoto, W. Iwanaga, H. Miyazaki, and K. Hayashi. Effects of static stress on the mechanical properties of cultured collagen fascicles from the rabbit patellar tendon. *Journal of Biomechanical Engineering*, 124(1):85–93, 2002.

[217] Y.-P. Zheng, A. F. T. Mak, and B. Lue. Objective assessment of limb tissue elasticity: development of a manual indentation procedure. *Journal of Rehabilitation Research and Development*, 1999.

[218] J. Zhu, H. Stoyanov, G. Kofod, and Z. Suo. Large deformation and electromechanical instability of a dielectric elastomer tube actuator. *Journal of Applied Physics*, 108(7):074113, 2010.

[219] G. Zurlo and L. Truskinovsky. Printing non-euclidean solids. *Physical Review Letters*, 119:048001, 2017.